MANNED SPACE FLIGHT EXPERIMENTS SYMPOSIUM

Gemini Missions III and IV

AUDITORIUM OF THE MUSEUM OF NATURAL HISTORY
10 TH. AND CONSTITUTION AVE., N.W.
WASHINGTON, D.C.   OCT. 18-19, 1965

NATIONAL AERONAUTICS AND SPACE ADMINISTRATION

FOREWORD

This is a compilation of papers on in-flight experiments presented at the first symposium of a series, Manned Space Flight Experiments Symposium, sponsored by the National Aeronautics and Space Administration. The results of experiments conducted during the Gemini Missions III and IV are covered. These symposiums are to be conducted for the scientific community at regular intervals on the results of experiments carried out in conjunction with manned space flights.

CONTENTS

INTRODUCTORY REMARKS — GEMINI EXPERIMENTS SYMPOSIUM

By George E. Mueller, Ph.D.
Associate Administrator for Manned Space Flight
NASA Headquarters

I would like to welcome all of you on behalf of NASA. This is the first of a series of symposia that will be held to report the results of Manned Space Flight experiments. We hope to hold such symposia at regular intervals, ordinarily within 90 days after the completion of a mission.

One of the fundamental objectives of the U.S. space program, spelled out in the National Aeronautics and Space Act of 1958, is the widest practicable dissemination of information about our space activities and their results. This series of symposia is aimed at accomplishing that objective.

The successful conduct of experiments on the first two manned Gemini flights marks a milestone in the program, in that it has demonstrated that we can make use of man's special characteristics for this purpose, even while we are perfecting the techniques of flying a new spacecraft system and learning its special characteristics. We have obtained significant results even while we were learning how to use the equipment.

We should keep in mind that some of the results to be reported are, of necessity, tentative. This is true for two reasons: first, the experimenters intend to make further analysis of the data they have obtained; and second, a number of these experiments will be repeated on future missions. The data will not be complete until all of the missions have been conducted.

But even recognizing the tentative nature of these results, I believe we can draw two important general conclusions from the Gemini III and Gemini IV experiments. The first of these are the data on man himself — the confirming results that the astronauts can adapt to the special environment of space and perform useful and effective work. The medical results of Gemini III and Gemini IV, and further substantiation from Gemini V — although the latter results are not being reported today — give great confidence that the manned space flight effort can move on as we have planned, without the introduction of requirements such as artificial gravity aboard the spacecraft.

The second is that there is further substantiation of the evidence provided in the Mercury program that man, with his ability to reason and recognize patterns, can see things in space that we do not program on instruments to see. On this point, I invite your attention particularly to the astronomy paper, first on today's program, by Drs. Dunkelman, Gill, and Roach.

The third general conclusion to be drawn from these experiments is that the outstanding quality of earth photographs that can be obtained from space goes a long way toward the demonstration of the feasibility of a number of significant applications of manned space flight for the improvement of life here on earth.

In the paper to be presented by Dr. Lowman, for example, you will learn of how synoptic terrain photographs have added to the store of knowledge of the geological structure of parts of North America and Africa. If we can increase our knowledge of geology, it follows that we can use this knowledge in the search for new sources of water, oil, and the other products of the earth that are so important to man's well being.

You will also see photographs that demonstrate how we can understand the oceans better by observation from space. Here again is an opportunity to increase knowledge in an area directly related to the welfare of the whole human race.

Lastly, the series of experiments being reported today on spacecraft technology and space environment provides extremely valuable data for future spacecraft design and operation, as well as a confirming understanding of designs already being prepared for flight.

The results of the experiments on these first two Gemini flights permit us to proceed with greater confidence in the definition of the Apollo Applications Program, in which we plan to employ the hardware and capabilities of the Apollo system for a number of missions other than the basic Apollo Program.

Finally, I would like to thank all of the experimenters for their response to our request for reports at this time. The American people are entitled to prompt reports of the results. We are started well along the road to filling their requirements.

Now let us proceed with the symposium.

1. GEO-ASTRONOMICAL OBSERVATIONS

By L. Dunkelman
Institute for Defense Analyses, Arlington, Va., and
NASA Goddard Space Flight Center

J. R. Gill, Ph. D.
Office of Space Science and Applications,
NASA Headquarters

Lt. Col. J. A. McDivitt
NASA Manned Spacecraft Center

F. E. Roach, Ph. D.
Institute of Telecommunication Science and Aeronomy,
Boulder, Colorado

Lt. Col. E. H. White II
NASA Manned Spacecraft Center

ABSTRACT

36101

The nature of airglow, aurora, zodiacal light, the twilight
scene and of other celestial phenomena are reviewed in conjunction with
observations made from manned spacecraft, and particularly from the
62-orbit Gemini IV mission of June 3-7, 1965. A progress report of ob-
servations on the following is made: zodiacal light, meteors (below
the spacecraft), auroras (over South Australia), nightglow, and twilight
horizon blue bands (first observed from Mercury 8 in October, 1962.)
The photographs of these bands were taken during orbits of Gemini IV.

INTRODUCTION AND SUMMARY

The Gemini IV mission was sufficiently lengthy -- in time -- to
permit repeated observations of sky phenomena under conditions largely
similar. The manned Mercury orbital flights had established the fol-
lowing general features:

(1) The night airglow band (which had been referred to as a "haze layer" by the Mercury 6 and the Mercury 7 astronauts) is, on the night side of the earth, visible at all times.

(2) Twilight is characterized by a brilliant, banded, multi-colored arc which extends along the horizon in both directions from the position of the sun.

(3) As seen through the Mercury window, the faintest stars observed at night, even under relatively ideal conditions, were described as of the fifth magnitude. However, from Gemini IV identification was made of even seventh magnitude stars in the southern constellation of Corona Australis. This identification was made through the right-hand pilot's window, which was of optical quality. However, any observation of stars under daylight conditions (ref. 1) continued to be (from Gemini IV) very difficult, if not impossible.

New or unique observations made by the Gemini IV astronauts, however, concerned:

(1) The structure of nightglow

(2) Polar auroras

(3) Meteors

(4) Photography of certain twilight bands

The Gemini IV astronauts employed the sextant (ref. 2) to make numerous measurements of the width of the nightglow. They also con-firmed results obtained by other means: (1) visually during the Mercury 7 mission (ref. 3), (2) photographically during the Mercury 9 mission (refs. 4 and 5), and (3) photoelectrically, since 1955, on many rocket flights (ref. 6).

Another dim, sky phenomenon, the zodiacal light, was identified also by Gemini IV, and was described as a "shaft of light." It was seen for a brief interval just before the sun came up. This zodiacal light had been seen first from Mercury 7. An artist's conception of this light is shown in figure 1-1. An isophotal map showing the rela-tive intensities of this light and of the "counter flow" (Gegenschein) plotted in polar coordinates is shown in figure 1-2.

Pertinent data were obtained also from the debriefing of the flight crew aboard the "Wasp" on June 9, 1965, also from onboard voice tape, from debriefing concerning the experiments, and from color photographs originally made on 16-mm film.

The Night Glow

The night glow (refs. 7 and 8) is also called night airglow. It has been described by all orbiting astronauts as layer-like. This night-glow layer is ever-present on the night horizon. It is illustrated in figures 1-3a, 1-3b, and 1-3c. Please observe figure 1-4 in this connection, to compare the brightness of the night glow with other features of the day and night skies.

The appearance of this airglow structure is illustrated in the sketch below:
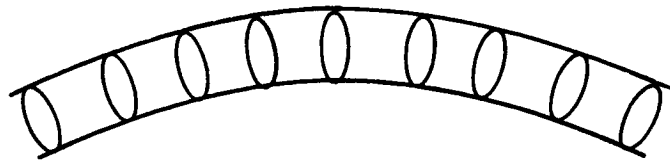
Astronaut Sketch from Gemini IV Logbook of Airglow Structure.

Even a rough estimate of the linear scale of the "flutings" is of interest for comparison with the structure of air-glow features deduced from ground observations. For example, assuming a height of 230 km, the air-glow circle is at a distance of 1687 km. At this distance a 1°-detail corresponds to $\frac{2\pi \times 1687}{360}$ = 29.4 km and a 10°-detail, to 294 km.

It seems reasonable that an astronaut looking through a window at a field of some tens of degrees width would record structural detail in the air glow layer only if the angular spacing were somewhere between the 1° and 10° numbers given above, and corresponding to linear dimensions between, say, 30 and 300 km. Ground observations over the years have suggested a large air-glow structure with patterns up to 2500 km in extent. Also on occasion smaller structural "cells" have been observed from the ground. Their sizes were in the 100-200 kilometer range (ref. 9).

Gemini IV observations of the Earth horizon confirm the observation made from the Mercury 9 mission that, under conditions of "no moon", the Earth horizon can be delineated. Gemini IV observations of the moonless night scene are summarized thus: There are three horizon bands. The top one is a bright night-glow band and is viewed "edge-on." The second band is more dimmed, while the third band is the faintest, or darkest, of the three. These differences in luminosity are due to differences in path length through the airglow.

The Polar Aurora

On two occasions the Gemini IV astronauts observed curtain-like phenomena that probably were polar auroras.

From the Earth surface the sighting of an aurora (Auroral Map, fig. 1-5) between geographic latitudes 33° N and S is relatively infrequent. Thus it becomes pertinent to inquire whether the Gemini IV sightings were due to the favorable position of that spacecraft.

One general advantage of that position is immediately apparent, namely the fact that from a spacecraft, it is possible to see from 13° (at perigee) to 17° (at apogee) farther along the earth's surface; thus, the extreme latitudes widen to around 50°. A second advantage is that the geomagnetic pole is some 11° from the geographic pole; thus at two parts of the orbit a "horizon" at a geomagnetic latitude of 61° becomes possible. This extreme possibility corresponds to an apogee sighting at the horizon over that part of Earth where the orbit is closest to either the north (western Atlantic) or the south (Australian) geomagnetic pole. Actually the optimum position is the latter, since apogee occurred in the southern hemisphere. The sightings were actually made over Australia and in precisely those regions that we might have anticipated (but did not).

The astronauts' report indicates that they saw one aurora projected against the solid Earth, and positioned so that the geomagnetic latitude of the phenomenon (assuming they were looking southward from Australia, which is near latitude 45°) was probably about 50° (about 5° south of the spacecraft).

We may now assemble a number of pertinent facts (taken chiefly from reference 7):

(1) At a geomagnetic latitude of 50°, ground sightings of auroras occur less than 5 percent of the time when the observations are normalized to a cloudless and moonless sky. If we take the Yerkes Observatory in the northern hemisphere as a reasonable example of conditions to be expected, auroras as observable there about 6 percent of the time (ref. 7, page 110).

(2) During sunspot minima, visual auroras are only about 25 percent as frequent as during the sunspot maxima (fig. 4.7 in ref. 7). Sunspot minimum occurred about in July, 1964, and activity has now just re-commenced, but only slightly, in the next new cycle.

(3) Auroras are strongly correlated with geomagnetic activity; that is, they are very infrequent where magnetic activity is low.

During the first week of June, 1965, magnetic activity was extremely low (K_p on the average being 1.5).

(4) Auroras occur most frequently during equinoxes (March and September) and most seldom during the solstices (fig. 4.8 in ref. 7).

Thus, all four factors listed above prove unfavorable for sighting an aurora from the ground. Furthermore, the auroral watch at Saskatoon reported no auroras during the first week in June. Our conclusion is that the auroral sightings from Gemini IV were probably the result of its unusually favorable position for making observations, as compared with the less favorable positions for any observers on the ground. The fact that Gemini IV observers reported no color associated with these phenomena suggests that the brightness was IBC I or possibly IBC II. (Colors can be distinguished for auroras of brightness II + or III -.) There is also the possibility that a fainter auroral feature might be visible against dark Earth background as seen from the spacecraft, but not against a night sky as viewed from the ground.

Meteors

Gemini IV astronauts were first to observe meteors in orbit; and they mentioned seeing the meteors precisely where they should have seen them, namely <u>below</u> their own altitude. Meteors on the average — and regardless of their brightness — appear at altitudes from 40 to 60 miles up in the earth's atmosphere. Meteor statistics show that their frequency greatly depends on the season, and that peak activity starts with the Perseid Shower around August 11. These meteor sightings suggest one useful observational experiment for future flights, namely the collection of sample meteoric counts for statistical purposes.

Twilight Bands

On Mercury 8 orbit during twilight, an astronaut made observation, for the first time, of a very remarkable scene. The scene is shown in figure 1-6, which is a black-and-white reproduction of a color painting. The painting was made from the astronaut's description. Moving up from the earth's horizon, first were observed orange bands; next above that came a dark blue band, then a lighter blue band, a dark blue band, and finally, at the top, a very high whitish layer. The transition of this whitish region into black sky resembled the "bottom of a rain cloud." This twilight scene was photographed from Gemini IV in color, through a 16-mm sequence camera. It shows vividly the blue banding described in figure 1-7. Analysis of this twilight scene is not yet finished. The structure in the foreground (lower left corner) is similar to that

recently reported (ref. 10) by a Russian astronaut who photographed it (in black-and-white) on June 17, 1963, from Vostok-6. Both the twilight aureole, and analysis, indicated two aerosol layers at 11.5 ± 1 km and 19.5 ± 1 km, respectively.

CONCLUSIONS

The implications of these Gemini IV observations and measurements contain suggestions for future flights, namely

(1) Statistical counts of meteors

(2) Photography of auroras

(3) Photography of airglow structures

(4) Probing of atmosphere by twilight measurements

(5) Photometry of the day sky

(6) Coordination of the results — with data from unmanned satellites.

(7) Further development of optical weather research.

In addition, observations to date are adding more data to this scene from space as shown in table 1-I. Table 1-II also lists phenomena and their luminance for each source. This table provides also a convenient reference for familiar objects in the visible region. Table 1-II lists ultra-violet phenomena which need further observations made by means of image converters (ref. 11). This table may serve as a guide when looking ahead to extra-vehicular activity or to the use of appropriate airlocks or of suitable windows.

REFERENCES

1. O'Keefe, J. A., Dunkelman, L., Soules, S. D., Huck, W. F., and Lowman, P. D., Jr.: Observations of Space Phenomena in Mercury Project Summary Including Results of the Fourth Manned Orbital Flight. May 15 and 16, 1963. NASA SP-45. Supt. Doc., U.S. Government Printing Office (Washington, D.C.), 1963, pp. 327-347.

2. Vallerie, E. M.: D-9 Experiment, Simple Navigation on Gemini IV. Paper 8 of Manned Space Flight Symposium on Results of Experiments for Gemini III and IV Missions.

3. Carpenter, M. S., O'Keefe, J. A., and Dunkelman, L.: Visual Observations of Nightglow from Manned Spacecraft. Science, vol. 138, 1962, pp. 978-980.

4. Gillett, F. C., Huch, W. F., Ney, E. P., and Cooper, G.: Photographic Observations of the Airglow Layer. J. Geophys. Res. vol. 69, 1964, pp. 2827-2834.

5. Hennes, J., and Dunkelman, L.: Photographic Observations of Nightglow from Rocket. Submitted to J. Geophys. Res.

6. Koomen, M. J., Gulledge, I. S., Packer, D. M., and Tousey, R.: Night Airglow Observations from Orbiting Spacecraft Compared with Measurements from Rocket Observations. Science, vol. 140, 1965, pp. 1087-1089.

7. Chamberlain, Joseph. W.: Physics of the Aurora and Airglow. New York, Academic Press, 1961.

8. Roach, F. E.: The Light of the Night Sky; Astronomical, Interplanetary, and Geophysical. Space Sci., vol. 3, 1964, pp. 512-540.

9. Roach, F. E.: Annales de Geophysique 17. Vol. 172, 1961.

10. Rozenberg, G. V., and Nikolaeva-Teleshkova, V.V.: Stratospheric Aerosole Measured from a Spaceship. Academy of Sciences, USSR, Izvestya, Atmospheric and Oceanic Physics, vol. 1, 1965, pp. 386-394.

11. Dunkelman, L., and Henners, J.: Ultraviolet Photography and Spectroscopy Using a Spectrally Selective Image Converter. Supplement to the Japanese J. Applied Physics, 1965.

TABLE 1-I.- LUMINANCE OF PHENOMENA

Phenomenon	Luminance, candles cm^{-2}
Milky Way, dimmest region, near Perseus	1×10^{-8}
Gegenschein	1.6×10^{-8}
Visible night glow (zenith)	2×10^{-8}
Aurora IBC-I	$\sim 2 \times 10^{-8}$
Milky Way brightest region, near Carina	4×10^{-8}
Zodiacal light (30° elongation)	1.2×10^{-7}
Visible night glow (edge-on)	6×10^{-7}
Great Orion nebula M42	5.6×10^{-6}
Full Moon	4×10^{-1}
Fluorescent lamp 4500 white	4×10^{-1}

TABLE 1-II.- RADIANCE OF PHENOMENA

Phenomenon	Radiance, ergs sec^{-1} cm^{-2} $ster^{-1}$
Middle UV night glow (nadir), 2600A	2×10^{-5} per 100A
Orion nebulosity (mean), 1225-1350A	6×10^{-5} per 100A
Orion nebulosity (most intense part), 1225-1350A	4×10^{-4} per 100A
Middle UV nightglow (edge-on), 2600A	5×10^{-4} per 100A
Hydrogen Lyman-alpha glow (mean), 1216A	3×10^{-3}
UV Aurora, Wallops Is., Nov. 22, 1960 (zenith), 1700-1800A	10^{-2}
UV Aurora, Wallops Is., Nov. 22, 1960 (zenith), 1300-1800A	10^{-1}
Sunlit earth albedo (nadir), 2600A	5×10^{-1} per 100A

Figure 1-1. - The Zodiacal light and the solar corona.
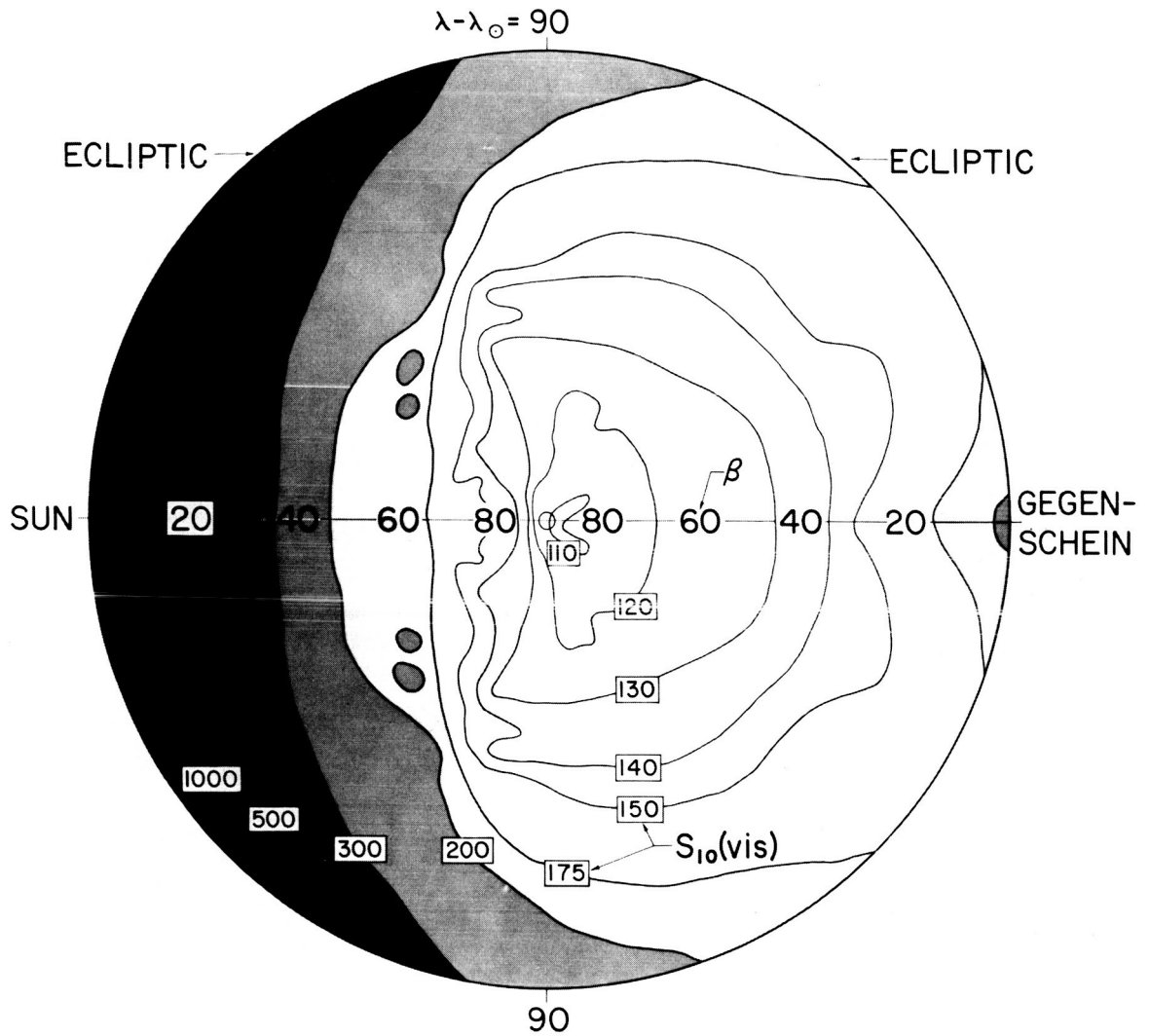
Figure 1-2.- Isophotal map of the Zodiacal light in Polar coordinates.
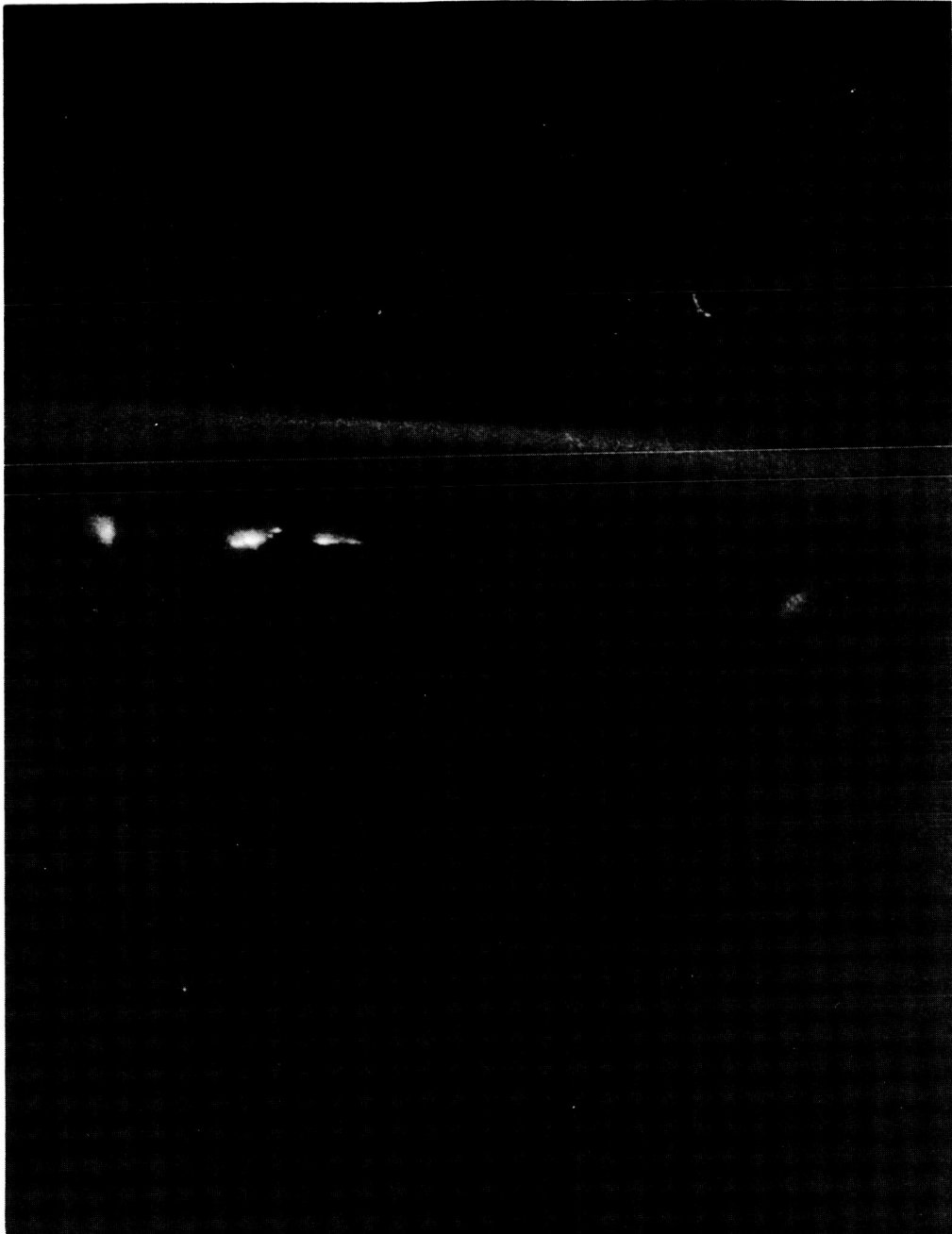
(a) Photographs from Mercury-Atlas 9 orbits.

Figure 1-3.- Airglow layer.
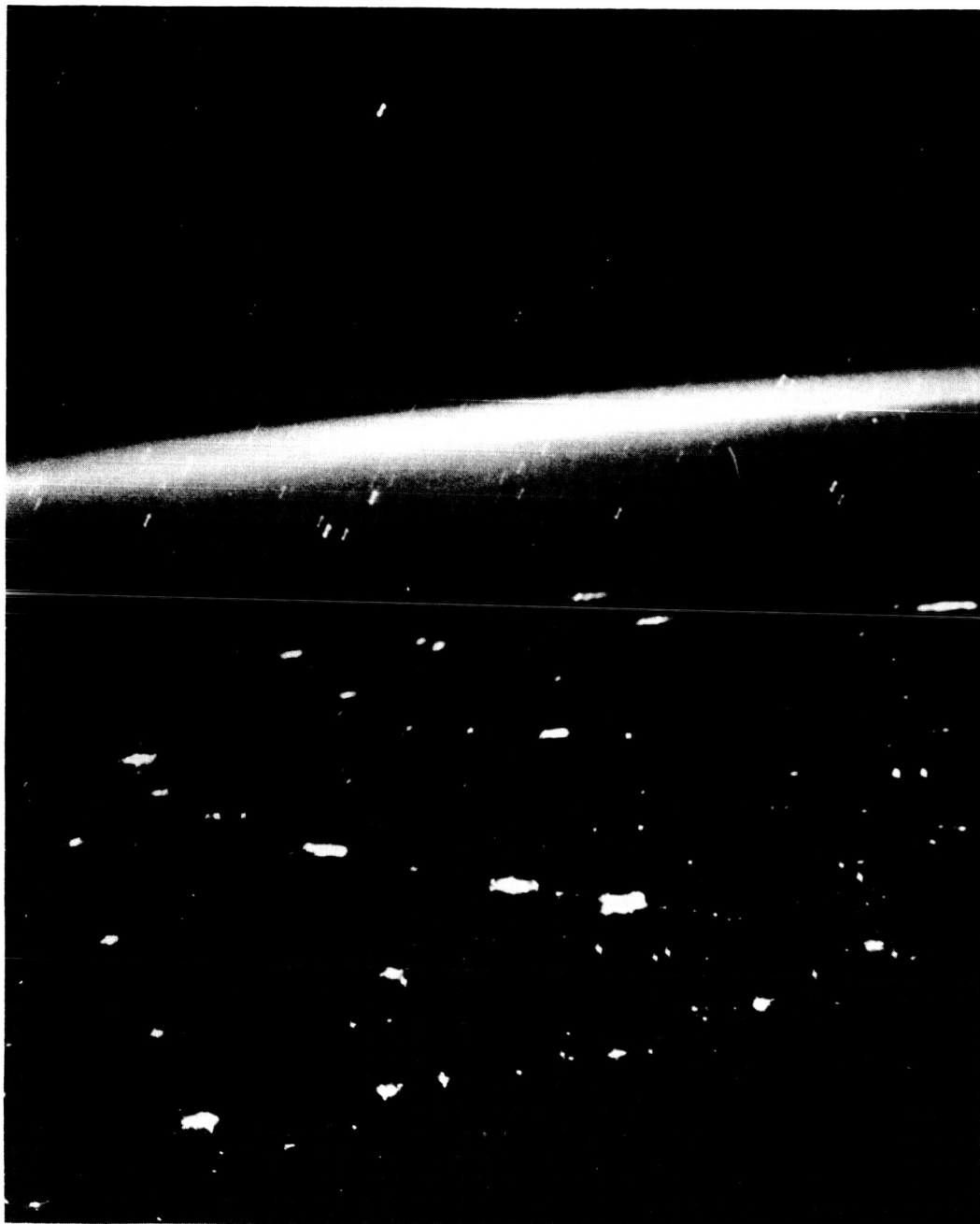
(b) Photograph of nightglow taken above Texas
from Aerobee rocket, November 30, 1964.

Figure 1-3.- Continued.
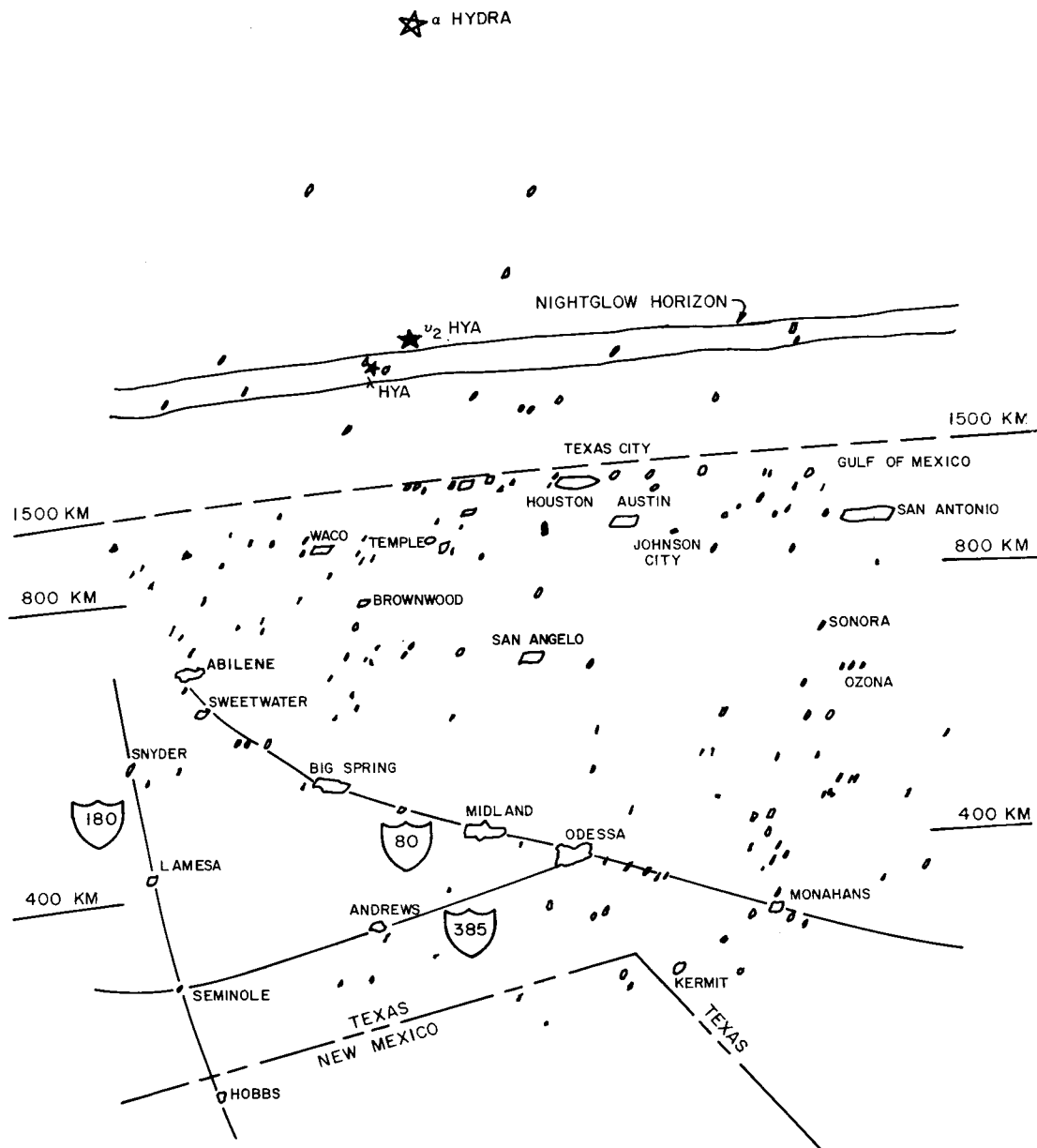
(c) Drawing of scene of figure 13(b) showing prominent ground features.

Figure 1-3.- Concluded.
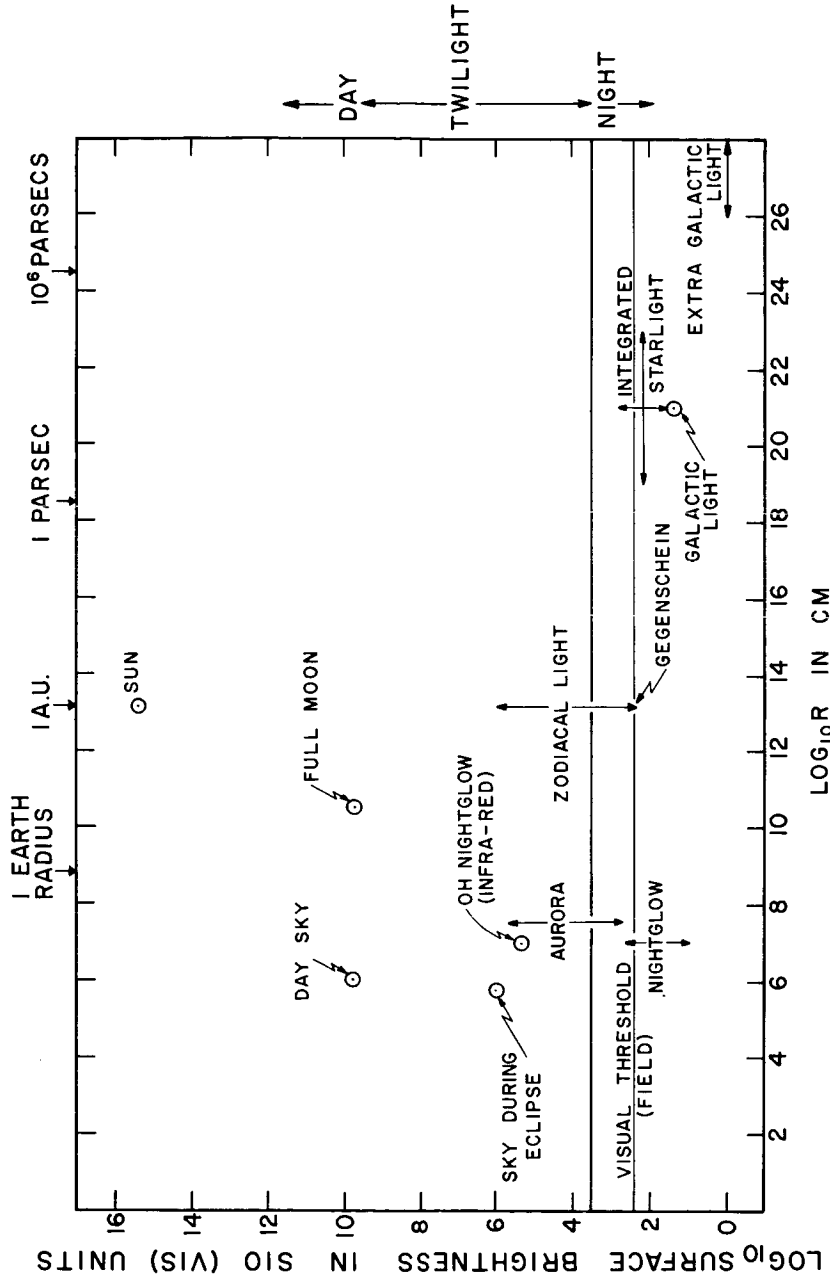
Figure 1-4.- Graphical representation of the brightness of components and features of both the day and night skies with the cosmic occurrence indicated by the distance of each along the Abscissa.
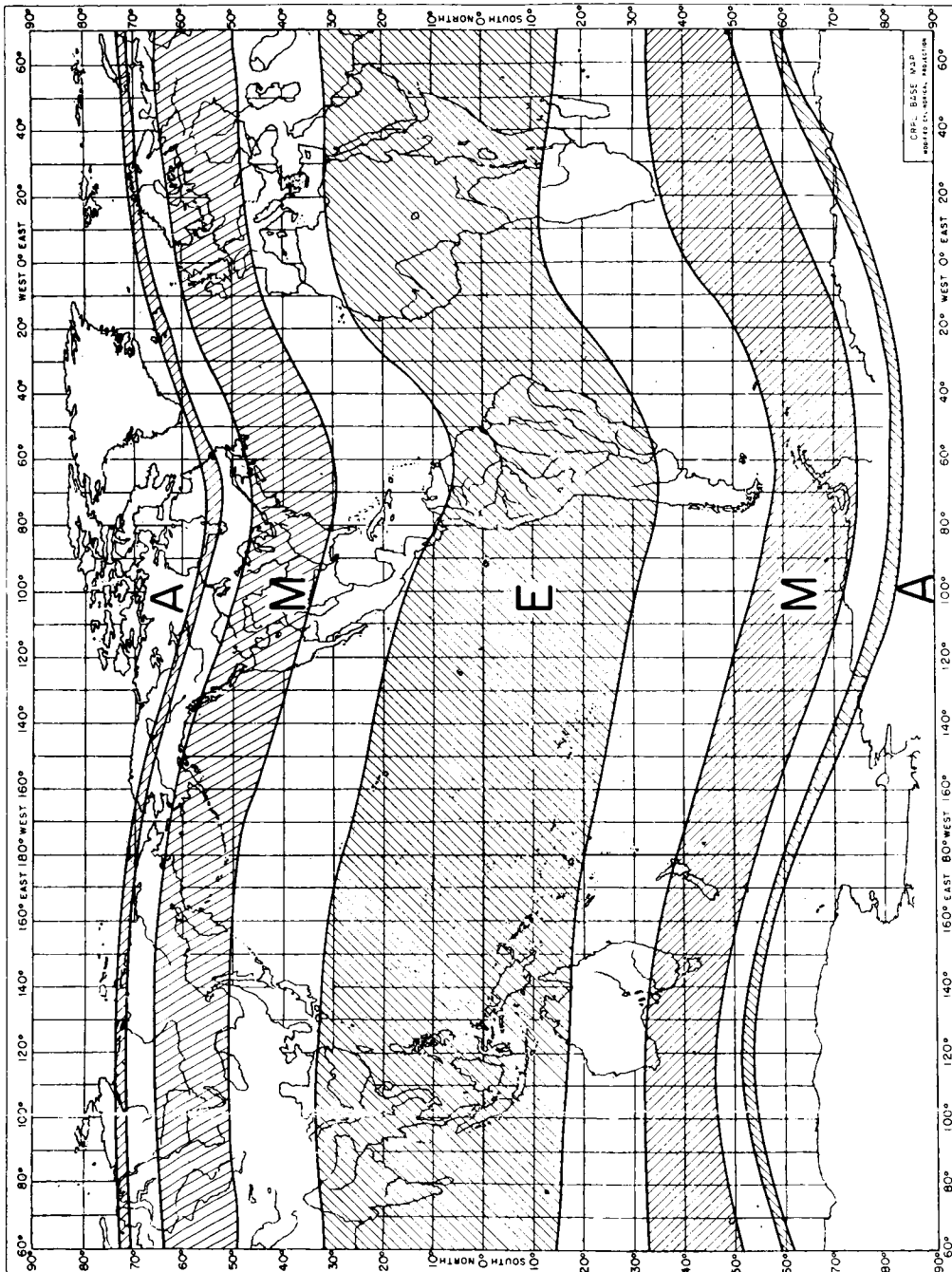
Figure 1-5.— Auroral map as seen from earth.

Figure 1-6.- Painting made from a Mercury 8 description of blue bands in twilight zone.
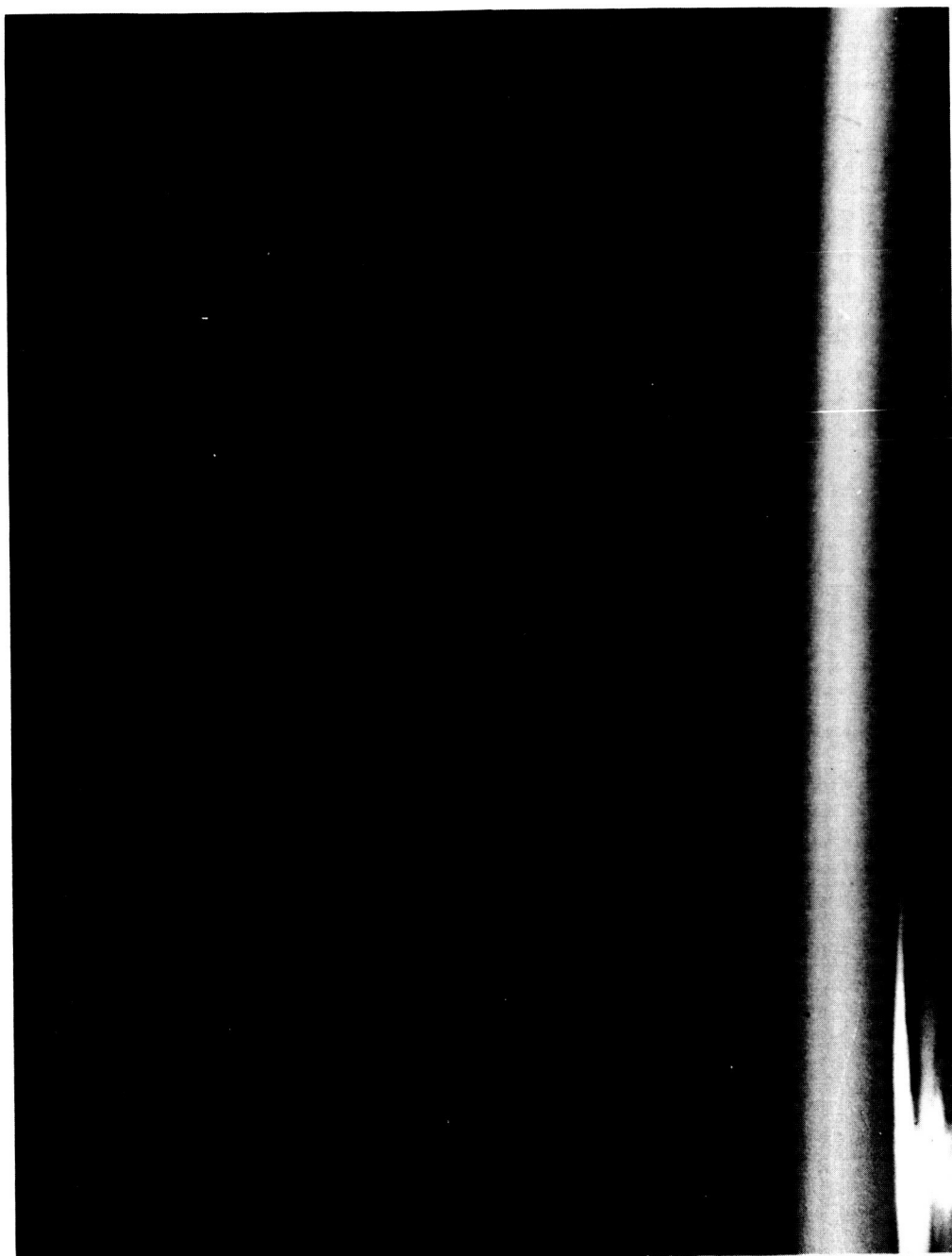
Figure 1-7.- Print from 16-mm color film exposed in Gemini IV and showing twilight bands.

2. EXPERIMENT S-5, SYNOPTIC TERRAIN PHOTOGRAPHY DURING GEMINI IV

Paul D. Lowman, Jr., Ph.D.
NASA Goddard Space Flight Center

The S-5, Synoptic Terrain Photography, experiment was successfully conducted during the Gemini IV mission. The purpose of this report is to summarize briefly the results of the experiment and to discuss some of the possible uses for the pictures taken during the mission. A NASA Technical Note describing the pictures more fully is in preparation.

The five magazines of 70-mm Ektachrome film exposed during the Gemini IV mission included approximately 100 pictures usable for terrain studies. Most are of excellent quality with respect to exposure, resolution, and orientation. It was requested that priority be given to photography of East Africa, the Arabian peninsula, Mexico, and the southwestern United States; pictures of all these areas were obtained. Spacecraft fuel and power restrictions prevented the flight crew from always orienting the spacecraft vertically, as preferred for photography. However, a continuous series of pictures with near-vertical orientation was taken. This series covered the flight path on the 32nd revolution from the Pacific coast of Mexico to central Texas.

The locations and times of all 70-mm Hasselblad pictures are listed in "Gemini IV 70-mm Photography: PTL Production Control Library, 8/27/65," issued by the Manned Spacecraft Center. A detailed description of all the terrain photographs would be beyond the scope of this report; instead, representative pictures are presented and briefly discussed.

Figure 2-1, the first of the series taken over Mexico and the United States during the 32nd revolution, shows an area about 75 miles on a side in Baja California; Bahia de Todos Santos, on the Pacific coast of Mexico, is visible at the lower left.

A large amount of geologic detail is visible in the picture. The contact between Quaternary alluvium (light colored material at upper and center right) and bedrock is easily drawn. A number of different igneous rock types can be distinguished on the basis of color, although they could not be identified on the basis of this picture alone. Perhaps the most striking geologic feature shown is the long linear valley

at lower left, parallel to the edge of the spacecraft window. This valley, immediately identified as a fault even on a preliminary examination of the picture, in fact follows the Agua Blanca fault zone, one of the major tectonic features of Baja California. A number of linear valleys, either parallel to the Agua Blanca fault zone or intersecting it, are apparent, and they presumably represent subsidiary faults.

The potential value of hyperaltitude photography for regional tectonic studies is illustrated strikingly by the fact that this fault, so obvious from space, was not discovered until 1956 (ref. 1), and then, interestingly enough, from aerial reconnaissance. The most recent prior authoritative publication on the geology of Baja California (ref. 2, 1948) gives no hint of the existence of the fault, nor does it show more than one rock type. Oddly enough, figure 2-1 shows no evidence of what was mapped (ref. 2) as a probable major fault (the San Pedro Martir fault) bounding the east side of the Sierra de Juarez.

It is likely that figure 2-1 itself will be of value in studying the tectonic structure of Baja California, since it is possible to delineate other faults outside the area mapped and reported in reference 1.

Figure 2-2 was the third photograph taken in the 32nd revolution series. It shows the mouth of the Colorado River entering the Gulf of California; the distance shown is about 70 miles across at the bottom of the picture.

Considerable geologic detail is shown, such as the various rock types near the eastern shore of the gulf and the fault just east of the Colorado River (the southward-trending linear feature outlined in white). Sand dunes in the desert (right) are also visible.

Of particular interest, however, is the amount of detail in the Gulf of California. The sinuous patterns off the river mouth resemble those near the Ganges River, which were photographed on the Mercury-Atlas 9 flight and identified as turbidity currents (ref. 3). However, the Naval Oceanographic Office (ref. 4) has demonstrated that this pattern is actually the bottom topography of the Gulf of California which is only a few feet deep at this point. Although reference 4 finds figure 2-2 unsuitable for actual depth mapping, it points out that the synoptic view of sediment distribution provided by the spacecraft altitude is of great interest to oceanographers.

Fifth in the 32nd revolution series, figure 2-3 shows part of the Gulf of California (left), the Pinacate volcanic field (center), and part of Yuma County, Arizona (upper right). The photograph is of geologic value in several respects. In addition to the submarine topography

in the Gulf of California previously mentioned, many major structural and lithologic features are obvious.

The most striking of these features is, of course, the Pinacate volcanic field. The Pinacate field has been known for hundreds of years; however, it is not delineated on the latest (1960) geologic map of Mexico, which has a scale about equal to that of the Gemini IV photograph. Figure 2-3 could also be used to revise the alluvium-bedrock contacts on the geologic map. Of greater interest, however, is that many bedrock lithologic units can also be differentiated and, with the aid of available geologic maps, identified. In Yuma County, for example, the contacts between Mesozoic granite (light) and Mesozoic schists and gneisses can be traced and, in many places, extrapolated across the Mexican border. The apparent similarity and continuity of granites in the various northwest-trending ranges tend to support the inference (ref. 5) that the entire area is underlaid by one or more batholiths.

From a preliminary study, it appears that most of the geologic detail shown by the 1:375,000 geologic map of Yuma County can be seen on the part of the county covered by figure 2-3 (with an original scale of about 1:2,000,000). Furthermore, some new information may be derived from the Gemini pictures; for example, just north of the Pinacate volcanic field, the bedrock appears to be cut by a series of north-trending fractures, outlined by drainage, which are not shown on the Yuma County map.

Figure 2-4, taken a few minutes later than figure 2-3 in the 32nd revolution, shows portions of southern New Mexico, Chihuahua, and Sonora (Mexico).

Two potential geologic applications of space photography are well illustrated by figure 2-4. The first application, a refinement of existing geologic maps, is typified by the Sierra Carizarilla — the cluster of dark circular hills near the center of the photograph. The mountains are easily identified as volcanoes (for comparison, see fig. 2-3) belonging to a single field. They are probably of relatively young age, judging from their fresh-appearing topography. On the geologic map of Mexico (1960), however, only a few isolated outcrops of volcanic rock are shown, and they are dated as pre-Quaternary (that is, over one million years old).

Another potential use of space photography is suggested by the fact that figure 2-4 covers, at one time, an area in which two major tectonic provinces merge. The linear mountains, at the left, are the continuation of the Sierra Madre Oriental, characterized by folds similar to those in the Appalachians. The mountains at the lower right, however, are chiefly block-faulted mountains, typical of the Basin and

Range Province, and are placed in the Basin and Range class by reference 5. It can be seen that these two types of mountain structure merge without marked change of direction, a relation which could only be realized by extensive field mapping in two countries.

Figure 2-5 was taken during the 25th revolution, looking northwest over the Tibesti Mountains in the Republic of Chad, North Africa. It has been chosen to illustrate the geologic applications of space photography in remote areas.

Despite the unfavorable angle, considerable topographic and geologic detail is visible. The most conspicuous feature is the crater of the volcano Emi Koussi, the highest point in the Sahara. Of equal geologic significance, however, is the concentric lineation pattern in the foreground. This pattern is believed to represent a regional set of fractures, which are emphasized in places by sand deposition. Although these fractures were partially shown on the latest Army Map Service (AMS) map of the area, their existence is not mentioned in any of the relevant geologic publications and apparently is not known to geologists.

Another structure, also shown on the AMS map but geologically unknown, is the circular feature in the center of the picture (about eight crater diameters to the right of the Emi Koussi crater). This structure appears to resemble many of the "fossil" impact craters that Canadian geologists have discovered in the Canadian shield through the study of aerial photography. Although there is no a priori reason for suspecting an impact origin for the Tibesti structure, especially in view of its nearness to a volcanic area, its discovery demonstrates the potential value of space photography in searching for ancient impact structures.

REFERENCES

1. Allen, C. R.; Silver, L. T.; and Stehli, F. G.: Agua Blanca
   Fault-A Major Transverse Structure of Northern Baja California,
   Mexico, Geol. Soc. Am. Bull., vol. 71, Apr. 1960, pp. 457-482.

2. Beal, C. H.: Reconnaissance of the Geology and Oil Possibilities
   of Baja California, Mexico, Geol. Soc. America Memoir 31, 1948.

3. Lowman, P. D.: A Review of Photography of the Earth from Sounding
   Rockets and Satellites, NASA Technical Note D-1868, 1964.

4. Gettys, R. F.: Evaluation of Color Photos Exposed from the Gemini
   (GT-4) Flight over the Gulf of California. Unpublished manuscript,
   Technical Production Department, U. S. Naval Oceanographic Office,
   Washington, D. C., June 1965.

5. Eardley, A. J.: Structural Geology of North America, 2d ed.,
   Harpers, New York, 1962.

Figure 2-1.- Baja California, taken on the 32nd revolution of Gemini IV.
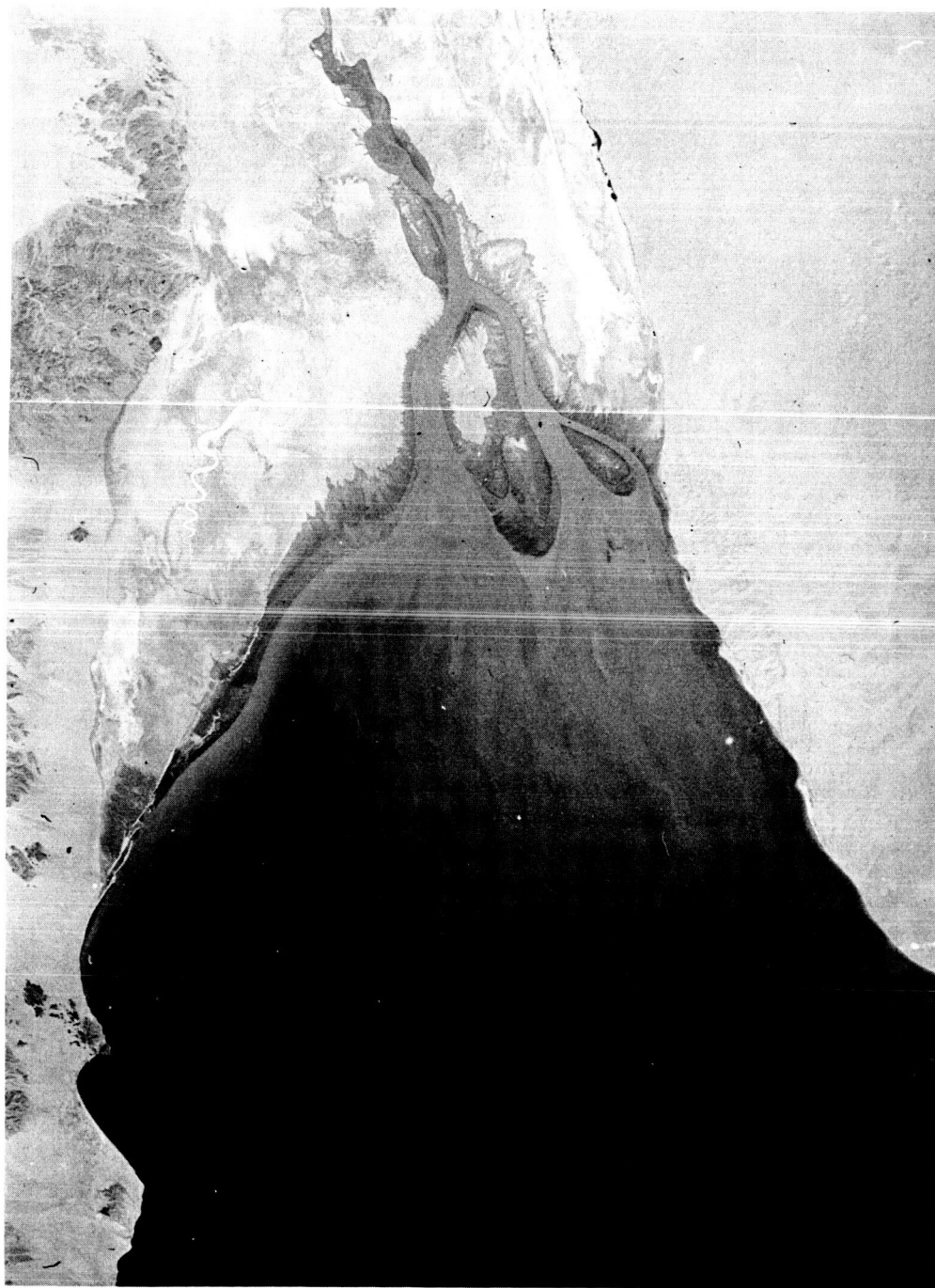
Figure 2-2.- Mouth of the Colorado River at the Gulf of California, taken on the 32nd revolution of Gemini IV.
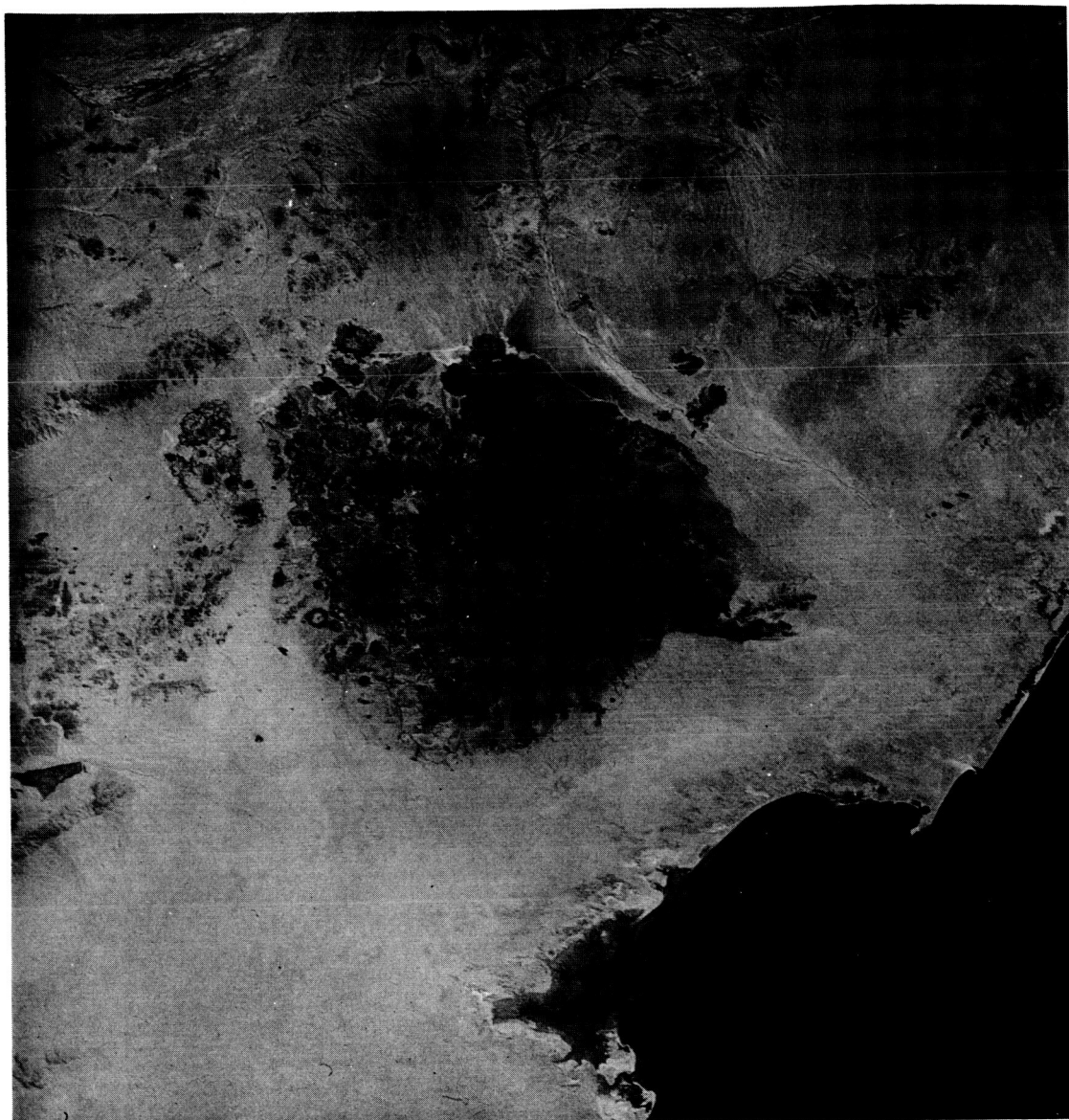
Figure 2-3.- Gulf of California, Pinacate volcanic field, and part of Yuma County, Arizona, taken on the 32nd revolution of Gemini IV.

Figure 2-4. - Southern New Mexico and Chihuahua and Sonora, Mexico, taken on the 32nd revolution of Gemini IV.
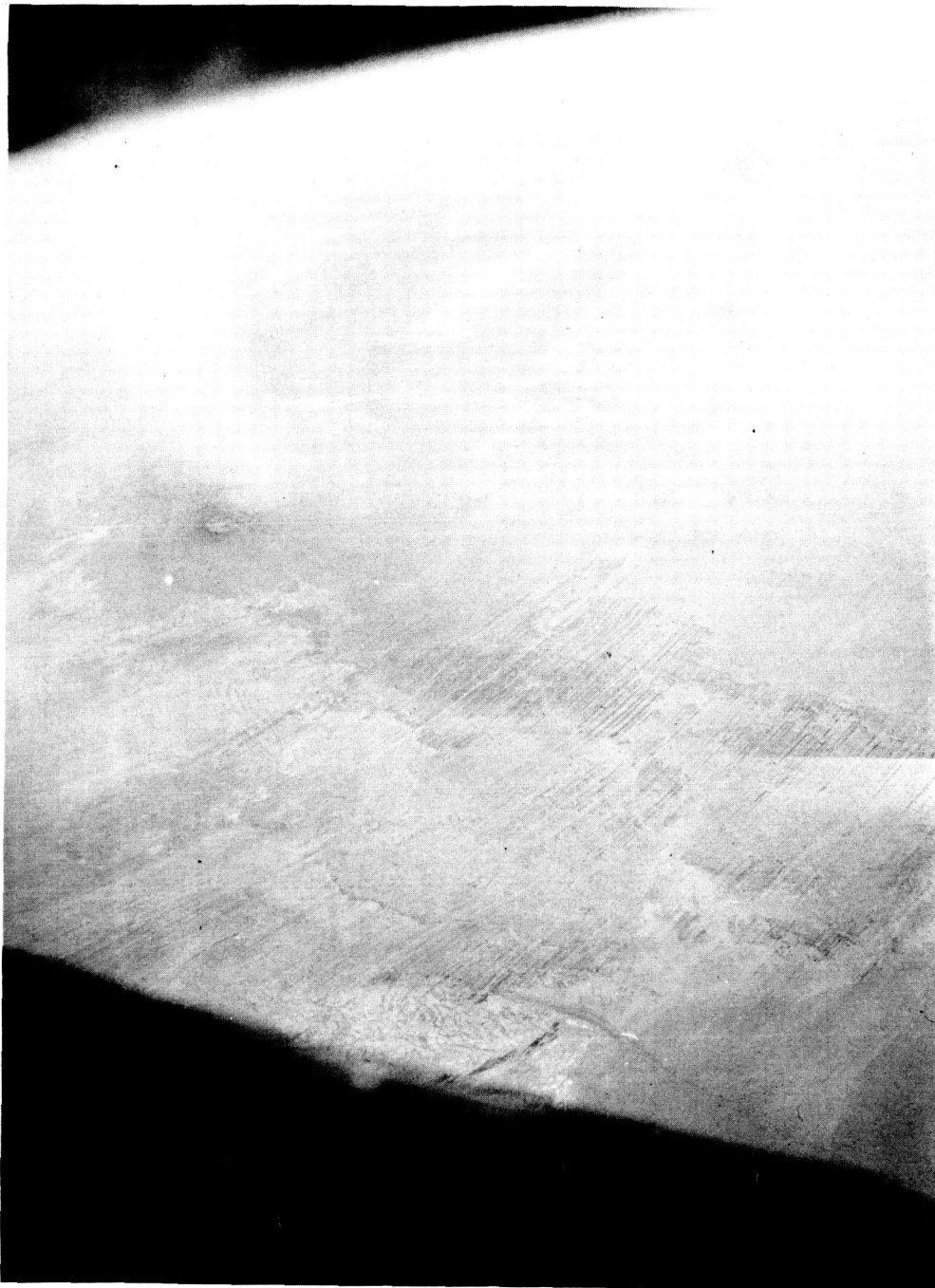
Figure 2-5.- Tibesti Mountains, Republic of Chad in North Africa, taken on the 25th revolution of Gemini IV.

3. EXPERIMENT S-6, SYNOPTIC WEATHER PHOTOGRAPHY

DURING GEMINI IV

By Kenneth M. Nagler
United States Weather Bureau, ESSA
and Stanley D. Soules
Meteorological Satellite Laboratory, NESC, ESSA

SUMMARY

Although many interesting photographs had been previously obtained on the Mercury missions and on the Gemini III mission, the Gemini IV mission was the first of several Gemini missions on which weather photography was specifically scheduled.

With its longer (four-day) mission, and with more film and specific efforts directed toward the photography of weather, the Gemini IV crew obtained a large number of meteorologically interesting pictures.

DESCRIPTION

The S-6 experiment is essentially a data-gathering effort, with the general purpose of providing a set of pictures which would cover a broad range of meteorological phenomena; the more specific purpose was to obtain views of a number of cloud systems that would be of particular interest for various investigators.

In both manned and unmanned Mercury missions and in the Gemini III mission, a number of good pictures of cloud systems were obtained. In addition, specific experiments were performed for Mr. Soules by the astronauts on the Mercury missions. Those experiments examined some of the spectral-reflectance characteristics of clouds, of land, and of water areas of the earth surface when viewed from outside the atmosphere.

With a number of photographs from space, and with the results of specific weather photography experiments already available, and also since there is daily meteorological satellite coverage of the greater

part of the world, one might ask why we want more pictures of earth cloud systems.

Obviously, TIROS satellites are contributing greatly to routine surveillance of earth weather. They are in fact, a primary source of information on which are based forecasts for much of the support of manned spaceflight operations. TIROS pictures, however, are televised from an altitude of 400 miles or more. Some pictures are imperfectly understood because the smaller features cannot be resolved. Therefore, for a number of selected meteorologically interesting cloud systems, it is desirable to have detailed color views obtained from actual photographs taken at lower altitudes and from manned spacecraft. Such pictures can verify and amplify information obtained from the weather satellites. In addition, some pictures are by themselves significant whether or not they can be associated with simultaneous meteorological satellite coverage.

Earth cloud systems vary greatly from time to time and from place to place. The result is a great variety of weather systems which might be understood better were photographs of them available.

Another need which can be satisfied through use of the manned satellites is the depiction of cloud systems at fairly short time intervals. For example, pictures could be obtained on successive revolutions of a Gemini spacecraft, so as to show the changes in, and the movements of, clouds at about 90-minute intervals at certain points over the ground track of the spacecraft.

As a result of the interest shown within the Weather Bureau and elsewhere, a weather photography experiment was proposed to the National Aeronautics and Space Administration for the Gemini program. This proposal was accepted for the Gemini IV, V, VI, and VII missions and also, tentatively, for one or two of the later Gemini missions, with the authors of the proposals as co-experimenters.

The experiments resulting were planned to use the same Hasselblad camera, (Model 500C) used in the S-5 Synoptic Terrain Photography experiment. Also the same 70-mm Ektachrome MS film was to be used. A total of five film magazines, each with film sufficient for 55 exposures, was carried on the spacecraft and was to be used on the S-5 and S-6 experiments and for general photography. To reduce the intensity of the blue light scattering back from the atmosphere, a haze filter was fitted to the standard 80-mm f2.8 lens.

Well in advance of the flight, a number of meteorologists (primarily from the National Weather Satellite Center) were queried as to the types of cloud system they would like to see and as to what particular earth

geographical areas were of interest. Several months before the flight, the aims of the experiment were discussed in detail with the flight crew. Approximately a dozen specific types of cloud were suggested as possibilities for interesting viewing on their mission. These types included cellular patterns, vortices in the lee of subtropical islands, thunderstorms, sunglint, shadows of cirrus clouds on lower cloud layers, intertropical convergence areas, and tropical storms.

The manned-satellite mission plan was arranged so that the pilots could devote part of their time to this cloud photography over the pre-selected areas. On the day preceding launch the pilots while at Cape Kennedy were briefed on several interesting features likely to be seen on their mission. This information was later revised and given to them again just shortly before they entered the spacecraft. During the mission, areas of interest were selected from time to time from weather analyses and from TIROS pictures. Whenever operationally feasible, this information was communicated to the crew from the Manned Spacecraft Center at Houston, Texas, well in time for them to locate and to photograph the clouds in question, provided this did not interfere with their other duties. So long as fuel was available for changing the attitude of the spacecraft for this purpose, the pilots were able to search for the desired locations. Otherwise, they could take pictures only of those scenes which happened to come into view.

RESULTS

In all, the pilots took a total of nearly 200 70-mm color pictures. Of these, about half displayed cloud formations or contained information of other meteorological interest. A selection from these 200 views is shown here, to illustrate the types of picture obtained.

Figure 3-1, a view of southern Florida, shows cumulus cloudiness over the land areas typical for during the day. The absence of cumulus clouds over most of the adjacent ocean area and over Lake Okeechobee is quite apparent.

In figure 3-2, Acklin's Island and Crooked Island in the Bahamas are shown nearly enclosing a shallow lagoon. To the left of the picture, the reflection of the sun from the sea surface is interrupted by the tiny dark shadows of clouds, which themselves cannot be seen against the brightly reflecting waters. Long-period swells are discernible near the edges of the sunglint area.

In figure 3-3 is a widespread area of cloudiness typical of disturbed tropical areas. This view was taken near latitude 16° N and longitude 178° E.

Figure 3-4 shows several vortices in the lee of some of the Canary Islands. Pictures from TIROS had often shown vortices in the lee of mountainous subtropical islands, but the fine cumulus lines which now delineate the eddy motion found in this view were quite too fine to be detected from TIROS.

Figure 3-5 shows convective cellular clouds over the Central Northern Pacific. Such cellular patterns had been observed in weather-satellite pictures over many areas of earth. They result from weakly organized convection currents in the absence of any significant vertical wind shear. Of particular interest in this picture are the vortices appearing along the boundaries of the cells. Such vortices had not been apparent in TIROS views.

Figure 3-6 was actually taken as part of a Terrain Photography experiment; but it is of interest also to the meteorologist. This view is from over central Texas. It depicts the area to the North and West of San Angelo. It shows two large dark areas which are due not to differences in the geographical or land usage, but a heavy rainfall on the previous day. In lighter areas, little or no rain had fallen during that period.

With the many different types of weather systems here of interest, and with the day-to-day and the seasonal changes in weather, there remain many meteorological features which we hope to have photographed during future missions. The crew of Gemini IV was not able to obtain views of the same area on successive passes. However, these views were obtained on Gemini V, and we hope it will be repeated during future flights.

In summarizing the results from these pictures, we do not expect to see some new breakthroughs in meteorology, abruptly bringing about a more accurate forecasting of certain weather phenomena. But we do expect these pictures to contribute to a better understanding of meteorological satellite pictures. These pictures have also stimulated a great deal of interest in cloud views on the scale obtainable from a Gemini altitude. Many meteorologists wish to study these pictures in connection with various atmospheric processes with which they are concerned. Also, other groups are interested in applying these pictures as teaching aids.

BIBLIOGRAPHY

Nagler, K. M.; and Soules, S. D.: Cloud Photography from the Gemini IV
     Spaceflight.   Bulletin of the American Meteorological Society.
     Sept. 1965.

Hope, John R.: Path of Heavy Rainfall Photographed from Space.   U. S.
     Weather Bureau Report (to be published).

Figure 3-1.- View looking southwestward across southern Florida
with Grand Bahama Island in the left foreground and Cuba in the
left background.
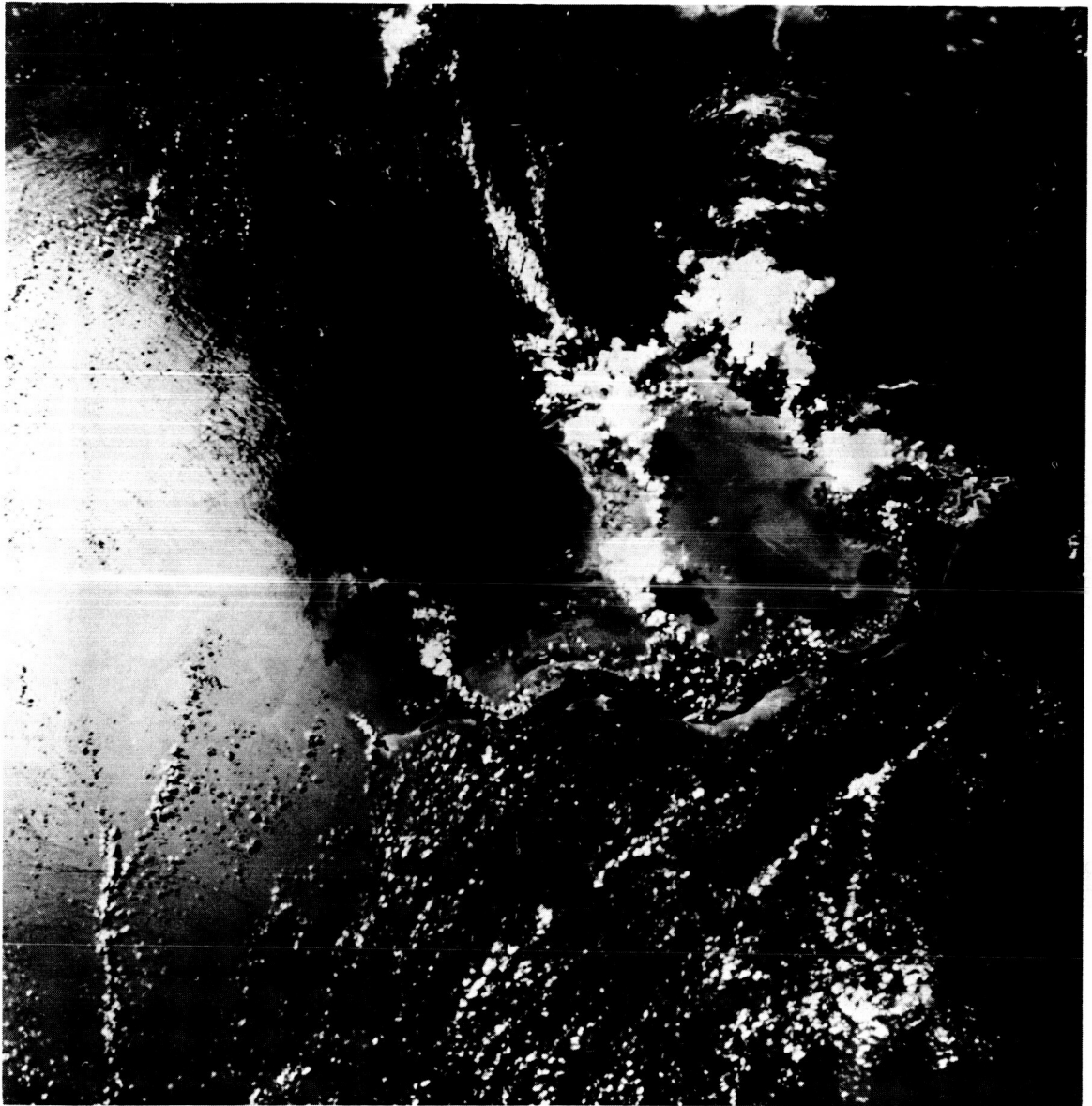
Figure 3-2.- Acklin's Island and Crooked Island in the Bahamas with
the sun reflecting at the left from the adjacent sea surface.
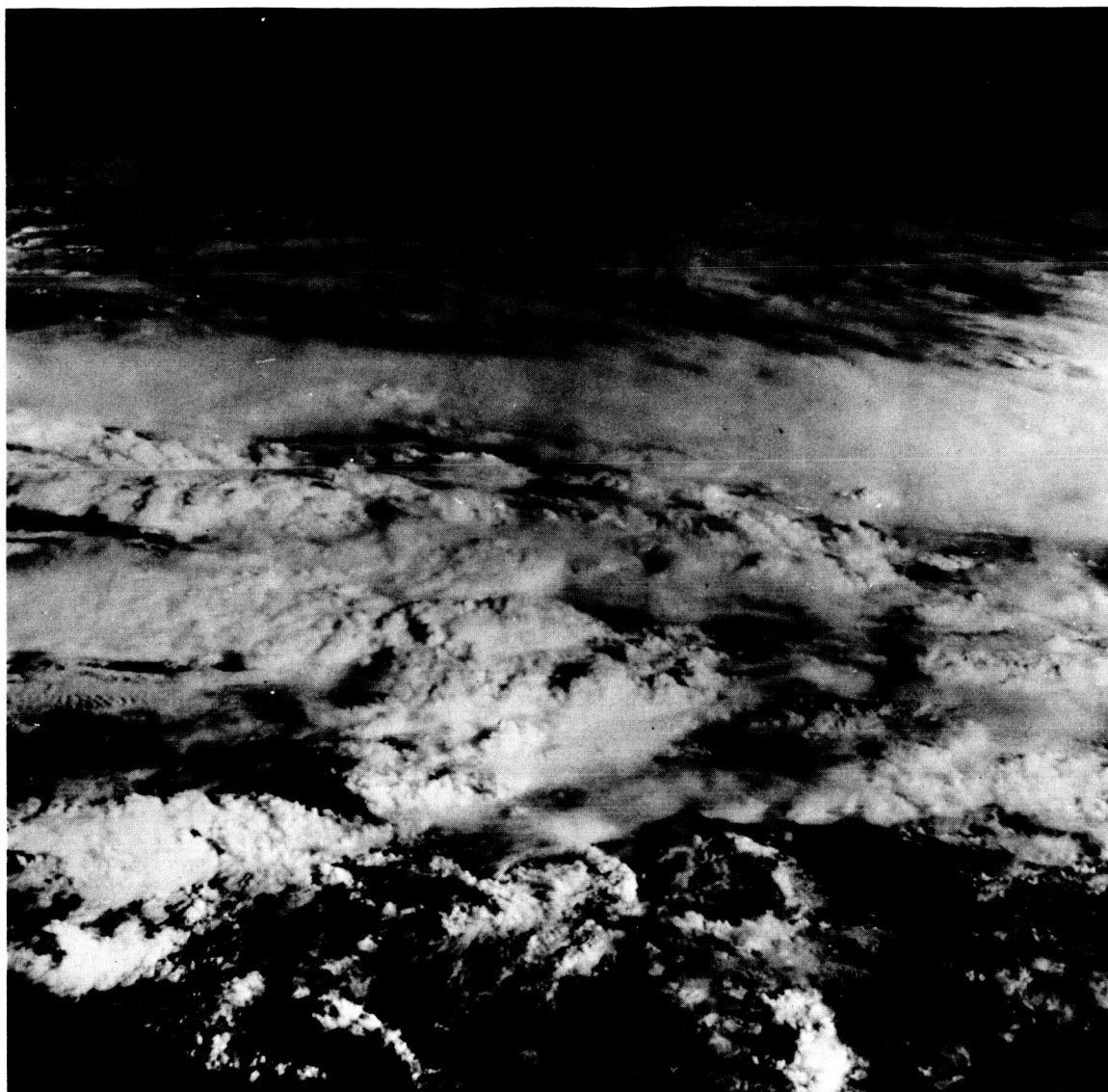
Figure 3-3.- A disturbed area over the tropical North Pacific Ocean.
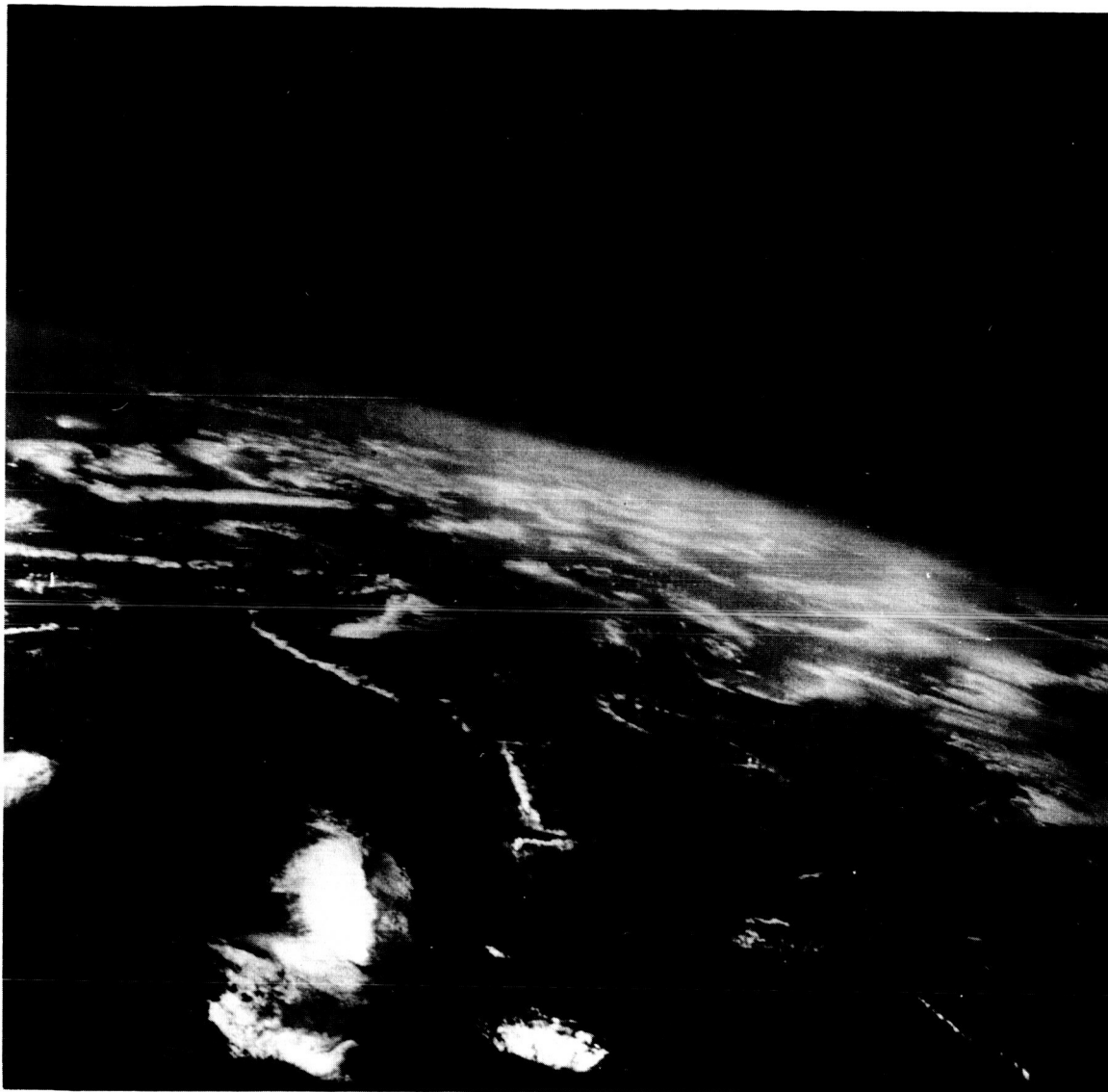
Figure 3-4.- Curving cloud lines locating eddies in the atmosphere near the Canary Islands.
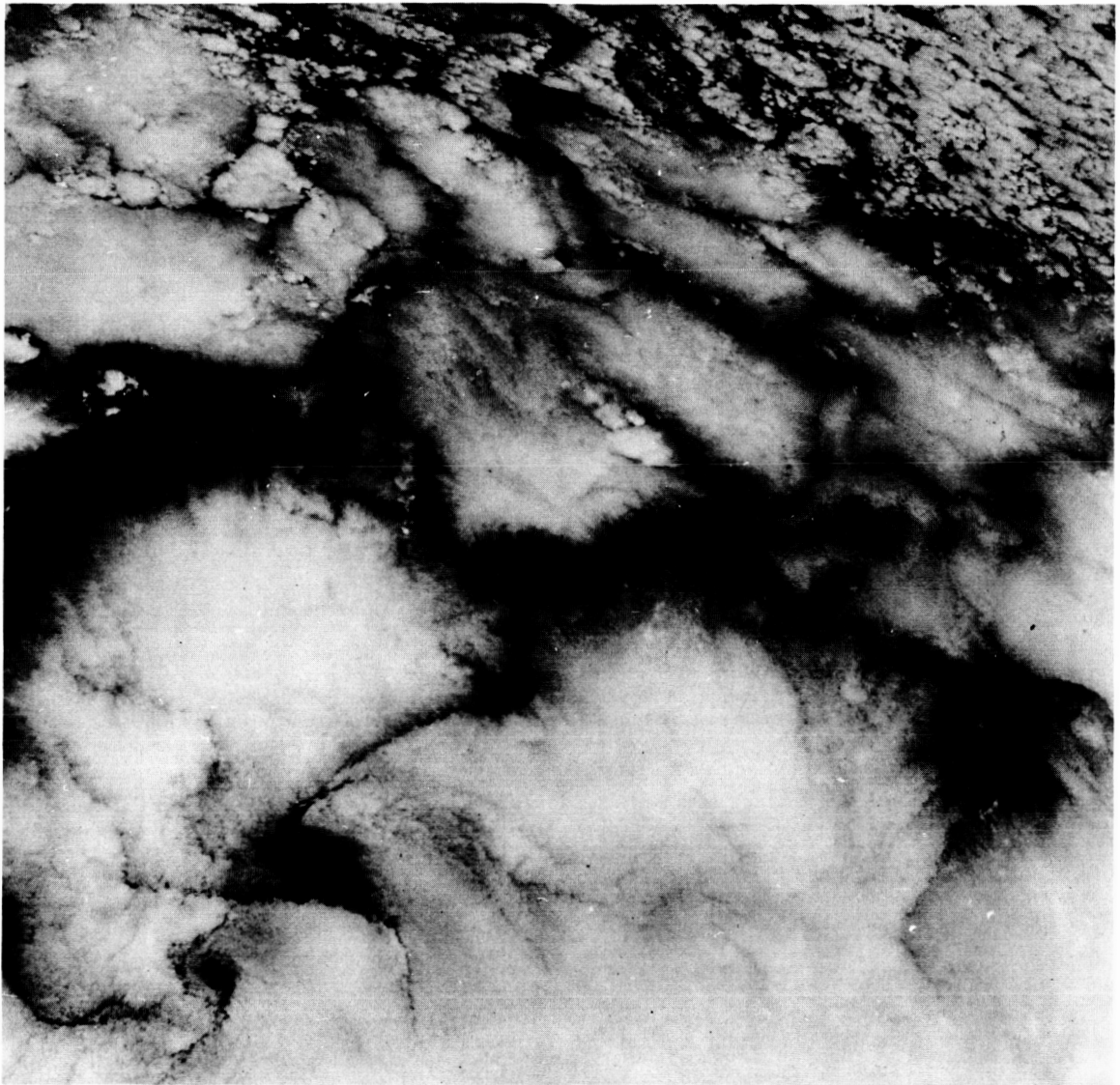
Figure 3-5.- Cellular cloud patterns over the Central North Pacific Ocean photographed by Astronauts McDivitt and White during the Gemini IV space flight.
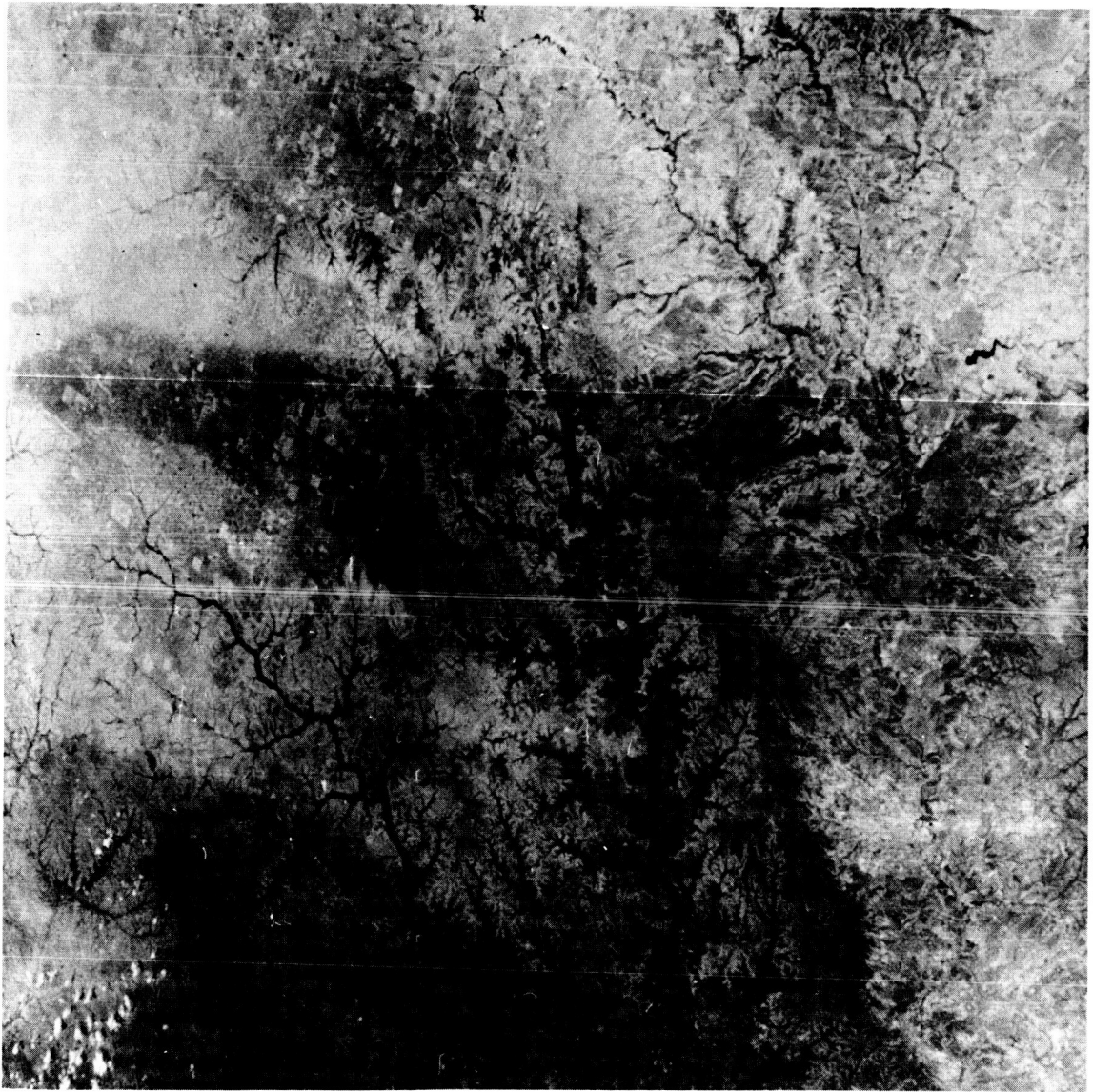
Figure 3-6.- Terrain shading in Central Texas, caused by heavy rainfall the previous day. The highway prominent in the upper left corner connects Odessa and Midland. The stream in the center of the picture is the North Concho River along San Angelo.

4. EXPERIMENT M-3, INFLIGHT EXERCISER ON GEMINI IV

By Lawrence F. Dietlein, M.D.
NASA Manned Spacecraft Center

SUMMARY

The response of the cardiovascular system to a quantified workload is an index of the general physical condition of an individual. Utilizing mild exercise as a provocative stimulus, no significant decrement in the physical condition of either of the two astronauts could be detected during the Gemini IV mission. The rate of return of pulse rate to preexercise levels, following inflight exercise periods, was essentially the same as that observed during preflight baseline studies.

OBJECTIVE

The objective of experiment M-3 was the day-to-day evaluation of the general physical condition of the flight crew with increasing time under space-flight conditions. The basis of this evaluation was the response of the cardiovascular system (pulse rate) to a calibrated workload.

EQUIPMENT

The exercise device, shown in figure 4-1, consisted of a pair of rubber bungee cords attached to a nylon handle at one end and to a nylon foot strap at the other. A stainless steel stop-cable limited the stretch length of the rubber bungee cords and fixed the isotonic workload of each pull. The flight bioinstrumentation system, figure 4-2, was utilized to obtain pulse rate, blood pressure, and respiration rate. These data were recorded on the biomedical tape recorder and simultaneously telemetered to the ground monitoring stations.

PROCEDURE

Exercise periods lasted for 30 seconds during which time the astronaut pulled the handle of the exerciser one pull per second. The device used in the Gemini IV mission required 63 pounds of force to stretch the rubber cords maximally through an excursion of 10.5 inches. Seventeen exercise periods for the pilot and four for the command pilot were originally scheduled in the mission plan.

RESULTS

During the early phase of the mission, the command pilot requested and received permission to perform additional exercises and completed the mission with a total of seven exercise periods. The pilot completed ten exercise periods. At approximately 32 hours elapsed time, all Type 2 Medical Data Passes (blood pressure-temperature-no exercise) were upgraded to Type 1 (blood pressure-exercise-blood pressure) and both astronauts were given permission to perform unscheduled exercises.

During the 67th hour ground elapsed time, the pilot reported that the latex cover on the exerciser had torn. This failure had no effect on the operation of the equipment or on the experimental results, and the crew continued to use the device in a satisfactory manner for the remainder of the mission.

Pulse rates were determined by counting 15-second intervals for 2 minutes before and after exercise, and for the first and last 15-second periods during exercise. Figure 4-3 shows the values for blood pressure and mean pulse rate of the pilot during preflight baseline control studies at 14.7 psia and 5.5 psia before the mission, and during the mission at 5.4 psia. Each plot represents the mean of several trials. This graph reveals that the preflight and inflight curves at one-third of an atmosphere are nearly superimposable and that the rate of return of the pulse rate to pre-exercise levels is essentially identical in the three modes for which data were available. Blood pressure changes were minimal.

Figure 4-4 shows similar data for the command pilot.

DISCUSSION

Comparatively speaking, the Gemini IV crew exhibited a more rapid rate of return of their pulse rates to preexercise levels than did the astronaut on the Mercury-Atlas 9 mission. The pulse rates of the crew on the Gemini IV mission returned to pre-exercise levels within 45 to 60 seconds after cessation of exercise. Figure 4-5 shows that Mercury-Atlas pilot's mean post-exercise heart rate during flight was still somewhat elevated (106 as opposed to a pre-exercise value of 89) for approximately 2 minutes after exercising. However, it must be remembered that the environmental control system of the Gemini spacecraft is superior to that which was available in Mercury, and therefore the data are not strictly comparable.

Evaluation of these data, then, indicates no significant difference between pulse-rate responses to exercise during the mission and those obtained before the mission for both crew members. Thus, using the rate of return of pulse rate to preexercise levels as an index of physical condition, there was no evidence of "deconditioning" at any time during the Gemini IV mission.

It should be noted that, although the crew demonstrated their ability to perform physical work during their 4-day mission, the crew commented that they felt no strong desire to perform heavy or strenuous exercise. They indicated, however, that periodic exercise during extended space flights is highly desirable.

CONCLUSIONS

On the basis of the data obtained during this mission, the following conclusions appear warranted:

(1) The response of the cardiovascular system to a calibrated workload is relatively constant for a given individual during space flight, at least for missions lasting up to 4 days.

(2) The crew are able to perform mild to moderate amounts of work under the conditions of space flight and this ability continues essentially unchanged for missions of up to 4 days in duration.

(3) Using a variant of the "Harvard Step Test" as an index of the physical fitness of the crew, there appears to be no decrement in the physical condition of the crew during a 4-day mission.
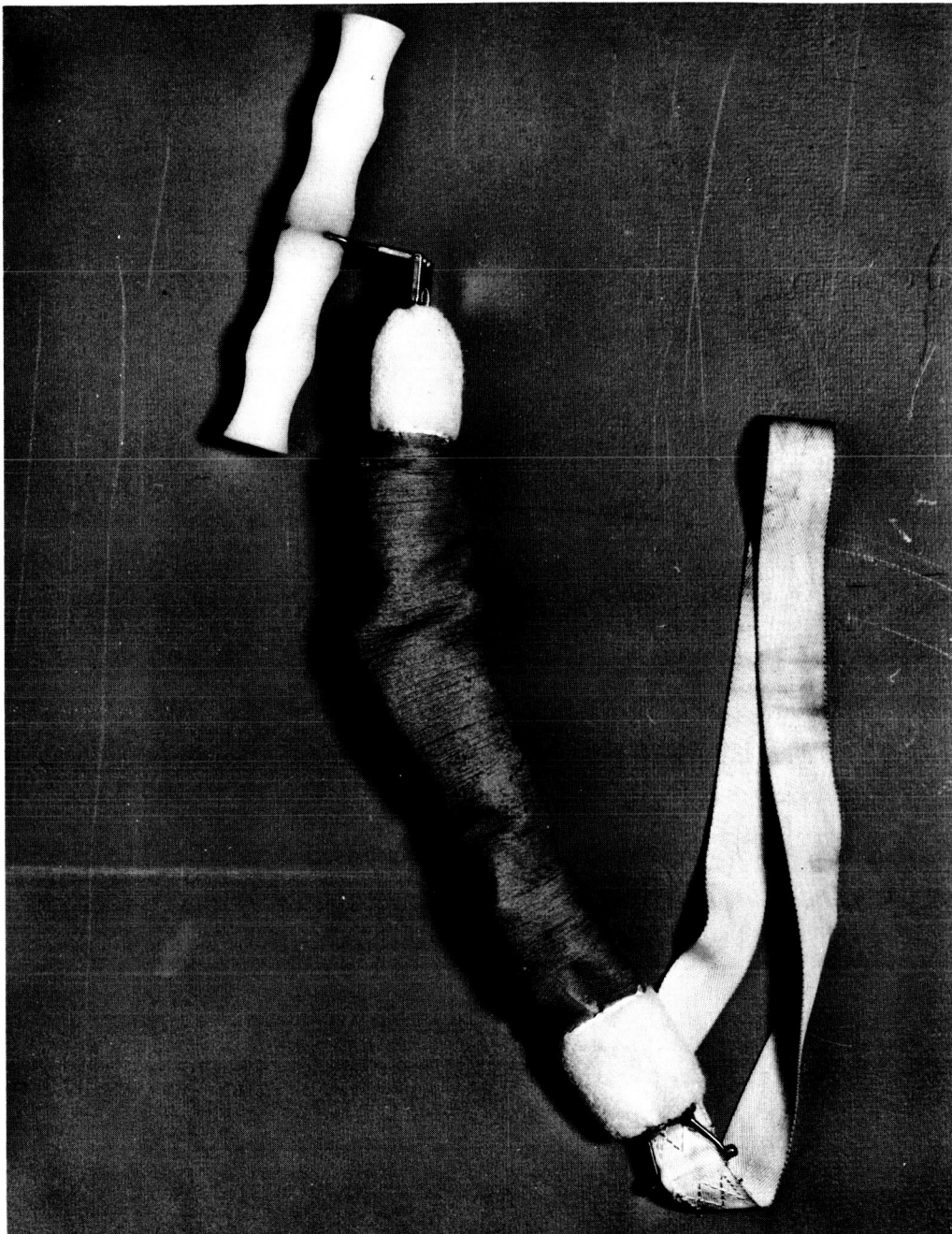
Figure 4-1.- Photograph of inflight exerciser used for experiment M-3 on the Gemini IV mission.
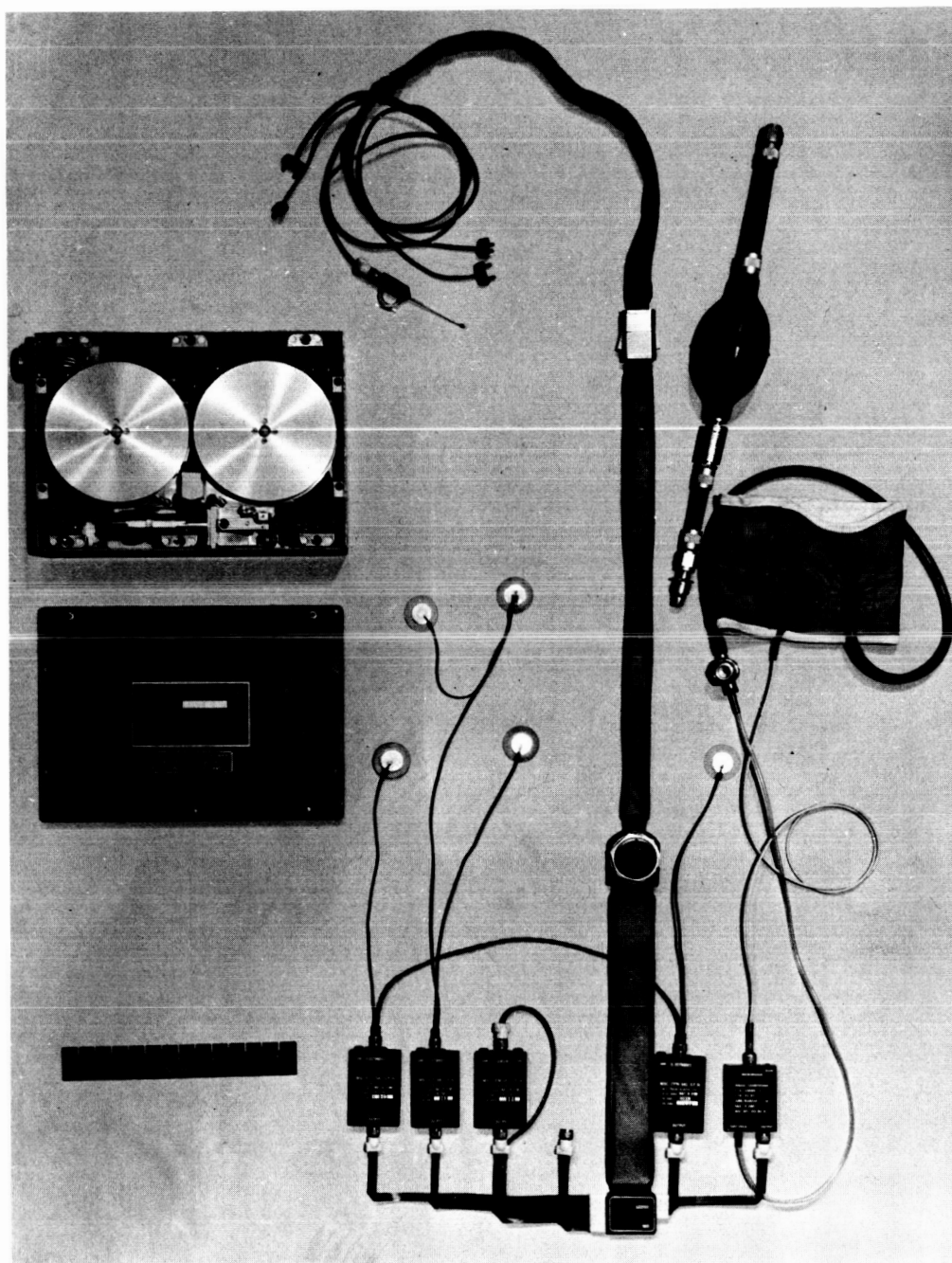
Figure 4-2.- The flight bioinstrumentation system
used on the Gemini IV mission.
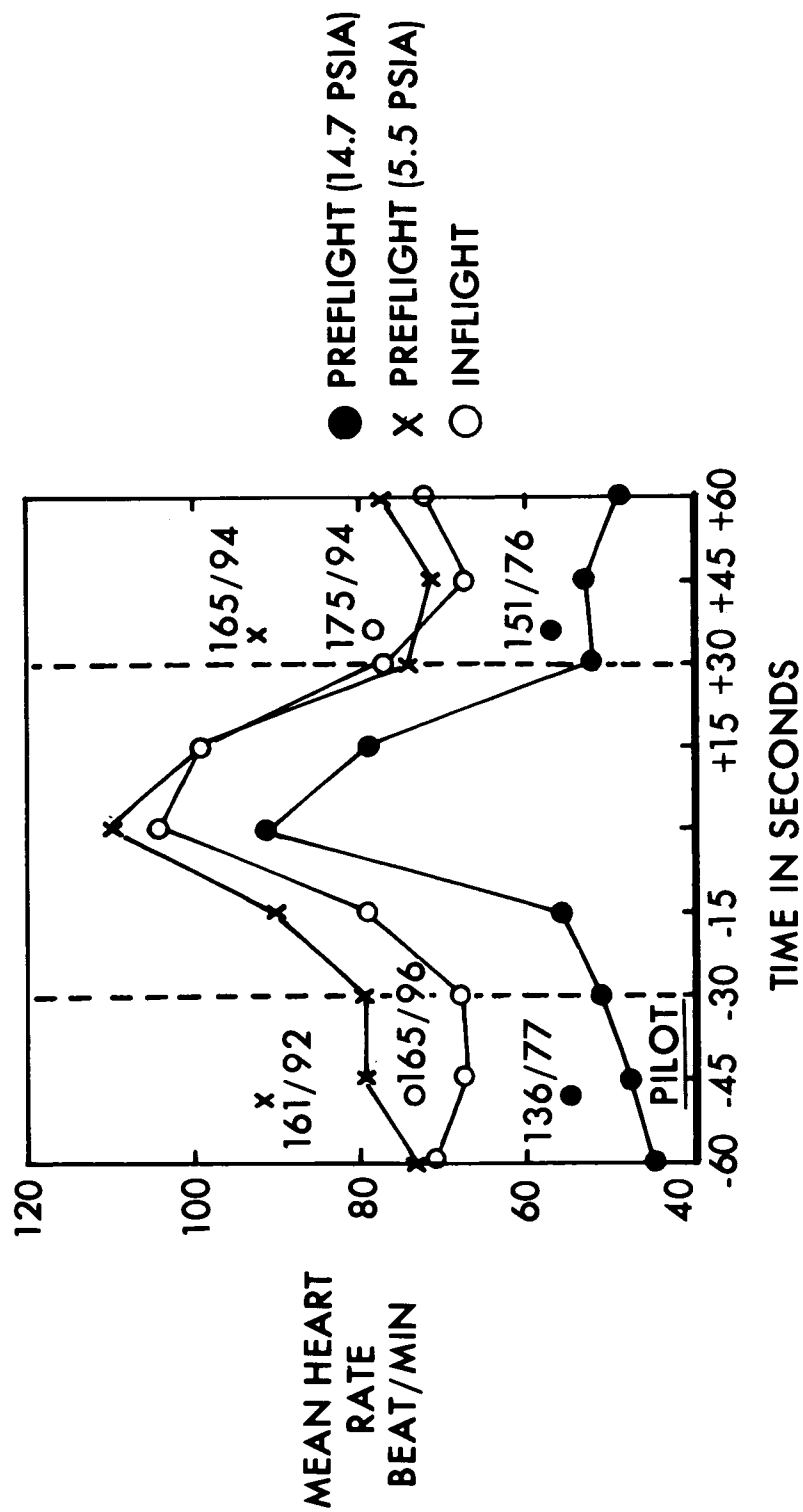
Figure 4-3. - Results obtained from medical experiment M-3 for Gemini IV pilot.
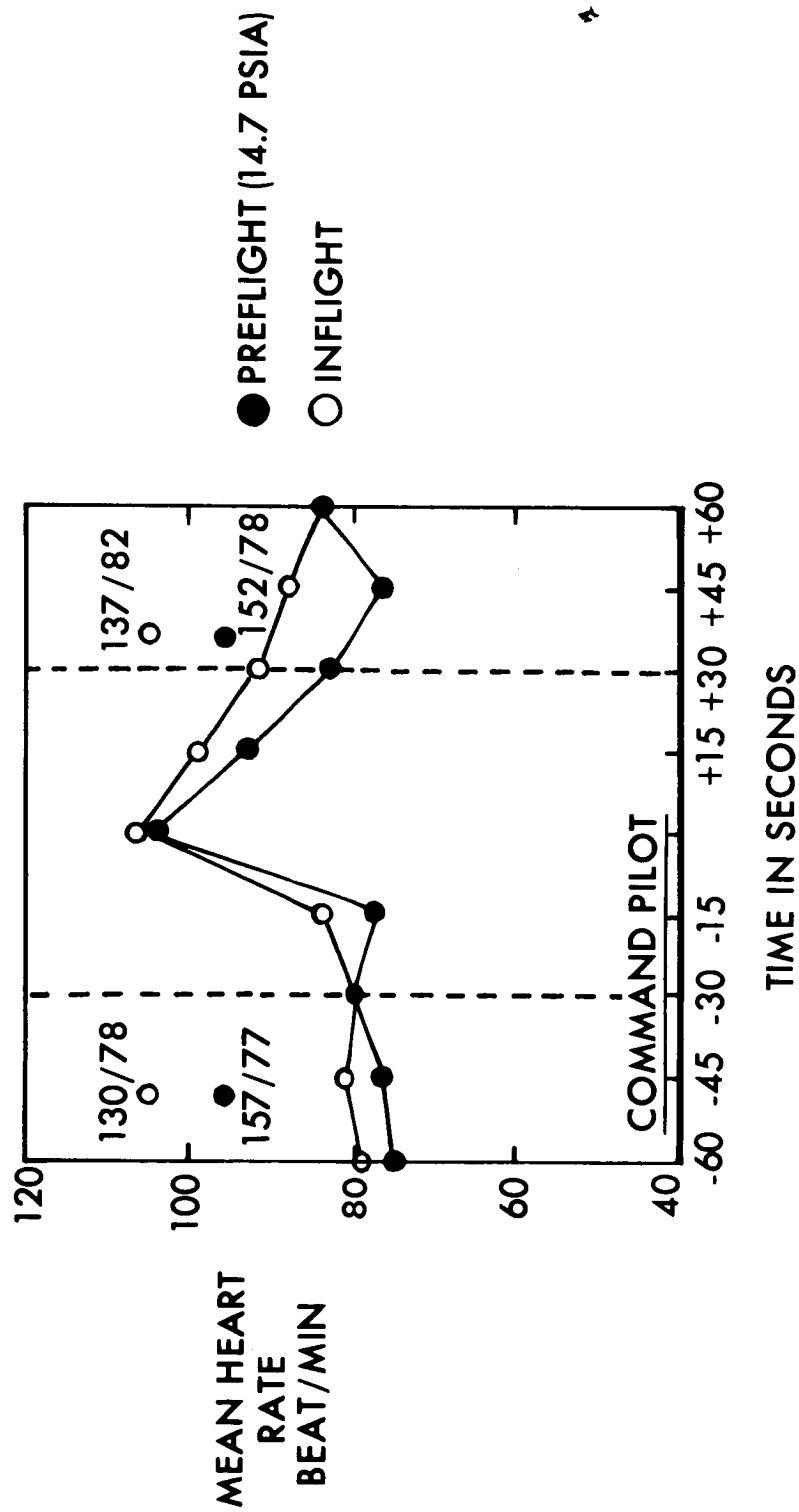
Figure 4-4.- Results obtained from medical experiment M-3 for Gemini IV command pilot.

	PREFLIGHT (5 DETERMINATIONS)		FLIGHT (2 DETERMINATIONS)	
	MEAN HEART RATE	MEAN BLOOD PRESSURE	MEAN HEART RATE	MEAN BLOOD PRESSURE
PREWORK	74	104/81	89	117/77
WORK	115	——	131	——
POSTWORK	85	111/79	106	124/95

Figure 4-5.- Results obtained from exercise experiment for Mercury-Atlas 9 pilot.

N65 36105

36105

5. EXPERIMENT M-4, INFLIGHT PHONOCARDIOGRAM

Lawrence F. Dietlein, M.D.
NASA Manned Spacecraft Center

SUMMARY

Simultaneous electrocardiographic and phonocardiographic data were obtained from both Gemini IV crew members. Analysis of these data revealed: no prolongation of the time interval between the onset of electrical systole (Q wave) and the onset of mechanical systole (first heart sound); no prolongation of systole (interval between Q wave and second heart sound); and a marked diurnal rhythmicity in the pulse rate of the command pilot based on the 24-hour Cape Kennedy time cycle.

OBJECTIVE

The objective of Experiment M-4 was to measure and correlate the various phases of the electrical and mechanical activity of the cardiac cycle in order to provide more insight into the functional cardiac status of flight crew members during prolonged space flight.

EQUIPMENT

The experimental equipment system consisted of three distinct parts: a phonocardiographic transducer, an electrocardiographic signal conditioner (preamplifier and amplifier), and the onboard biomedical tape recorder.

The signal conditioner was identical with that used for electrocardiographic measurements. Both the transducer and signal conditioner were worn within the Gemini pressure suit. The sensor was applied parasternally in the left fourth intercostal space of each flight crew member.

The phonocardiographic transducer used on Gemini IV was a 7-gram piezoelectric microphone 1 inch in diameter and 0.200 inch in thickness

(fig. 5-1). The transducer was secured to the astronaut's chest wall by means of a small disc of "Stomaseal" doublebacked adhesive. A 10-inch length of flexible, 0.10-inch diameter shielded cable delivered the phonocardiographic signal to the Gemini (electrocardiographic) signal conditioner (fig. 5-2) which was housed in a pocket of the undergarment. The phonocardiographic signal was conducted from the signal conditioner output to the suit bioplug, and then to the biomedical recorder (fig. 5-3).

The transducer or sensor responds to the translational vibrations imparted to the chest wall during each contraction of the heart. Phonocardiographic signals were recorded simultaneously with electrocardiographic signals derived from the M-X (manubrium-xiphoid) lead. Analog data from the biomedical tape recorder were then played back in real time, digitized, and analyzed by computer techniques.

PROCEDURE

Experiment M-4 was accomplished on Gemini IV by means of the instrumentation system previously described. In essence, the system transduces and presents the phonocardiographic signal to the Gemini biomedical recorder for postflight reduction and analysis. The sternal (M-X) electrocardiographic signal is recorded simultaneously on the biomedical recorder. The procedure is entirely passive and requires no active participation on the part of the astronaut.

RESULTS

Examination of the lowest plot of figure 5-4a indicates that the interval between the Q wave and the first heart sound was relatively constant; that is, it did not increase as the time in flight increased. The same was true in the case of the pilot (fig. 5-4b, lowest plot).

The duration of systole (fig. 5-4a, middle plot), which is the interval between the Q wave and the second heart sound, also remained constant during the 4-day mission.

Heart rates (figs. 5-4a and 5-4b, top plots) obtained maximum values at liftoff, reentry, and the pilot's extravehicular activity. The Q wave to first sound and Q wave to second sound (duration of systole) for the pilot (fig. 5-4b, lowest and middle plots) remained essentially constant for the duration of the mission. The heart-rate

plot for the command pilot showed a definite circadian rhythmicity based on the Cape Kennedy 24-hour day-night cycle. The command pilot exhibited low heart rate during periods coinciding with midnight, Cape time.

The Q wave to first sound intervals for both command pilot and pilot were shortened during flight relative to preflight baseline values. This is interpreted as an adrenergic response of the cardiovascular system to mild stress.

Figure 5-5a shows the plots of the duration of systole (lower curve) and the systolic ratio (upper curve) for the command pilot. Figure 5-5b represents similar values for the pilot. The systolic ratio is simply the observed systolic duration over the predicted value for systole. The regression equation proposed in references 1 and 2 was used to predict the values of the duration of systole.

In general, an increase in heart rate results in a shortening of systole (with a proportional shortening of both isotonic and isometric phases) and diastole. However, a shortening of the duration of mechanical systole in excess of that predicted for the increase in rate occurs under the influence of adrenergic agents (sympathetic discharge) or digitalis. In addition to a positive inotropic effect, it is likely that these agents speed up the metabolic reactions of the myocardium during systole. Cholinergic agents produce the opposite effect, resulting in an increase in the ratio of observed to predicted systole. A ratio lower than 1.0 suggests the influence of adrenergic factors. Examination of figures 5-5a and 5-5b reveals that both crew members exhibited systolic ratio values between 0.9 and 1.0, indicating a mild adrenergic influence throughout the mission.

CONCLUSIONS

The command pilot exhibited a circadian rhythmicity of pulse rate, based on Cape Kennedy time reference.

Phonoelectrocardiographic data on both crewmen reveal no significant decrease in duration of systole (Q wave to second heart sound interval) or in the Q wave to first heart sound interval.

The systolic ratios of both crew members suggest a mild adrenergic response throughout most of the four-day mission.

REFERENCES

1. Hegglin, R. and Holzmann, M.: Die klinische Bedentung der Verlän-
    gerten QT – Distanz im Elektrokardiogramm. Ztschr. F. klin. Med.
    132: 1, 1937.

2. Hegglin, R.: Die Klinik der Energetisch-dynamischen Herzinsuffiz-
    ienz. Bibliotheca Cardiologica, Sup. Cardiologia, Basel, 1947.
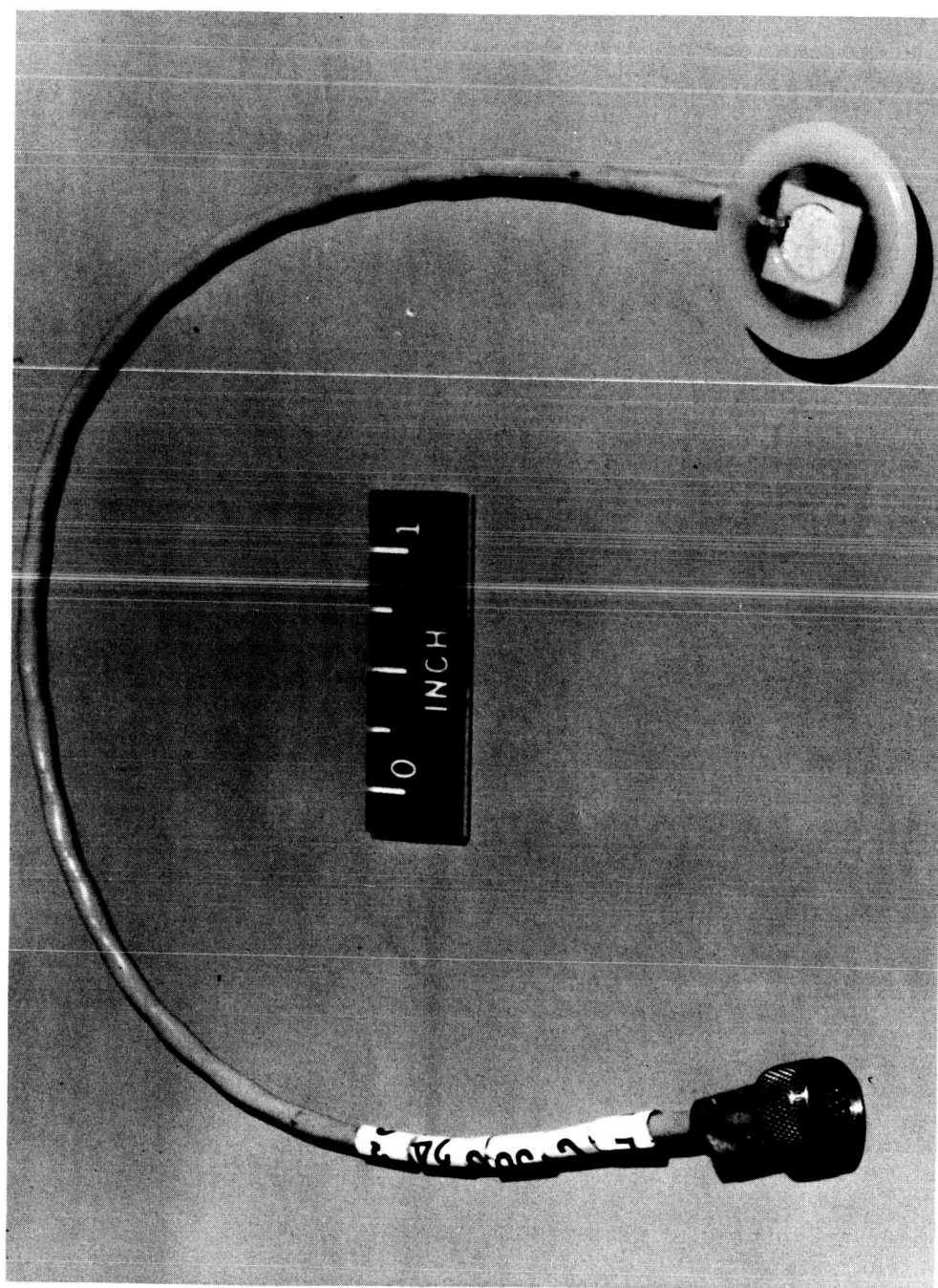
Figure 5-1.- Phonocardiographic transducer (piezoelectric microphone).
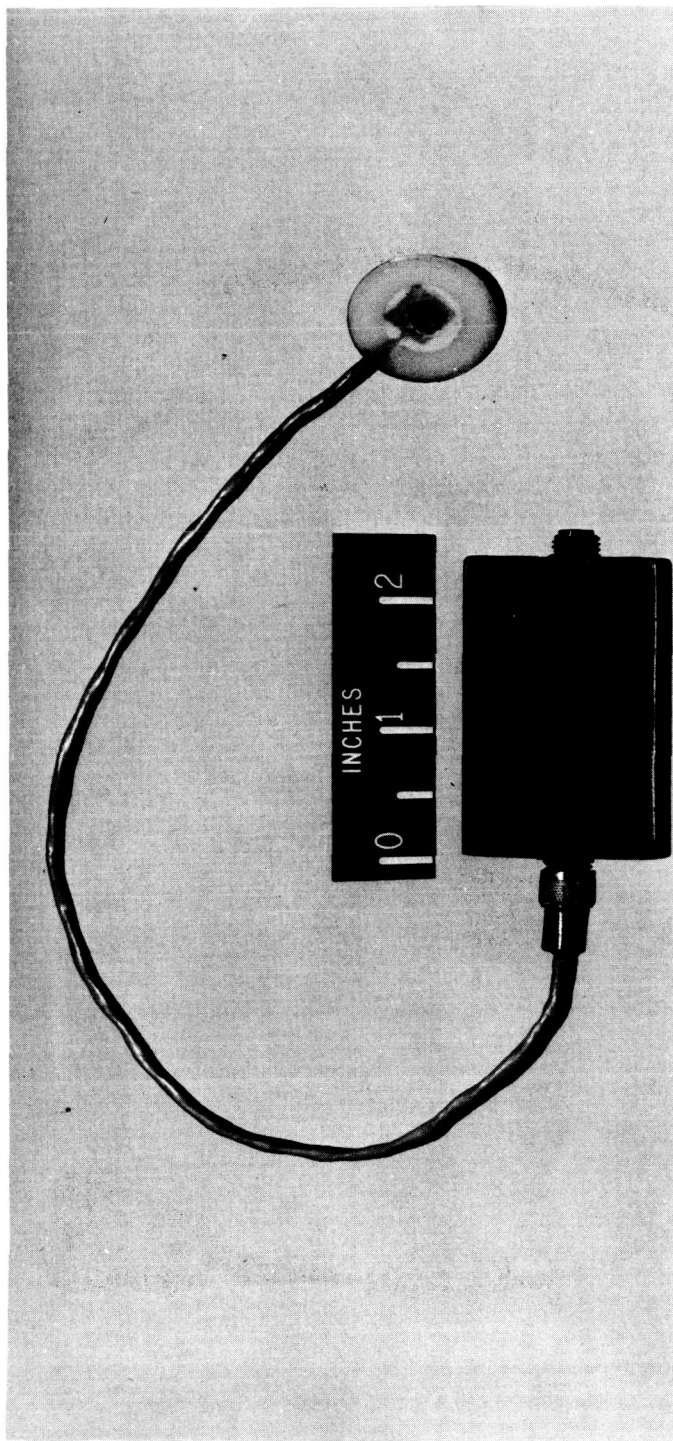
Figure 5-2.- Prototype phonocardiogram transducer and signal conditioner.
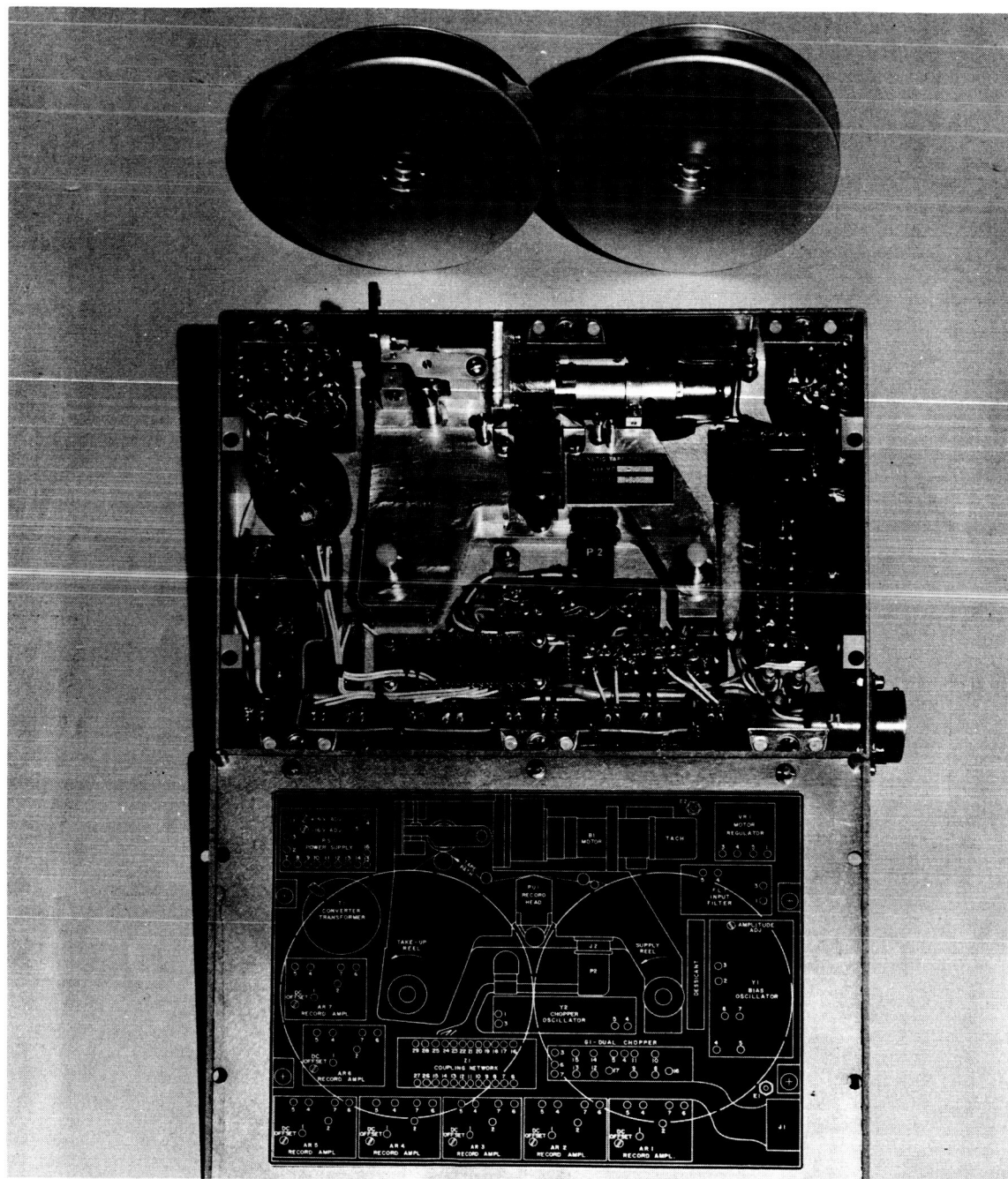
Figure 5-3.- Gemini biomedical recorder.

56
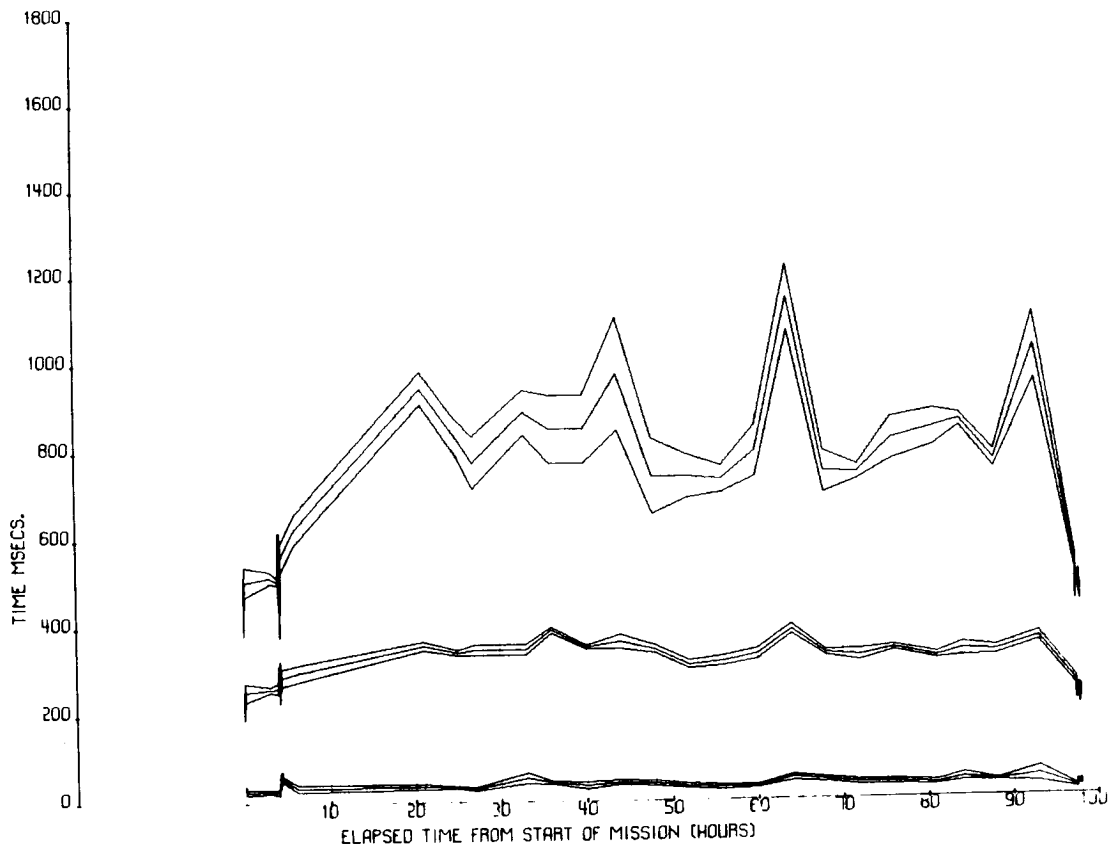
(a) Data from command pilot, Gemini IV.

Figure 5-4.- Lowest plot indicates values for interval between Q wave
and first heart sound from liftoff to splash. Middle plot indicates
duration of systole (Q wave to second heart sound). Top plot indi-
cates heart rate (R to R interval expressed in milliseconds).
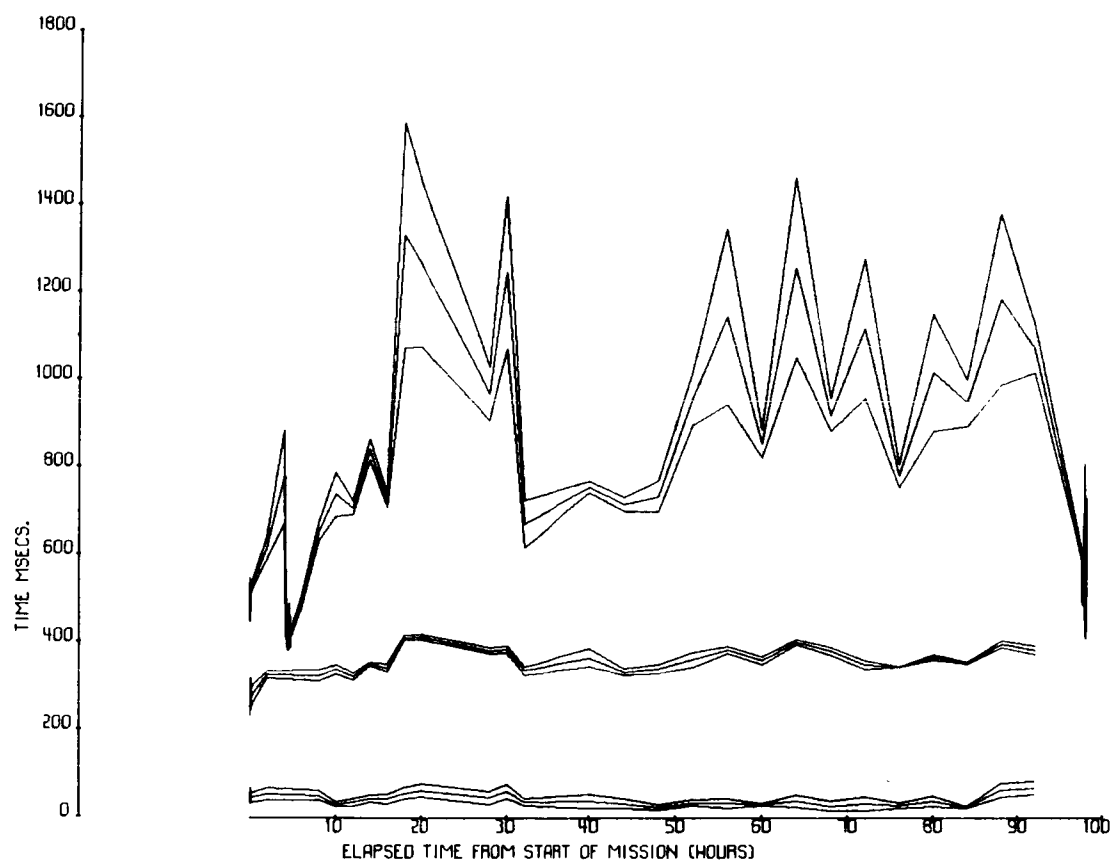
(b) Data from pilot, Gemini IV.

Figure 5-4.- Concluded.
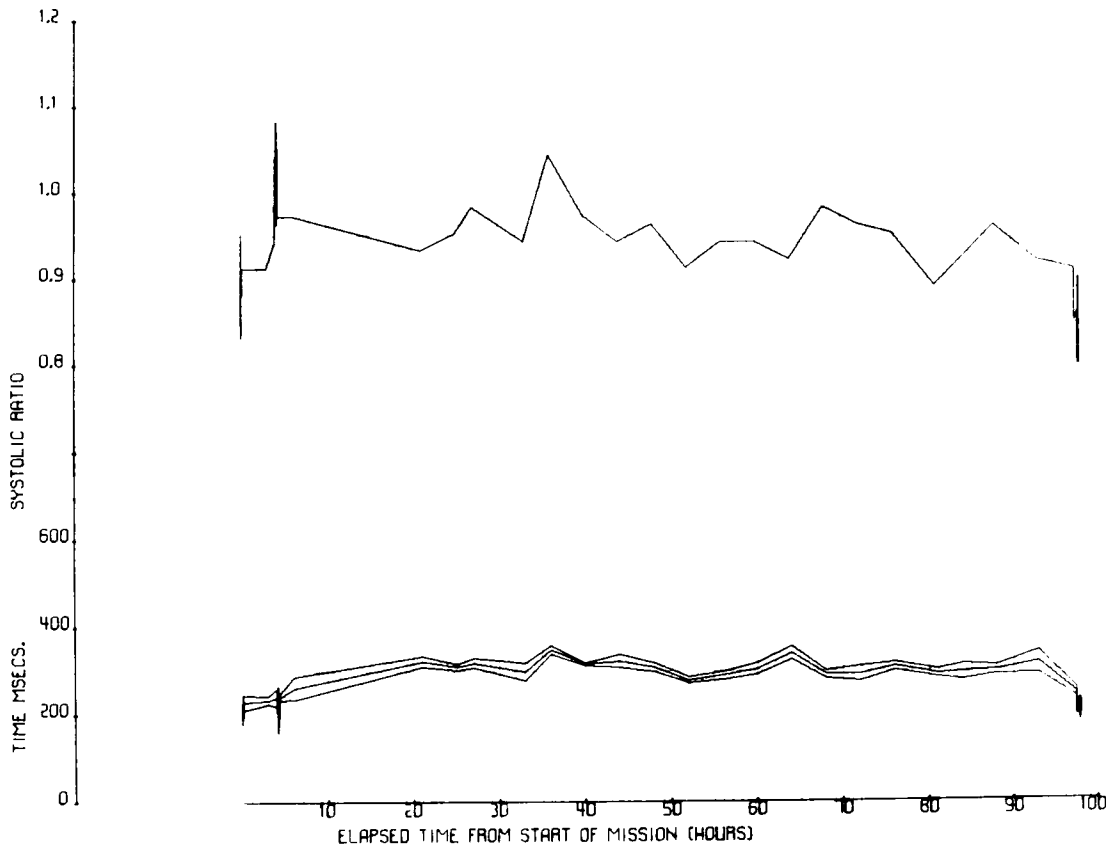
(a) Data from command pilot, Gemini IV.

Figure 5-5.- Lower plot indicates duration of systole (Q wave to second
   heart sound). Upper plot indicates systolic ratio (the ratio of the
   observed value for the duration of systole to the predicted value of
   the systolic interval).
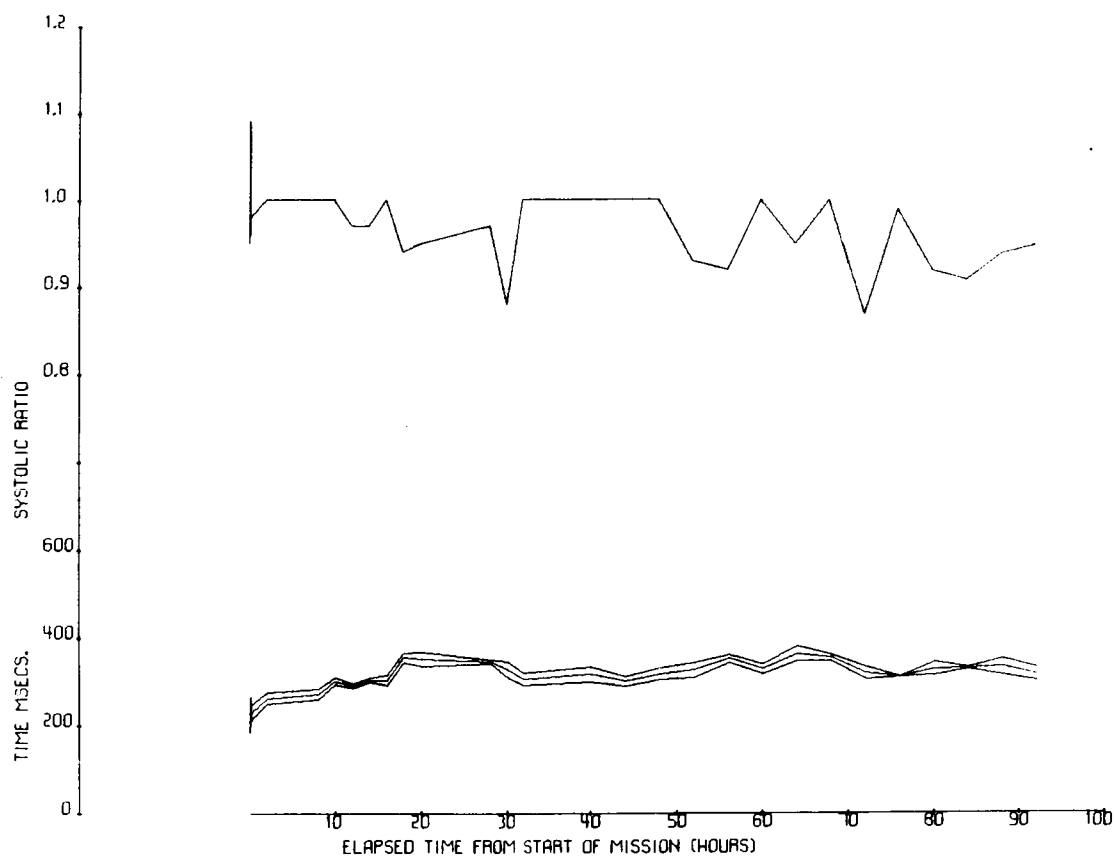
(b) Data from pilot, Gemini IV.

Figure 5-5.- Concluded.

6.   EXPERIMENT M-6, BONE DEMINERALIZATION ON GEMINI IV

By Pauline B. Mack, Ph. D.
Nelda Childers Stark Laboratory for Human Research

George P. Vose
Texas Woman's University

Fred B. Vogt, M.D.
Texas Institute for Rehabilitation and Research

Paul A. LaChance, Ph. D.
Manned Spacecraft Center

SUMMARY

A bone demineralization study based on radiographic bone densitometry was conducted on the crew of the four-day Gemini IV mission. The study was conducted by investigators from the Texas Woman's University (TWU). Radiographs were made of the lateral view of the foot and of the posterior-anterior view of the hand of the crew. The radiographs were made: (a) nine days and three days before lift-off, respectively, at Cape Kennedy; (b) on the morning of lift-off also at the Cape; (c) immediately after recovery on the Carrier Wasp; and (d) at the Manned Spacecraft Center 16 days and again 50 days following recovery. Members of the research team were stationed during the flight not only on the Carrier Wasp in the Atlantic, but also in the Hawaiian Islands in preparation for a possible descent in either ocean.

It is the practice of TWU laboratories to calibrate the X-ray machine before each exposure by means of an R-meter, in order to standardize the exposure conditions of the radiographs. The calibration of each film is effected by the use of an aluminum alloy wedge radiographed simultaneously on the same film as the bone undergoing evaluation. Conditions of exposure, involving milliamperage, kilovoltage, and time have been selected so as to minimize the protein image and to maximize that of the mineral elements in bone.

Losses in X-ray absorbance (in terms of X-ray equivalent aluminum alloy mass) in different sites in the os calcis, ranging from 6.20 to 13.42 percent, have been found in the crew of Gemini IV, with losses in

finger phalanx 5-2 falling within a comparable range. X-rays made of
the crew at two periods postflight have shown progressive increases in
X-ray absorbance in these anatomical sites, which reached or approached
preflight levels. It should be emphasized that changes of 6.20 to
13.42 percent in X-ray absorbance do not imply that changes in elemental
calcium of this magnitude occurred.

For comparative purposes, the losses in X-ray absorbance as exhib-
ited radiographically are compared in this report to losses in healthy
young men in the Texas Woman's University bed rest studies. They had
undergone bed rest immobilization for the same length of time and had
consumed a similar daily level of calcium. In all cases the losses in
the crew exceeded those in the bed rest subjects, indicating that re-
striction of body movement did not represent the sole factor involved.
Other possible responsible factors are discussed, with the conclusion
that further studies are needed on a larger number of subjects to iso-
late some of the variables, including weightlessness, which probably are
operative.

An important finding of the study is the fact that the X-ray absorp-
tion losses in bone, which have been found, are recoverable within com-
paratively short periods of time.

METHODS

Bone Densitometer Assembly

The equipment assembly used to evaluate sections of bone from the
exposed radiographs is a special analog computer consisting of a series
of subassemblies, all designed to operate together as a completely in-
tegrated system. The basic units of the overall assembly have been de-
scribed in references 1 and 2.

The history of the development of the scanning technique for meas-
uring bone mass from X-rays has been reported in references 2, 3, and 4.

X-ray Film

The film used in this investigation was Type AA Industrial X-ray
film.

Radiographic Exposure Technique

The three X-ray machines used in the study were calibrated by means of similar equipment, in order to standardize the exposure conditions of the films. Settings for milliamperes, kilovolts, and time were set to give an exposure level of 0.167 ± 0.001 roentgen.

The calibration of each film was effected by the use of an aluminum alloy wedge radiographed simultaneously on the same film as the bone undergoing evaluation. Two wedges functioned in this study. They had been constructed so as to give as nearly identical scans as possible when the films were standardized and traced by means of the special computer used in the bone mass measurements.

Bone Mass Evaluations

Central os calcis section. - Because of the natural provision of anterior and posterior landmarks on the central os calcis, a trace the width of the scanning beam (1.3 millimeters), known in the laboratory of the experimenters as the "conventional scan," was made on the successive films of this longitudinal series. Each radiograph was made with extreme care so that the image of the os calcis on each film could be superimposed exactly over that of the initial film. With a small steel needle, the initial film was punctured at each end of the bone; this defined the limits of the central or conventional trace. The two needle pricks could be identified by means of the magnification unit in the densitometer, which makes possible exact positioning of the film preparatory to scanning. The same treatment was given to the image of the calibration wedge on the same film.

Before tracing the same segments in each successive film, each film was superimposed over the initial film with the steel-needle pricks made in exactly the same positions.

The anatomical location of the scan by which the central os calcis section was evaluated is shown in figure 6-1.

Multiple parallel os calcis evaluations. - Without removing the film from its position in the densitometer after making a conventional scan, parallel scans 1.0 mm apart were made, beginning with a scan 1.0 mm above the conventional position, and continuing to the bottom of the os calcis. For the os calcis bone of the command pilot, 37 scans were needed to cover this area of the os calcis. For the pilot, 40 parallel scans were needed. (See figures 6-2 and 6-3.)

Individual bone X-ray absorption values were recorded from the data secured from the multiple scans. These values are reported in four groups

covering approximately one-fourth of the total area scanned. These values are also reported as an overall value.

Sections of phalanx 5-2. - The second phalanx of the fifth digit likewise was scanned by parallel cross-sectional traces. (See figure 6-4.) The first proximal scan was marked by needle pricks which were followed for each film in each series.

Control of scan widths. - For both the os calcis and the phalanx scans, the measured width of each individual bone segment was used to define the length of the scan for that specific segment for each film in the series for each crew member.

INTERPRETATION OF TERM "X-RAY ABSORBANCE" BY BONE

The term "X-ray absorbance" by bone as used in this report refers to the mass not only of calcium present in bone but also of phosphorus and of the other components of bone; and it includes whatever interstitial and extra-bone protein in the under- and over-lying tissue which may be reflected in the radiograph. Conditions of exposure, involving milliamperage, kilovoltage, and time, have been selected so as to minimize the protein image and to maximize that of the mineral elements in bones. This is possible because of the higher atomic numbers (related to the structure of the atoms) of calcium and phosphorus in comparison with the other elements involved in bone.

RESULTS

X-ray Absorption Changes in the Central Os Calcis Section

The X-ray absorption values (in terms of calibration wedge equivalency) obtained from the central os calcis section (the so-called "conventional" segment of this bone) throughout the Gemini IV study are shown in figure 6-5 and table 6-I. Based on an average of preflight wedge equivalency values, the command pilot showed a change of -9.53 percent in this section of the bone, with a -7.80 percent change when the immediate postflight value was compared with the immediate preflight bone mass level. The corresponding values for the pilot were -6.20 and -10.27 percent.

CHANGES IN MULTIPLE SECTIONS OF THE OS CALCIS

As noted, 37 one-millimeter scans were made on each of the os calcis films of the command pilot, all parallel to the "conventional" or central os calcis section. The first scan was made one millimeter above the conventional scan, with 35 successive scans below the scan of this central os calcis site.

On the os calcis series for the pilot, a total of 40 scans were made in each case because of the larger bone. The first scan was made one millimeter above the scan of the conventional section, with 38 parallel scans below this section. (See figures 6-2 and 6-3.)

In the series of multiple as calcis scans for both crew members, the values immediately after flight were lower than those before flight, and there were no exceptions. An example is given in table 6-II, in which the integrator counts from the densitometer assembly are given for the 40 parallel segments of the os calcis of the pilot immediately before and immediately after the four-day orbital flight.

COMPARISON OF FOUR GROUPS OF OS CALCIS

PARALLEL SECTIONS

In order to compare different areas of the os calcis for changes in bone mass equivalency during flight, the multiple scans were divided into four groups each, and the sums of the values for each group were compared. An example of the findings is shown in figure 6-6, in which the wedge mass equivalency values for the pilot are given for the four os calcis sections. The first quarter represents the proximal section and the fourth represents the distal section of the combined scans. The graph is based on a comparison of the immediate preflight radiograph with that of the immediate postflight X-ray.

The four plots begin with the mean wedge mass equivalency values for the preflight films (zero time on the graph), followed by the values obtained from the individual postflight radiographs in succession. The changes in the four os calcis sections of the pilot, from the averages of the preflight values to the values obtained from the radiographs which were taken immediately after the orbital flight, were as follows:

(1) Proximal Section (segments 1 millimeter above the convention scan through segment 8 below), -7.88 percent;

(2)   Second Section (segments 9 through 18 below the conventional scan), -7.69 percent;

(3)   Third Section (segments 19 through 27 below convention scan), -7.05 percent; and

(4)   Distal Section (segments 28 to bottom of bone), -2.52 percent.

COMPARISON OF OVERALL SERIES OF SEGMENTS

Figure 6-7 shows plots of a summation of wedge mass equivalency values for the respective multiple segments of the os calcis of the crew. The plot for the command pilot is based on the 37 segments shown in the X- ray positive in figure 6-2 and that for the pilot on the 40 segments indicated in figure 6-3. The value shown at zero time in both plots represents that of the first of the three preflight films, with the remaining series of radiographs following in order. When the value for the immediate preflight radiograph is compared with the immediate postflight value, the command pilot exhibited a total loss in the os calcia of 6.82 and the pilot of -9.25 percent.

BONE MASS CHANGES IN FINGER PHALANX 5-2

It is remarkable that the phalanx of the fifth digit, which was evaluated for bone mass in cross-sectional segments in this study, experienced some losses in X-ray absorption in as short a time as four days. In the Texas Woman's University bed rest series, no changes of noteworthy magnitude in bone absorption by phalanx 5-2 site has been found, except during the last one-half of 30-day bed rest periods.

As in the case of the os calcis, multiple scans were made across Finger phalanx 5-2 for the wedge mass equivalency values obtained from evaluations of the films taken during this study. The scans were made across the posterio-anterior view of the finger as shown in figure 6-4.

For assistance in the interpretation of the data obtained from this bone, the scans were combined into five groups from the proximal to the distal end of this phalanx. Figure 6-8 consists of a plot of the wedge mass equivalency findings from one of the five groups of scans of the phalanx of the command pilot. The change in wedge mass equivalency of this section of the bone for this subject was -10.74 percent calculated from the values obtained from the radiograph taken immediately before lift-off to that obtained immediately after the crew reached the Carrier Wasp.

DISCUSSION

In the first venture into the field of measuring changes in skeletal mass during space flight, an entirely new environment for healthy men is being explored. In extensive bed rest studies at the Texas Woman's University, the level of dietary calcium consumed during and previous to bed rest immobilization has been found to affect calcium loss from the body as well as changes in bone mass. These dietary relationships have been reported in references 5 and 6.

Exercise also has been demonstrated as effective in reducing bone mass losses, and the study was reported in reference 7. The possibility of stress as a factor in bone mass loss has been discussed in reference 7.

In this Gemini IV study, bone mass losses were experienced by the crew, and these losses were greater in the central os calcis section than was shown by TWU bed rest subjects during the same time, on a similar level of daily dietary calcium. In finger phalanx 5-2, distinct losses in bone mass were shown by the crew in comparison with only minor losses in the bed rest subjects, except in the case of prolonged periods of bed rest immobilization, as has been noted. For example, the losses in bone mass of the central os calcis section for the crew during the four-day flight, in comparison with those of TWU bed rest subjects on similar dietary calcium levels for the same length of time, are shown in table 6-III.

The reduction in bone mass in the TWU bed rest immobilization
studies have been accompanied by urinary and fecal losses of calcium,
phosphorus, and nitrogen, which have been higher during bed rest than
during ambulation. The loss in bone mass as stated earlier in this re-
port, does not represent solely a loss in calcium, but is based on losses
of all of the mineral components of bone, including small amounts of
protein.

Because spacecraft parameters change, it is not possible to come to
definite conclusions concerning all of the variables which have entered
into the findings of this study. More data on a larger number of sub-
jects are needed for a more thorough interpretation of the results of
this first experiment in skeletal change in healthy men in space. One
result has been demonstrated, however, and that is the fact that, of
every anatomical site investigated, bone values showed a negative change
in four days, and the change was greater than losses shown by healthy
men in bed rest studies during the same period of time and on the same
dietary level of calcium. Further evidence that bone loss had occurred
during spaceflight was demonstrated by increases in bone mass levels when
the astronauts returned to their regular activities on the surface of the
earth.

REFERENCES

1. Mack, Pauline Berry; Vose, George P; and Nelson, James Donald:
    New Developments in Equipment for the Roentgenographic Measure-
    ment of Bone Density, American Journal of Roentgenology, Radium
    Therapy, and Nuclear Medicine, vol. 82, p. 647, 1934.

2. Mack, Pauline Berry: Radiographic Bone Densitometry. Conference
    under sponsorship of the National Aeronautics and Space Adminis-
    tration and the National Institutes of Health, Washington, D.C.,
    March 25-27, 1965.

3. Mack, Pauline Berry; O'Brien, Anne T.; Smith, Janice M.; and
    Bauman, Author W.: A method for Estimating the Degree of Mineral-
    ization of Bones from Tracing of Roentgenograms, Science, vol. 89,
    p. 467, 1939.

4. Mack, Pauline Berry; Brown, Walter N.; and Trapp, Hughes Daniel:
    The Quantitative Evaluation of Bone Density, American Journal of
    Roentgenology and Radium Therapy, vol. 61, p. 808, 1949.

5. Mack, Pauline Berry; Klapper, Elsa A.; Pyke, Ralph E.; Alford,
    Betty B.; and Gauldin, Ruth: Fourth Semiannual Report to the
    National Aeronautics and Space Administration, Mar. 31, 1965.

6. Ibid, Fifth Semiannual Report to the National Aeronautics and
    Space Administration, Sept. 30, 1965.

7. Vogt, F. B.; Mack, P. B.; Beasley, W. G.; Spencer, W. A.; Cardus, D.;
    and Valbonna, C.: The Effect of Bedrest on Various Parameters of
    Physiological Functions, Part XII. The Effect of Bedrest on Bone
    Mass and Calcium Balance, Texas Institute of Rehabilitation and
    Research, Report to the National Aeronautics and Space Adminis-
    tration, Apr. 1965.

TABLE 6-I

EVALUATION OF CENTRAL OS CALCIS POSTERIO-ANTERIOR

"CONVENTIONAL" SEGMENT

(a) Command pilot

Radiographs	X-ray absorption values in terms of calibration wedge equivalency, g
Mean of values from preflight film	2.397
Film taken immediately before lift-off	2.353
Film taken immediately after end of flight	2.169
Film taken 16 days after end of flight	2.216
Film taken 50 days after end of flight	2.274

(b) Pilot

Mean of values from preflight films	2.642
Film taken immediately before lift-off	2.762
Film taken immediately after end of flight	2.479
Film taken 16 days after end of flight.	2.419
Film taken 50 days after end of flight.	2.593

TABLE 6-II

COMPARISON OF CALIBRATION WEDGE MASS EQUIVALENCY VALUES BASED ON INTEGRATOR

READINGS FROM 40 PARALLEL SEGMENTS OF THE OS CALCIS FROM RADIOGRAPHS MADE

ON ASTRONAUT WHITE IMMEDIATELY BEFORE AND IMMEDIATELY AFTER THE FOUR-DAY

ORBITAL FLIGHT

Position of scan	Integrator counts from the densitometer computer		Percent change from film A to film B
	A. Film taken immediately preflight	B. Film taken immediately postflight	
1 mm above	15, 162	13,675	-9.80
Conventional trace	15,346	13,770	-10.27
1 mm below	14,404	12,920	-10.30
2 mm below	13,752	12,508	-9.04
3 mm below	13,286	11,921	-10.27
4 mm below	13,198	11,753	-10.95
5 mm below	13,139	11,524	-12.29
6 mm below	12,984	11,558	-10.98
7 mm below	12,889	11,530	-10.54
8 mm below	12,692	11,368	-10.43
9 mm below	12,542	11,414	-8.99
10 mm below	12,104	10,516	-13.12
11 mm below	11,673	10,282	-11.92
12 mm below	11,136	10,094	-9.36
13 mm below	10,791	9,871	-8.52
14 mm below	10,407	9,336	-10.29
15 mm below	10,266	9,118	-11.18
16 mm below	9,961	8,784	-11.82
17 mm below	9,734	8,428	-13.42
18 mm below	9,562	8,448	-11.65
19 mm below	9,032	8,168	-9.56
20 mm below	8,684	7,846	-9.65
21 mm below	8,358	7,539	-9.80
22 mm below	8,168	7,478	-8.45
23 mm below	7,997	7,351	-8.08
24 mm below	7,784	6,980	-10.33
25 mm below	7,594	6,963	-8.31
26 mm below	7,336	6,881	-7.16
27 mm below	7,138	6,834	-4.26
28 mm below	7,046	6,612	-6.16
29 mm below	6,801	6,595	-3.03
30 mm below	6,667	6,528	-2.08
31 mm below	6,583	6,388	-2.96
32 mm below	6,508	6,286	-3.41
33 mm below	6,442	6,130	-4.55
34 mm below	6,271	6,106	-2.63
35 mm below	6,136	5,964	-2.08
36 mm below	5,783	5,354	-7.57
37 mm below	5,517	4,920	-10.82
38 mm below	4,923	4,422	-10.18
TOTAL	385,774	350,084	-9.25

TABLE 6-III

COMPARISON OF WEDGE MASS EQUIVALENCY LOSSES IN CENTRAL

OS CALCIS OF GEMINI IV CREW AND OF TWU BED REST SUBJECTS

ON SIMILAR DAILY INTAKES OF DIETARY CALCIUM

Subjects	Number of days	Average calcium consumed per day, mg	Central os calcis wedge mass equivalency change (percent)	
			Based on mean of preflight values	Based on last value before launch
Command pilot	4	679	-9.53	-7.80
Pilot	4	739	-6.20	-10.27
TWU bed rest				Based on value before bed rest
Subject 1	4	675	X	-2.67
Subject 2	4	659	X	-4.25
Subject 3	4	636	X	-3.39
Subject 4	4	636	X	-3.59

Figure 6-1.- Positive of os calcis X-ray on the Gemini IV command pilot
indicating location of conventional tracing.
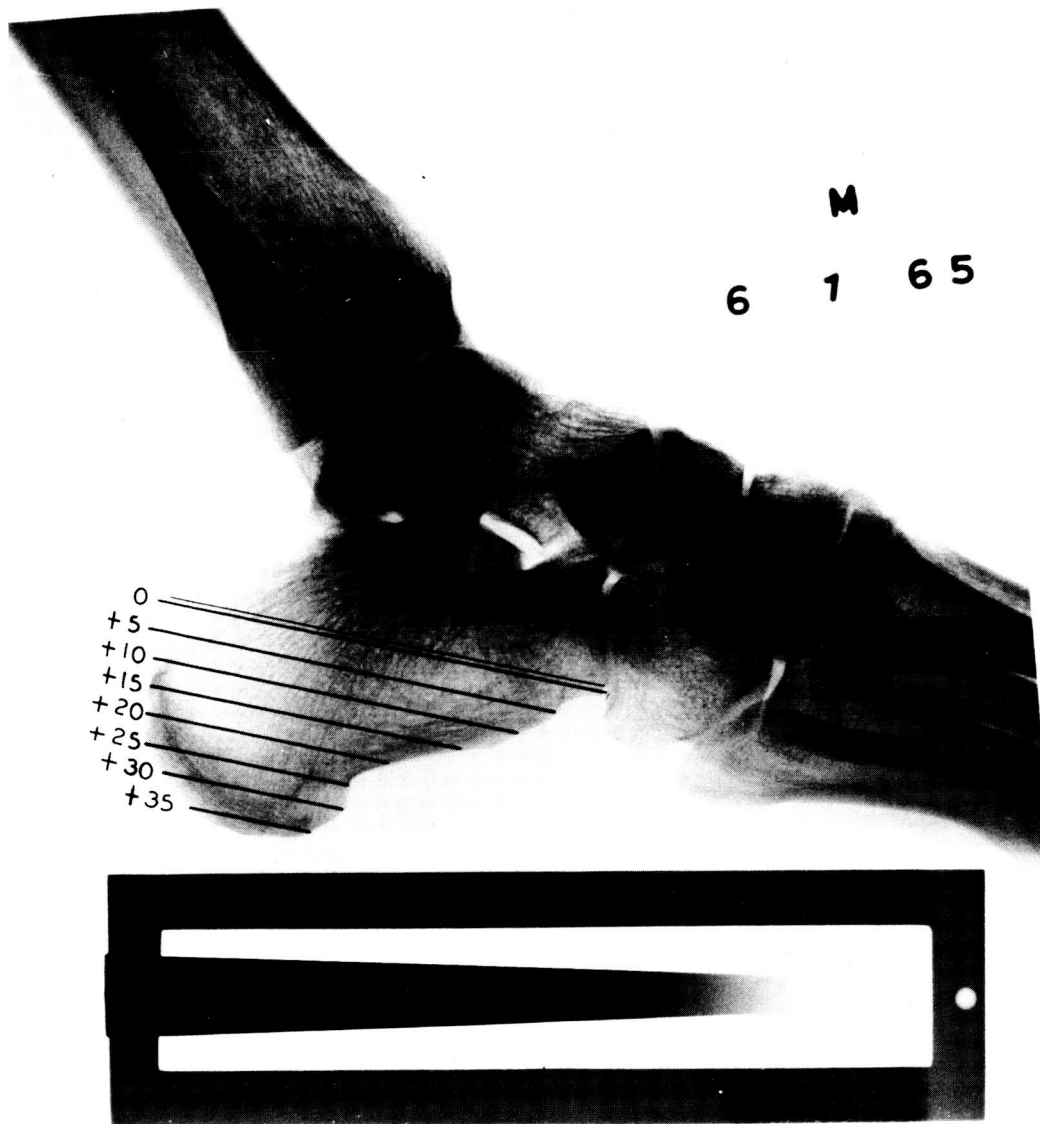
Figure 6-2.- Positive of os calcis tracing paths on the Gemini IV
command pilot, indicating parallel paths.
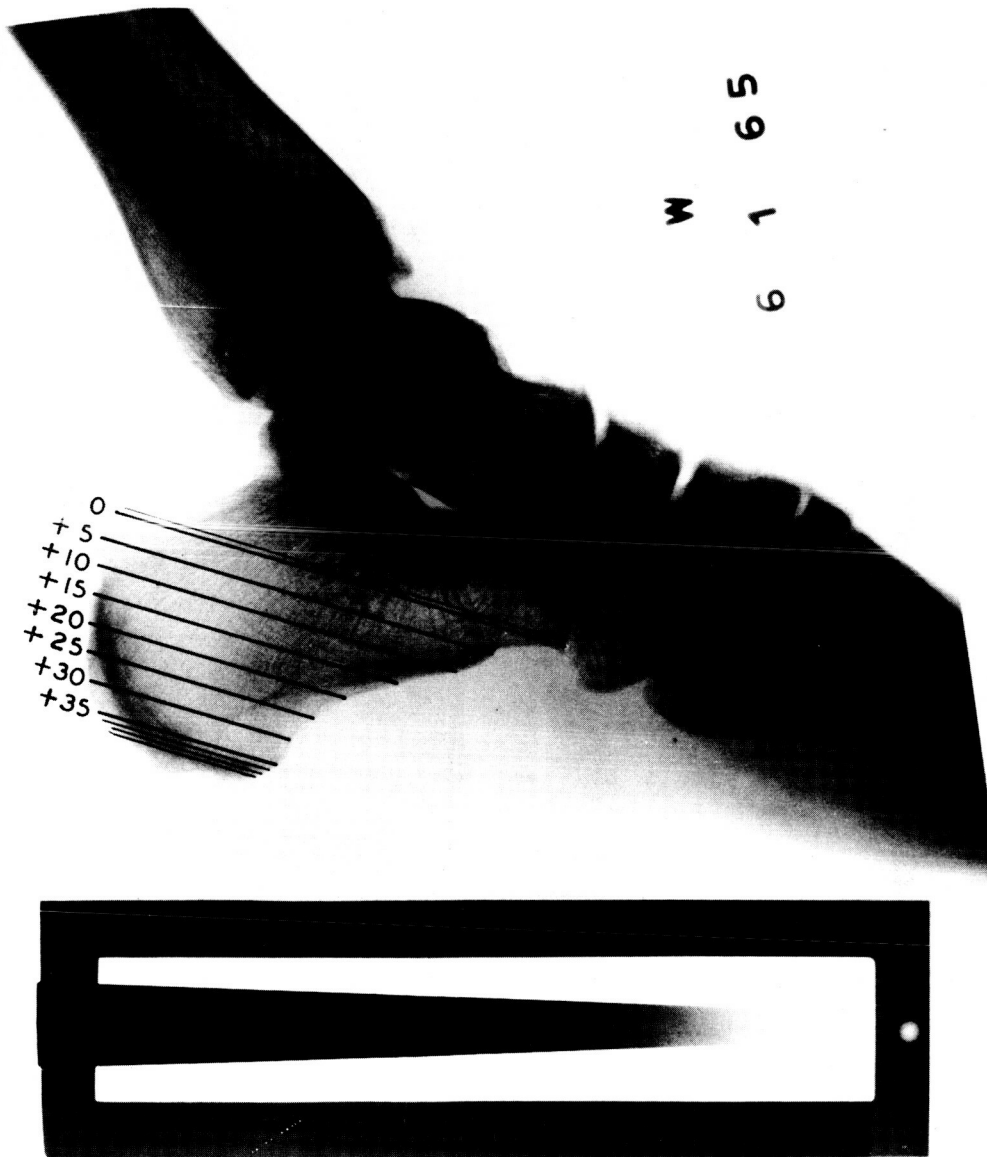
Figure 6-3.- Positive of os calcis X-ray on the Gemini IV pilot, indicating parallel tracing paths.
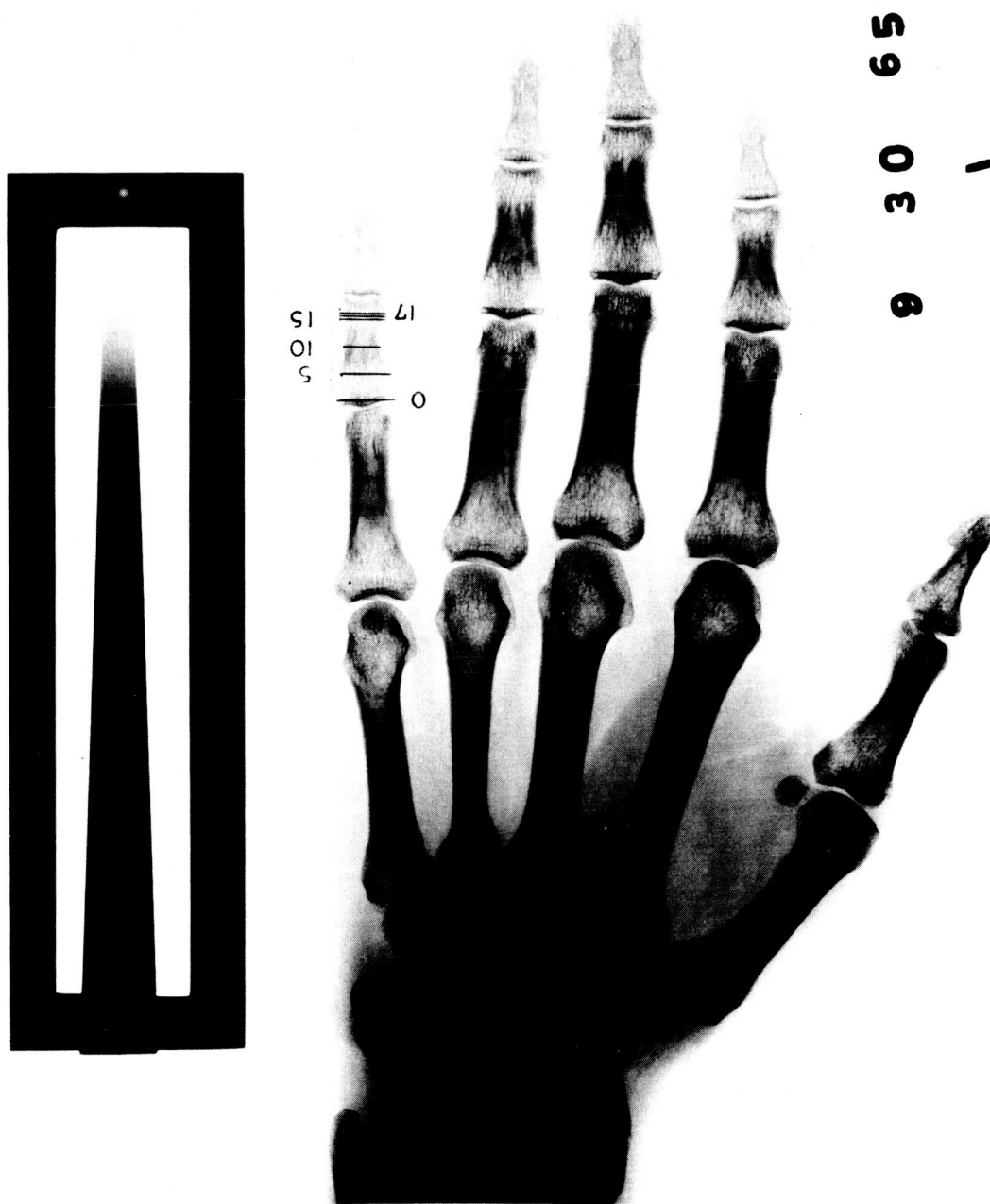
Figure 6-4.- Positive of X-ray of left hand, indicating parallel tracing paths on left digit.
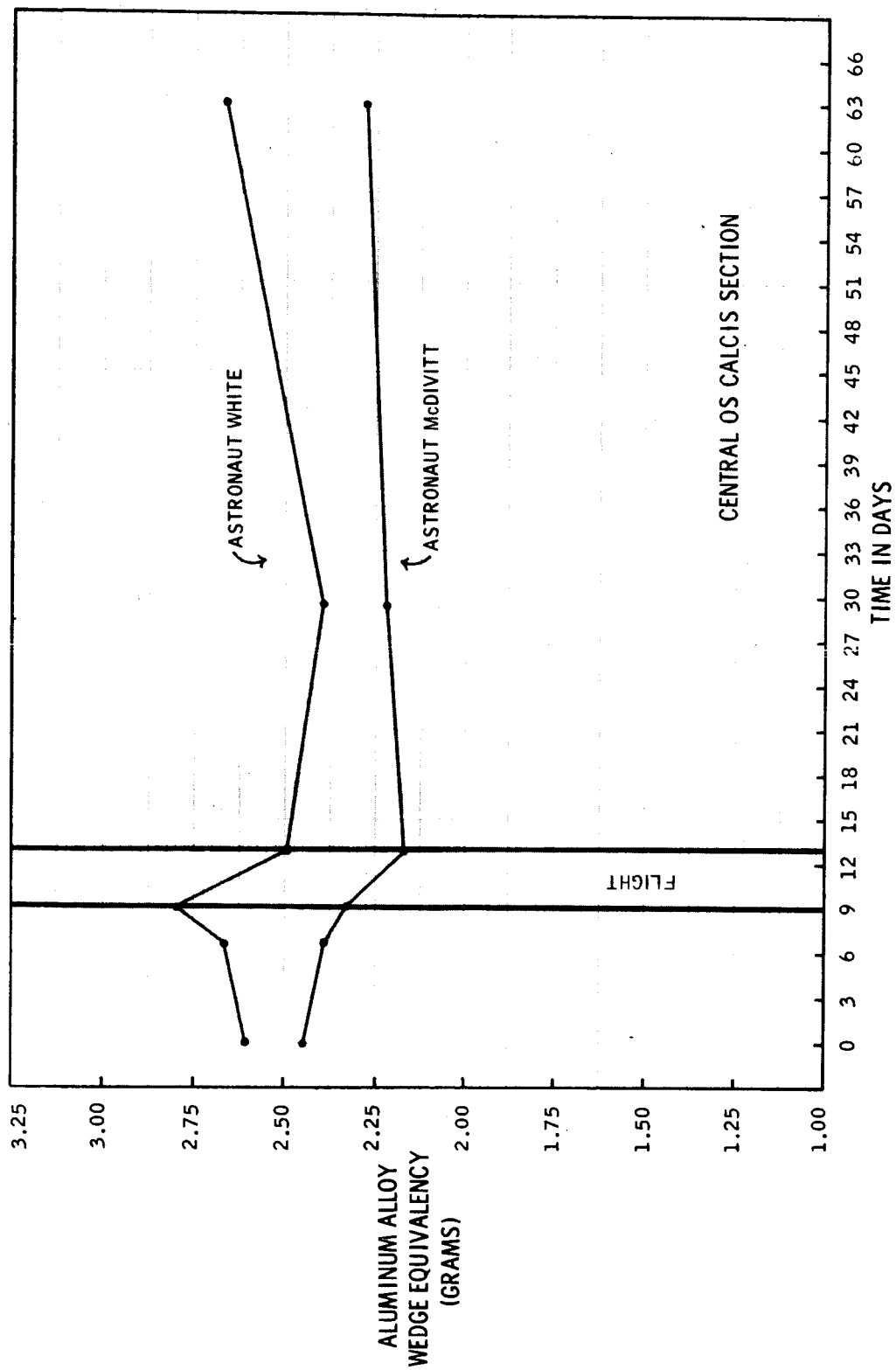
Figure 6-5.- Changes in the aluminum alloy wedge X-ray equivalency of the central os calcis segment ("conventional" segment) of Gemini IV command pilot and pilot throughout the Gemini IV program.
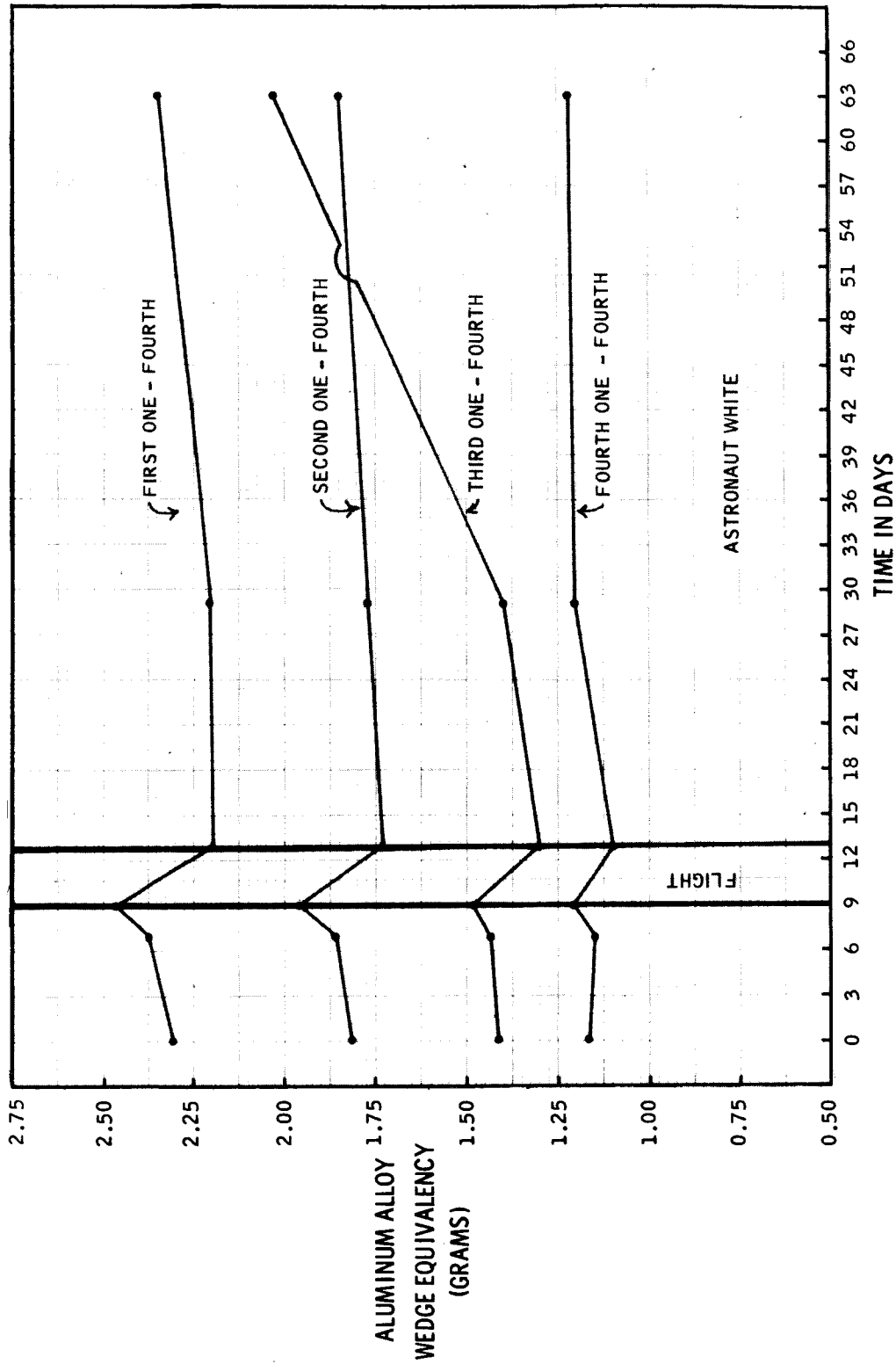
Figure 6-6.— Changes in the mean aluminum alloy wedge equivalency values for four groups of parallel segments of the os calcis of the Gemini IV pilot.
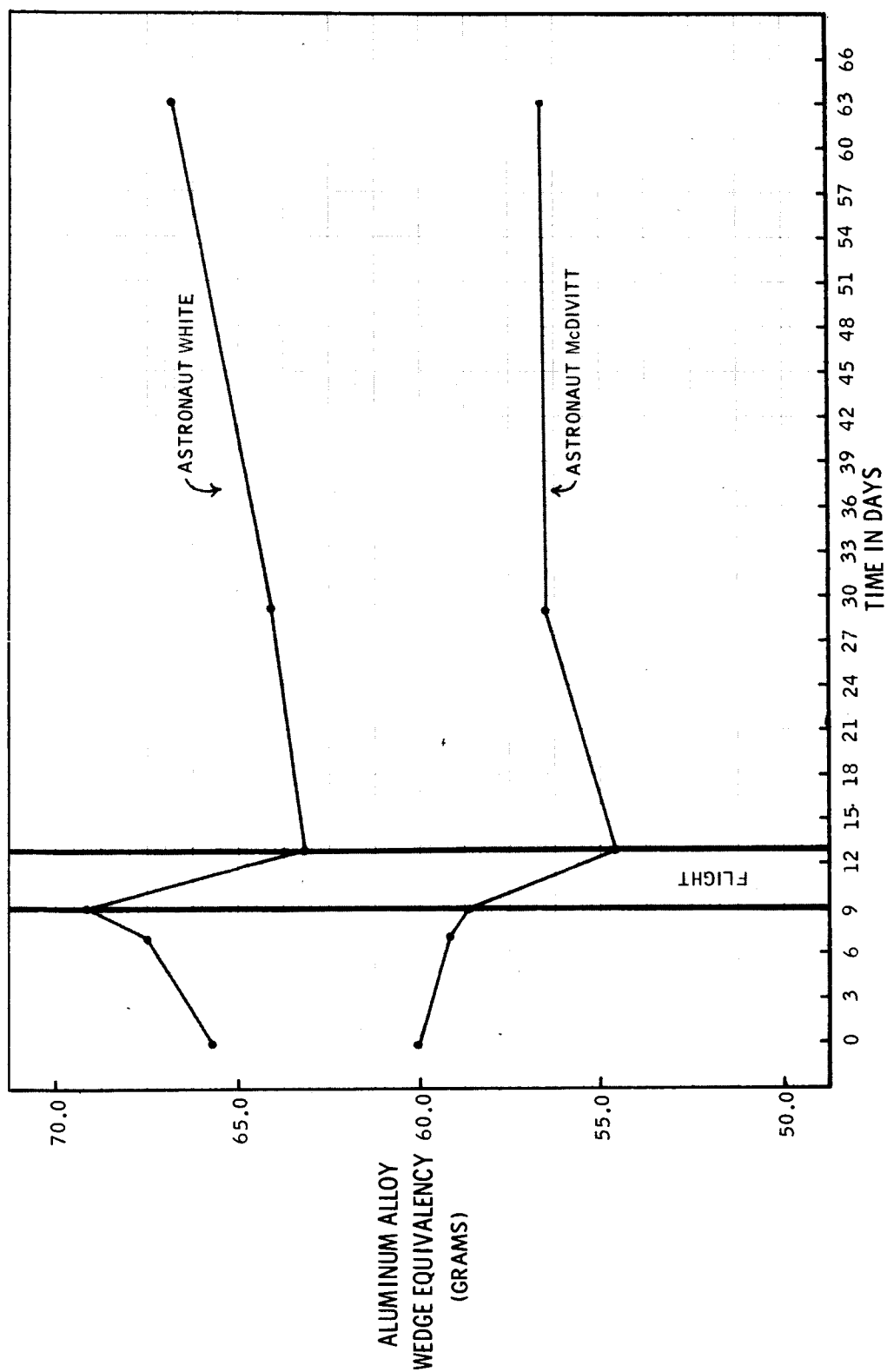
Figure 6-7.- Overall changes in bone in terms of mean aluminum alloy wedge equivalency of the entire series of parallel segments.
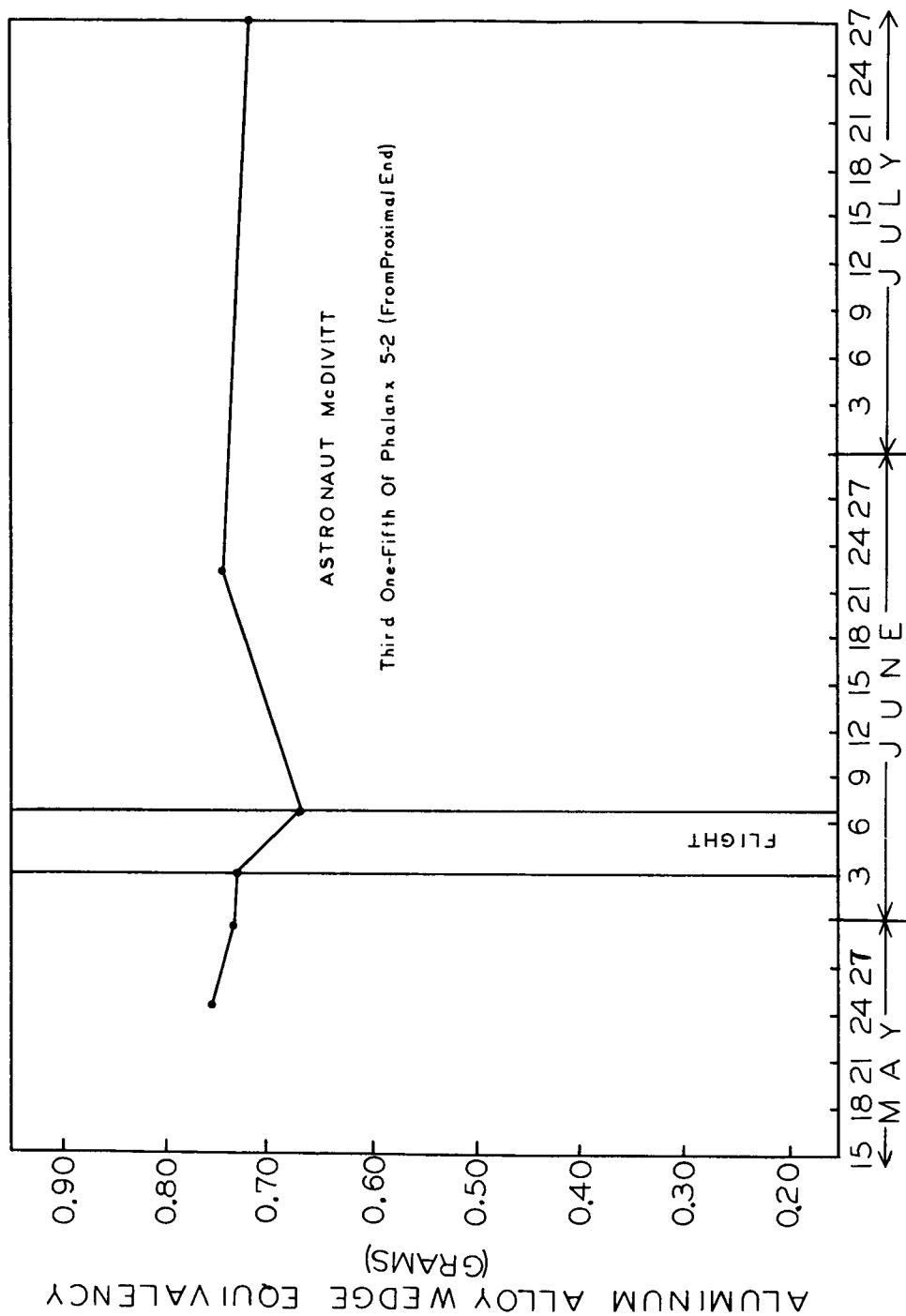
Figure 6-8.- Changes in wedge mass equivalency of a band of segments across finger phalanx 5-2 representing one-fifth of the length of this segment.

7. EXPERIMENT T-1, REENTRY COMMUNICATION ON GEMINI III

By Lyle C. Schroeder, Theo E. Sims, and William F. Cuddihy
NASA Langley Research Center

SUMMARY

36/07

A method of overcoming reentry blackout by injecting water into the flow field was demonstrated during the Gemini III mission. Significant levels of signal-strength increase during the early portion of the water-injection sequence were received on UHF telemetry (230.4 Mc) and UHF voice (296.8 Mc) frequencies. Enhancement of C-band beacon (5690 Mc) signal was observed during the latter portions of the water-injection sequence. UHF signal received during water injection exhibited an antenna pattern beamed in the radial direction of the water injection from the spacecraft.

INTRODUCTION

The communications blackout problem has been studied for several years by Project RAM (radio attenuation measurement) at the Langley Research Center. Early work was devoted to attempts to understand the problem and to arrive at a method of predicting radio-signal attenuation levels, whereas much of the more recent work has been directed toward development of methods of alleviating communications blackout and measurement of attenuation-sensitive parameters under simulated and actual flight conditions.

One of the most promising techniques investigated for communications-blackout alleviation has been that of material addition to the ionized flow field. The additive reduces the concentration of electrons in the ionized media through droplet surface recombination, cooling, and electrophilic mechanisms to cause a reduction in signal attenuation. Tests conducted on a 1-inch-nose-radius model immersed in a rocket-exhaust plasma have shown that water addition causes complete restoration of the attenuated signal. Similar results were found during a flight test of a 4-inch-nose-radius model. In the tests cited, water injected in a sector of the flow field caused complete omnidirectional signal recovery

for very moderate flow rates. This signal restoration in the tests led
to the conclusion that the material-addition technique was feasible for a
spacecraft of the shape and size of Gemini.

Some of the advantages in testing the material-addition technique on
a Gemini spacecraft are as follows:

(1) Gemini is a practical vehicle in that it is a manned, blunt
     spacecraft with an ablative heat shield.

(2) The size of Gemini is 10 times that of the last RAM flight-test
     vehicle.

(3) The reentry velocity of Gemini is about 7000 ft/sec higher than
     that of the last RAM flight-test vehicle.

(4) The information is timely for application to future space re-
     entries.

However, many conditions were not favorable for conducting the
experiment on the Gemini III spacecraft. The most important of these
are as follows:

(1) The UHF antenna was located far from the injection nozzles in
     the aft end of the spacecraft in a separated flow region.

(2) Spacecraft flight parameters, particularly roll attitude (upon
     which signal recovery level is highly dependent), were such
     that the water-injection window was not pointed toward ground-
     receiving stations.

In any case, the experiment is an evaluation of the technique as
applied to this large, blunt, ablative body. It is believed that the
results obtained under such unfavorable conditions are quite significant.

EXPERIMENT DESCRIPTION

System Geometry

The Gemini spacecraft begins reentry with the heat shield facing
forward. The Gemini III spacecraft was banked $45°$ to the left at the
start and throughout most of the blackout period. This orientation of
the spacecraft as viewed from the south side of the flight path is shown
in figure 7-1. Several aspects of the geometry of the experiment can be
pointed out from this figure. The reentry UHF antenna was on the aft end

of the spacecraft and the C-band antennas were on the conical portion. The experiment compartment (the right main landing-gear door) is outlined by dashed lines. It can be seen from this figure that the injection nozzles were on the circumference of the conical portion about 15° above the southern horizontal. Also shown in this figure is the anticipated distribution of the water injected. Figure 7-2, which illustrates these locations in more detail, shows that the injection nozzles are about 30° to the right of the bottom or windward sides. (Since the spacecraft flies at an angle of attack, it was determined that water requirements would be less if injection took place from the windward side.) From this detailed illustration it can be seen that injection nozzles were pointed forward so that the direction of injection was about 20° off the spacecraft surface. This arrangement was used in order to increase the dwell time of drops in the vicinity of the spacecraft.

The flow field on the windward side of the Gemini spacecraft is "attached" in such manner that an inviscid layer extends from the vehicle boundary layer out to the shock. However, the air on the aft end of the spacecraft near the UHF antenna is separated from this inviscid layer, and is circulating at a relatively much lower velocity. The implications on the experiment resulting from this separation of flow were considered.

Window Size

The "window" is defined as the volume distribution of water in the flow field. It is assumed that the attenuating mechanisms are relieved in the window, and hence the window might be considered a "hole" in the plasma with free space properties. The size of the window created by water injection was at first assumed and later examined in wind-tunnel tests.

Since the spacecraft and plasma sheath are large with respect to a UHF wavelength, it was suspected that the major radiation from the spacecraft would be beamed through the window created by water addition. Studies were performed to determine the pattern-beamwidth characteristics and signal recovery expected with various assumed window sizes. The results which confirm that beaming would occur are presented in a subsequent section.

Water-Injection System

The onboard experiment consisted of a water-injection system which was designed into the right main landing-gear door. Figure 7-3 illustrates the installation of the experiment equipment on the inside of

this door. The electrical details of the system are presented in figure 7-4. The system was completely independent of other spacecraft interfaces except for the electrical actuation switch and the leads to the astronauts' cabin. This gas pressurized water-injection system is shown schematically in figure 7-5. The system was designed to be actuated by the astronaut on the right side, which simultaneously supplied water expulsion pressure through the regulator to the water tank and started the mechanical timer. Once every 15 seconds the timer opened and closed contacts to each of three solenoid valves from which water was injected. This system was designed to produce pulses alternately of low, medium, and high flow rates with durations of 1/2, 1/4, and 1/10 second. Figure 7-6 shows one injection cycle. The water supply is depleted after about 12 cycles.

The planned experiment actuation time for the Gemini III mission was 45 seconds after the beginning of UHF blackout. It was possible to update predictions for the beginning of UHF blackout after retrofire. Figure 7-2 shows the number of nozzles used and indicates the orifice sizes.

Frequencies Transmitted

Three frequencies were in operation during reentry: UHF telemetry at 230.4 Mc, UHF voice at 296.8 Mc, and C-band at 5690 Mc. On the UHF telemetry system, a power of 2 watts is transmitted into a quarter-wave stub antenna with a gain of 2.5 over isotropic and a VSWR of about 2.1:1. On the UHF voice system, a power of 3 watts is transmitted into the same stub antenna with about the same gain and a VSWR of about 2.85:1. (During the injection period, the astronaut was requested to key the UHF transmitter to attempt communication on this link also.) The C-band radar transponder operates at 1-kilowatt peak power which is fed to three helical antennas to form a circular roll pattern.

Ground Stations

During the experiment operation period, ground stations located near the reentry flight path were requested to monitor signal strength on UHF telemetry, UHF voice, and C-band frequencies. Stations requested to monitor signal strength are given in the following table:

Station	Frequencies monitored		
	UHF telemetry	UHF voice	C-band
Eglin Air Force Base	X	X	X
Mission Control Center at Cape Kennedy	X	X	
Telemetry Site II at Cape Kennedy	X	X	
Mila at Cape Kennedy			X
Patrick Air Force Base			X
Grand Bahama Island	X		X
Grand Turk Island	X		X
Anclote Point (Eglin AFB)	X	X	X
Key West (Langley Research Center van)	X	X	
Homestead (Langley Research Center van)	X	X	
Aircraft (4)	X	X	

The locations of the stations with respect to the spacecraft during blackout and experiment are shown in figure 7-7.

GROUND SUPPORT STUDIES

Penetration and Flow Rate Studies

A study was made to determine flow rate requirements and to optimize the penetration.

Estimates of the water-flow-rate requirement were extrapolated from the RAM B2 flight results and calculated by using equilibrium cooling theory. While there are more accurate methods now available, this method was the best approach known at the time of the calculations. Three flow rates, low, medium, and high, were selected for the experiment.

Under the conditions of fixed pressure and nozzle size, penetration could not be optimized throughout the blackout altitude range. For this reason, "design" altitudes were chosen for each flow rate at which penetration was optimized. Penetration distance was chosen to extend to the shock at these altitudes by proper choice of nozzle size. Verification of proper penetration was confirmed by wind-tunnel testing. (Lateral and longitudinal penetrations were also measured to determine the size of the RF window.)

Figure 7-8 is a plot of the variation of penetration with altitude for the conditions of the Gemini III flight. Shown also in this figure is the distance from the body to the shock and the optimum penetration distance. It is seen that penetration decreases greatly with altitude. It was assumed that overpenetration would result in signal recovery, but that underpenetration would not. Hence, penetration for the actual Gemini III mission would be sufficient above about 240 000 feet altitude. (Gemini III angle of attack was much lower during flight than predicted, and as a result, the flow field on the windward side was 25 percent thicker, and optimum penetration was reached at higher than predicted altitudes.)

Antenna Pattern Studies

It has already been stated that since the size of the spacecraft and associated flow field was large relative to a UHF wavelength, it was suspected that transmitting through an aperture in a plasma would cause the signal to be beamed. A directive signal would cause the experiment to be dependent on vehicle roll attitude for signal acquisition; further, since in flight at normal spacecraft attitude the injection nozzles are pointed upward, signal would be beamed away from ground stations. As a result, a series of tests was conducted by Francis Russo of Langley Research Center to determine the degree of recovery and antenna pattern produced when a slot is opened in the ionized flow field. In these tests, a transmitting model was immersed in lossy-medium shrouds to simulate the Gemini in a plasma sheath. Slots of varying aperture size were cut in the shrouds and corresponding antenna patterns recorded.

The antenna pattern for a slot size corresponding to the anticipated distribution of droplets, as determined by wind-tunnel tests, is shown in figure 7-9. It was noted, however, that the beamwidth characteristics did not depend strongly on slot size, so long as the window extended lengthwise beyond the UHF antenna. It can be seen from the plot of roll angle against signal strength in this figure that beaming occurs in the direction of injection. Therefore, for the Gemini III mission, receivers tracking the spacecraft at roll aspect angles greater than approximately 50° around from the RF window would not have been expected to receive much signal.

RESULTS

Reentry Events

The variation of altitude with time is shown in figure 7-10; the reentry flight path was previously shown in figure 7-7. In both figures, special reference is made to times important in the experiment. UHF blackout began at 4:39:59 (hr:min:sec elapsed from lift-off) at an altitude of about 318 000 feet. At about 4:36:26 (3 min 33 sec before blackout), the spacecraft banked 45° to the left, placing the injection nozzles about 75° south of straight up or about 15° above the horizontal. The experiment was actuated at 4:41:16 (1 min 17 sec after blackout began) at an altitude of about 272 000 feet, and it ended after 3 minutes at an altitude of 160 000 feet. Blackout ended at 4:45:00 at an altitude of about 134 000 feet.

Water Flow Rates

The flow rate of the water-injection system was determined by preflight calibration and was not monitored in real time. Twelve cycles of three different flow rates were employed over the data period. The flow-rate sequence was shown previously as figure 7-6. Table 7-1 is a tabulation of the mission times during which flow rate pulses occurred. Pulse times during the first 45 seconds and the last minute of the injection period were verified by signal strength pulses; the remaining pulse times were determined by extrapolation.

TABLE 7-1.- STARTING TIMES OF FLOW RATE PULSES

(TIMES AFTER LAUNCH)

Cycle	Small flow rate hr:min:sec	Medium flow rate hr:min:sec	High flow rate hr:min:sec
1	4:41:15.9	4:41:19.9	4:41:24.6
2	4:41:31.2	4:41:35.2	4:41:39.9
3	4:41:46.5	4:41:50.5	4:41:55.2
4	4:42:01.8	4:42:05.8	4:42:10.5
5	4:42:17.1	4:42:21.1	4:42:25.8
6	4:42:32.4	4:42:36.4	4:42:41.1
7	4:42:47.7	4:42:51.7	4:42:56.4
8	4:43:03.0	4·43:07.0	4:43:11.7
9	4:43:18.3	4:43:22.3	4:43:27.0
10	4:43:33.6	4:43:37.6	4:43:42.3
11	4:43:48.9	4:43:52.9	4:43:57.6
12	4:44:04.2	4:44:08.2	4:44:12.9

Duration of pulses:
  Small - 0.46 sec.
  Medium - 0.21 sec.
  High - 0.10 sec.

Signal-Strength Measurements

Signal-strength records from all stations have been analyzed.
The signal-strength records from Key West, Homestead, aircraft 3, air-
craft 4, and Grand Bahama Island show that significant levels of signal
recovery were observed on UHF telemetry and UHF voice frequencies cor-
responding to the early portion of the water-injection sequence. The
latitude and longitude and altitude when pulses were noted are shown
in figures 7-7 and 7-10. In figure 7-11, plots of signal strength
against time for the Key West station show two well-defined signal-
recovery pulses plus a third less definitive one. Each pulse corresponds
to the high water flow rate. Aircraft 3, aircraft 4, and Grand Bahama

Island stations did not receive the third signal-recovery pulse. No signal recovery was received from the low and medium flow rates.

Function records from Mila (Cape Kennedy) and Grand Bahama Island C-band radars show signal strength enhancement pulses corresponding to the latter portion of the injection sequence. In figure 7-12, a tracing of the C-band signal strength oscillograph record is shown. The record is broken so that each line is one injection period long. The time during which injection occurs is indicated. Pulses of significant level can be seen corresponding to the medium and high flow rates. The stations at Grand Bahama Island and Mila were tracking in the beacon mode. The other Cape Kennedy radar was tracking in the skin-track mode and consequently did not record any enhancement pulses. C-band radar records at Eglin Air Force Base did not show these enhancement pulses. Anclote Point data are inconclusive.

DISCUSSION

UHF Results

It has been reported that the Gemini UHF signal which had been completely blacked out was increased to a high level above receiver noise by water addition. The significance of these results is that the material-addition technique of radio-signal attenuation alleviation has been shown to work for a body of the size and shape of Gemini. Of added significance are the facts that signal recovery was noted even though aspect angles to the ground stations were far from optimum and that the predictions are based on a flow field which is not well known. It is indicated that much improvement can be made in applying the technique if the experiment can be performed under more suitable conditions.

No stations north of the flight path received UHF signal-recovery pulses except Grand Bahama Island, where the aspect angle at the time of signal recovery was almost directly forward. On the south side of the flight path, four stations (not including Grand Bahama Island) received the UHF signal recovery pulses. These results are in agreement with Langley pattern-beamwidth studies which predicted that the signal would be beamed toward the south side of the flight path.

Recovery was recorded for the first three high flow rate pulses between altitudes of 275 000 and 245 000 feet. Recovered signal was very strong but became marginal on the third pulse, and afterward was lost altogether. This aspect of reduced effectiveness during the latter part of the data period was analyzed quite thoroughly from a fluid mechanics standpoint, but it appears that several factors could be involved as follows:

(1) The long distance from the injection sites to the UHF antenna. The decrease of effectiveness of material addition on attenuation with distance aft was noted on the RAM B2 flight test, where three antennas were located from about 2 to 10 feet downstream of the injection site. The forward antenna saw almost complete recovery, while the middle antenna saw less effect, and the antenna farthest downstream saw still less. While it is conceded that these antennas are of different design, the decreasing recovery effect with distance downstream may be significant to the Gemini case, since the UHF antenna is about 8 feet downstream of the injection site.

(2) Penetration less than predicted. Since angle of attack during flight was less than predicted, the flow field on the windward side was almost 25 percent thicker than expected. As a result, penetration would have decreased below required levels at higher altitudes than predicted. The penetration requirements to account for the lower angle of attack were recomputed. These calculations show that penetration decreased below required levels at the altitude when signal recovery terminated (for the high flow rate). They also indicate that the medium and lower flow rates could not achieve sufficient penetration to cause signal recovery during the altitudes experienced during flight.

(3) Unknowns of the Gemini flow field. The addition of ablative products containing sodium and potassium are known to cause the electron concentration to the flow field to increase. The location of the UHF antenna in a separated-flow wake region where assumptions such as simple flow field cooling and distribution are not applicable could conceivably contribute to lower-than-predicted recovery levels.

(4) Unfavorable aspect angle. Since signal recovery was very dependent on aspect angle, it is conceivable that minor deviations in aspect caused by flight could contribute. For the Key West and Homestead stations, for example, roll aspect angle increased from about 20° during the second large flow rate pulse to about 30° during the third such pulse.

C-Band Results

Signal recovery on C-band frequency was not really anticipated, since the onboard antenna locations were not favorable. However, signal strength enhancement pulses were noted for both medium and high flow rates on Cape Kennedy and Grand Bahamas Island radars for the

portion of the experiment from 100 seconds to 175 seconds after experiment initiation. These pulses were not received at the Eglin station, which beacon tracked during the early portion of the reentry, and Anclote Point data are inconclusive. Attempts are being made to link these C-band results with pattern and penetration parameters.

CONCLUDING REMARKS

An experiment was conducted during the Gemini III mission to determine whether water addition is effective in establishing communications links during the reentry portion of the flight. Attenuation levels were measured with and without water injection at UHF frequencies of 230.4 Mc and 296.8 Mc and the C-band frequency of 5690 Mc. UHF signals which had been blacked out were restored to significant levels during early portions of the water-injection sequence by the high flow rate injection. C-band signal was enhanced during the latter portion of the injection period by medium and high flow rate injections. The UHF signal recovered during water injection exhibited an antenna pattern beamed in the radial direction of injection from the spacecraft.

The minimum flow rate required was not determined, since penetration and the antenna location were not optimum. Postflight analysis shows that the UHF recovery agrees very well with injection penetration theory.

While the experimental results verified that signal recovery from Gemini blackout can be achieved, much can be done to improve the technique. Future experiments are under consideration for Gemini and Apollo missions which utilize more ideal antenna locations and injection sites and which are designed to minimize the problem of signal directionality. These experiments would result in more efficient use of water and could lead to operational systems to eliminate blackout on manned space flight.
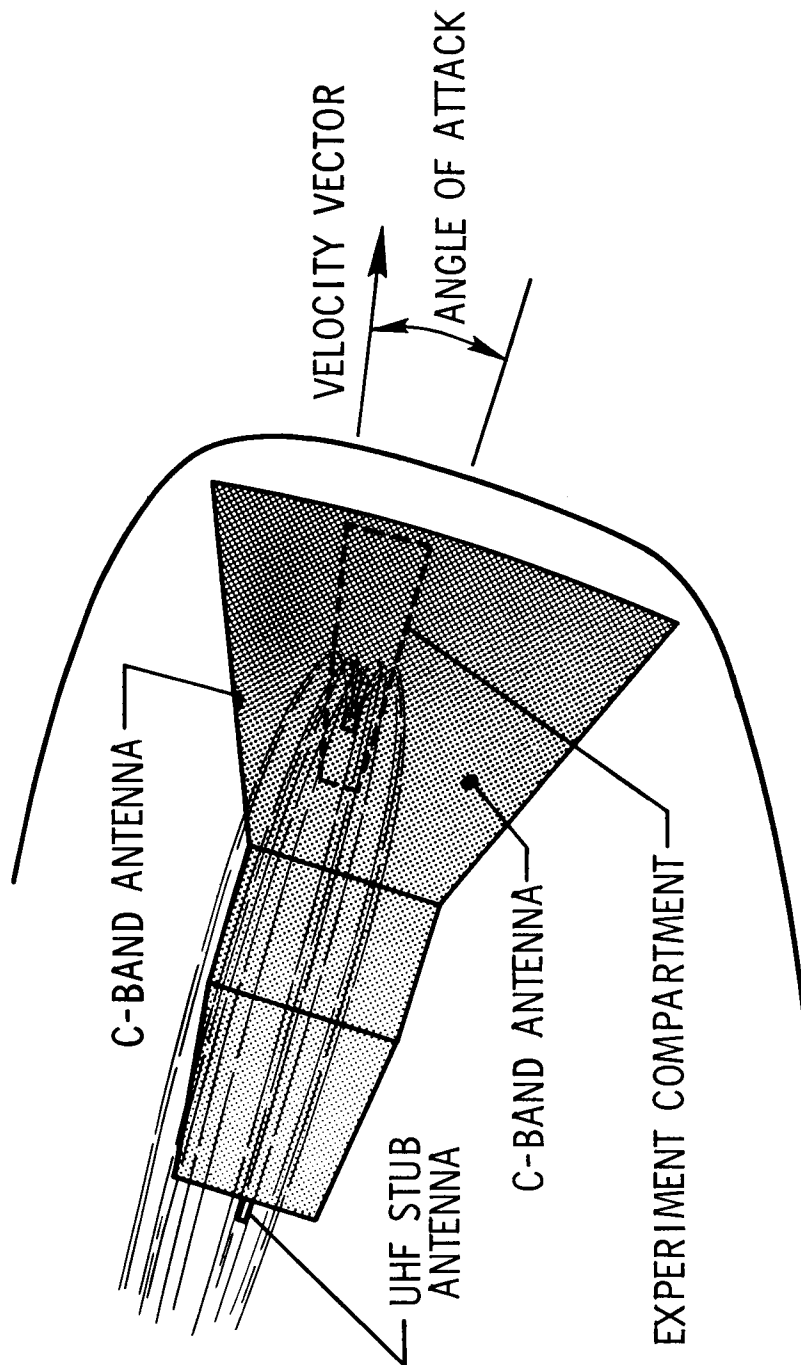
VELOCITY VECTOR

ANGLE OF ATTACK

C-BAND ANTENNA

UHF STUB
ANTENNA

C-BAND ANTENNA

EXPERIMENT COMPARTMENT

Figure 7-1.- Gemini experiment location on spacecraft.

MEDIUM
FLOW RATE

LOW
FLOW
RATE

HIGH
FLOW
RATE

WATER INJECTION NOZZLE

RIGHT MAIN LANDING-
GEAR DOOR
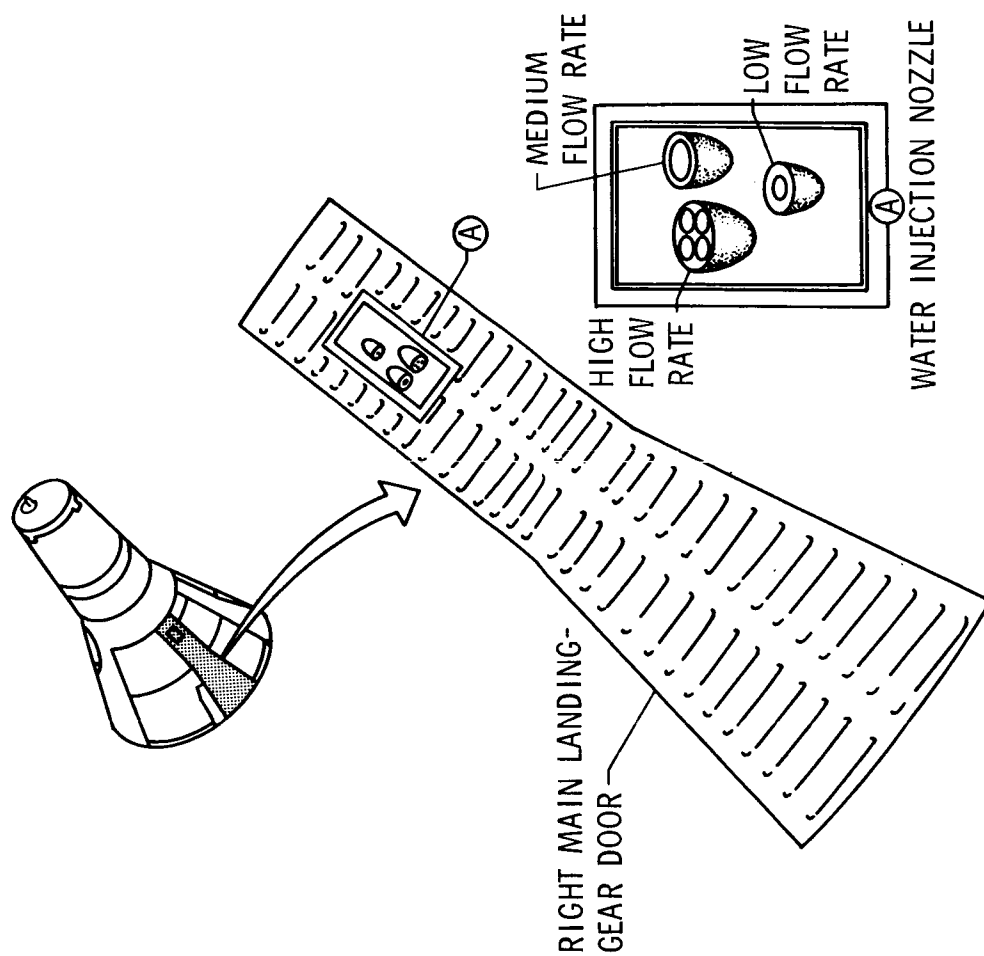
Figure 7-2.- Location of reentry communications experiment on Gemini spacecraft.

HIGH FLOW RATE SOLENOID

WATER CHARGING VALVE

MEDIUM FLOW RATE SOLENOID

LOW FLOW RATE SOLENOID

NITROGEN PRESSURE TANK

NITROGEN HIGH PRESSURE
RELIEF VALVE

NITROGEN PRESSURE REGULATOR
& SOLENOID SHUTOFF VALVE

WATER STORAGE TANK

RIGHT MAIN LANDING-
GEAR DOOR

WATER PRESSURE RELIEF VALVE

NITROGEN CHARGING VALVE

ARMING RECEPTACLE

ELECTRICAL COMPONENT ASSEMBLY

NITROGEN PRESSURE TRANSDUCER

NITROGEN LOW PRESSURE
RELIEF VALVE

INJECTION SEQUENCE
PROGRAMER

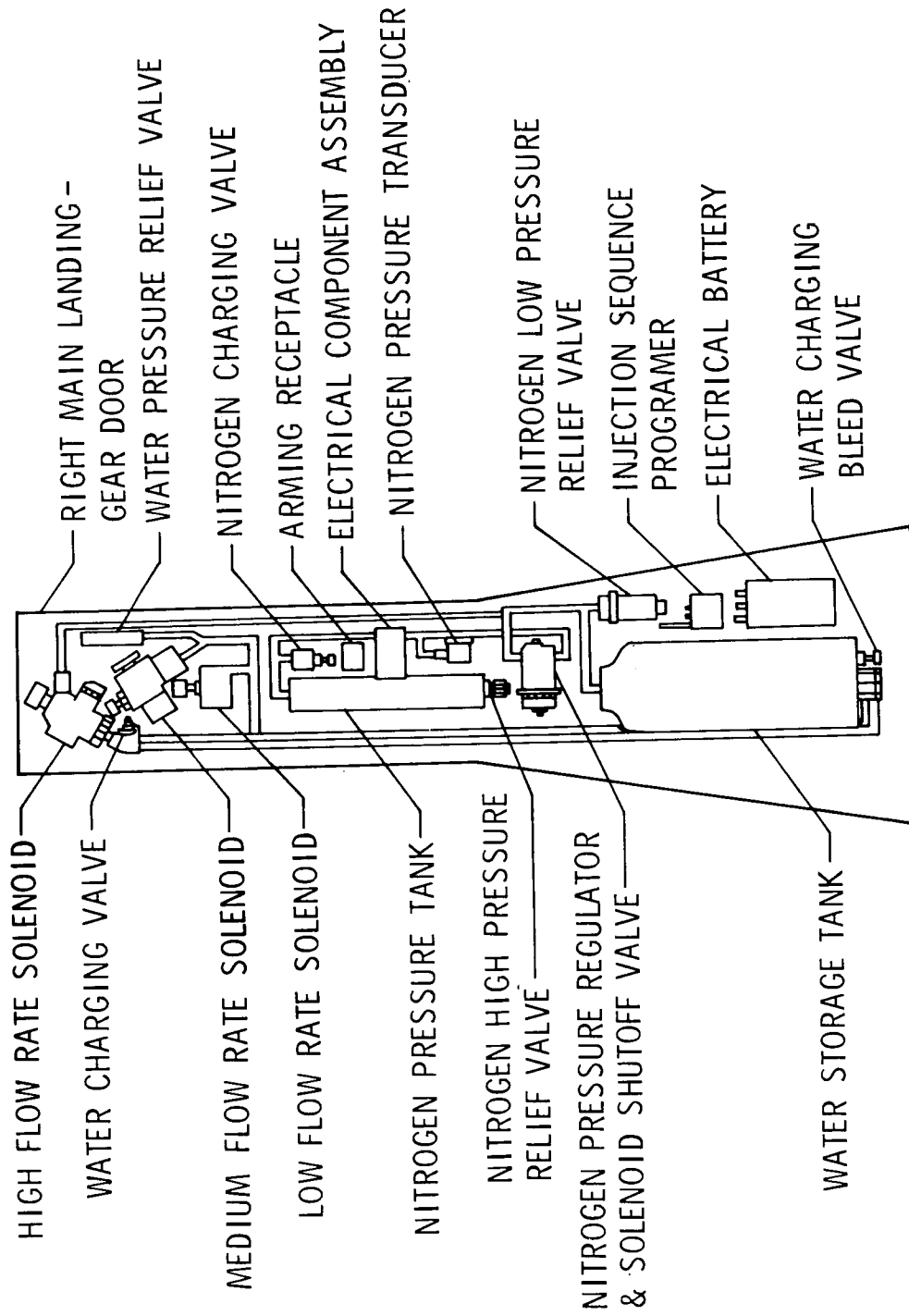ELECTRICAL BATTERY

WATER CHARGING
BLEED VALVE

Figure 7-3.- Reentry communications experiment equipment installation on inside of
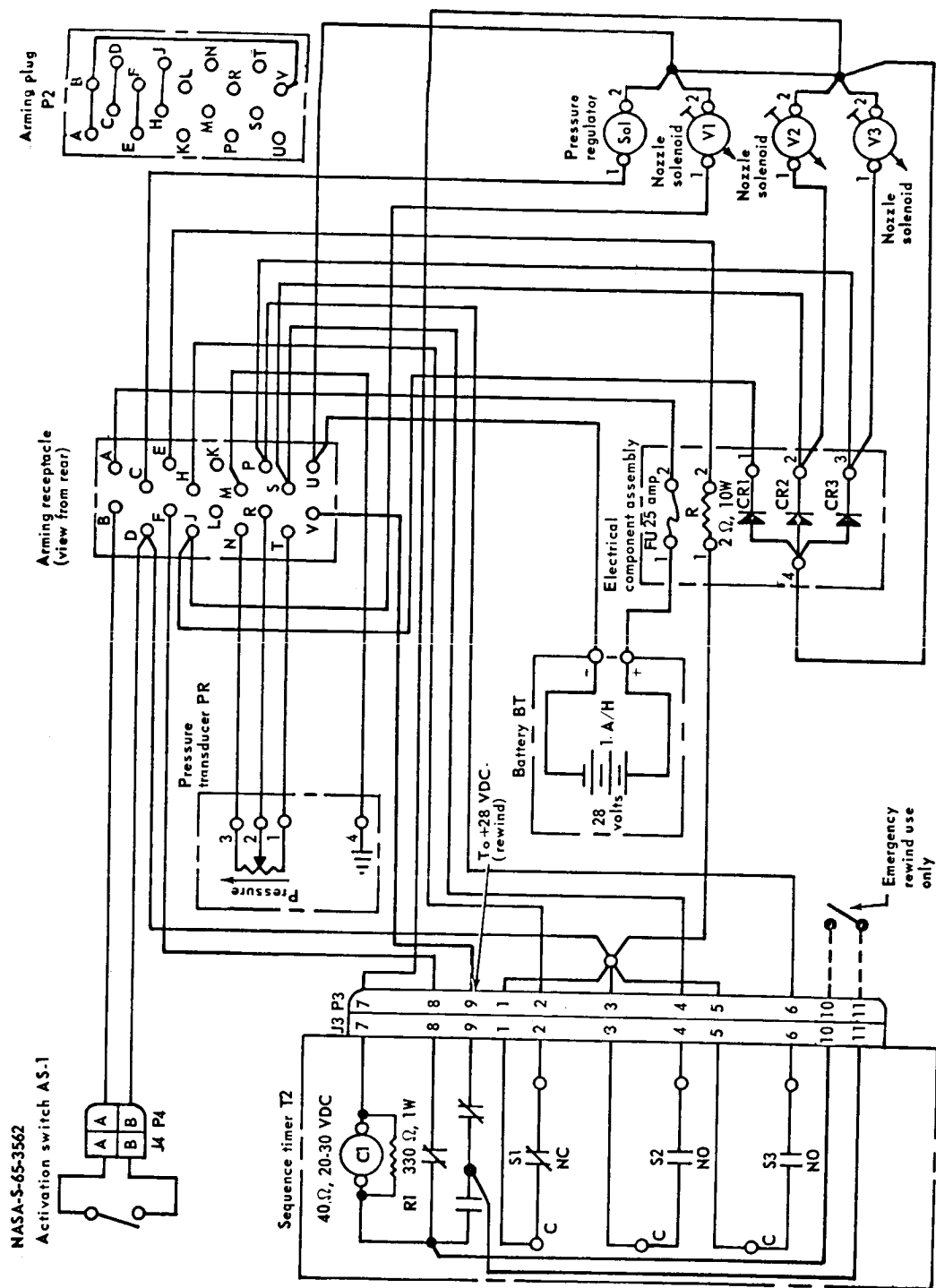right main landing-gear door.

Figure 7-4. - Reentry communications experiment wiring diagram.
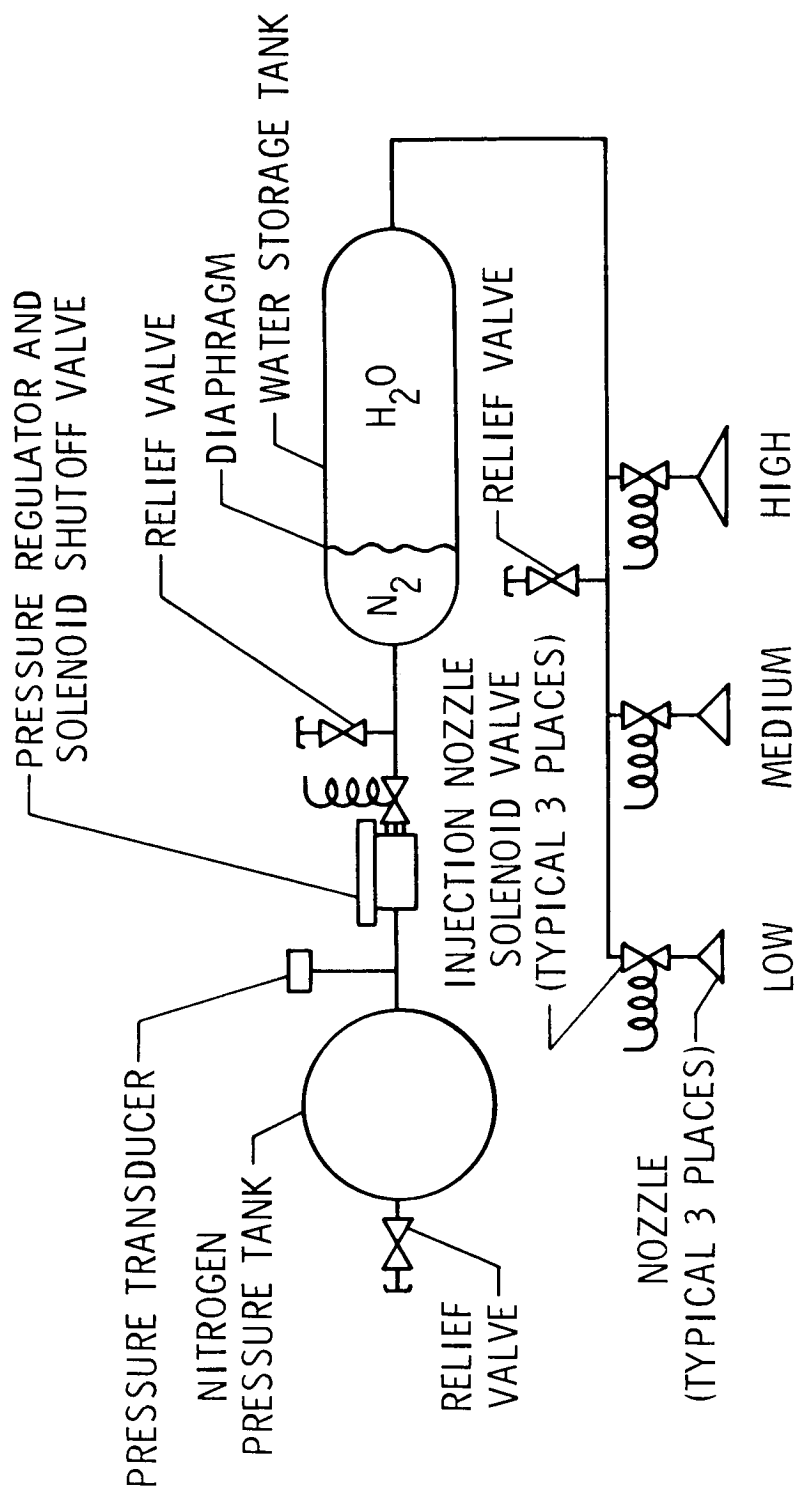
Figure 7-5.— Schematic of Gemini reentry communications experiment.

t = 0 CORRESPONDS TO ACTUATION TIME;
EXPERIMENT DURATION IS ABOUT
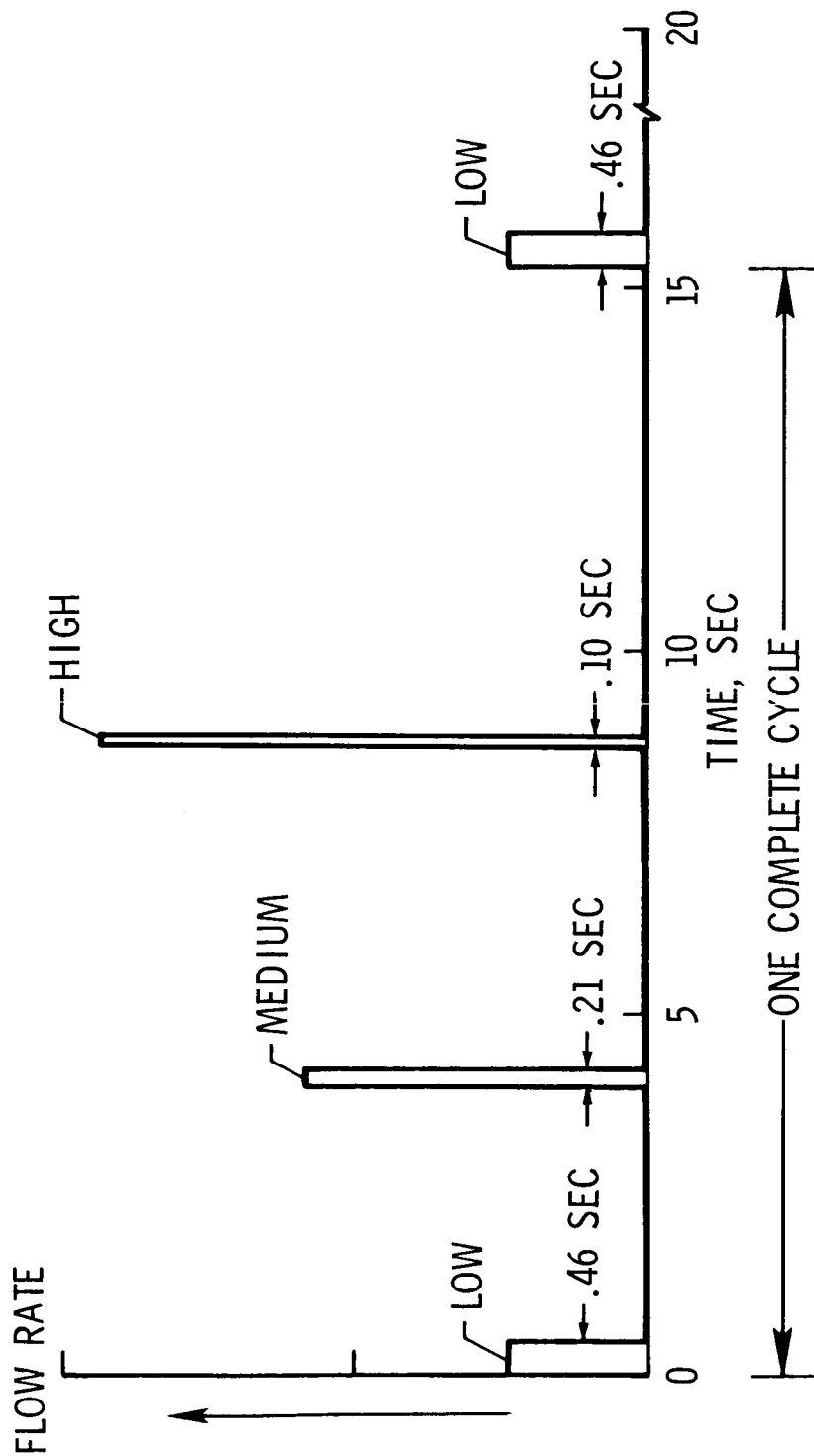12 COMPLETE CYCLES

FLOW RATE

LOW

.46 SEC

MEDIUM

.21 SEC

HIGH

.10 SEC

LOW

.46 SEC

0   5   10   15   20

TIME, SEC

ONE COMPLETE CYCLE

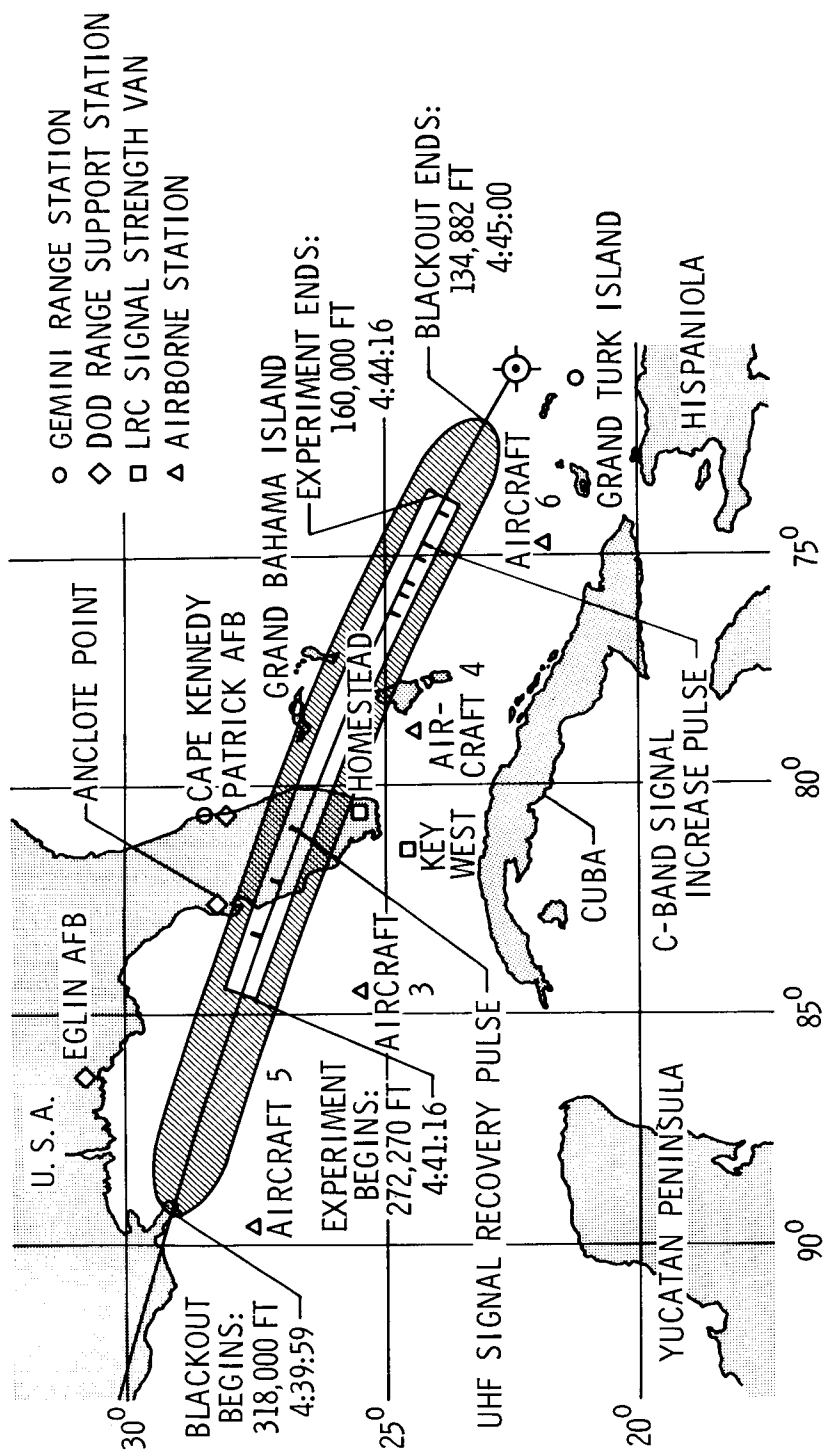Figure 7-6.- Flow-rate cycle for Gemini reentry communications experiment.

98

Figure 7-7.— Ground stations for Gemini reentry communications experiment.

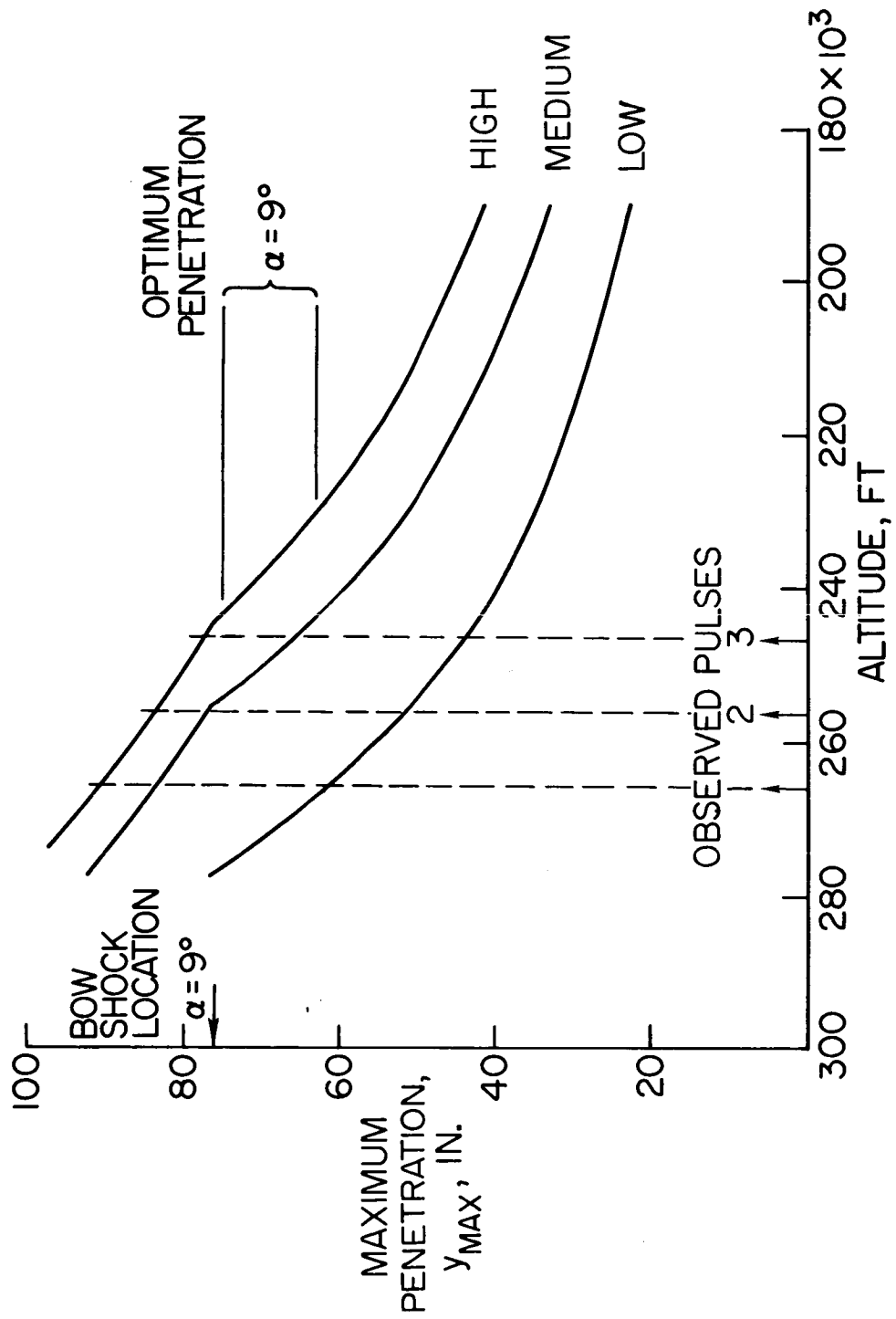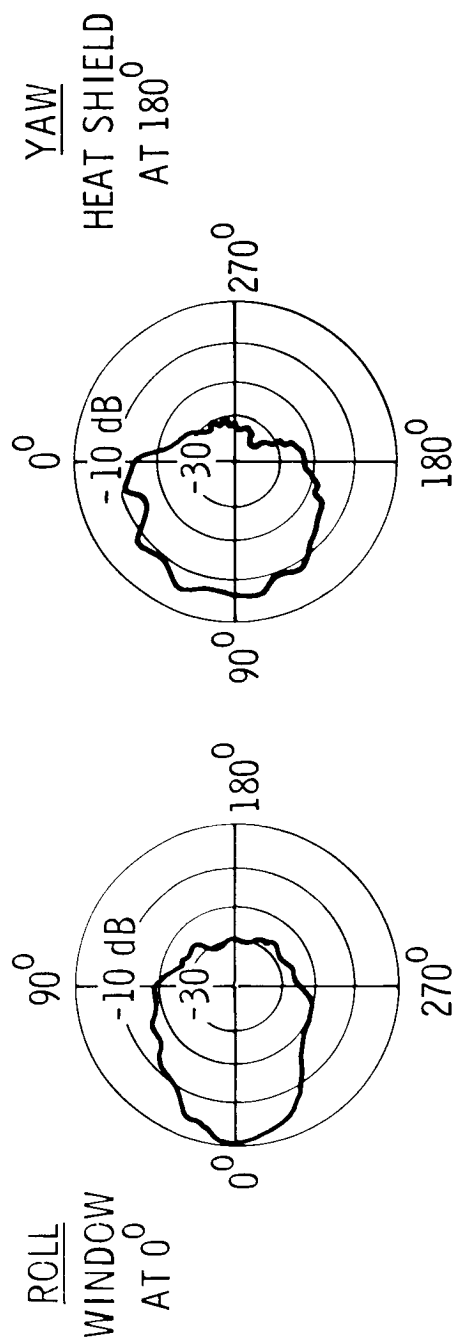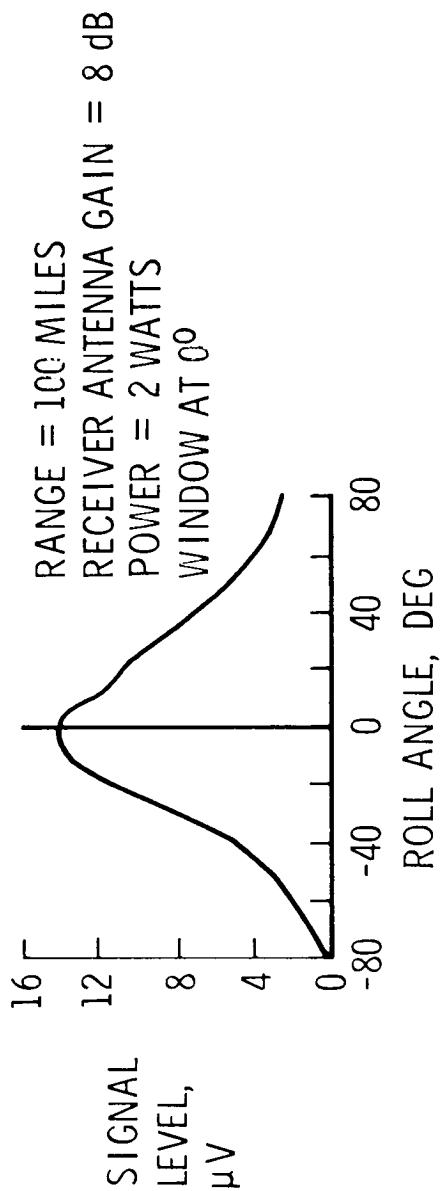Figure 7-8. - Penetration required plotted against altitude.
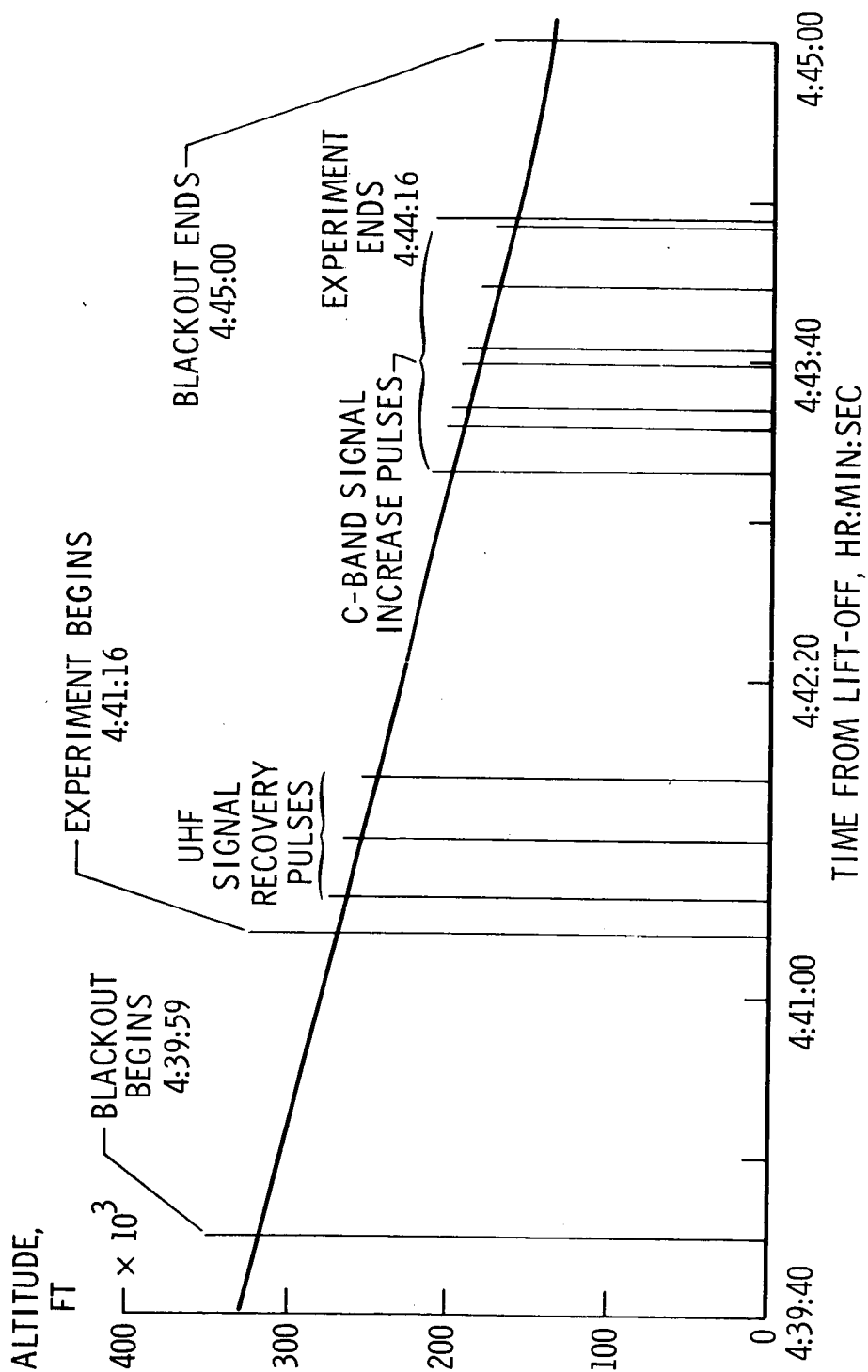
Figure 7-9.- Simulated Gemini antenna patterns.
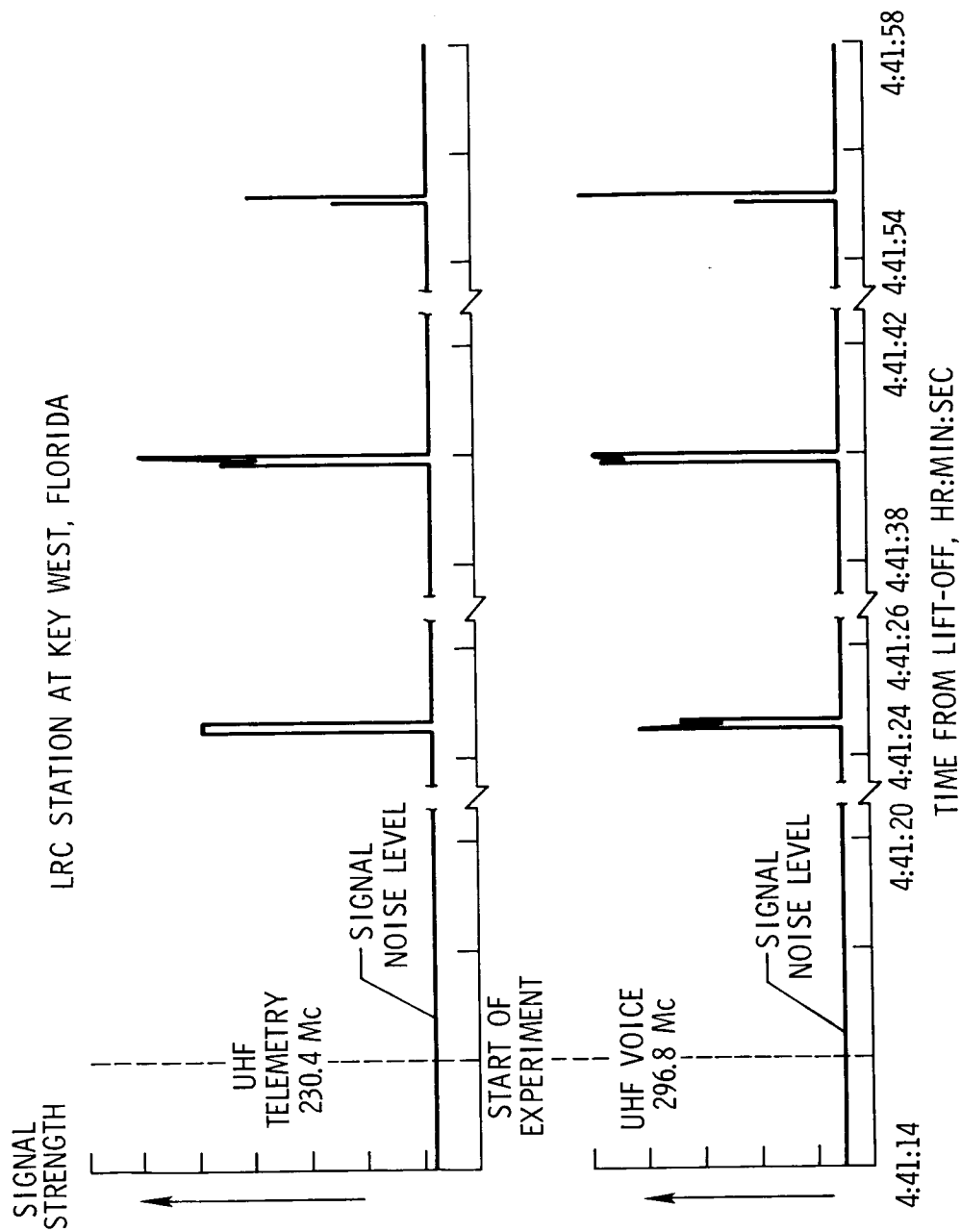
Figure 7-10.- Reentry altitude plotted against time.

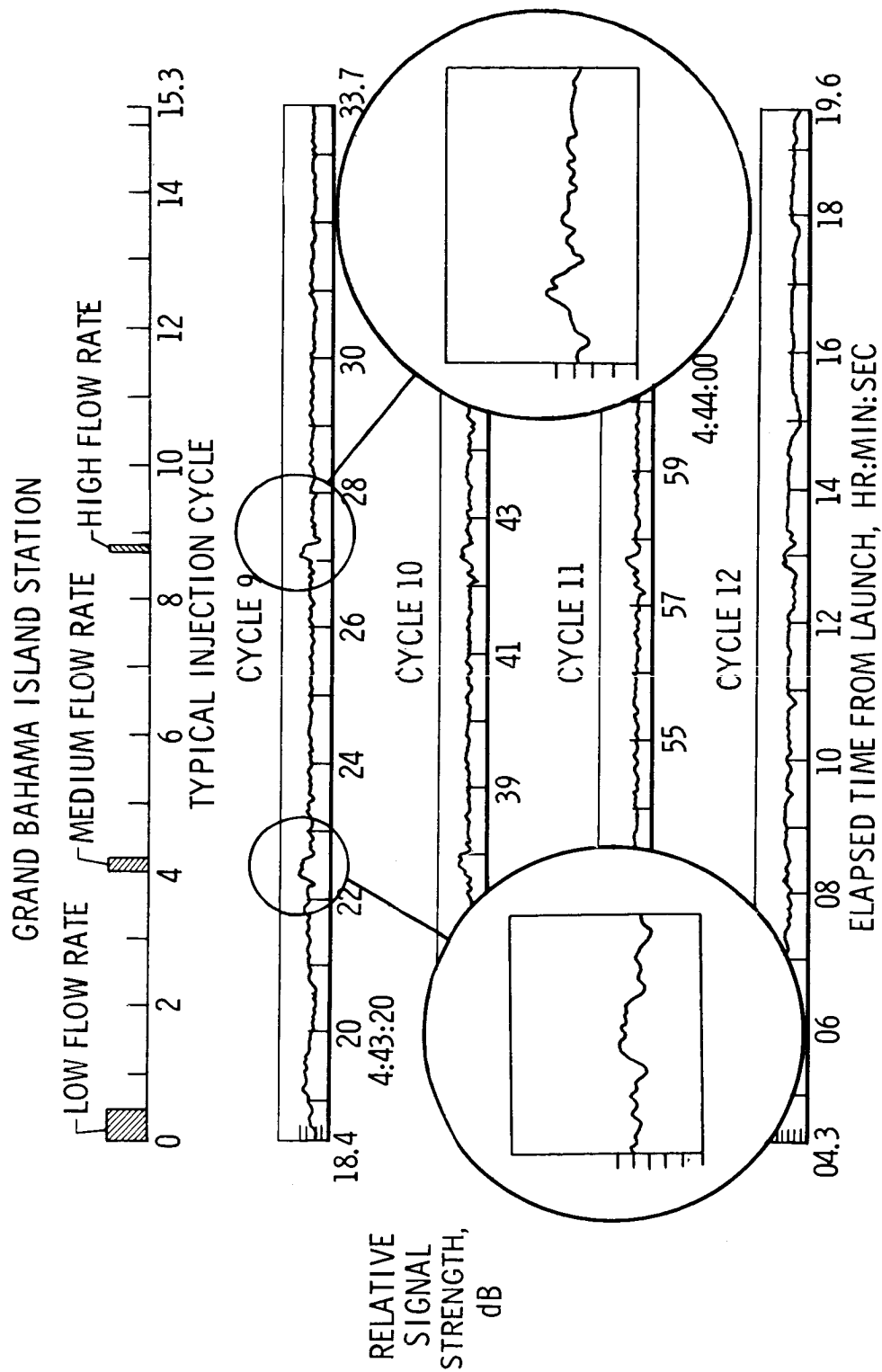Figure 7-11.- Signal strength plotted against time.

Figure 7-12.— Time history of C-band signal strength.

8. EXPERIMENT D-9, SIMPLE NAVIGATION ON GEMINI IV

By Capt. E. M. Vallerie, USAF
Space Systems Division

The United States Air Force has been investigating space position fixing techniques for over four years. A review of Space Navigation and Guidance development programs indicated that most were based on automated systems with no manual capability (fig. 8-1). If the automatic space navigation and guidance equipment or the communications equipment did not function correctly, man in the spacecraft had no tools in which to help return him safely to earth. The Air Force Avionics Laboratory, Wright-Patterson AFB, Ohio, decided to proceed with the development of a purely manual navigation and guidance technique. The technique under development these past several years, is one which not only provides full backup in case of complete power failure but can be merged and interfaced with primary automatic systems (fig. 8-2).

The approach taken toward the development of a manual space navigation technique was both classical and logical, which includes the following:

(1) Mathematical analysis and test.- Mathematical analysis was concentrated on reducing the extremely complex orbital determination mathematics used in automatic systems to a very simple scheme that could easily be computed by hand through the use of tables or with a simple hand held analog computer. One solution presented itself which divided the normal sixth dimensional analysis (fig. 8-3) into two separate and distinct three dimensional problems. The first three dimensional problem would easily and simply determine the size and shape of the orbit and the second three dimensional solution would give orbit orientation.

The measurements necessary to implement this mathematical solution are also quite simple. The first measurement needed is the altitude above the earth, and from this the angle from the center of the earth to the horizon can be computed. The second measurement needed is the co-altitude of a star; that is, the angle from the spacecraft zenith to the star (fig. 8-4). If the altitude above the earth can be obtained, the angle between the local vertical and the horizon can be obtained. Couple this with an angular measurement from horizon to star and it is very simple to determine the co-altitude measurement.

Before the instruments were designed, the mathematical procedure was tested aboard a KC-135 aircraft (fig. 8-5). It may seem strange that an aircraft was used to solve an orbital problem, but the manner in which the flight test was accomplished makes this somewhat more logical. The aircraft was flown from South America to Africa along the equator at a constant altitude of 35 000 feet. In this way, it could be assumed that the size and shape of the orbit was known exactly. With a circular orbit 35 000 feet above the earth, the calculated orientation could be tested against the known orientation of the equator. A standard aircraft sextant (fig. 8-6), was used for co-altitude measurements.

From these measurements the trace of the aircraft zenith on the celestial sphere was related back to earth, and this trace compared with the equator (fig. 8-7). The results were much better than anticipated. The best results showed an angular deviation of only 1 minute of arc while the maximum angle deviation was only 14 minutes of arc. After the successful completion of this phase, development of a space sextant and a space stadimeter was undertaken.

(2) <u>Instrument development and construction</u>.- Primary concern with the sextant was the field of view necessary to allow the astronaut to readily identify stars. An astronaut does not have the direction and attitude reference that aircraft or ship navigators have on earth. To simulate this situation, a navigator was placed in a test facility and the attitude variations simulated by moving a star field in relation to him, thus disorienting him (fig. 8-8). It was found that if a field of view less than 14° was used, it was impossible for him to identify stars. Anything less than 20° was extremely difficult. The first hand held space sextant (fig. 8-9), weighed only 8 lbs, was extremely rugged, and was much like the standard ship sextant used on board all naval vessels except that the field of view is larger and its light gathering power is quite improved. The design of the stadimeter was more difficult. A classical way to measure the altitude above the earth would be to take angular measurements from one earth limb to the other, and then take half of this angle to determine the angle from the horizon through the space-craft to the center of the earth. This, of course, is extremely difficult for the near earth orbit. As the angle subtended by the earths' limbs approaches 180° the observations through a window become impractical for the hand held instrument because of the infringed field of view. There-fore, it was decided to develop a unit which generates an angular meas-urement when three cardinal points on the horizon are superimposed through adjustment of instrument controls.

(3) <u>Flight test</u>.- The next and very important step was the actual test of the instruments in the Gemini Program. It was decided to fly the hand held sextant on Gemini IV to acquire needed information for present and future applications as soon as possible.

a. The first portion of the experiment was to evaluate man-
    spacecraft operational suitability of the space sextant, and
    to obtain quantative data for accessing the limits of accuracy
    of the sextant for optical rendezvous type measurements. This
    portion of the experiment was of primary interest to the NASA
    Apollo Program. It was felt that the objective could be obtained
    by making angular measurements between known stars and angular
    measurements between a known star and the Titan booster during
    the planned rendezvous with the booster. The rendezvous with
    the booster was not accomplished; therefore the scheduled star-
    to-launch vehicle sightings were not performed. Of the fifty
    scheduled star-to-star measurements programmed, there were
    forty-seven measurements recorded. An evaluation of the man-
    sextant operational capability was the accuracy with which the
    measured angle between two stars could be repeated. The repeat-
    ability of these star-to-star measurements was limited only by
    the readout accuracy of the sextant which was 30 arc seconds.

b. The second portion of the experiment consisted of studies of
    various star and horizon phenomena and specific star-to-horizon
    measurements to obtain data for postflight calculations and
    accuracy determinations of navigational position. This portion
    of the experiment was of primary interest to the Air Force.
    There were two basic space phenomena which appeared to be most
    stable and useful for space navigation purposes. These are
    the blue haze and the 5577$\overset{\text{o}}{\text{A}}$, green emission line. In addition
    there is the normal day horizon and the night shade differentia-
    tion between the black of the dark earth and the black of space
    behind it. The sextant was equipped with neutral-density, blue-
    haze, and 5577$\overset{\text{o}}{\text{A}}$ filters to accentuate the horizons to be inves-
    tigated during specific sightings.

    There were 160 scheduled star-to-horizon measurements using
    the 5577$\overset{\text{o}}{\text{A}}$ green emission line at night, and both the natural
    and blue haze horizons during the day. Real-time flight-plan
    changes necessitated that these sextant sightings be performed
    later in the mission than originally scheduled. On the first
    daylight sequence it was found that the selected stars were not
    visible on the daylight side of the revolutions. All sextant
    sightings were transferred to the nightside of the orbits and
    no evaluation of the blue filter and blue haze horizon could
    be made. Movement of these sightings created other problems
    since the stars selected for the original star-to-horizon
    measurements were not all time-phased for the nightsides of
    the orbits and required the flight crew to deviate to a

real-time type sighting. There were 45 star-to-horizon
sightings accomplished to the natural night horizon and to the
5577Å green emission line. Measurements to the green emission
line, air glow layer, were made with and without the special
filter. The green emission line was more defined with the
filter. Measurements were made to the top, middle and bottom
of this layer.

Significant data is summarized as follows:

Experiment D-9

Apollo Sightings (star-to-star)   47

    Repeatability   30 arc second

    Stars used   6

    Maximum angle   21° 36'

Air Force Sightings (star-to-horizon)   45

    Useful horizons   (2-Natural earth and 5577Å emission line)

    Stars used   11

    Maximum angle   31° 3' 30"

    Number of green horizon layers observed   2

    Thickness of 5577Å layer   2° 42'

    Star transit time through green layer $49\frac{1}{2}$ sec.

    Star transit time from 1st appearance
      to top of green layer   3 min 23 sec

(4) Results and Conclusions.- An evaluation of the navigational
accuracy using the star-to-horizon measurements has not been completed.
However, valuable qualitative information was obtained on the availa-
bility of the observable phenomena as follows:

  (a) Stars at night were visible down to fifth magnitude and
      constellations were easily indentifiable.

(b) Although stars were not visible during the day portion of the orbit, it was felt by the Gemini IV crew that stars would be visible with a dark adapted eye and a shaded window.

(c) The launch vehicle lights were visible at night and in daylight when within range.

(d) The observation of the thickness and number of the horizons used for sightings make it possible to determine the best horizon-filter combination under particular conditions.

(e) The 5577$\overset{\circ}{A}$ green emission line was readily available at night and was quite wide with a secondary bright band. Most measurements were made to the top of the bright band in the 5577$\overset{\circ}{A}$ green emission area.

(f) The restricted field of view of the Gemini window caused maneuvering problems in attempting to acquire both high rising stars and the earth's horizons.

(g) The basic sextant concept utilized on this mission was proven feasible.

It is felt that the data gathered from Experiment D-9 on Gemini IV has provided the baseline foundation for successful development of purely manual navigation and guidance technique.

REFERENCES

1. Baghinov, I. K.:"Method of Autonomous Guidance During Flight In Near-Planet Orbits" Translation of paper presented at 2nd Annual Conference of the Americal Astronautical Society, Chicago. NASA TT F-369 May 1965.

2. Lampkin, Bedford A.:"Sextant Sighting Performance For Space Navigation Using Simulated and Real Celestial Targets" Ames Research Center, Moffett Field, Calif.

3. "Space Position Fixing Techniques Phase 1" ASD, AFSC, Wright-Patterson AFB, Ohio, Report No. ASD-TDR-63-521, April 1963.

4. Silva, Capt. R. M. and Jorris, Lt. T. R.: "The USAF Manned Space Navigation Experiment on Gemini and Its Implications on MOL"

Air Force Avionics Laboratory, Wright-Patterson AFB, Project
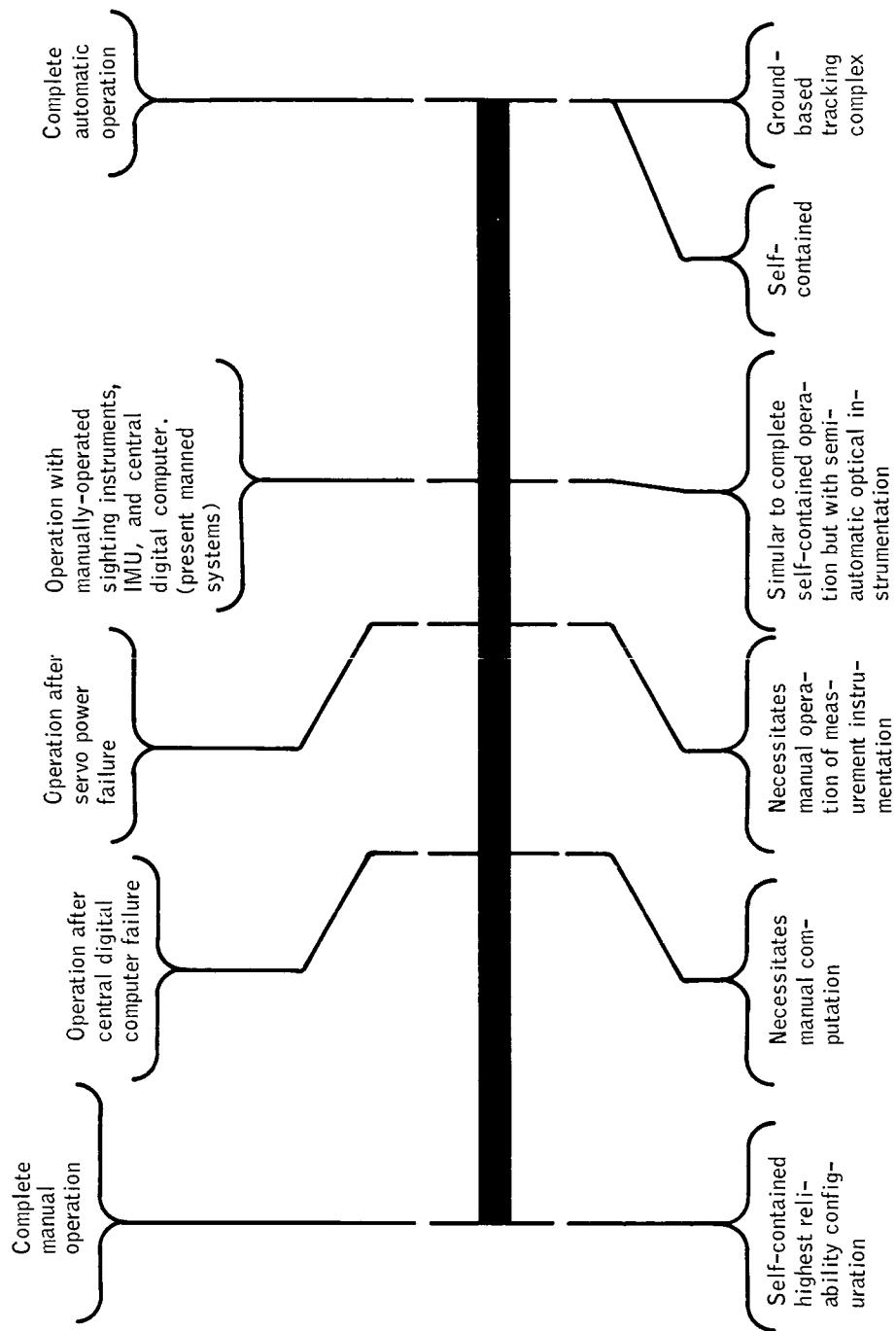No. 4200, Task No. 420013, April 1964.

Figure 8-1.- Navigation instrumentation.
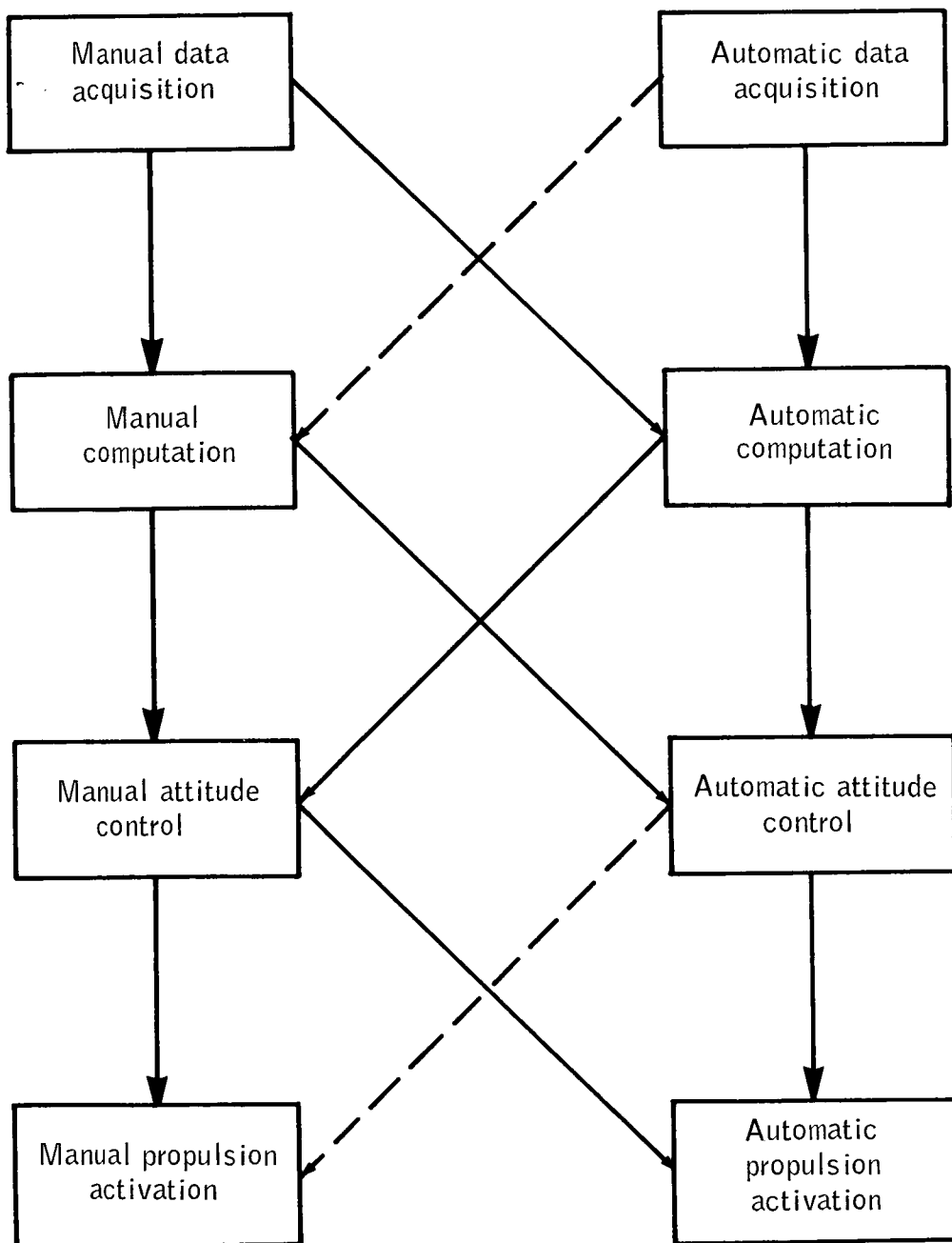
Figure 8-2.- Interfaced functions in a total navigation system.
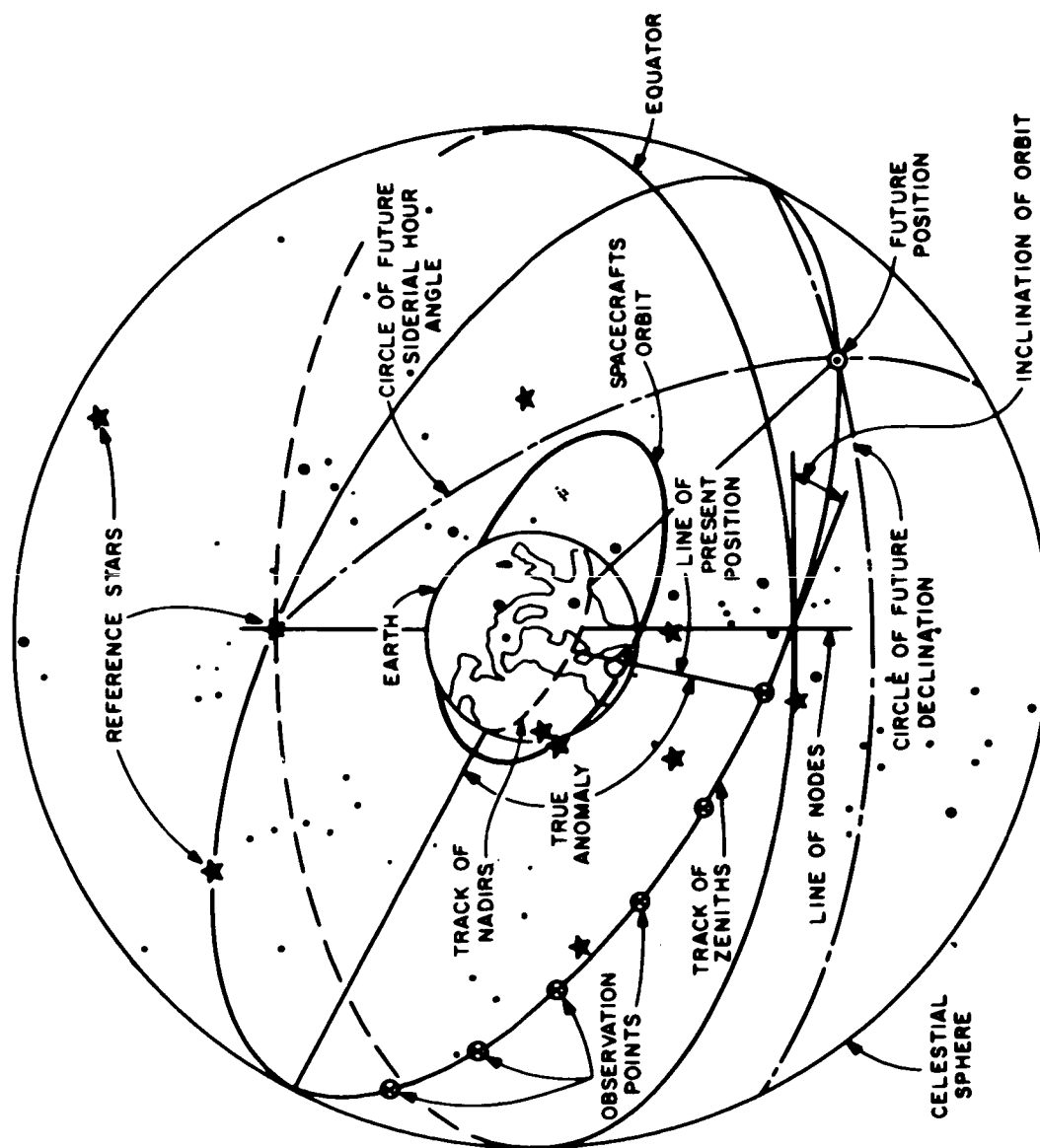
Figure 8-3.- Geometry of the orientation parameters problem.
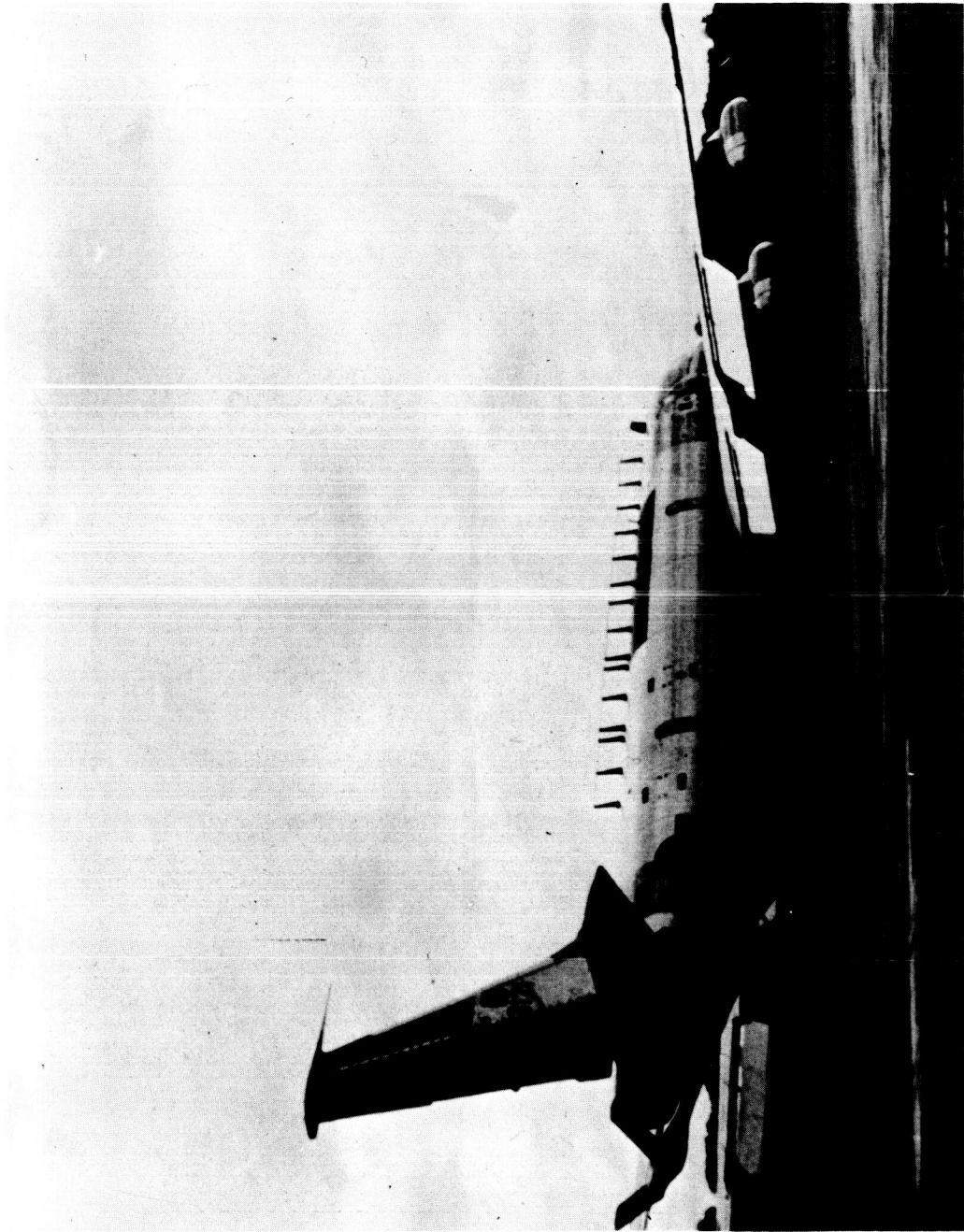
Figure 8-4.- Star coaltitude determination.

Figure 8-5.- KC-135 aircraft to simulate orbital problem.

Figure 8-6.- Standard aircraft sextant to simulate orbital problem.
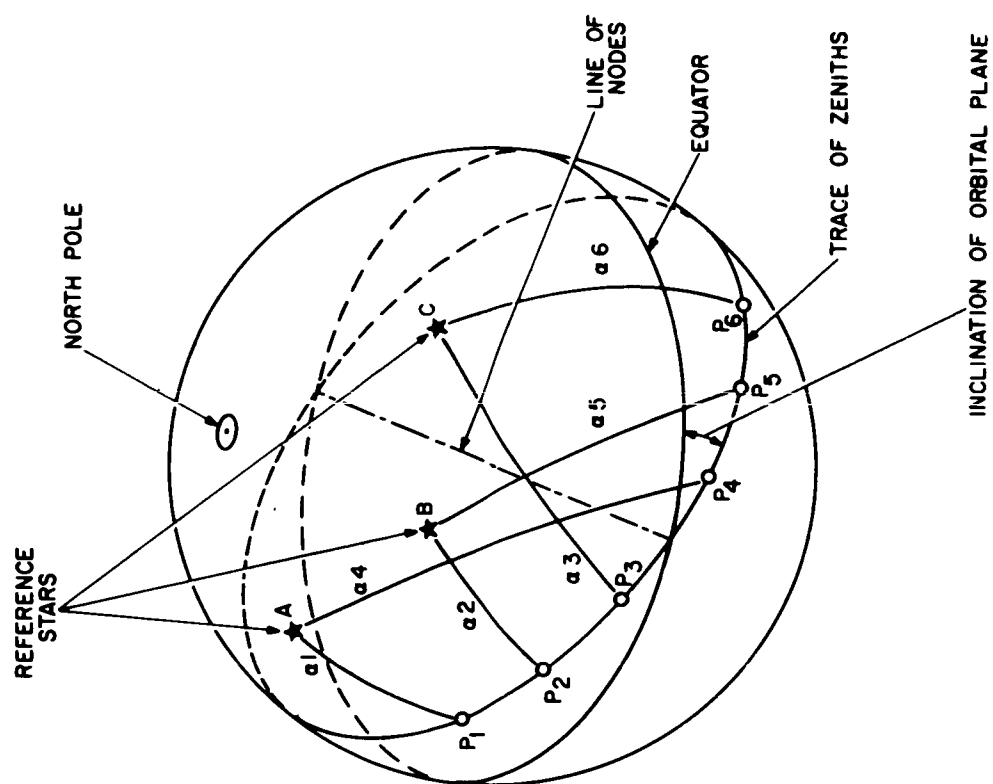
Figure 8-7.- Geometry of the graphical solution.

118
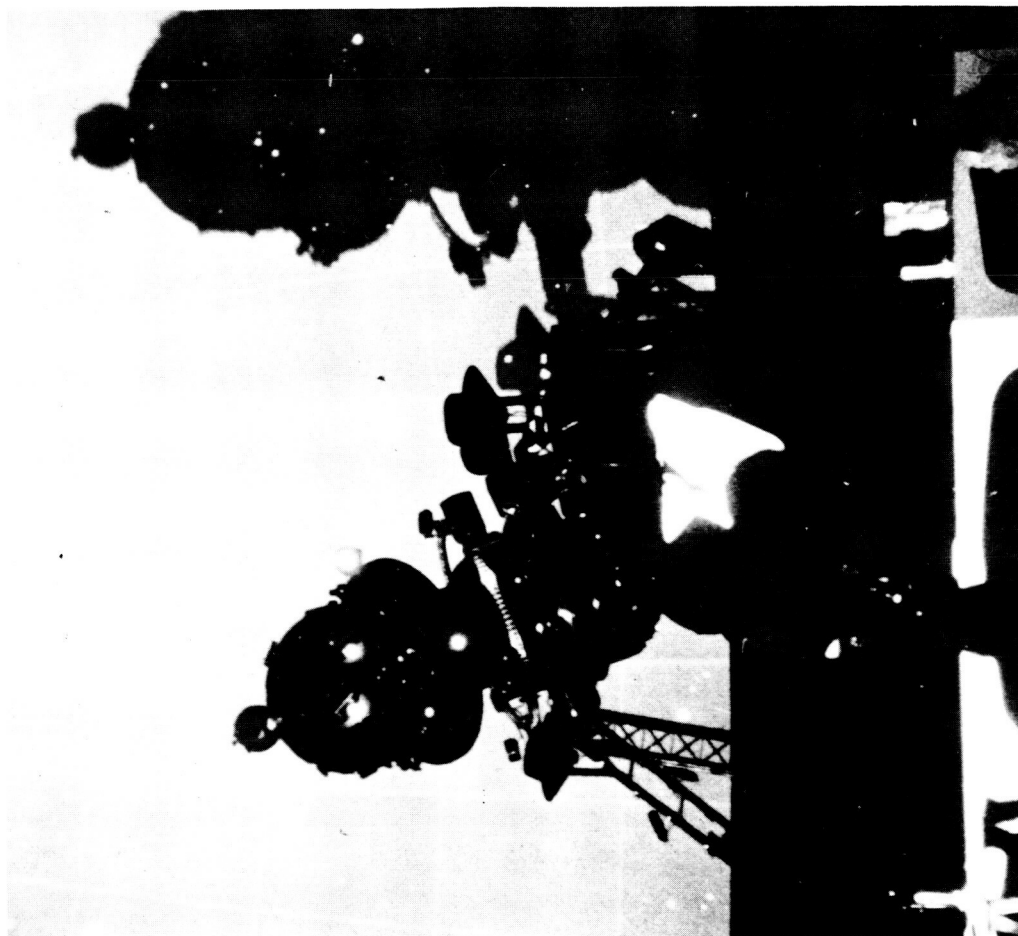
Figure 8-8.- Disorienting navigator with limited simulated star view.

NASA-S-65-6026

Prism scanning control

Eye piece

Reticule illumination rheostat

Counter illumination switch

Battery containers

Left side-rear view

Scanning prism

Blue filter lever

Fixed field-of-view prism

Timer

Counter illumination housing

Counter

Green filter lever
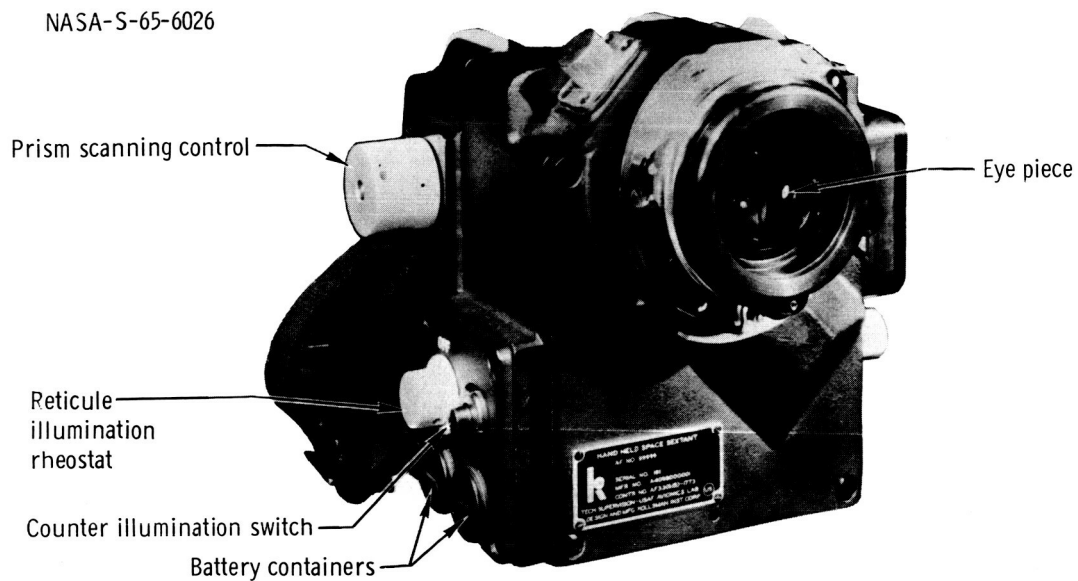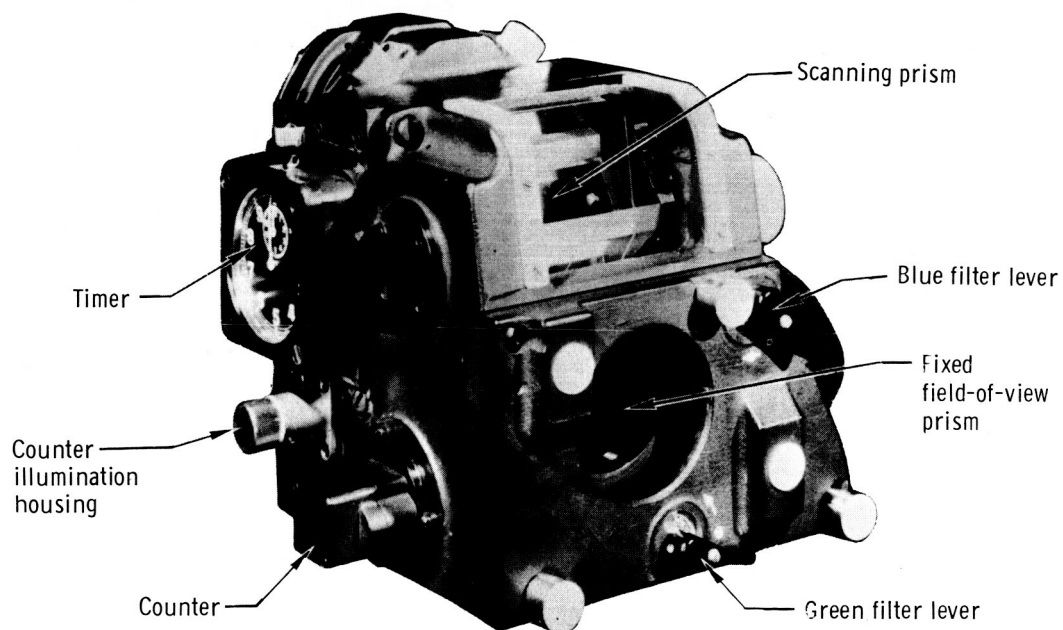
Right side-front view

Figure 8-9.- Space sextant.

9.   EXPERIMENT MSC-10, TWO-COLOR EARTH LIMB PHOTOGRAPHY

FOR GEMINI IV

By Max Petersen, Ph. D.
Massachusetts Institute of Technology

SUMMARY

Of the Gemini IV two-color earth limb photographs, 24 of the 30 taken have been measured by microdensitometer procedures and calibrated by step-wedge exposures on the edges of the film. Primary attention was given to the comparison of the terrestrial elevation of the blue above the red portion of each photographed limb, by means of an arbitrary reference line drawn on the negative. It was found that, while the excess elevation of the blue limb tends to increase with the scattering angle, other factors made the correlation far from obvious. The blue limbs are generally less sharp than the red, in a ratio of as much as 2 to 3; this makes the assigned excess elevation dependent on the feature chosen to define the limb. The profiles of the blue limbs are more regular than the red in their brighter parts. Comparative values of the peak radiances, blue and red, of various limbs vary by nearly 50 percent.

This is a preliminary report of this study; it remains to evaluate the densitometric photometry data into radiance values in order to judge the validity of Rayleigh scattering theory to account for the blue limb profiles.

INTRODUCTION

This experiment is a sequel to the similar photography of the Mercury 7 flight. The findings of the photographs then taken raised questions that could be answered, in part, only by a new series of pictures, extended in respect to the involved scattering angle of the sunlight. The general plan of the experiment proposed for Gemini IV was similar to that used earlier. It is therefore useful to review the considerations that prompted these two experiments.

The plans for guidance and navigation of our Apollo mission require observation of the earth, presumably its limb, in order to make a navigational fix. The precise definition of the observable limb is essential. The uncertain state of the lower atmosphere, with its tropospheric storms, and the accompanying clouds prompt a consideration of observing higher levels of the atmosphere, which scatter more pronouncedly the shorter wavelengths of light in a manner that may approach Rayleigh scattering. For this, if it be realized, there is satisfactory predictability.

With this prompting the writer made some simple if slightly tedious calculations regarding the scattered-light phenomenon of a sunlit earth's limb. It was assumed that the light was to be scattered by an atmosphere, defined by the U.S. standard atmosphere, irradiated by a zenith sun. Calculations were carried through with several different scattering coefficients assignable to various wavelengths of the extended visual region. The wavelength assignments need not be initially made. They will depend on whether simple Rayleigh scattering prevails. The relation of the total attenuation befalling incident irradiation entering the atmosphere and passing through it to light scattered in a particular direction (as, for example, at 90° to the incidence) is, for Rayleigh scattering, a well-known integral relation. The scattering attenuation of light is a physical phenomenom well known to astronomy.

RESULTS

A comparison of observed extinction coefficients for the extended visual spectrum with calculated coefficients for an atmosphere of pure air is given in the following brief table cited from reference 1.

Wavelength	3530Å	4220Å	4880Å	5700Å	7190Å	10 300Å
Observed τ	0.488	0.268	0.166	0.126	0.053	0.028
Pure air τ	0.474	0.226	0.125	0.066	0.026	0.006

The differences between the coefficients for the several wavelengths indicate that, while calculations which proceed in terms of the numerical values of the extinction coefficients can yield relative profile curves of significance, these curves can have only provisional

wavelength ascription until their comparison to some observed limb profiles is possible. Initially, therefore, such wavelength ascription will be foregone.

The variable τ is defined by the equation for the observed brightness of a star at zenith distance,

$$b = b_0 e^{-\tau \sec \xi} \tag{1}$$

τ may be called the "optical thickness" of the atmosphere and may be related to a "local extinction coefficient," β, by the relation

$$\tau = \int_0^\infty \beta \, dh \tag{2}$$

in which, for a clear sky, β depends only on the density of the atmosphere, and one can write

$$\tau = \beta_0 h_1 \tag{3}$$

where h_1 is the "reduced height" of the atmosphere (the height that the air above the observer would have if it were all compressed to sea-level density). The numerical values for observed τ apply to the atmosphere above Mount Wilson Observatory (h = 6.44 km). The pure air values correspond to 6.44 km of pure air as explained by van de Hulst (ref. 1).

In the calculations here considered one thinks of a plane lamina of atmosphere having, at its closest point to the earth, a perigee altitude h_0. It is normally irradiated by the sun. The various scattering elements of this lamina vary in density with their altitude, from that at h_0 to a negligible density. They vary slightly in solar irradiance because of the air above them and because of its extinction. They vary more importantly in the transmission of their locally scattered light toward the observer because of the light's scattering along that path. Secondary scattering has not been included.

These varying factors are evaluated in terms of the pertinent geometry and the density profile of the atmosphere, as given by the ARDC Model Atmosphere, 1959 (ref. 2)*. The choice of extinction

---

*These calculations were initiated prior to the availability of the U.S. Standard Atmosphere 1962. The difference for this problem is trivial.

coefficients and (tentatively) the specific 90° scattering function, while intended to embrace the extended visual spectrum, does not require wavelength ascription. However, one can surely not ascribe pure Rayleigh scattering to the lowest perigee height involved.

Consider a lamina of atmosphere which, normal to the radius at its perigee point, has a terrestrial altitude h_0 (fig. 9-1). The lamina's several small segments, such as that centered at P_i, are more distant from the earth's center by the sagitta S_i that is given, closely enough, by the rule $D_i^2 = S_i \times 2R_\oplus$. The density of the scattering air in the element at P_i is that for the altitude $\left(h_0 + S_i\right)$. The scattering mass per unit cross sectional area equals that density times the element of length. (The chosen elements of length subtended 20' of arc about the earth's center, and ranged from 37.11 to 37.64 km. The sagittae, calculated on the earth's diameter (6357 × 2 km), range from 0.108 to 48.04 km. Given a spectral density of solar flux outside the earth's atmosphere, $f\lambda$, the flux falling on unit area of a scattering element at P_i in a spectral interval $\Delta\lambda$ will be measured by $f\lambda\Delta\lambda \exp\left(-\tau H_i\right)$, in which H_i is the "reduced height" of the atmosphere above P_i at the level $\left(h_0 + S_i\right)$. The light scattered by the element at P_i will be proportional to its mass, $\rho_i \Delta D_i$, and to the scattering coefficient, of which the solid angle integral defines τ. In the present consideration this scattering coefficient is that for 90° scattering. The light scattered in the observer's direction will be attenuated by the air mass between P_i and the observer. This can be obtained as the sum $\sum_i^z \rho_i \Delta D_i$, in which sum the zth element has no

significant atmosphere beyond it. The total transmitted light from all elements in the lamina from the far side to the observer's near side, for a unit exterior solar flux density and spectral range, may be measured by the sum:

$$\sum_{-z}^{+z} c\tau \cdot \rho_i \Delta D_i \exp\left[-\tau\left(H_i + \sum_i^z \rho_i \Delta D_i\right)\right].$$

The use of $c\tau$ for the 90° scattering coefficient, where τ is a measured or observed attenuation coefficient, needs brief comment.

The initial brightness of the 90° scattered radiation from an element of the lamina per unit of solar irradiance is given by a scattering function whose solid angle integral is the attenuation coefficient. In the application of these concepts to the problem in hand, since only the relative brightness for various laminae of different h_0 values is

sought, it is assumed that the scattering coefficient for a 90° angle is proportional to the attenuation coefficient. For Rayleigh scattering the scattering function is of the form

$$\beta\ (\phi,\ \lambda)\ =\ A\lambda^{-4}\left(1\ +\ \cos^2\ \phi\ \right).$$

This is related to the attenuation coefficient of the equation for flux depletion for flux crossing a path differential dr (d F/F = -b . dr) by the relation

$$b\ =\ 2\pi\ \int_0^\pi\ B(\phi)\ \sin\ \phi\ d\phi.$$

The hazard involved in substituting the attenuation coefficient for the specific scattering coefficient is that, for any given wavelength of light, the ratio of the two will be significantly different at the different altitudes pertinent to the applicable results (namely, 10 km and higher). Evidence in this matter which extends to 9200 M is presented in reference 3. This point, which is tantamount to the assumption of a Rayleigh atmosphere, may not be overlooked.

The detailed calculations involved in the assembly of the summations for several points of a limb profile, given any one scattering coefficient, are somewhat tedious and will not be described. For a given scattering coefficient, light transmission sums were calculated for h_0 values of 5, 10, 15, 20, 25, 30, and 40 km. This was done for each of five scattering coefficients, 0.00641, 0.0106, 0.0175, 0.0358, and 0.0503 per km air at normal temperature and pressure (NTP).

The results of these calculations are displayed in the curves of figure 9-2. Certain features of these curves merit attention:

a. The maximum slopes of the several curves do not much differ. Contrary to a sometimes expressed notion that the blue "horizon" is less sharp than the red, recent photographs (obtained in two-color frames with a camera mounted in an X-15 plane) confirm the Gemini IV findings that the blue and red horizons do not much differ in relative appearance.

b. At terrestrial levels lower than 10 km the curves for larger scattering coefficients show a fall-off brightness. The source of this "mischief" is evident from curves of figure 9-2, describing the relative contributions from the successively more remote elements of a given lamina for the scattering coefficient 0.0175/km NTP. It might reasonably be expected that because secondary scattering has here been ignored,

this recession of brightness will not be observed. The blue limb
photographs do not support this surmise.

   c. Insofar as any particular scattering coefficient leads to a
curve with an inflection point significantly below the tropopause, one
may view these calculated results as unobservable, or unreal. This is
because these calculations embraced single scattering only, neglecting
multiple scattering and the influence of the albedo of the earth or
clouds. In reference to these effects, the brightness of the zenith
sky is cited in reference 1, page 73 as 0.0427 for single scattering
alone, 0.0515 for multiple scattering, and 0.0559 for a ground albedo
of 0.1.

   The experimental procedure proposed for the Gemini IV flight was
simply to take, with a hand-held camera, a series of groups of three
photographs of the earth's limb at intervals of about five minutes
during the sunlit part of one revolution. These photographs required
the installation in the camera magazine of a two-color (red in the center
and blue on its sides) Wratten filter mosaic, mounted closely in front
of the focal plane, behind the dark slide. The thin frame of this filter
mosaic reduced the picture area to about 44 by 43 mm with a narrow verti-
cal center mullion. The margins beyond the filter panel thus made edge
strips of the film available for densitometric exposures. The magazine
could be loaded with film enough for nearly 40 exposures. Extended
panchromatre film (Linograph Shellburst) was used. The filters used,
no. 92 and no. 47B, gave transmission regions of 400-470 nm centered at
about 432 nm, and 640 to 710 nm centered at about 675 nm.

   The manner of getting the pictures, in view of spacecraft and
power exigencies, was simply to take the pictures forward, in the direc-
tion of the orbit as judged by the astronaut. (This caused the loss of
the early morning pictures when the sun was just right of straight ahead
and shown on the window.) The pictures were measured on the micro-
densitometer of the Harvard University Physics Laboratory. The micro-
densitometer records directly the transmission data by tranversing the
limb image across a fine slit which is set parallel to the limb. It
travels once across and back, normal to the limb, in the blue part of
the image and then again in the red, each time close to the filter joint.
Repeating on the other side of the picture affords a check on the paral-
lelism of an artificial reference line (a fine ink line drawn on the
negative closely parallel to the limb at an arbitrary convenient dis-
tance from the limb profile). This reference line is a satisfactory
means to establish the difference of location of the limbs in the earth's
radial direction. The hand-held camera affords no means to record the
terrestrial limb.

The radiance profile of the limb can be drawn, in arbitrary units, by the reference to a step-wedge calibration exposure. Since the sharpness or definition of the limb is the principal feature available from these photographs for use in Apollo navigation observations, such profiles have been investigated. For this purpose the film prepared for Gemini IV carried on each edge a series of densitometric exposures made in an E G & G flash-lamp sensitometer, using a Kodak step-wedge of 21 steps. The exposures on one edge were made through a no. 92 red filter and those on the other through a no. 47B blue filter. Each earth-limb photograph can be interpreted by reference to the adjacent step-wedge exposures. The film was developed in a Versamat machine in the MSC photographic laboratory.

The initial inspection of the pictures on the microdensitometer showed that the limb profiles in the blue were generally not so sharp as those recorded in the red. This results in the need to adopt a useful feature of a limb profile to designate its terrestrial elevation in the red image as compared with the blue, both with respect to the arbitrarily located reference line. The point that was chosen with regard to the gamma values for red and blue was that having four times the transmission of the limb brightness peak on the negative; these points, in view of the difference of λ values for red and blue images, represent local limb brightness of close to one-third that at the peak.

In terms of this designation, table 9-I presents the values of the excess elevation of the blue limb over the red in the measured photographs. These photographs were taken in groups of three, each such group taken in prompt succession and followed by another group after close to five minutes, until sunset. The picture numbering reflects the fact that the first two groups were useless because the window was sunlit.

The measurements, complemented by ephemeris data for the orbit and the sun, yield the blue limb excess elevation over the red and the relevant scattering angles tabulated in the table.

Regarding the data in table 9-I, it may be noted that the scale of the microdensitometer charts was about 1.5 mm per km; the variation of repeated measurements of a single picture was about 0.5 mm. The measurement of two sides of each photograph afforded a check of any ill-drawn reference line.

Figures 9-3 and 9-4 show positives of several typical photographs, one printed to show the aspect of the limb primarily and the other to show the face of the earth's atmosphere, or ground appearance.

It has been remarked that detailed measurements of a blue limb profile and its accompanying red limb show unequal peak values of the brightness gradient. The ratios which may represent the sharpness of the limb are fairly, but not entirely, constant. This means that what is reported as the excess elevation would be different if another feature were the criterion. If one chose the point of half-peak brightness rather than the one used, the excess elevation would be less. Inasmuch as the several limb brightness gradients among the different photographs hold a nearly constant ratio of the red limb to the blue, the excess elevations would retain the same relative aspects.

These thoughts underlie the conclusion that the correlation between the blue limb excess elevation and the scattering angle is not as good as had been thought from the earlier Mercury 7 photographs. It is pertinent also to note that in those photographs the blue limb gradients more nearly equaled those of the same limits observed in the red.

The presence in the blue limb elevation of factors other than scattering angle is obvious. The question of the varying albedo of the lower atmosphere, because of its effect on the importance of secondary scattering (which has not been included in the analysis of a Rayleigh atmosphere), is surely involved. As to the terrain itself, the flight log indicates which groups of photographs were taken of limbs over land (groups 5, 6, and 7). Three of the photograph groups disclose land in the foreground. The flight passed over Africa, from Morocco to Saudi Arabia. Two of the groups over Africa were not as internally consistent as others; however, from so few pictures, any generalization is hazardous.

One feature of the data thus far evaluated relates to the values of the limb gradients in the several pictures, in which first attention went to the arbitrarily defined excess blue-limb elevation. The limb profiles do not show well-defined inflection points. Examination of the details of the limb gradients reveals an unexpectedly long gradient far out into space, having at a distance of 200 km a density as great as 0.4, compared to a peak brightness density of 2.5, which corresponds to a radiance ratio of nearly 1.5 percent, since the gamma value was was about 1.25. The red image tail was only one-third as pronounced. This preponderant blue far-out scatter has been found most markedly on the photographs taken late in the series. In the fourth group the far-out scatter was about equal in the red and the blue; in the earliest groups it was stronger in the red. (Such was not observed in the earlier pictures from the Mercury 7 and 9 flights.) The blue far-out scatter is thought to be artifical, due either to the unclean window surface or to some stray light. The reason for its variance with the time of day is not obvious. The scatter is totally without pattern, being bounded by the filter frame alone.

In order to obtain a concise survey of the peak value of gradients of the earth limb radiance, attention thus far has been primarily confined to an arbitrary feature easily available from the many microdensiometer traces. The definition of the gradient chosen has been the difference in terrestrial elevation occurring between points on the limb having one-half and one-fourth, respectively, of the peak image densities of that limb.

In the red these differences (which correspond to a brightness ratio of $\log^{-1}$ 0.20 for λ equal to 1.5) average 4.8 km, the greatest being 6.0 and the least 4.0 km. In the blue they correspond to a ratio of $\log^{-1}$ of 0.24, λ being about 1.26. Here they average 7.2 km, greatest and least being 8.6 and 5.2 km.

These numbers indicate that, with a limb sensing device capable of measuring to 2 percent, the red limb accuracy would be about 0.2 km, with a blue limb accuracy of about 0.27 km. Referring to the analytically derived curves for a Rayleigh scattering atmosphere, one finds for the ratio of $\log^{-1}$ 0.300 a difference of 8.1 km, which is between the estimated values for the blue and the red limb gradients for the Gemini IV negatives. These numbers are assembled below in slightly revised form:

Limb gradient (log radiance ratio per km)	Limb	Precision of observing with 2 % sensor, km
0.042	Average red	0.21
0.033	Poorest red	0.27
0.050	Best red	0.18
0.033	Average blue	0.27
0.027	Poorest blue	0.33
0.046	Best blue	0.20
0.037	Rayleigh, calc., single scatter	0.24

In regard to peak values of the limb radiances, it is not now possible to give any appraisable numbers. Comparative values between the blue and red limbs, which were frequently obtained when two parts

of the same limb were scanned without any change in the microdensitometer slit, showed variations of nearly 50 percent; the two opposite sides of the same limb repeatedly showed significant difference. This part of this study is continuing.

In the examination of numerous traces, several times traces of outer aerosol scatter seemed to occur, but these are too fragmentary to deserve discussion. The 28 to 30 km dust maximum is also not obvious.

The study completed thus far leads to the conclusion that the dependence of the excess blue-limb elevation is less obviously determined by the scattering angle than was suspected from the Mercury 7 photographs. In several cases, factors that enter cause three photographs taken as one group in rapid succession to vary as much as one group varied from the next. The blue limbs are generally less sharp than the red (the "worst" case is in the ratio of 2 to 3). As a consequence of this, the measured excess blue-limb elevation will usually depend on the feature chosen to define it. As to the practical matter of the precision of observing the blue earth limb, a sensor of 2 percent accuracy could afford a limb-sensing accuracy of about 0.27 km for a limb distance of 1600 km.

It is a reasonable surmise that the variation of the values of excess blue-limb elevation arises principally from the red limb variance, because the form of the blue limb profiles, at least in their upper part, is more regular than that of the red.

REFERENCES

1. van de Hulst, H. C.: "Scattering in the Atmosphere of the Earth and Planets". Chapter 3 of Atmospheres of the Earth and Planets, G. P. Kuiper, Ed. Univ. Chicago Press, 1952.

2. Minzner, R. A.; Champion, K. S. W.; and Pond, H. L.: The ARDC Model Atmosphere, 1959. Air Force Surveys in Geophysics No. 115 (AFCRC-TR-59-267), Air Force Cambridge Res. Center, Aug. 1959. cf. NASA; U.S. Air Force; and U.S. Weather Bureau: U.S. Standard Atmosphere, 1962, U.S. Government Printing Office, Dec. 1962.

3. Middleton, W. E. K.: Vision Through the Atmosphere, Univ. Toronto Press, 1952.

TABLE 9-I. - EXCESS ELEVATION OF THE BLUE LIMB OVER THE RED

1 Photo number	11 Elevation difference blue-red		111 Scattering angle
	Km	Av.	
7 8 9	4.35 4.00 4.30	4.2	53°
10 11 12	7.2 7.0 6.0	6.7	68°
13 14 15	7.3 8.5 6.1	7.3	83°
16 17 18	4.5 5.4 4.5	4.8	99°
19 20 21	5.2 5.0 5.2	5.1	113°
22 23 24	5.5 5.7 6.3	5.8	125°
25 26 27	5.7 6.9 6.6	6.4	133°
28 29 30	7.8 8.7 6.5	7.7	138°

Figure 9-1.- Lamina of earth's atmosphere.
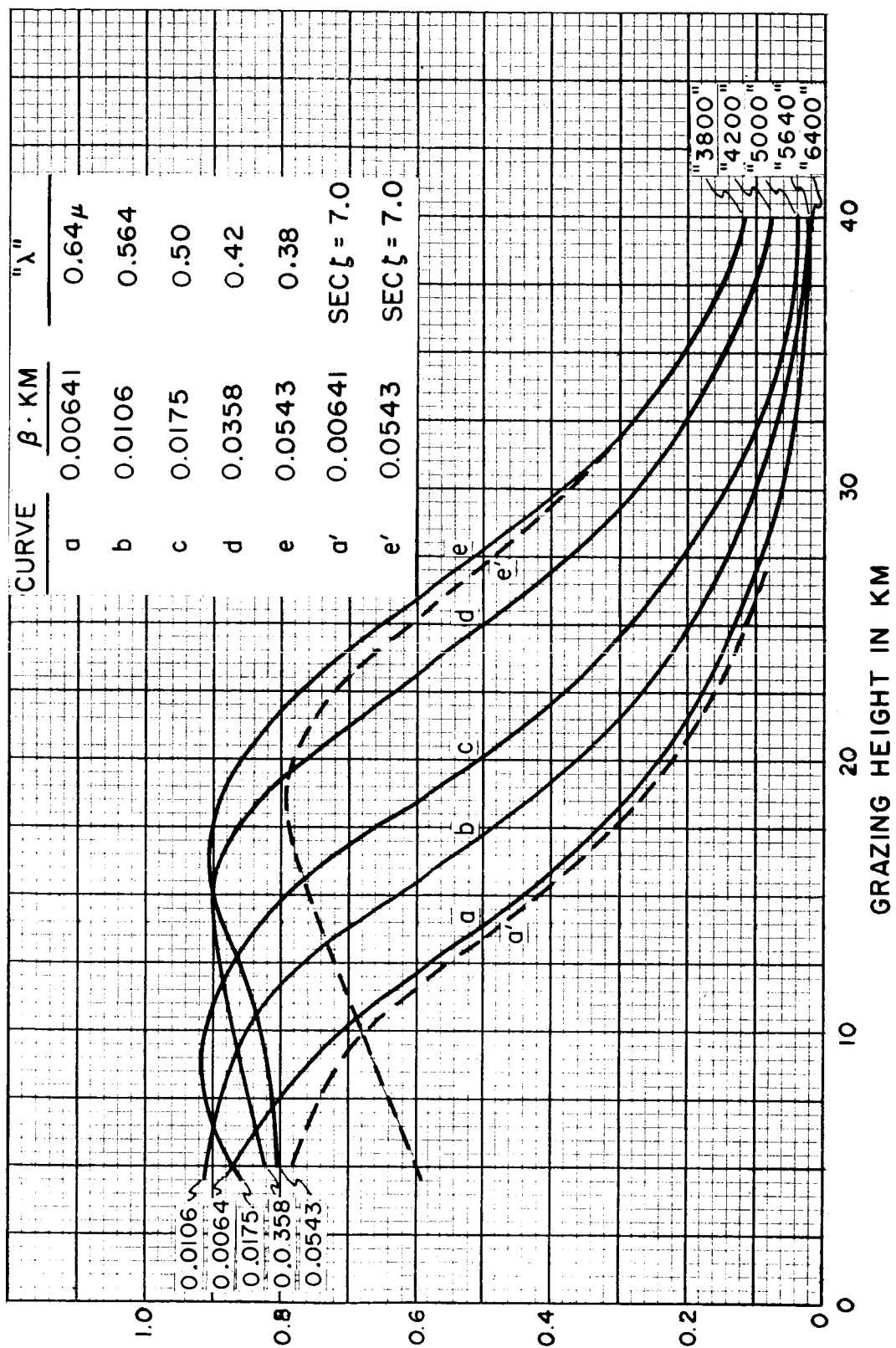
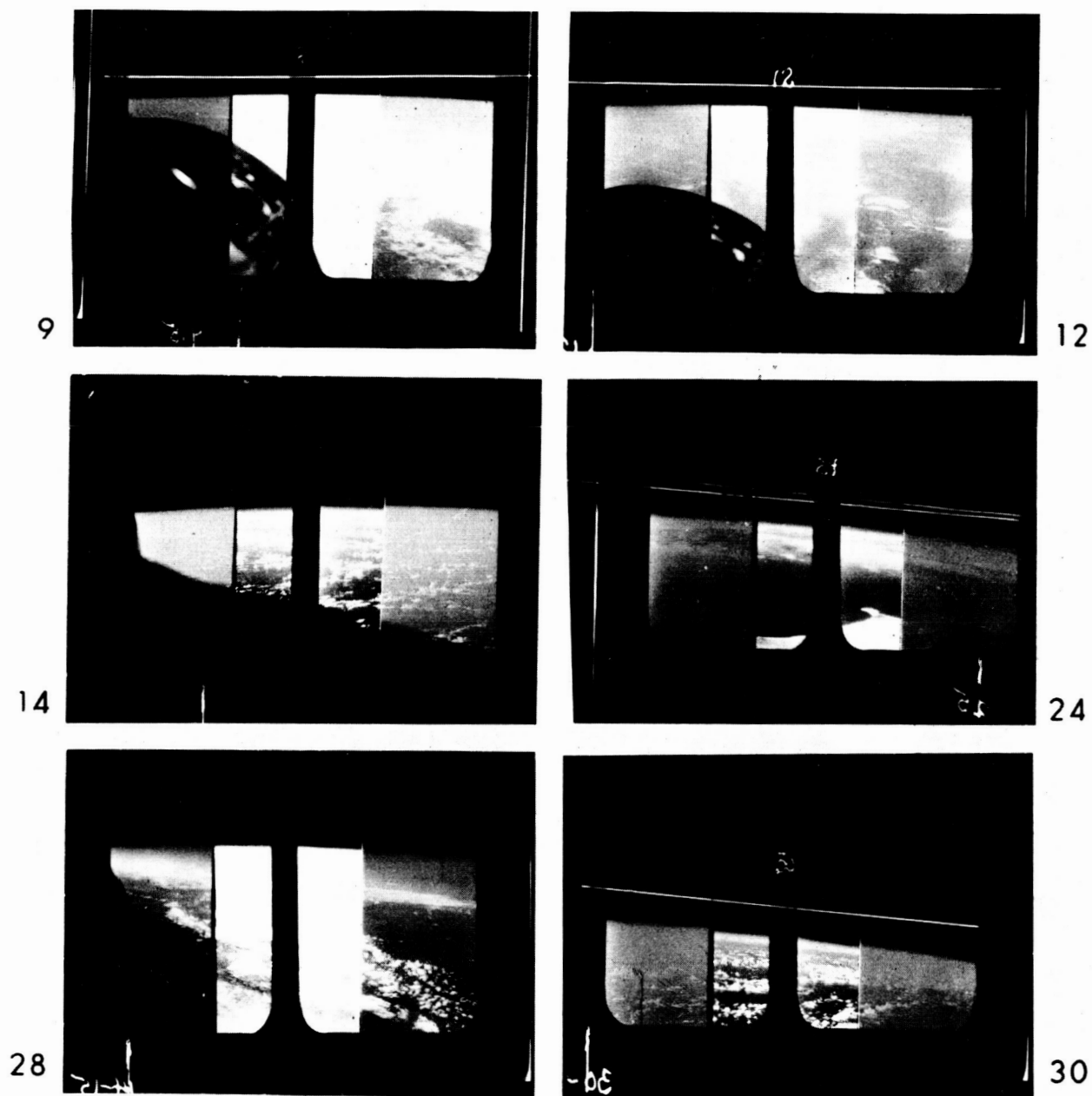Figure 9-2.— Radiance of earth's limb in arbitrary units referred to solar radiance.

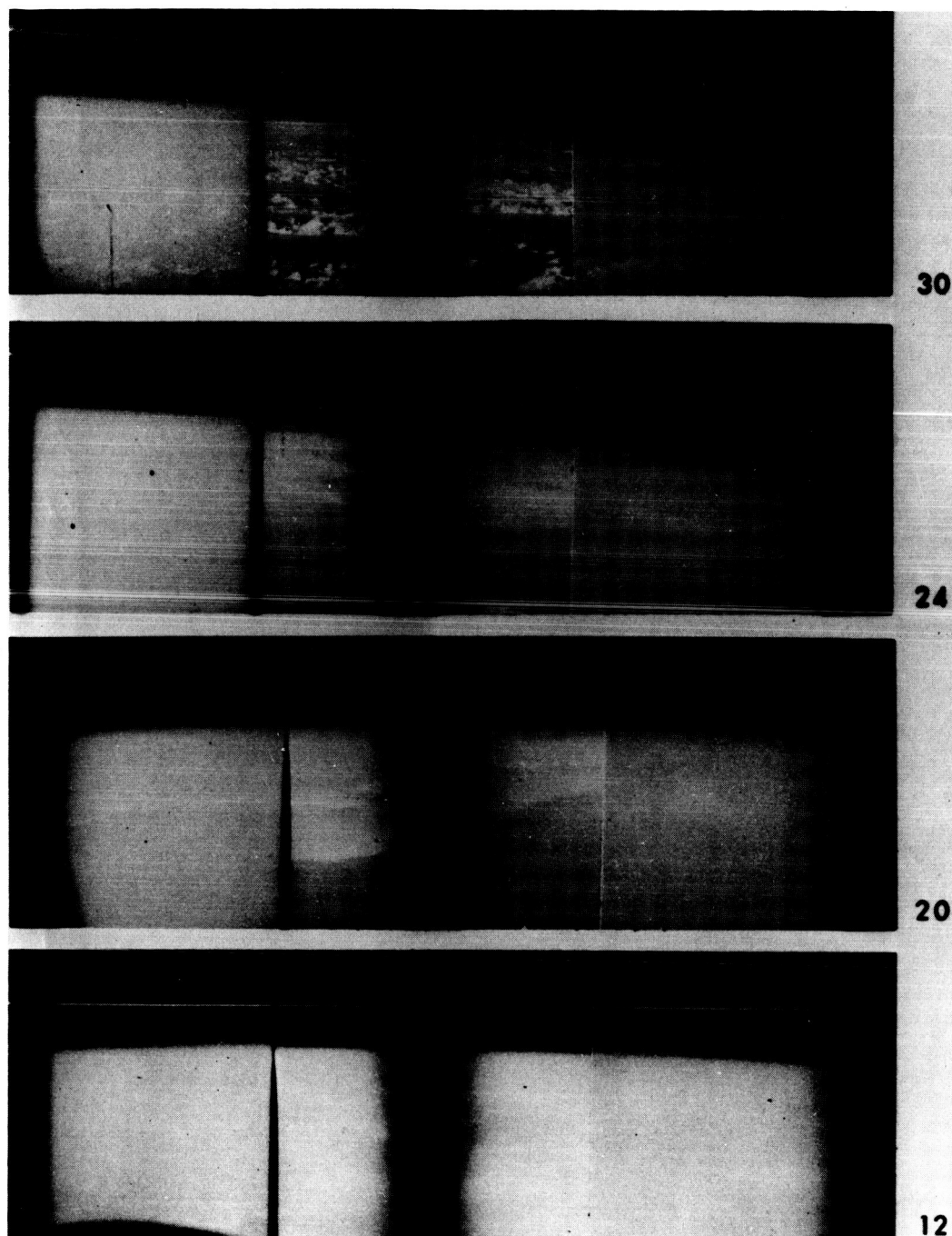Figure 9-3.- Two-color earth's limb photographs (Gemini IV flight).

Figure 9-4.- Two-color earth's limb photographs (Gemini IV flight).

10. EXPERIMENT MSC-1, ELECTROSTATIC CHARGE ON GEMINI III AND GEMINI IV

By Patrick Lafferty
NASA Manned Spacecraft Center

SUMMARY

36110

The Gemini IV, MSC-1 data indicated an electric field at the space-craft surface that was appreciably higher than what was expected. Post-flight testing showed that the experiment instrument was sensitive to radio frequency interference (RFI) and fluxes of charged particles.

The experiment was also carried on the Gemini V mission, but the equipment was modified from that carried on Gemini IV to inhibit the electric field incident on the sensing face of the sensor unit so that a measurement could be obtained of the remaining stimuli. The results indicate that the contribution of an electrostatic field charge on the Gemini IV instrument was negligible.

DESCRIPTION

Equipment

The electrostatic charge experiment was performed on Gemini IV in an attempt to define the potential of a Gemini spacecraft during a typical mission. The experimental instrument was an electric field sensor (fig. 10-1). The instrument consisted of two units, the sensor unit and the electronics unit. The two units were mounted in the spacecraft retrograde section as illustrated in figure 10-2, and were interconnected by electrical wiring, with the electronics unit wired to spacecraft power and telemetry.

The sensor unit contained a sensing-head assembly and a variable-gain amplifier. The electronics unit contained logic and power-conditioning circuitry. The electric field sensor had two outputs. These were monitored by two analog telemetry channels which had a sample rate of 1.25 samples per second. The experimental instrument controls consisted of a power circuit breaker and an on-off power switch which were operated by the pilot.

Instrument Sensing Principle

When a conducting surface in an electric field is locally deformed, the surface charge density will be altered. By electrically isolating the deformed region from the remainder of the surface, a potential difference will appear which will be a linear function of the electric field. (In the Gemini IV instrument, the region took the form of a circular disk, and the deformation was a sinusoidal motion normal to the surface.) If the disk is connected to the surface through a resistance, an alternating current will flow. The magnitude of this current is proportional to the diameter of the disk, the frequency with which it oscillates, the amplitude of the oscillations, and the electric field strength. That is,

$$I = - (4\pi f a \epsilon_o E_o) \, d,$$

where

f = disk oscillation frequency

a = radius of disk

ϵ_o = permittivity of free space

E_o = field at conductor surface, and

$d = d_o \cos(2\pi f t)$ = distance between outer surface of disk and conducting surface.

Figure 10-3 illustrates the calculation of I for three different cases. To sense the current, a large resistor is placed in the connecting wire. By measuring the voltage developed across this resistor, it is possible to determine E_o in terms of a, f, I, and d.

A block diagram of the Gemini IV instrument is shown in figure 10-4. As indicated in the figure, the sensor faces away from the spacecraft toward space. The spacecraft charge distributes itself on the surface of the spacecraft and the sensor disk. As the disk is vibrated by the driver, which is excited by the oscillator output current, an ac voltage is developed across the input of the variable gain amplifier. The amplifier output is converted into a dc signal by the demodulator and routed to the spacecraft telemetry system via the buffer and telemetry clamps.

The amplitude of the channel 1 output signal is proportional to the field incident on the spacecraft. When the amplifier output goes above or below the operating range of the level detectors, the automatic ranging logic alters the gain of the amplifier to stabilize the outputs.

Voltages representing the operating range of the amplifier and the polarity of the input field are summed by the digital-to-analog converter and routed to the telemetry system via channel 2. The squaring circuit, buffer amplifier, and phase detector provide a polarity signal to the digital-to-analog converter.

Figure 10-5 shows how the instrument outputs would appear if the input electric field varied from the maximum detectable negative value to the maximum detectable positive value.

RESULTS

The electric field readings on Gemini IV were extremely large compared with what was expected on the basis of past measurements of potential on satellites, and with the short discharge times one would expect for a vehicle in the ionosphere.

The Gemini IV data gave no reason to suspect any electrical or mechanical malfunction of the instrument. Consequently, investigations were made to determine whether the apparent electric field was due to some cause other than a true electric field at the surface of the spacecraft.

Postflight tests confirmed that the instrument was responsive to radiated RF energy and to charged plasma-current particles incident on the sensing face of the sensor unit.

The time available between the conclusion of postflight Gemini IV tests and the launch of Gemini V precluded any internal modifications being made to the Gemini V instrument, which was originally identical in configuration to that on Gemini IV. However, an external modification was incorporated, the primary purpose of which was to shield the sensor from electric fields terminating on the spacecraft. This modification consisted of a conducting screen assembly which covered the sensing face of the sensor unit.

By comparing the outputs obtained on Gemini V with those obtained on Gemini IV, it was anticipated that an estimate could be obtained of the contribution of the electric field toward the output levels observed on Gemini IV.

Figure 10-6 shows a comparison plot of the data obtained during the initial three orbits of Gemini IV and Gemini V. As previously mentioned, the Gemini V instrument was screened from measuring electric field. However, since the calibrations of both instruments were in terms of electric field, the units used to plot the ordinate of figure 10-6 are called

measurement units, where one measurement unit equals one volt/cm of
apparent electric field.

Since the instrument is responsive to fluxes of charged particles,
it is possible that the high readings during the initial orbits of both
missions were due in part to enhanced ionospheric charged-particle con-
centrations resulting from outgassing of the spacecraft. There is some
evidence to support this hypothesis.

Since heating of the spacecraft would accelerate outgassing, one
would expect the ionosphere to be enhanced during the daylight portions
of the initial orbits. During the first three orbits of Gemini V, sus-
tained high readings did occur during daylight. A dropoff of one to two
orders of magnitude occurred during a period of approximately five min-
utes preceding total darkness, followed by lower readings during the sub-
sequent period of total darkness. The available Gemini V data shows that
the output begins to increase upon exit from total darkness. The total
darkness periods for Gemini V on figure 10-6 were from 42 minutes to
1 hour 21 minutes, from 2 hours 12 minutes to 2 hours 50 minutes, and
from 3 hours 40 minutes to 4 hours 20 minutes ground elapsed time (g.e.t.).

Further support for the enhanced-ionosphere hypothesis was obtained
from Gemini V air-to-ground communications. The Gemini V crew reported
a slight yawing of the spacecraft due to operation of the water boiler
before 45 minutes g.e.t. An enhanced ionosphere, due to the ejection of
steam, may have contributed toward the high readings from 25 to 37 min-
utes g.e.t. The Gemini V crew also reported fuel-cell purging in pro-
gress at 1 hour 50 minutes g.e.t. A sharp increase in instrument output
occurred at 1 hour 45 minutes g.e.t.

Still further support for the enhanced-ionosphere concept is found
in comparing the outputs during the initial orbits of Gemini IV with out-
puts later in the mission. Figure 10-7 shows Gemini IV data from 46 hours
5 minutes to 47 hours 10 minutes g.e.t. These outputs are comparitively
steady; the maximum output is two orders of magnitude lower than the
highest readings taken in the initial orbits. This is perhaps an indica-
tion that outgassing is no longer taking place.

CONCLUSIONS

Additional data is necessary for detailed comparisons between
Gemini IV and Gemini V data. These include: (1) electron concentration
versus altitude profiles from stations along the ground tracks of
Gemini IV and Gemini V (this program is underway), and (2) natural
electron and ion flux contributions to the outputs of the Gemini IV and
Gemini V instruments. (A computer program has been developed at MSC

that resolves the spacecraft velocity vector along a set of axes fixed in the sensor unit, and defines the angle between the normal to the sensing disk and the sun. Data from this program will soon be available and will make it possible to estimate these contributions.)

In addition to this data, continuing analysis is required to define the transmitter-antenna combinations operating coincident with the instrument. Raw instrument data will then be compared with this information. Analysis also continues of air-to-ground transcripts, onboard voice recorder transcripts, and crew logs to further define and isolate mission operations that might have affected the instrument outputs.

As previously mentioned, the Gemini V instrument was inhibited in responding to electric fields corresponding to charge on the spacecraft. However, readings were obtained on Gemini V that were as high or higher than those obtained on Gemini IV. This could be interpreted as a gross indication that the contribution of an electrostatic field charge on the Gemini IV spacecraft measurements was negligible.
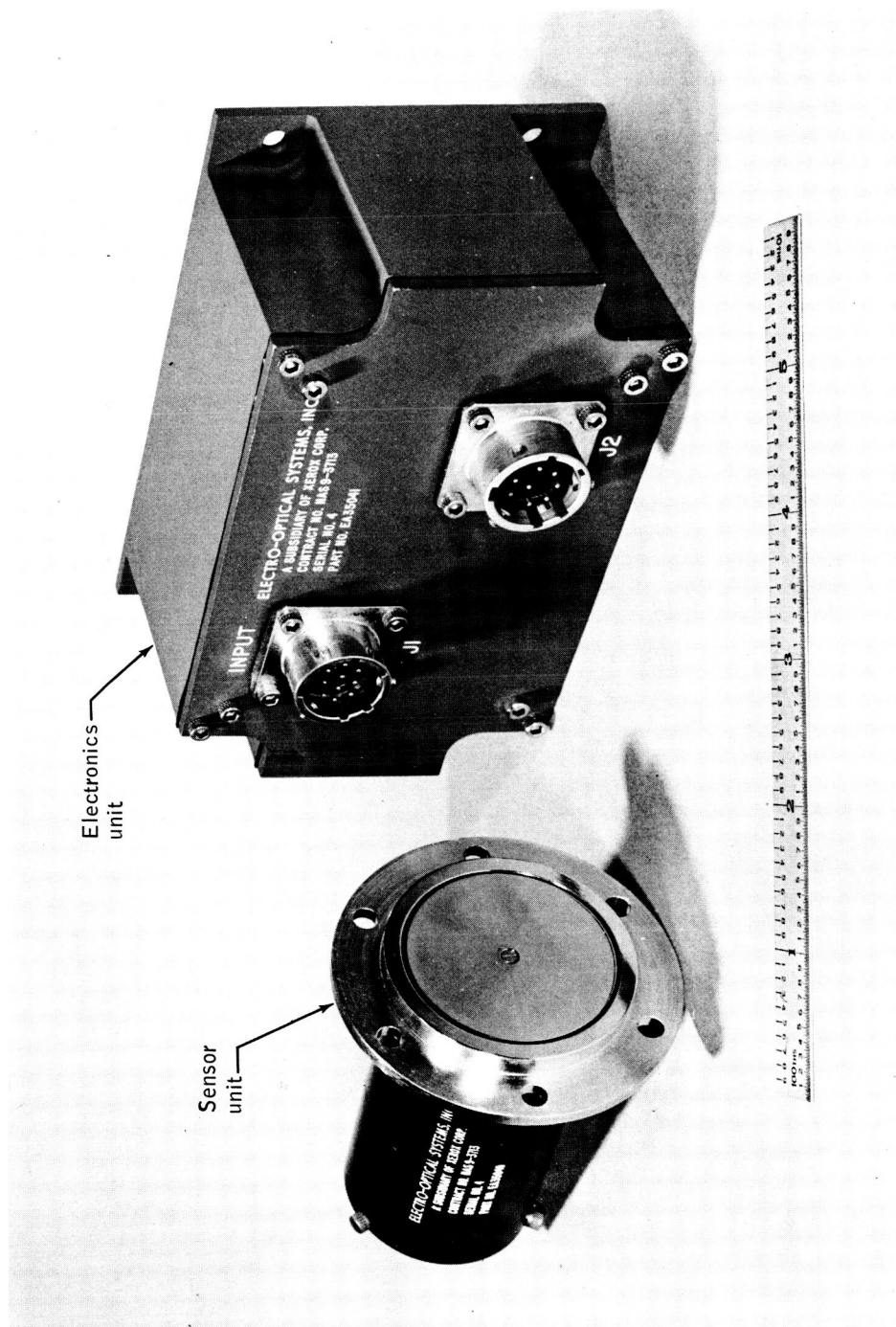
NASA-S-65-6508

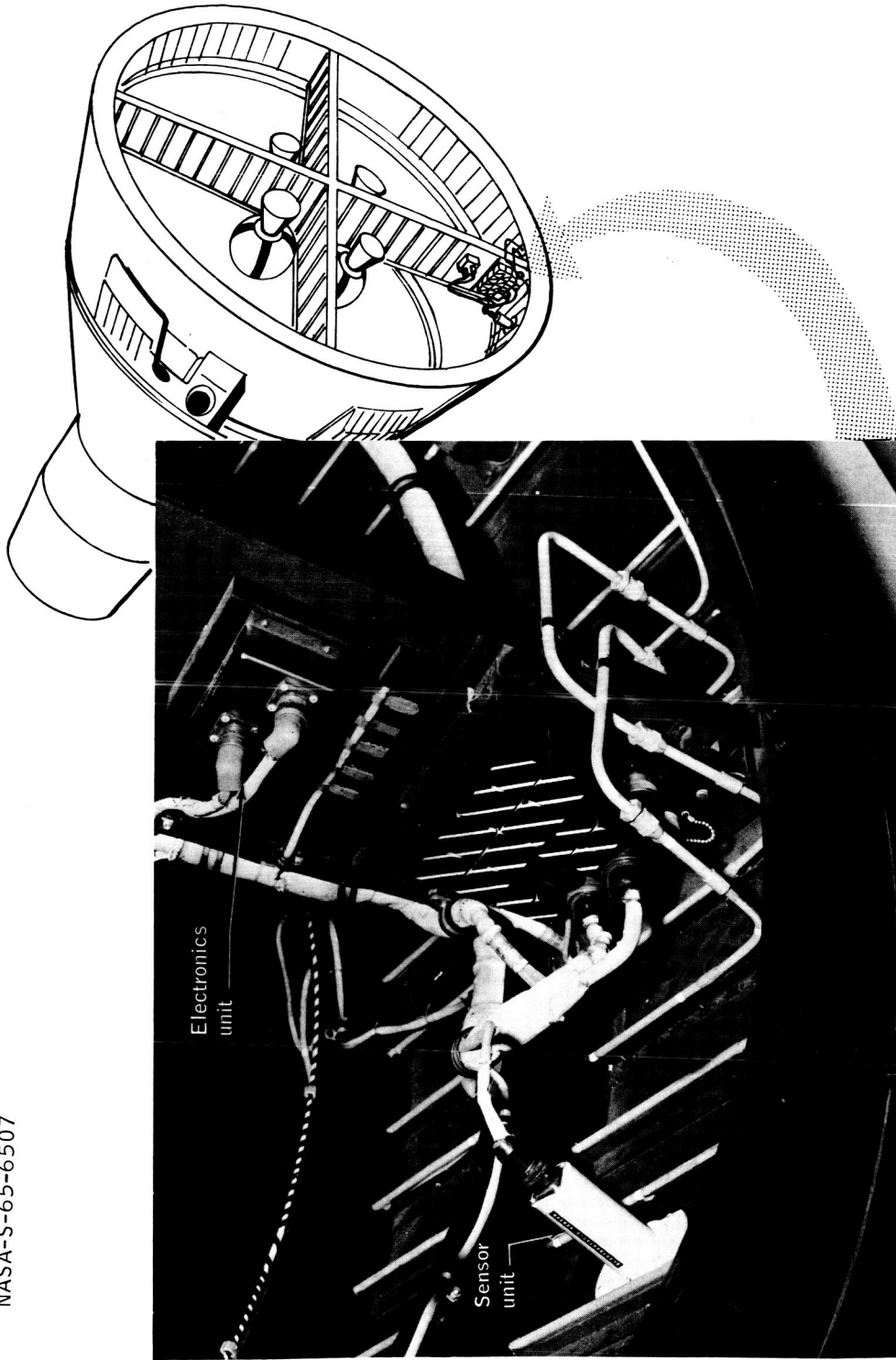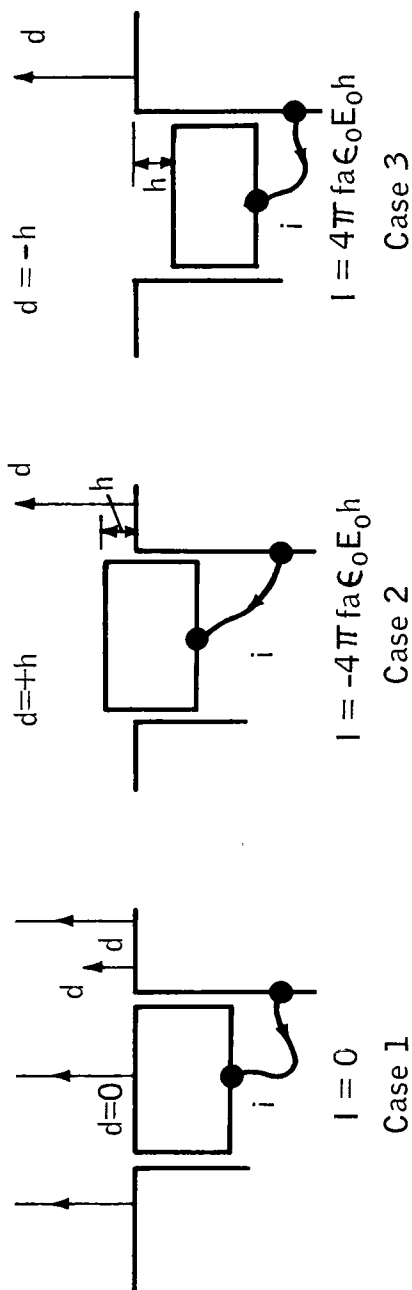Figure 10-1.- Experiment equipment components.

NASA-S-65-6507

Electronics
unit

Sensor
unit

Figure 10-2.- Experiment equipment location.

Case 1

$I = 0$

$d = 0$

Case 2

$d = +h$

$I = -4\pi\,fa\,\epsilon_o E_o h$

Case 3

$d = -h$

$I = 4\pi\,fa\,\epsilon_o E_o h$

$I = -(4\pi\,fa\,\epsilon_o E_o)\,d.$

Where f = disk oscillation frequency,
     a = radius of disk,
     ϵ_o = permittivity of free space,
     E_o = field at conductor surface, and
     d = $d_o \cos (2\pi$ ft) = distance between
             outer surface of disk and conduct-
             ing surface.

Figure 10-3.- Current calculations.
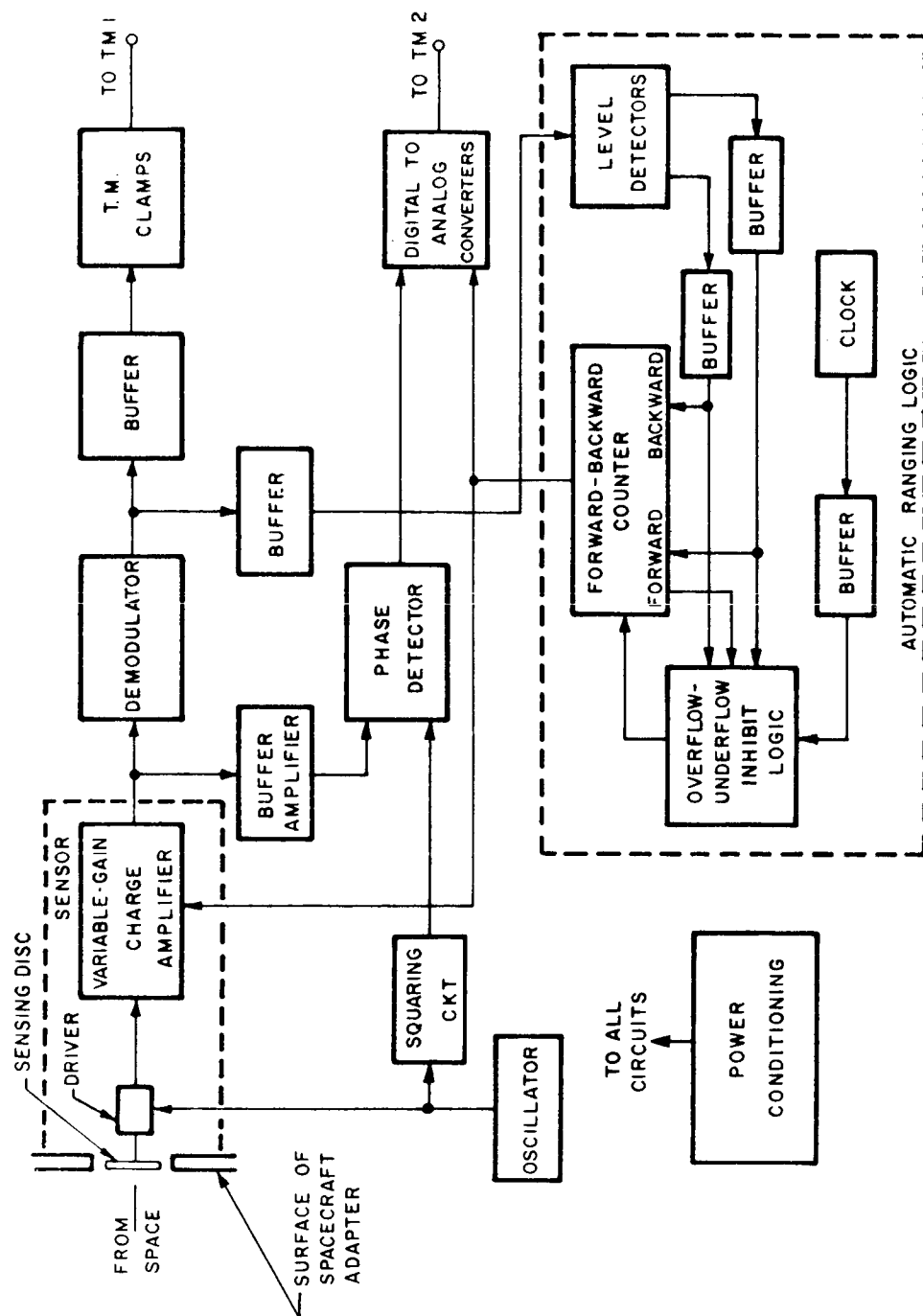
Figure 10-4.- MSC-1 instrument block diagram.
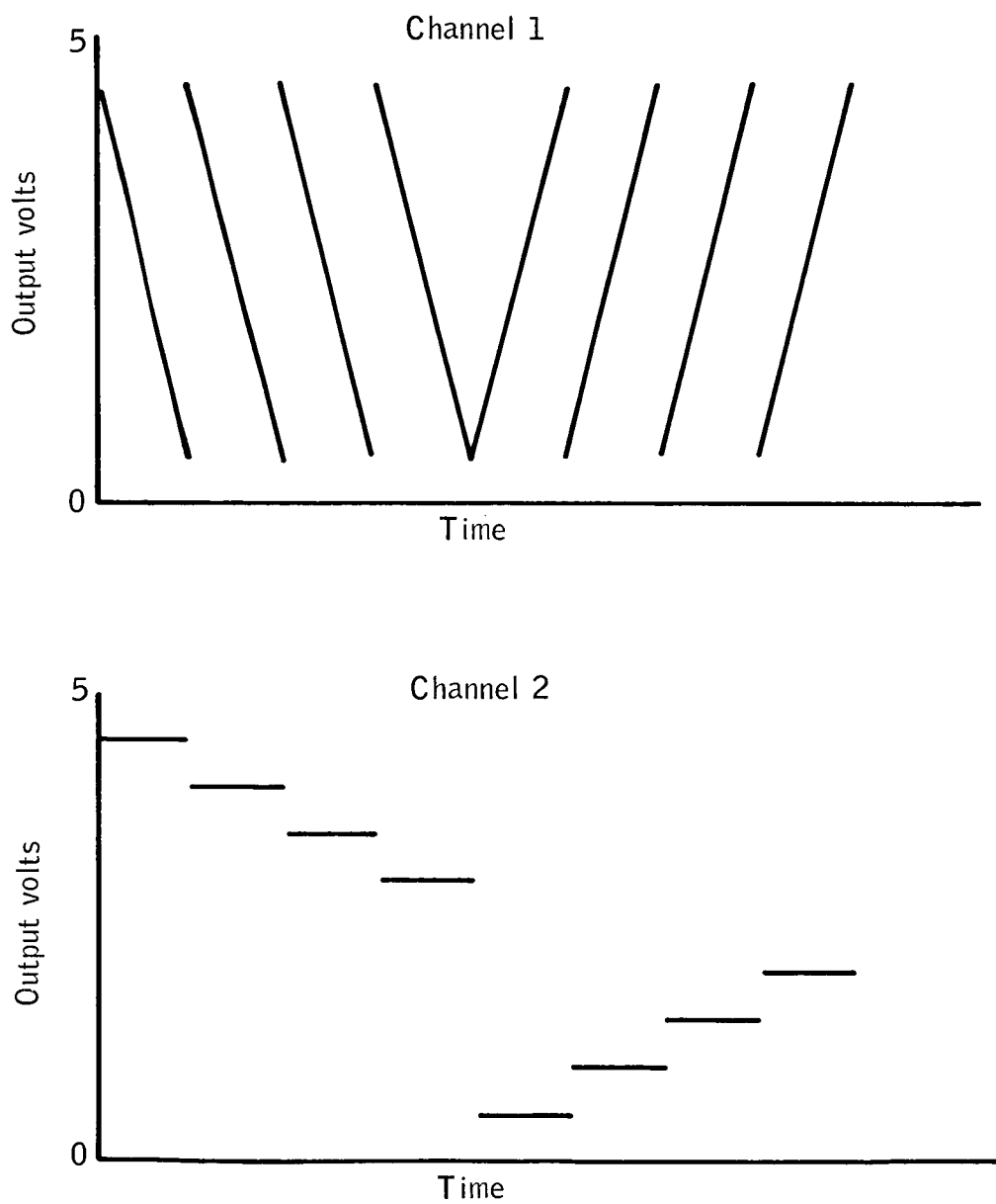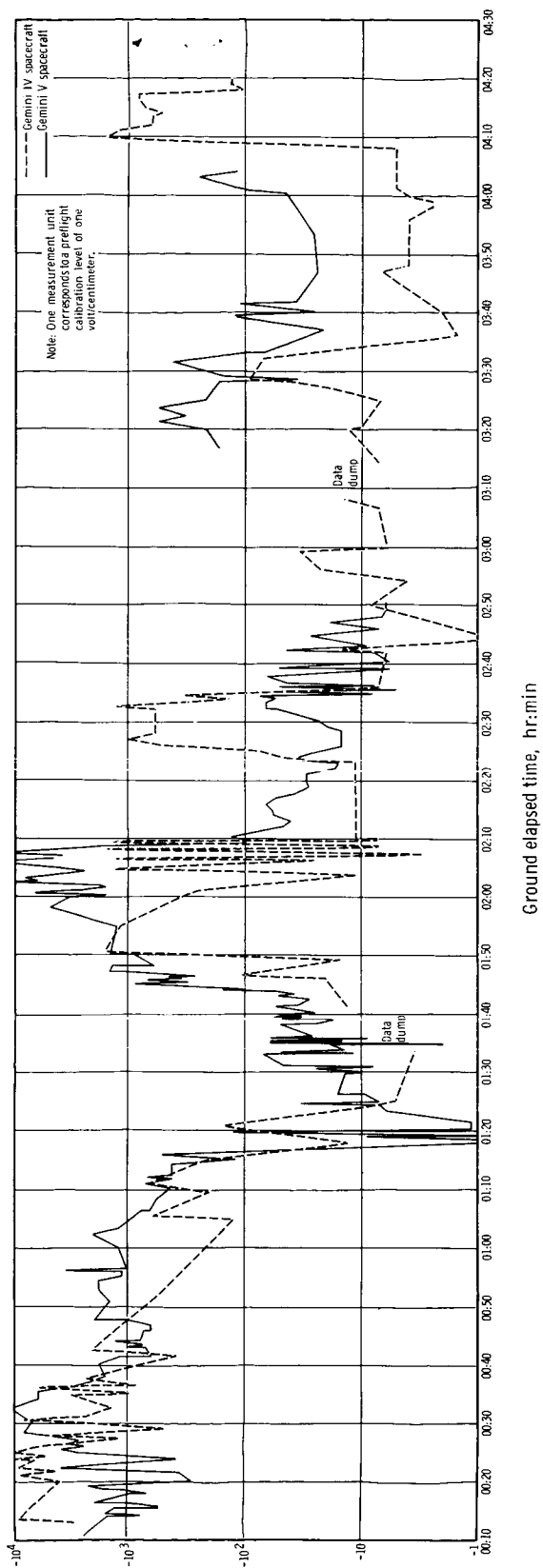
Figure 10-5.- Instrument outputs.

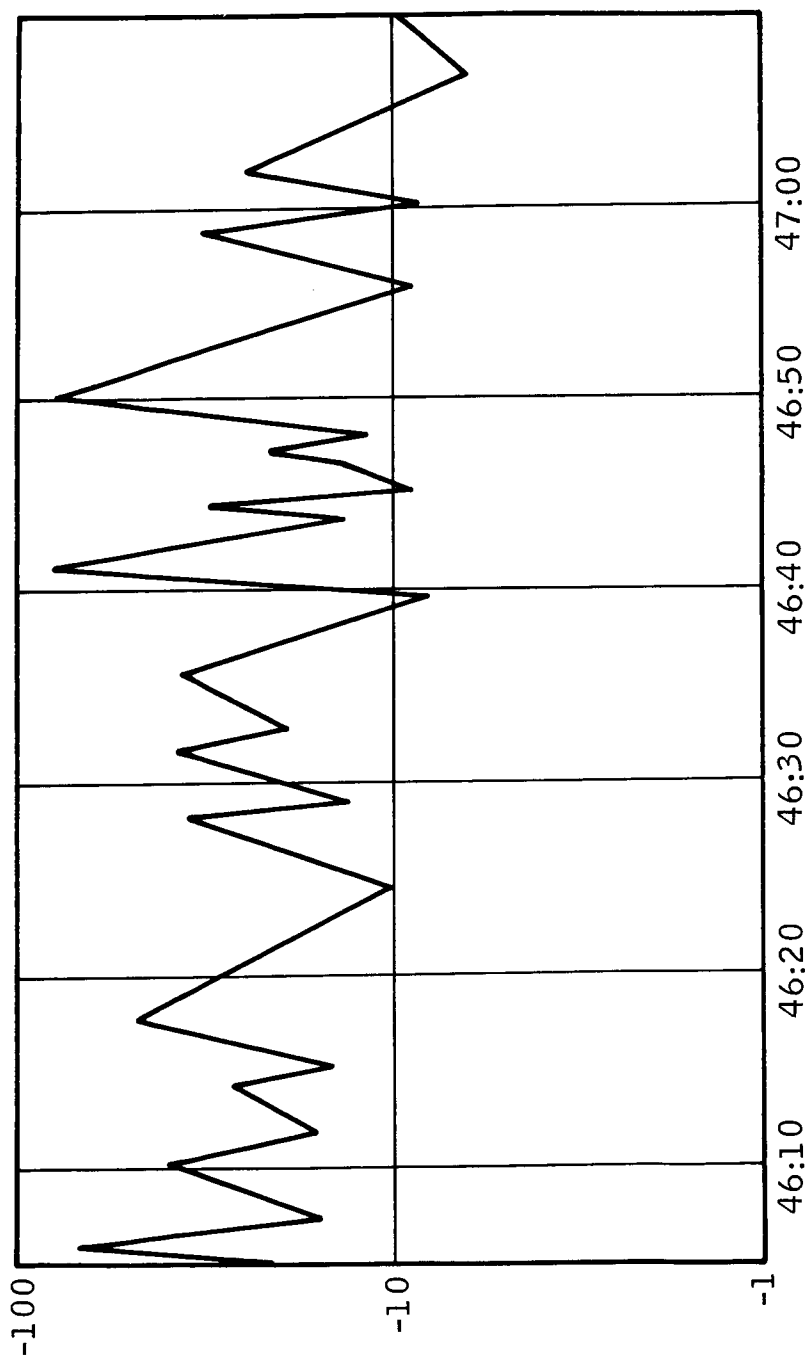Figure 10-6. – Instrument measurement during first three revolutions.

Figure 10-7.- Measurement during revolution 30 of Gemini IV.

11.   EXPERIMENT MSC-2,

PROTON-ELECTRON SPECTROMETER ON GEMINI IV

by James Marbach
NASA Manned Spacecraft Center

INTRODUCTION

The MSC-2 experiment was one of a series of engineering experiments carried out by Manned Spacecraft Center on the Gemini IV mission to provide a detailed description of the radiation environment encountered by the spacecraft and crew. The data from these experiments are used as source terms for the calculation of radiation doses received by the crew members. The dose calculations not only require an exact description of the radiation environment, but also a detailed shielding breakdown of the spacecraft and knowledge of the modes of interaction between the spacecraft and the nuclear particles. Comparison between theory and experiments is accomplished by using dosimeters to monitor the integrated dose received by each crew member.

In general, the orbital altitude of the Gemini IV mission was well below the altitude where the protons and electrons trapped in the earth's geomagnetic field are encountered. However, an anomaly in the geomagnetic field occurs over the South Atlantic, approximately between latitudes of 15° S. and 55° S., and longitudes of 30° E. and 60° W., where the field lines drop to lower altitudes. The revolutions of charged particles about a given field line, dictated by the particles' magnetic moment, consequently bring them to an altitude that was intersected by the Gemini IV orbits beginning with the 4th revolution and continuing through the 10th, and are repeated every 16 revolutions thereafter.

EQUIPMENT

The Gemini IV spectrometer was designed, constructed, and calibrated by the experiment equipment contractor. The chief scientist in charge had made several similar charged particle measurements previously. A very similar spectrometer to that for Gemini IV was used on a polar

orbiting Air Force satellite; the results of the experiment are presented reference 1.

A cross section of the spectrometer is shown in figure 11-1. The main scintillator acts as detector for both protons and electrons and is shaped to provide an approximately uniform path length over a solid angle of about 1.2π steradians. Average thickness over the solid angle is about 5.0 gm/cm^2.

Completely surrounding the main scintillator, except for the aperture and the photomultiplier tube coupler, is identical pilot B plastic which is optically separated from the main scintillator by reflective paint. Its function is to provide anticoincidence to all particles entering the main scintillator through any portion of the instrument other than the entrance orifice. A photomultiplier (PM) tube monitors the main scintillator through a lead-glass light pipe, while the anticoincidence scintillator is monitored with three parallel connected PM tubes. In order to minimize anticoincidence rate and provide a rugged mounting, the entire package (including electronics) is set in an aluminum case. The 5.1 gm/cm^2 shielding provided by the lead-glass light pipe coupling the main scintillator to its PM tube, combined with the PM tube and electronics, and the packaging will reduce to a negligible quantity the number of particles entering through that area not controlled by the anticoincidence scintillator.

The spectrometer, which weighed approximately 12.5 pounds was located, with the MSC magnetometer, on a mounting pedestal affixed to the blast-shield door on the Z-axis of the equipment adapter. The measurement is made by looking true aft through the thermal curtain to the outside. (Calibrations correct for effects of the thermal curtain.)

The mounting location is shown by a diagram in figure 11-2 and by a photograph in figure 11-3.

To measure the radiation environment in the anomaly, it is necessary to be able to distinguish between low fluxes of protons and high fluxes of principally fission electrons. Since electron measurements using a proven instrument have already been made, it was decided to use this basic electron instrument and to modify it to adapt to proton measurement as well. The result is equipment that uses rather straightforward and proven pulse height analysis techniques with special gain shifting and discriminating to delineate protons from electrons.

In order to monitor the flux and energy of both electrons and protons, a combination of shielding and a knowledge of the approximate proton-electron flux ratios in the anomaly is employed with gain shifting

in the preamplifier of main scintillator circuit. The ranges of particles to be measured were chosen to be $0.3 \leq E \leq 4.5$ Mev for electrons and $12 \leq E \leq 80$ Mev for protons. While the instrument is in the proton detection mode, negligible error due to electron contamination is expected, since fluxes of electrons of $E > 12$ Mev are known to be very small. Some contamination of low energy protons in the electron measurement is expected, but all available data on anomaly fluxes indicate that the electron flux exceeds the proton flux by a large factor. The net contribution to the overall electron spectrum measured is thus expected to be negligible. The recent evidence that proton anomaly spectra may show a large number of protons present at energies below 10 Mev has been considered and, in fact, a spectrometer scheduled for Gemini mission VII will resolve this question and provide a check on the assumption made in this design. The 0.001 gm/cm^2 aluminized Mylar light shield covering the entrance aperture will help to minimize low-energy proton contaminations also.

DATA AND CONCLUSIONS

Figure 11-4 shows preliminary count-rate data of protons (lower curve) and electrons (upper curve) from a typical pass through the anomaly. As expected, the data show a smooth rise to peaks of approximately 6×10^4 electrons/cm^2-sec and 10^2 protons/cm^2-sec. The magnetometer data show that the spacecraft was tumbling during this pass, which produced the apparent dip in the data. The magnetometer showed that the spectrometer axis was within $1°$ of being along the field line, and since the detector does not have a 2π solid angle, the decrease is apparently due to the directional response of the detector.

Figure 11-5 shows data from revolution 52. The data are similar to those from revolution 7, reaching peaks of 3×10^4 electrons/cm^2-sec and 10^2 protons/cm^2-sec. The dip in the proton data shown is unexplained, but further analysis must be conducted before conclusions are drawn.

Figure 11-6 is typical electron spectra taken at different times through the anomaly on revolution 7. The energy spread over the channels noted is from 0.3 to 4.5 Mev. The proton spectra taken on the same revolution are shown in figure 11-7. The energy spread over the channels is from 12 to 80 Mev.

The data shown are only preliminary and await more detailed analysis. The data appear to be of such sufficient quality that, when the analysis is completed, the detailed sort of information required for dose calculations

will be provided. Combined with the MSC magnetometer data, the MSC-2 experiment is considered to be a complete success.

REFERENCE

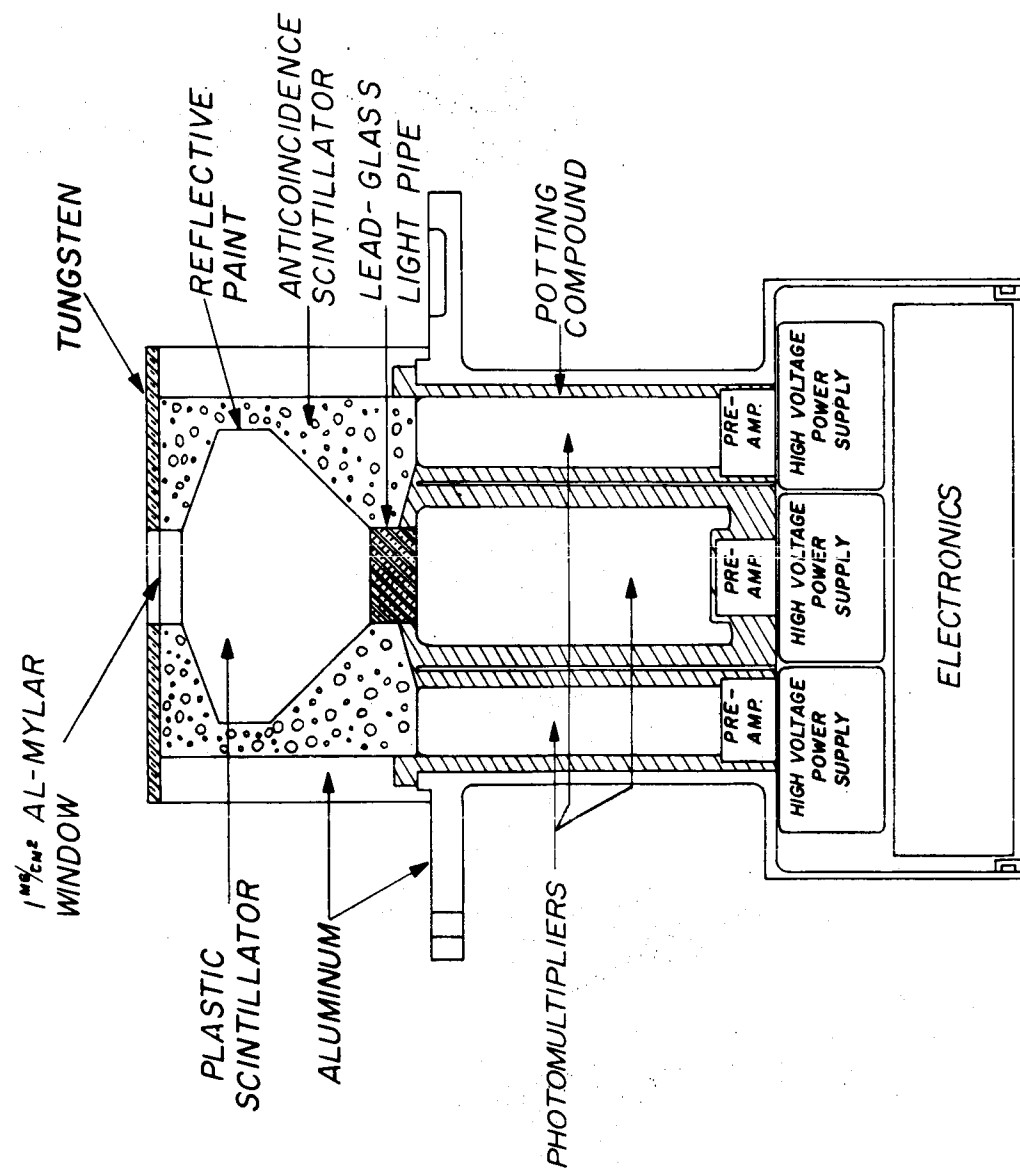1. Geophysical Research, vol. 70, p. 569, Feb. 1, 1965.

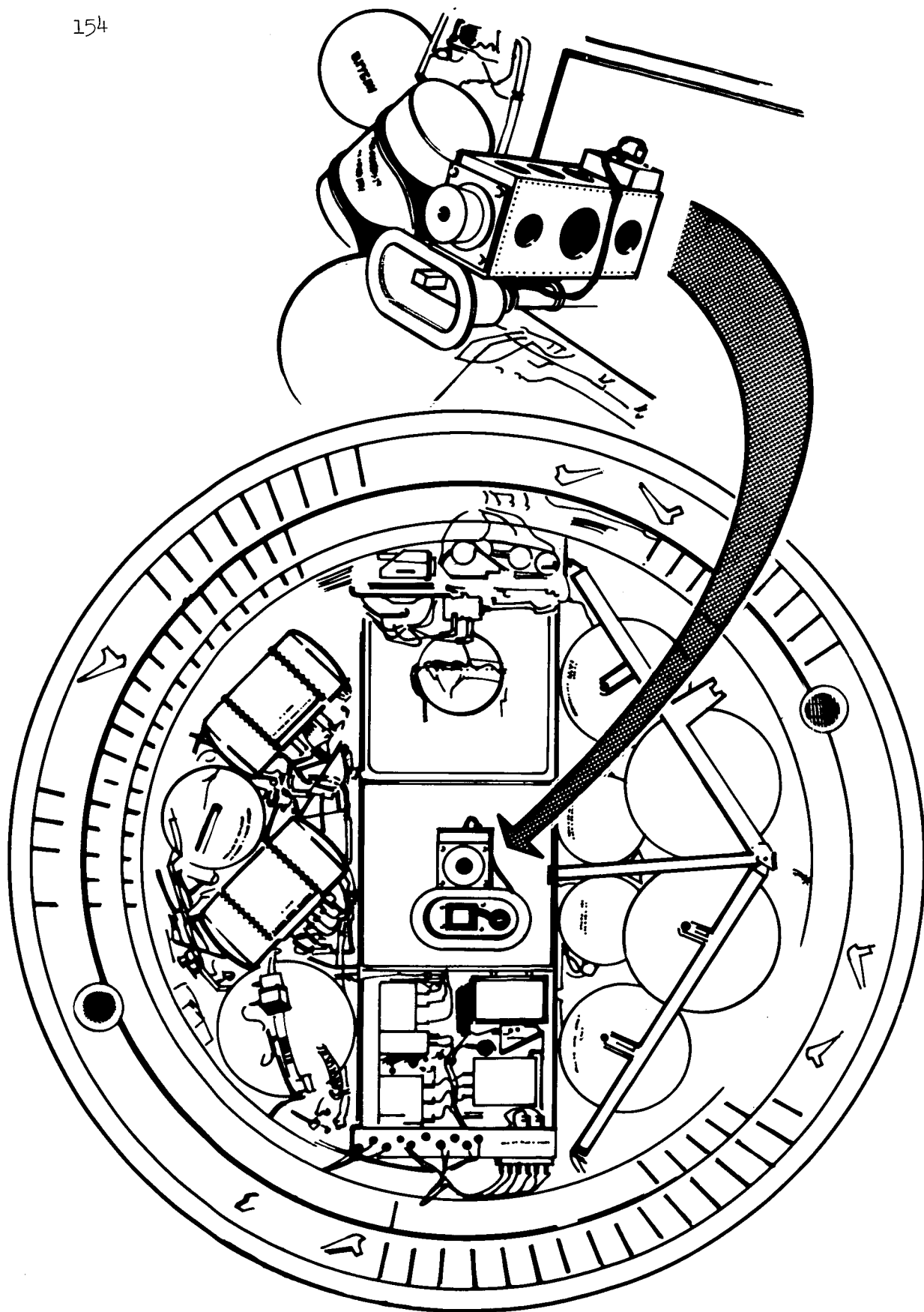Figure 11-1.— Cross section diagram of proton-electron spectrometer.

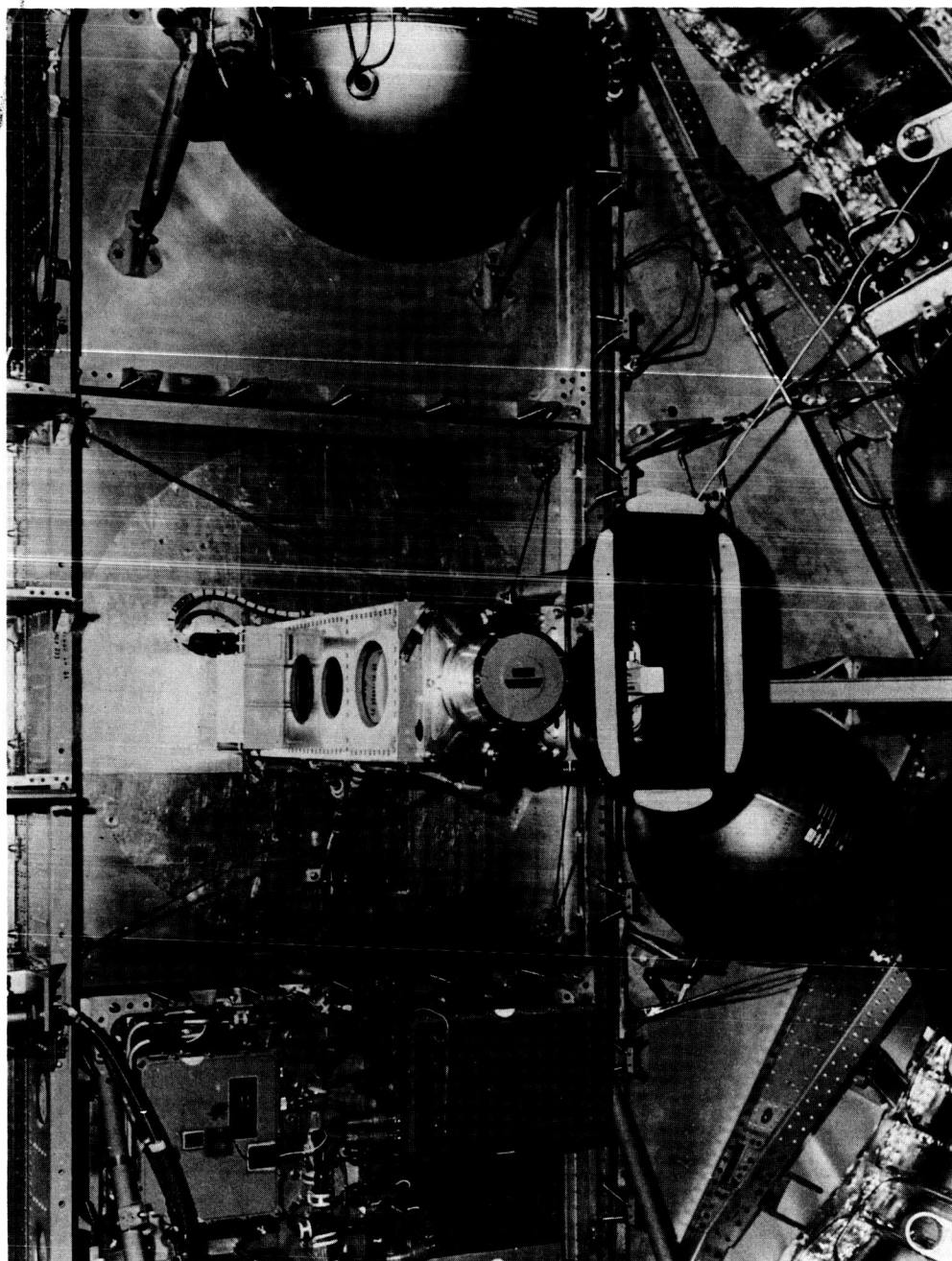Figure 11-2.- MSC-2 and 3 equipment location.
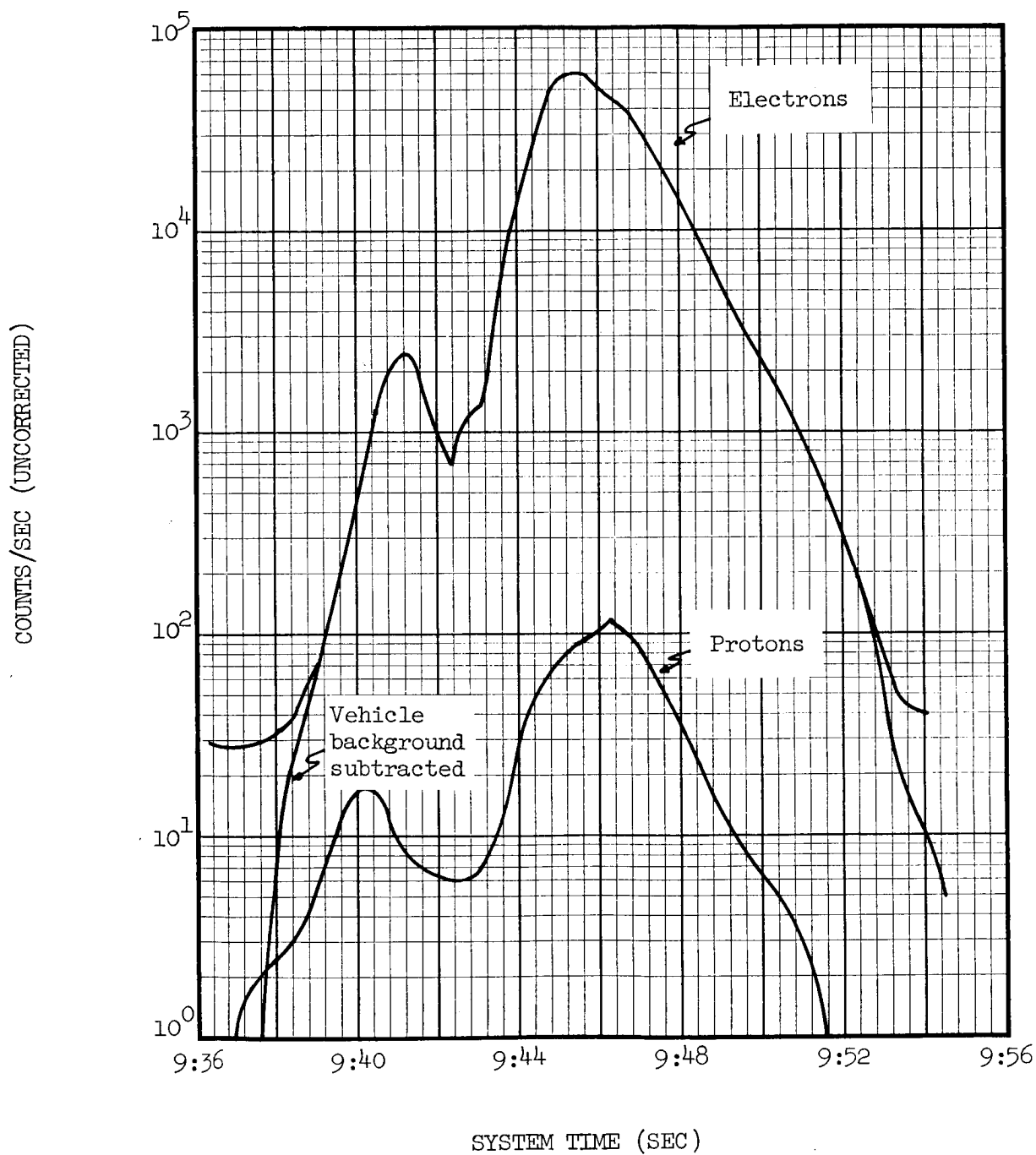
Figure 11-3.- Equipment location.

156

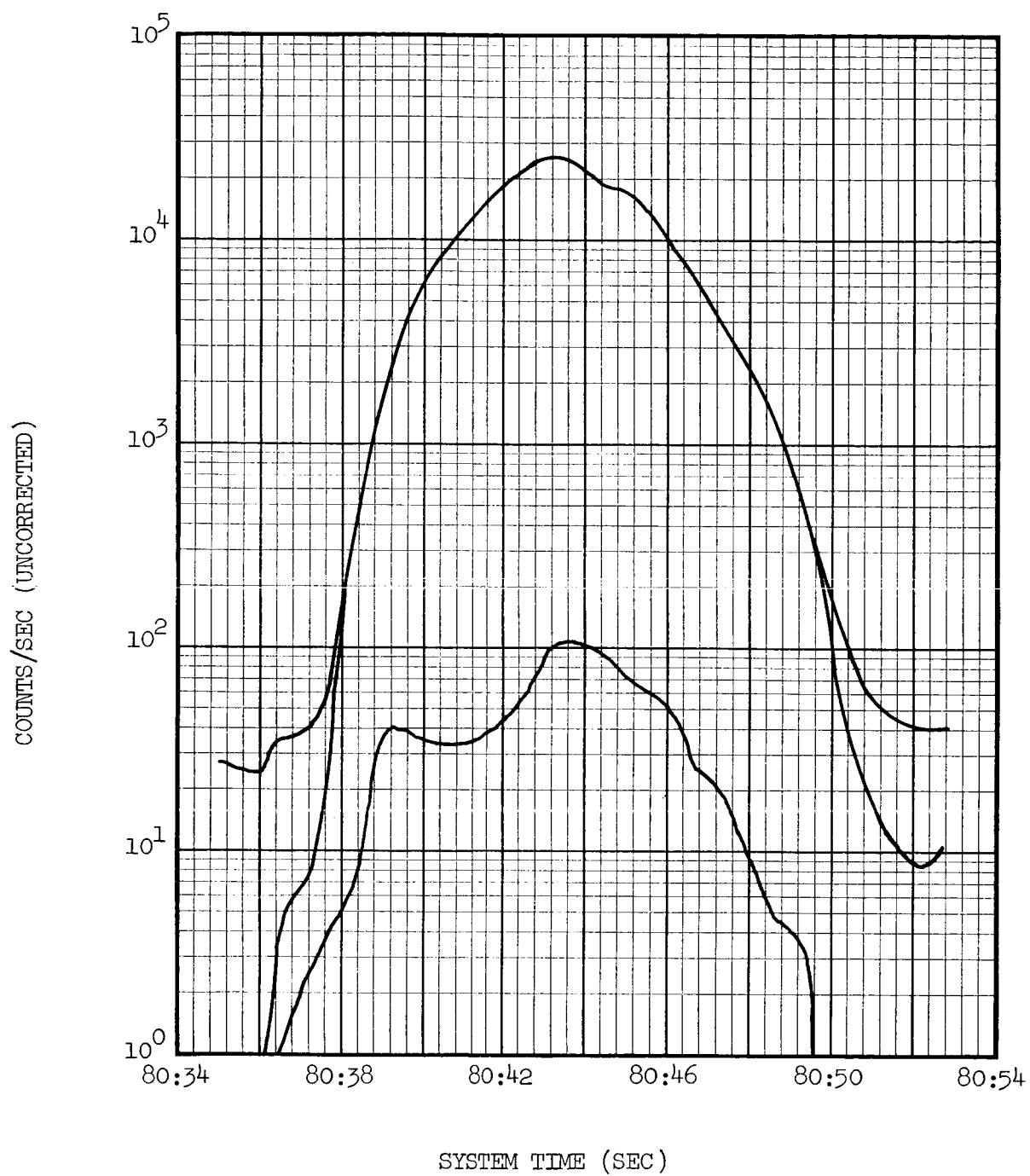Figure 11-4.– Gemini IV proton-electron spectrometer, revolution 7.

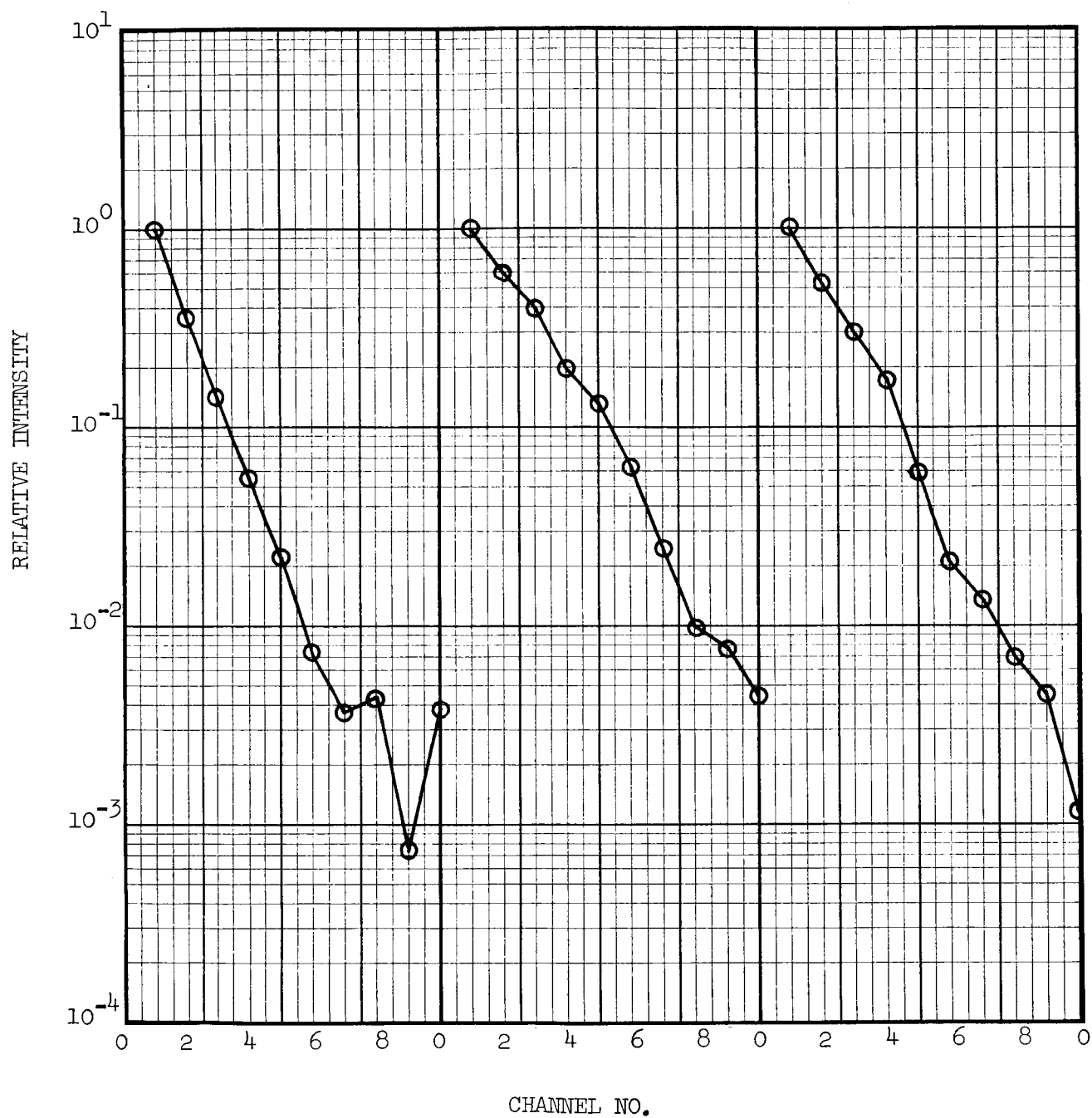Figure 11-5.- Gemini IV proton-electron spectrometer, revolution 52.
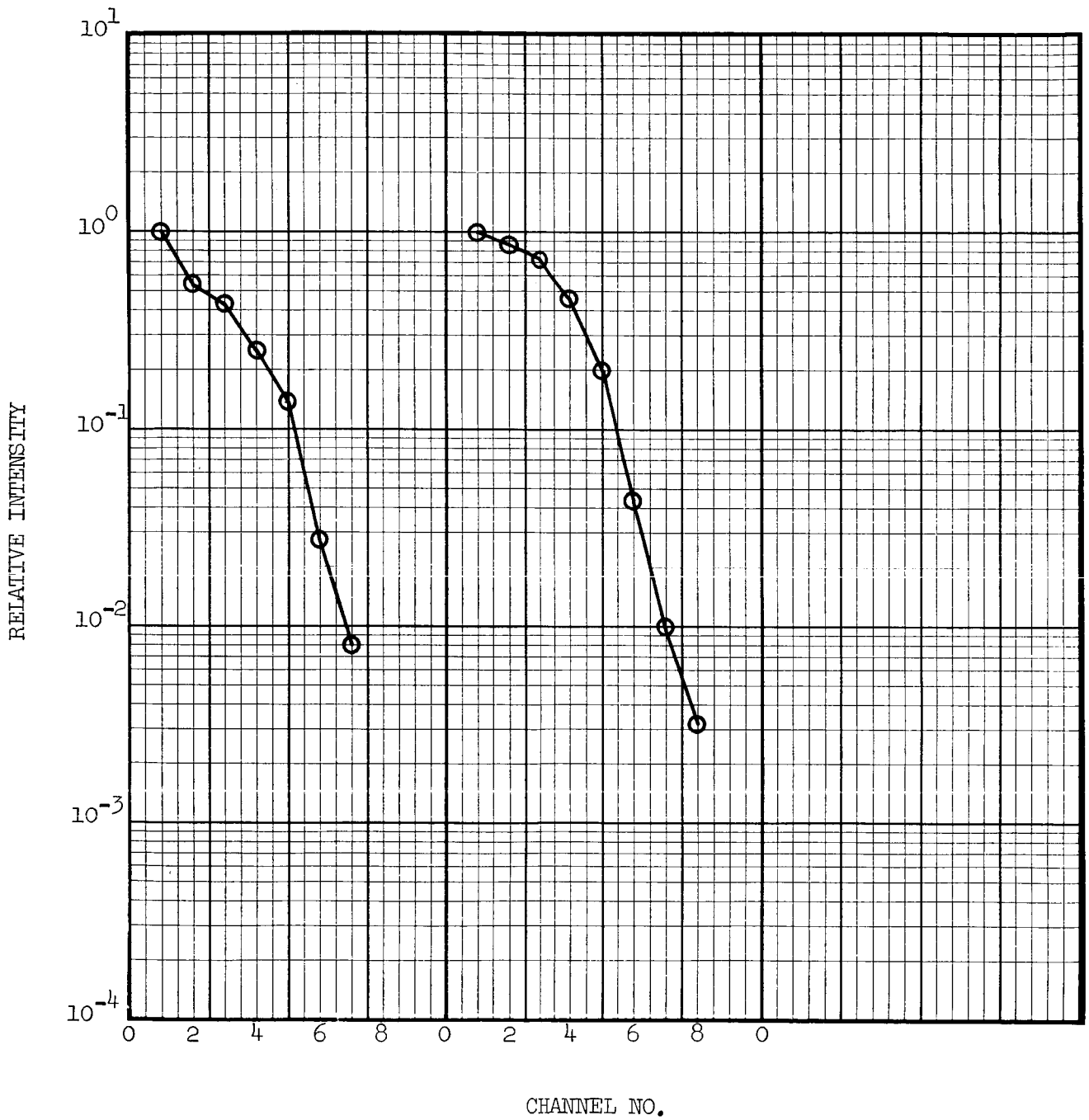
Figure 11-6.- Electron spectra, revolution 7.

Figure 11-7.- Proton spectra, revolution 7.

12. EXPERIMENT MSC-3, TRI-AXIS MAGNETOMETER ON GEMINI IV

By William D. Womack
NASA Manned Spacecraft Center

OBJECTIVE

A tri-axis magnetometer was used on Gemini IV spacecraft for the purpose of determining the magnitude and direction of the local geomagnetic field with respect to the spacecraft. These data are useful in the interpretation of results from the MSC-2 experiment, Proton-Electron Spectrometer, and will be essential in interpreting data from later Gemini missions where directional spectrometers will be employed. Knowledge of the direction of the local geomagnetic field is necessary because of the strong directionality of charged-particle fluxes in the anomaly region where the particles pitch angles are near 90°. Pitch angles are those angles between the particle direction and the magnetic field line about which it is spiraling (fig. 12-1).

The dependence of pitch angle on local magnetic field strength follows from consideration of the first adiabatic invariant of trapped charged-particle motion which states that the particle's magnetic moment may be considered a constant of the motion. This leads to the relation $\frac{\sin^2 \gamma}{B}$ = constant, where γ is the particle pitch angle and B is the magnetic field strength. Since γ is near 90° in the anomaly region, a measurement of the local magnetic field strength allows for the directionality of the particles.

DESCRIPTION

The magnetometer was designed to measure three orthogonal components of the field. The magnetometer consists of separate electronics and sensor units (fig. 12-2). The electronics unit contains the necessary components to drive the sensor, detect the vector magnetic-field sensor signals, and convert the signals to analog dc voltages. The sensor unit contains three orthogonal monoaxial second-harmonic probes.

The unit is capable of measuring a ±0.6 gauss magnetic field with a 0 to 5 volt output.

To minimize any stray magnetic fields produced by other instrumentation on borad the spacecraft, the sensor unit was extended from the spacecraft after insertion into orbit (figs. 12-3 and 12-4).

RESULTS

Data from three revolutions 7, 22, and 51 are taken as typical examples of data from the magnetometer while operating through the area bounded by 15°S. and 55°S. latitude and 30°E. and 60°W. in longitude known as the South Atlantic anomaly region.

Figure 12-5 shows the magnitude of the field for each of the revolutions. The variations in magnitude depicted is a result of the geocentric altitude changes of the spacecraft in each revolution. The magnitude of the field from the magnetometer data compares favorably with the 48-term expansion of the Jensen-Cain coefficient.

The angle θ on figure 12-6 displays the direction of the magnetic field vector with respect to the proton-electron spectrometer and the Z-axis of the spacecraft. It can readily be seen from revolution 7 data that the angle θ ranges from 90° to 0°. This illustrates the tumbling effect of the spacecraft during drifting flight.

Data from revolution 22 display an attitude change in yaw or pitch but without a tumbling effect as seen in revolution 7. During the mission the crew noted in their flight log that while performing a blunt-end-forward maneuver through the anomaly region during revolution 22, the yaw attitude of the spacecraft was not held within ±5°.

Data from revolution 51 illustrate an exceptionally good small-end-forward maneuver of the spacecraft by the crew. The angle θ does not vary over ±5° for the 20 minutes displayed.

Figure 12-7 shows a comparison between raw data taken from revolution 7 through the anomaly region, the 48-term expansion of the Jensen-Cain coefficient, and the data compiled after applying a correction factor for stray magnetic field from the spacecraft. This is conclusive evidence that a magnetometer can be flown on Gemini spacecraft for determining the direction and magnitude of the magnetic field to be used in interpreting data from directional spectrometers, which was the purpose and objective of this experiment.

Data from other revolutions have been examined and appear very similar to the three examples shown here. All data from the magnetometer have been sent to the MSC-2 experiment contractor for pitch-angle interpretation on results of proton-electron spectrometer. From these data the contractor has been able to attribute sharp decreases in the flux spectrum of protons and electrons to an increase in the angle of the spectrometer and the magnetic field line.

CONCLUSIONS

Conclusions can be made from the data on the magnetometer experiment that are not only important to the proton-electron spectrometer experiment but also to any directional charged-particle experiments that may be conducted.

The first conclusion drawn was that, even though the Gemini spacecraft is not magnetically clean, the data can be reduced to a form which supplies directional information on magnetic field relation to spacecraft.

Another conclusion, made during spacecraft testing, was that the stray fields were results of spacecraft structure rather than current flows produced within the spacecraft electrical systems.

The experiment, as proposed, was a complete success and efforts are being made on future missions to reduce spacecraft stray fields, thus enabling more accurate data to be obtained.
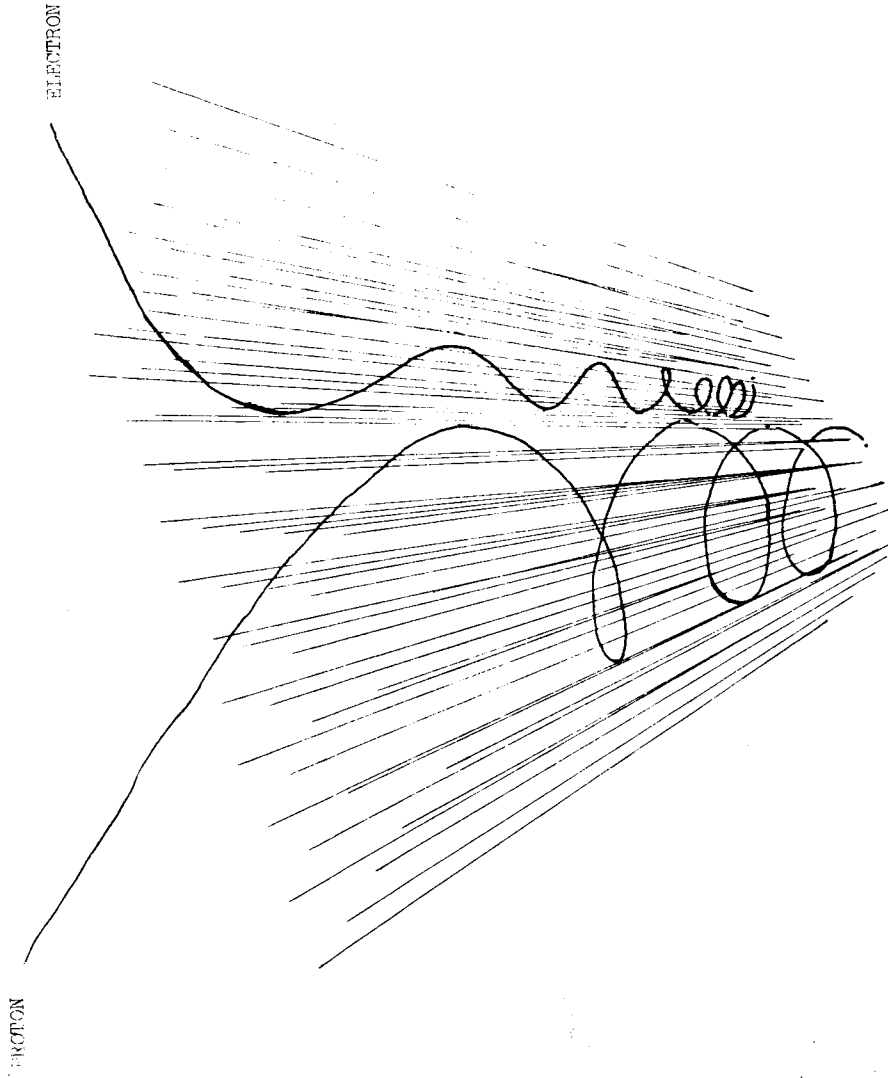
Figure 12-1.- Diagram showing proton and electron as they spiral through a magnetic field. Field strength increases toward bottom of diagram and pitch angle increases.
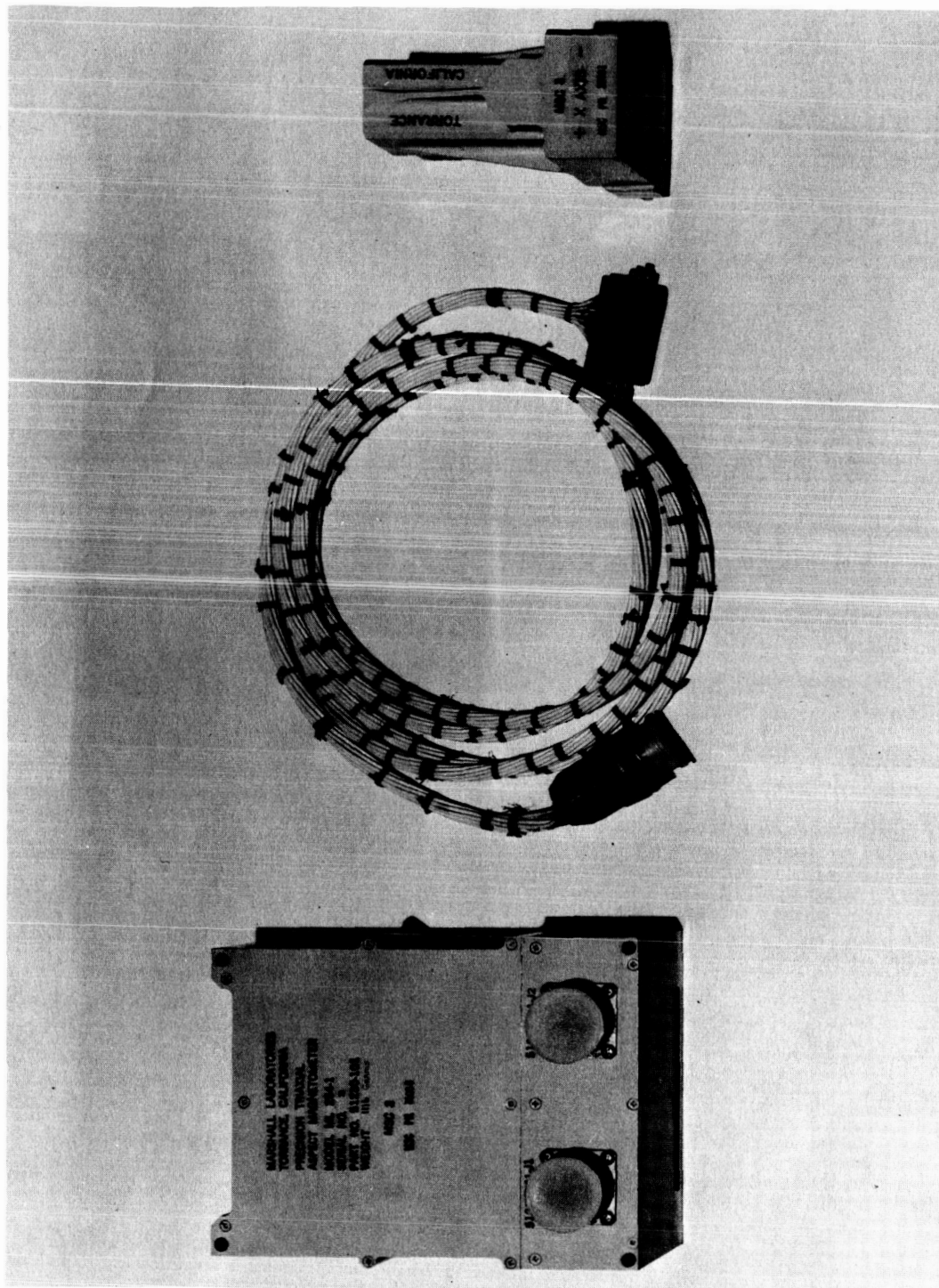
Figure 12-2.- Photograph of electronics and sensor units of the magnetometer.
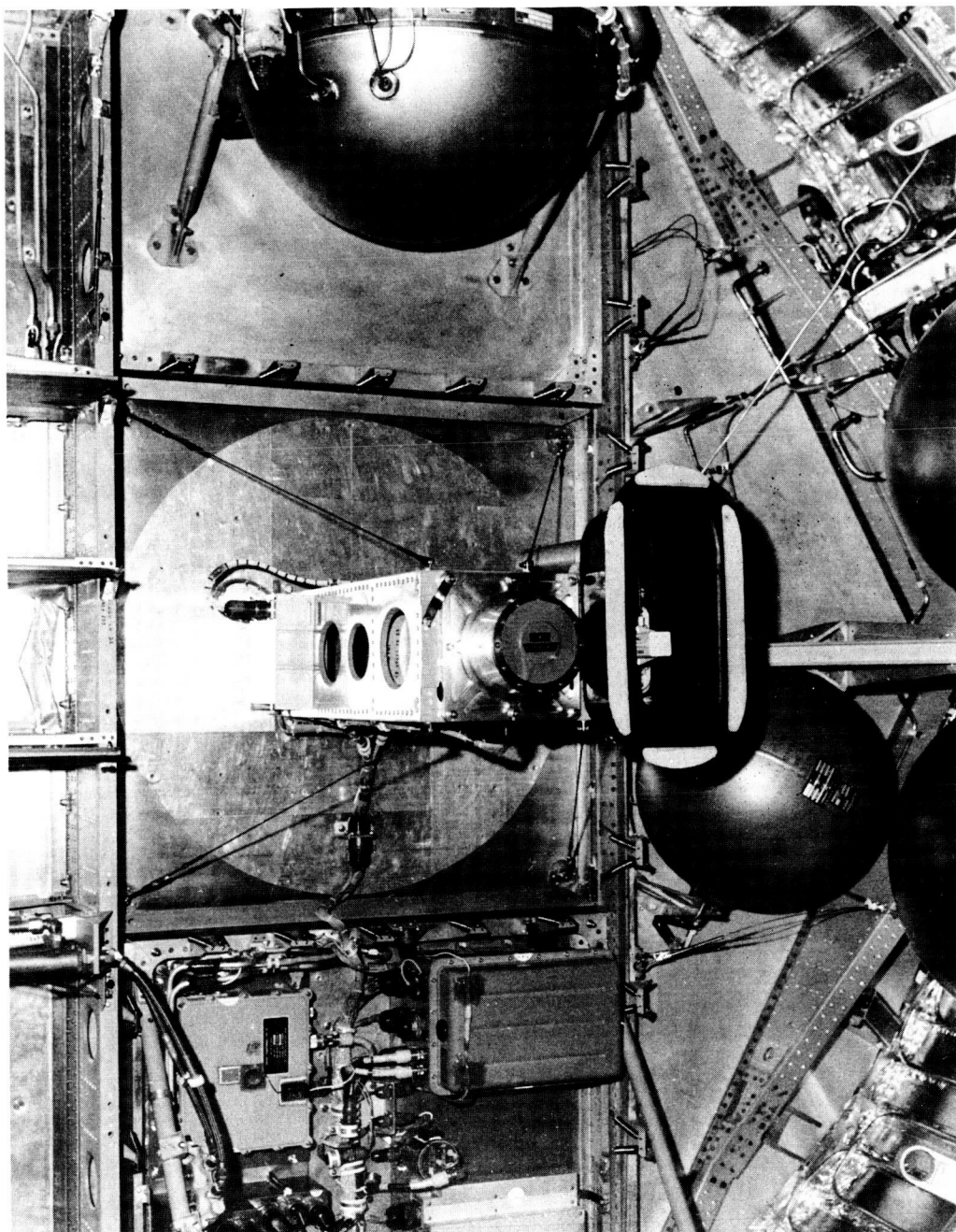
Figure 12-3.- Magnetometer location.

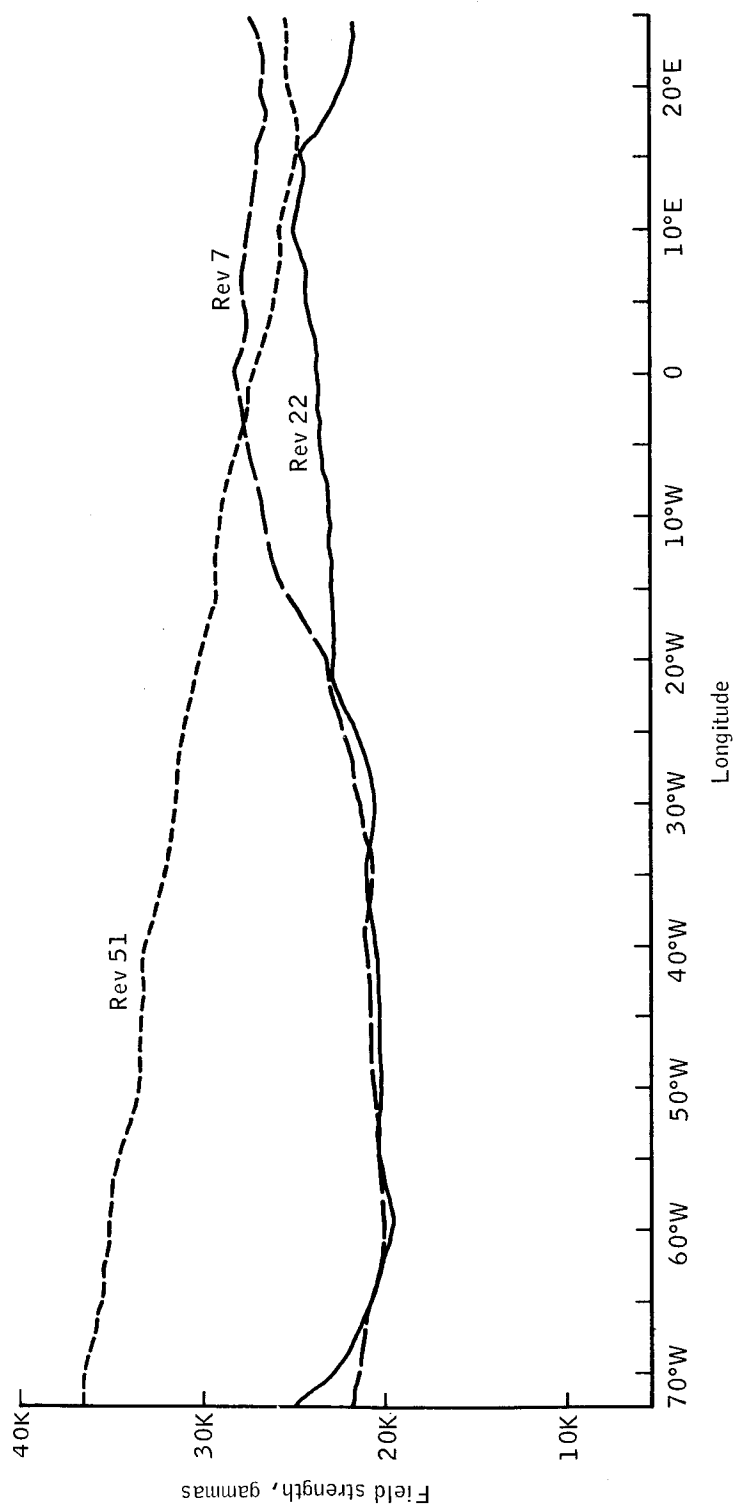Figure 12-4.- Magnetometer boom extension.

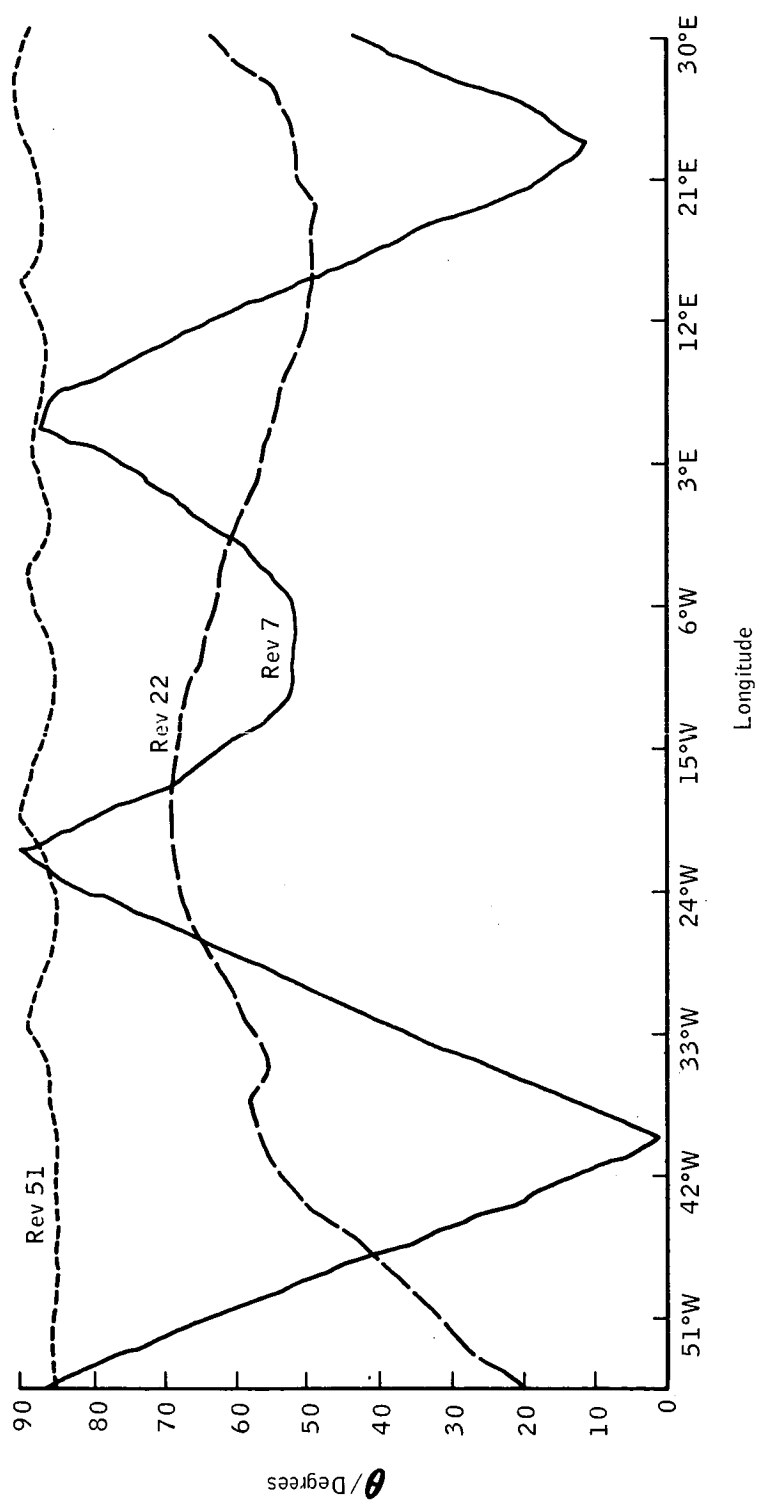Figure 12-5. - Magnitude of anomaly field.
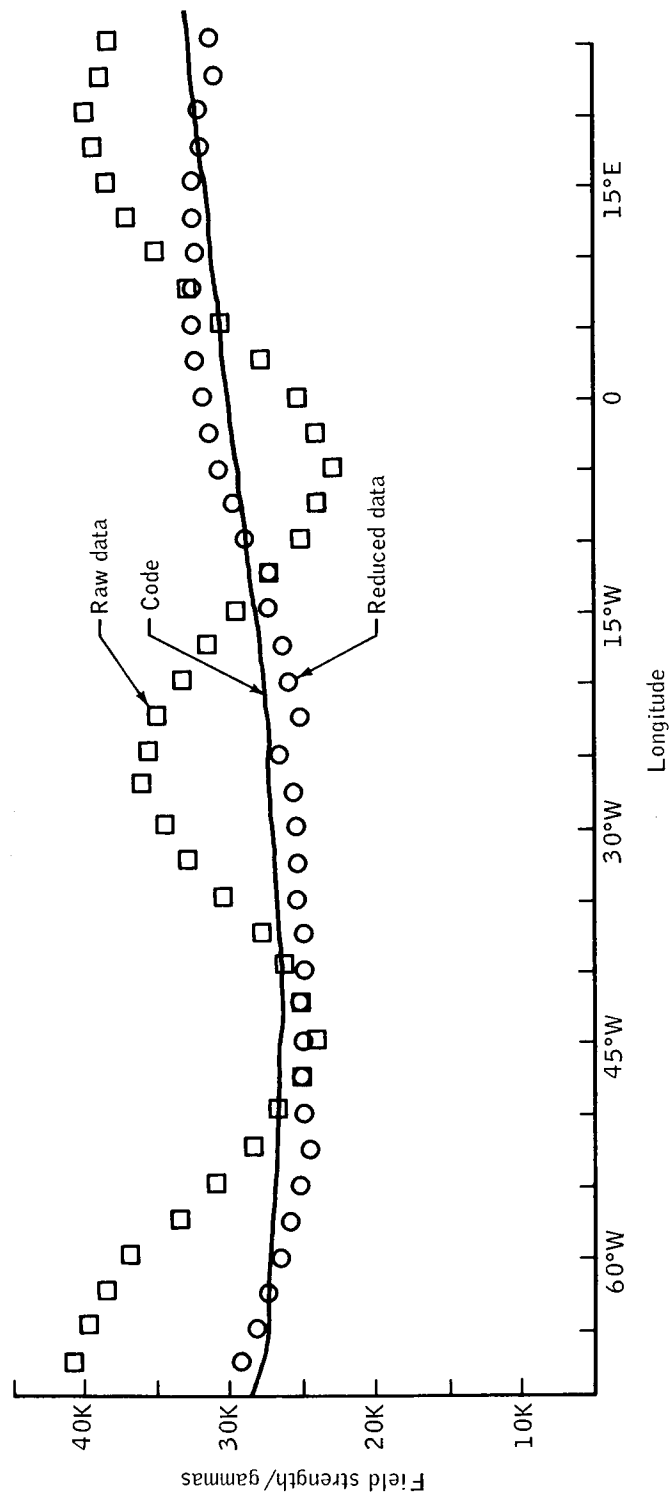
Figure 12-6.- Magnetic field direction.

Figure 12-7.- Comparison between raw data, the 48-term expansion of the Jensen-Cain coefficient, and corrected data from revolution 7.

N 65-36113

13. EXPERIMENT D-8, RADIATION

IN SPACECRAFT GEMINI IV

By Lt. M. F. Schneider, Lt. J. F. Janni, and Lt. G. E. Radke
Air Force Weapons Laboratory
Kirtland Air Force Base, New Mexico

INTRODUCTION

One prerequisite to successful completion of future manned-space mission-planning studies is the gathering of adequate data concerning (1) the radiation environment, (2) its shielding interactions, and (3) the dose rate levels to be encountered. Such data is necessary to insure the astronaut's protection against ambient and oftenties hostile space radiation. This experiment was performed to obtain a series of precision measurements looking toward reliable empirical dosimetry data for use in those space-planning studies where an accurate prediction and interpretation of the biological effects produced in man would be of vital importance.

The specific measurements performed in this effort resulted in quantitative and qualitative characterizations of the radiation levels associated with the Gemini mission. Since these measurements were carried out under normal ambient conditions, the radiation environment encountered was made up, in the main, of those energetic protons and electrons present in the inner Van Allen belt and encountered each time the Gemini spacecraft passed over the South Atlantic Anomaly region. In this region the radiation belt dips close to Earth, due to the anomalously low strength of the Earth magnetic field. The instruments designed for this experiment were optimized for the radiation-level responses that were anticipated in this geomagnetic anomaly region. In order to allow for measurement of the very low cosmic-radiation intensities to be encountered outside of the anomaly region, the dynamic range of the instrumentation was extended for detection of all energy-deposition rates above the level of 0.1 millirad/hour.

The experiment included also a determination of the ionizing and the penetrating power of various primary and secondary radiations which

were present within the Gemini spacecraft, by measurement of the contributions to dose according to profile, to particle type, to time, and to position (or location) within the spacecraft.

The experiment was carried out utilizing two distinct types of dosimeter systems. In nautre, one system was active while the other provided only a passive response to ionizing radiation. Each system and the measurements obtained from each will be discussed separately.

ACTIVE DOSIMETRY

Instrument Theory and Design

The active instruments included tissue-equivalent ionization chambers of which the response characteristics for all ionizing radiation match closely those of soft muscle. The tissue-equivalent chambers were operated in the Bragg-Gray mode which provide a basis for the energy-deposition dosimetry measurements performed. Briefly, the Bragg-Gray relationship is given by:

$$E_m = S_m \, W \, J_{gas}$$

where

E_m = Energy absorption in the material in (eV/gm) sec-1

S_m = Relative mass-stopping power of the wall to the chamber-filling gas

J_{gas} = Ion current in (Ion Pairs/gm) sec^I

W = Average energy dissipated in gas per ion formed in gas

This relationship relies on the assumption that the gas cavity will be traversed by the same flow of corpuscular radiation as exists in the material under consideration. If the gas within the cavity is matched closely to the atomic composition of the walls, the cavity size will not disturb the flux of the secondary particles. Fano's theorem provides the basis for this conclusion: "In a medium of given composition exposed to a uniform flux of primary radiation, the flux of secondary radiation is also uniform and is independent of the density of the medium, as well as of density variations from point to point."

This cavity-ionization principle, therefore, permits determination of the energy absorbed in a solid medium (here, in soft-muscle tissue) through ionization measured in a small gas-filled cavity within that medium.

Two distinct types of active dosimeter were employed in the data-gathering process; one was fixed; the other, portable. Figure 13-1 and 13-2 show the mechanical design of each instrument.

Instrument Calibration

Calibration of the active dosimeters consisted in a vigorous, many phased program to determine (1) the radiation input-to-output voltage-transfer functions, (2) the radiation response time at various radiation levels, and (3) any temperature-time effects on the transfer or calibration curves. The initial calibration was effected approximately 90 days before launch, using cesium 137 and cobalt 60 gamma-radiation natural emitting sources at the Air Force Weapons Laboratory, Kirtland Air Force Base.

Several two-week time drift-rate tests were performed on each system following this initial calibration. Upon completion of the time drift-rate test, the radiation response-time calibration to different levels of radiation in the range from 0.5 millirad/hour to 100 rad/hour was effected. All instrumentation was then temperature cycled from -40°F to 160°F, in order to check for any possible temperature-dependent characteristics in the instruments. Drift rates of less than 10 percent were observed in the outputs of the instruments. The effects of temperature on instrument outputs were negligible, owing to the relative constancy of cabin temperature during the Gemini mission.

The instruments were then recalibrated, using cesium 137 and cobalt 60 gamma radiation prior to shipment to the spacecraft contractor's facility for installation on the spacecraft. A specially designed portable 0.1 millicurie strontium 90 beta-particle source was utilized for performance of the functional calibration checks on the instruments during preinstallation acceptance, and the spacecraft-systems testing. This beta-particle source was utilized also to perform the final functional recalibration at launch-minus-7-days at Cape Kennedy.

The active dosimeters were recalibrated, at the Air Force Weapons Laboratory (Kirtland AFB, N. Mexico), using the NBS calibrated gamma ranges for cesium and cobalt and this was done approximately 20 days after the termination of the Gemini IV mission to insure the highest accuracy in the final-data analysis.

Flight instrument prototypes were calibrated at Oak Ridge National Laboratory, using 40 MeV and 60 MeV protons of various beam diameters and intensities, to obtain (1) proton-dose to voltage-calibration curves and (2) directional sensitivity-response curves. These were used to correct for the essentially omnidirectional measurements performed in the spacecraft. Similar calibration and response data was gathered using 3.0, 2.0, 1.0 and 0.5 MeV electrons. All data presented in this report have been corrected for the small directional-response differences between the two instruments, in the matter of to charge-particle radiation.

Experimental Method

The fixed active dosimeter, designated Type I, was mounted on the left hatch of the spacecraft. The portable unit, designated Type V, was mounted in a symmetrical location on the other hatch. Figure 13-3 shows the mounting location of the portable instrument on its hatch.

Both instruments were powered from the spacecraft carrying regulated voltage. The output from each instrument was recorded continuously throughout the flight. Each instrument was capable of recording instantaneous dose rates ranging between 0.1 millirad/hour and 100 rad/hour. This wide range allowed the instruments to respond also to low-intensity cosmic-ray fluxes as well as to any unusual, but possible, high-dose rates encountered in the South Atlantic Anomaly Region. The active dosimeters also have an advantage in that their instantaneous outputs may be integrated directly, so as to determine the total accumulated dose, for purposes of comparison with the passive-dosimetry components of the experiment.

The active portion of the experiment began at spacecraft lift-off. During five ensuing selected passes through the central portion of the South Atlantic Anomaly Region, the sensing head of the portable Type V unit was removed from its mount on the hatch and positioned in the following locations by the Gemini pilot:

(1) Against the chest, the sensor being covered with a glove

(2) Between the legs in the area of the groin

(3) Under the left armpit

(4) In front of the cabin window

(5) In front of the instrument panel, about midway between the floor and the ceiling

(6) On the floor of the spacecraft between the feet.

These six positions are illustrated in figure 13-4 through 13-9.

The sensor was fixed in each of the above locations for a period of 1.0 minute, to insure that full response by the instrument to the chosen radiation field would be attained.

As measured, the dose-rate levels were thus functions of position (1) in the spacecraft and (2) in depth in the astronaut, since portions of the astronaut's body were used as a shield. As a function of time, the dose-rate level beneath the hatch of the spacecraft was obtained from the fixed Type I dosimeter. So, these data were used as a base line from which to compare measurements as made in the various positions by the portable unit.

Data and Results

The active portion of Experiment D-8 is discussed most conveniently in terms of two general areas of interest: (1) Experimental determination of the dose levels obtained outside of the South Atlantic Anomaly Region, and (2) measurement of the radiation characteristics during spacecraft passage through the anomalous region of the inner radiation belt. The active-radiation sensors functioned perfectly throughout the mission and the five scheduled radiation-level surveys within the cabin as made by the pilot were performed during the "anomaly" passes of the spacecraft.

Cosmic radiation dose measurements.- Outside of the South Atlantic Anomaly Region, the principal contribution to the biological dose received by the astronaut was from cosmic radiation. The average, maximum and minimum dose levels obtained (1) during 19 revolutions of the spacecraft and (2) through regions excluding the Anomaly dosages are presented in table 13-I. The average dose rate was obtained every 3.2 seconds for each revolution. The maximum and minimum dose levels were determined as the lowest or highest readings observed during at least a 1.0 minute period for each revolution. The average dose rate for all "non-anomaly" revolutions analyzed here was found to be 0.15 millirad/ hour.

Since the revolutions selected for analysis cover the entire span of the Gemini IV mission, the average dose rate presented may be readily extended to obtain excellent approximations of the total integrated dosage for the complete mission. This may then be projected to estimate cosmic radiation levels for more extended missions at the Gemini operating altitudes. Using this average yield, the total

integrated dosage due to cosmic radiation during the four-day mission was approximately 15.0 millirad. The cosmic radiation levels are thus generally very low and so constitute a quite permissible exposure dose for extended periods at Gemini operating altitudes.

Assuming a nominal period of 90 minutes for each revolution, total accumulated tissue dose is approximately 0.23 millirad per revolution. The average daily radiation level received inside the cabin of the Gemini spacecraft and due to cosmic radiation is approximately 3.5 millirad/day. Such radiation levels are also very low and constitute a quite permissible magnitude of exposure.

During a portion of revolution 3 and during the period of astronaut egress, the right hatch remained open so as to expose the Type V portable dosimeter to an essentially external space-radiation environment. The radiation levels measured by the Type V instrument during this time exceeded at no time those obtained by the Type I unit. This indicates clearly a total absence of softer (or trapped) corpuscular radiation in those regions of space where the astronaut was extravehicular. Figure 13-10 illustrates the cosmic radiation dose profile as a function of orbital elapsed time and corresponding L-shell values. These dose profiles indicate a buildup to approximately 0.5 millirad/hour at higher L values, and a rapid drop below 0.1 millirad/hour for L values of near -1.0 earth radii. This effect is consistent with the predicted magnetic cutoff values encountered by the Gemini spacecraft. Since the spacecraft traversed only the lower geomagnetic latitudes, dosage was less than the polar, or the free-space, values which nominally run as high as 14 millirad/day during solar minimum periods.

Anomaly region dose levels.- Dose rate data obtained from the South Atlantic Anomaly Region shows rapid and pronounced rise in magnitude over the cosmic levels of radiation. The "anomaly" dose rate experienced during revolution 7, for example, rises two orders of magnitude; that is, to more than 100 millirad/hour. Figures 13-11 through 11-19 indicate the dose levels encountered by the two active dosimeters for nine orbits of the Gemini spacecraft beginning with the 7th revolution and continuing through the 54th revolution. The peak dose levels varied from 107 millirad/hour on revolution 7 to only 20 millirad/hour for revolution 51. The curve in figure 13-11 shows that an appreciable dose level was present 15 minutes during revolution 7 which was made on a deeply penetrating orbit. For a grazing orbit, such as revolution 39, the "anomaly" transit time was less than 7 minutes. For most passes, this transit time averaged approximately 12 minutes.

The dose-rate differences between the two dosimeters shows the effects of the different shieldings interposed between the sensing elements and the radiation field being measured. The Type V (portable)

dosimeter generally read slightly higher than the Type I (fixed) dose-rate meter. Revolutions 7, 21 , 22, 38, 39, and 54 are orbits in which the Type V dosimeter reads slightly higher than the Type I dosimeter during the "anomaly" penetration. Revolutions 36 and 51, which were very similar types of orbits, show an interchanging of readings between the two dosimeters, On revolutions 36 and 51, for example, five distinct intersection points between the fixed and the portable dosimeter readings result. It is interesting to note that during revolution 51 attitude control was exercised by the spacecraft so that yawing motion only was being executed by the spacecraft. These two curves clearly demonstrate that a degree of directionality definitely is associated with the radiation entering the Gemini spacecraft. At the time of this writing tumble rates and attitude data had not been analyzed in conjunction with the dosage measurements. These phenomena will be more thoroughly analyzed following the Gemini VI mission. At this time, however, it can safely be concluded that the radiation field had appreciable directionality associated with it at a number of different places in the anomaly region. Spectrometer measurements performed in this region indicate also the same results as concern the directional properties of the radiation flux.

The Gemini VI pilot performed the series of radiation surveys, at locations shown in Figures 13-4 through 13-9, during five separate orbits through the anomaly region. Only revolutions 8 and 52 have produced data available for analysis at this time. Figures 13-20 and 13-21 illustrate the results of the survey for revolutions 8 and 52, respectively. It is apparent that considerable reduction in the dose levels was resulted whenever the sensoring element was buried beneath but a few grams per square centimeter of material. As the spacecraft approached the anomaly region, the portable dosimeter indicated slightly higher dose levels than did the fixed base-line instrument. When the sensor was moved to the chest position, with the gloved hand covering the sensing element, a reduction in dose level of 50 percent was measured. Placement of the sensor at the groin and under the armpit lead to an even greater attenuation in the dose level. In these two areas the dose was reduced to one-third of the fixed dosimeter levels; with the sensor head placed in front of the window, the dose level was again reduced to approximately one-half of the base-line reading. The panel and floor areas dose rates were again only one-third of the hatch area values. During revolution 52 the hatch values of the dose were attenuated by approximately the same magnitude as they were on revolution 8 at the chest, groin, and armpit locations. However, the window, panel, and floor areas appear to have been somewhat less effective radiation attenuators than they were during the 8th pass. The survey of the window, panel, and floor areas were performed at the edge of the anomaly region where the radiation levels are so low, and so poorly defined, that a comparison between base-line data and the portable-dosimeter data

is very difficult to accomplish with high accuracy. The excellent
agreement is attenuation between the two orbits at the chest, groin,
and armpit which were performed deeper in the anomaly region; and
indicated, however, that orbits similar to revolution 8 would have pro-
duced the same attenuation in dose levels at the window, panel, and floor,
respectively. The radiation surveys to be performed during Gemini VI
mission will provide additional data in support of this mission. Tables
13-II and 13-III show the tabular values obtained at the various locations
of survey, compared to the base line or hatch readings at the same instant
in time for revolutions 8 and 52. The survey readings were taken 30 sec-
onds after the sensing element had been fixed in place at a given lo-
cation to make sure that equilibrium response had been reached there.

An integration of the dose rate for the Type I (fixed) baseline dosimeter was performed for all anomaly-region orbits during the Gemini IV mission.

Revolution Number	Integrated Dose, (millirads)
6	3.0
7	8.4
8	10.45
9	3.5
21	2.87
22	7.10
23	6.0*
24	3.0*
36	3.32
37	5.90
38	3.26
39	2.50
51	1.72
52	2.26
53	2.0*
54	2.0
Total millirads	67.28

*These data are not measured, but are extrapolated
from plots of revolutions of similar type.

The total integrated dose for the Gemini IV orbits is 67.28 millirads. The total extrapolated dose for other orbits near the fringe areas of the anomaly did not exceed 2.0 millirads. The Type V portable-dosimeter dose rates were not integrated because, during five passes through the anomaly region, surveys were being performed which obviously would have an appreciable effect on the dose readings.

Figure 13-22 illustrates an isodose mapping of the South Atlantic Anomaly for a 280-kilometer altitude for Gemini IV spacecraft. The

contours were mapped by taking the highest dose rate reading from either instrument. The isodose contours have their maximum values at 37° of west longitude and 32.5° south latitude. Revolutions 7 and 8 were thus shown to penetrate more deeply into the belt than did other orbits. Revolutions 22, 23, 37, 38, 52, and 53 follow a pattern resembling at least one of the revolutions shown in figure 13-22.

Comparison of data with computer code information.- One of the main objectives of the D-8 Experiment was to compare the dose rate measured by the active instruments with the dose rate predicted by the existing computer codes, in order to test the validity of the codes. Predicted dose rates were computed using the actual Gemini trajectories. Radiation flux maps compiled describing the radiation environment were utilized in conjunction with a 720-sector analysis of the Gemini spacecraft supplied by the spacecraft contractor describing the spacecraft shielding. Figures 13-23 and 13-24 show comparison of the measured dose rate with the anticipated electron and proton environment in the anomaly region during revolution 7. This measured dose rate is the average-dose reading of the two active instruments. It is evident from these curves that the dose rates are highly dependent on the proton component of the radiation belt and yet are fairly independent of the electron spectra at the same region in space. The data from the film emulsion flown in the passive portion of the experiment supports this conclusion. It is evident that the electron component could not have exceeded 5 percent of the total dose for the mission, which is consistent with the active results.

Initial theoretical predictions of the dose levels carried out with the computer code using the Vette grid provide dose values that are approximately three times in excess of the measured values for the Gemini anomaly orbits. Since these values depend on the flux map generated from the data gathered early in 1963, when the electron population was much greater than it was at the time of the Gemini IV flight, the present measured values would be expected to be much lower at the time of the Gemini IV mission.

The predicted proton dose rate is in fair agreement with the measured values. The difference could be due (1) to the low altitude of the Gemini orbit, or due (2) to the fact that the proton flux map used was generated from data gathered before September 1963: the proton population may have shifted slightly since then. Another experiment on the Gemini IV mission (MSC-2) was designed to measure particle fluxes and spectra external to the spacecraft. Simultaneous spectral measurements from this experiment will become available in the future, to allow the existing code to provide a more accurate prediction of the dose rate at Gemini altitudes and at other operational situations at still higher altitudes and under different known environmental conditions.

PASSIVE DOSIMETRY

Instrument Theory and Design

The five passive dosimetry packages* located in the spacecraft cabin were designed to ascertain both total accumulated dose and the intensity of radiation causing it. These packages, each including several passive dosimeters, were located at the maximum and minimum shielding locations shown in figure 13-25. Package 1 was mounted near the Type I active dosimeter to provide an empirical comparison between the dose measured by the passive unit, and the integrated dose; that is, the dose obtained by integrating the dose rate over the total measurement time. Three other passive units were located at points of intermediate shielding, and a fourth unit was placed on the debris guard beneath the instrument panel--an area of heavy shielding.

Since the experiment might have been adversely influenced by the contribution to ambient radiation levels from sources carried aboard the spacecraft, the three on-board radiation sources were investigated for possible significant effects.

The strongest of these, a 0.9 millicurie Amerecium 241 source, is located in the carbon-dioxide monitoring systems between and under the two seats. Although the shielding on the source was sufficient to stop all α-particle emission, the soft 60 keV γ component emanating from the Americium was not attenuated enough to make its effect negligible to the experiment measurements. Three experimental dose-rate measurements extending from the surface out to 10 centimeters were made, in addition to a theoretical estimate of the total emission of the 60-keV γ-rays at distances greater than 10 cm. The evaluation of the dose rate delivered by the Americium considered only air attenuation and did not take into account the shielding provided by the seats and equipment located between the source and the nearest PDX unit. This dose rate, shown in figure 13-26, is therefore an upper limit.

The dose rate at the surface of the luminous-dial watches worn by the crew was measured and found to be less than 0.1 millirad/hr. Since dose rate varies inversely as the square of the distance, the fact that no dosimeter in the cabin is closer to a wristwatch than several inches, indicates that radiation from this source is negligible.

---

*These packages are occasionally referred to as PDX units

The third possible significant radiation source was located some distance behind the ablation shield in the adapter section. It includes in those elements of the adapter section containing thoriated magnesium, which is slightly radioactive. As the combination of shielding and distance for this source made its radiation extremely weak, no attempt was made to measure the dose rate delivered by this source alone.

The total contribution of all radiation sources in the spacecraft cabin was measured by five passive dosimeters placed aboard the craft at Cape Kennedy for the 31-hour simulated, wet mock countdown period. Launch area radiation control was in effect at this time, and the measurements made on the passive units are a good indication of the cabin-ambient radiation level. These measurements indicated an ambient dose rate of less than one millirad/day, including the dose delivered by radiation and of sufficient energy to penetrate the spacecraft cabin.

From the above radiation measurements it was determined that nearly all of the background radiation aboard the capsule was cosmic. For this reason, no corrections were applied to on-board sources, although ground-control background readings were subtracted from the data.

The ground-level ambient dose was measured by a calcium fluoride dosimeter for the 14 days between its preparation and evaluation. The dose for that period was found to be 12.9 ±1.2 millirads. This error estimate is not absolute, but represents a standard deviation.

The five flight units and the ground control were assembled and placed in a shielded aluminum container. They remained together there until 26 hours before launch, when the flight items were removed for installation in the spacecraft. Extremely rigid controls governing the location of all radiation sources in the launch area were put into effect to avoid any undesired exposure of the dosimeters, some of which are capable of detecting radiation doses as low as 3 millirads. The ground control unit was separated from the flight units for 11 hours after splashdown as well as for the 26 hours before launch. It was carried to the Manned Spacecraft Center immediately after launch, and it was reunited with the flight units after splashdown and immediately returned with the flight units to the Air Force Weapons Laboratory for evaluation. All dosimeters had previously been checked for reproducibility, for absolute accuracy, and for dose fading.

Two types of photoluminescent glass dosimeters were selected for Experiment D8. One - the "glass needle" system - employs twelve very small, lightweight glass needles which are sensitive to radiation. Although such a dosimeter is not very sensitive (maximum sensitivity $\cong 1$ rad), it was still included because it requires very little space and produces no weight problems. It was flown in the package on the left

hatch, its pre-dose having been previously determined. Its readings were not statistically significant, and could not be distinguished from those of the ground-control needles.

The second photoluminescent-glass dosimetry system, the Toshiba Glass system, is extremely sensitive and can read doses as low as 25 millirads. Two Toshiba Glass units were flown; one shielded, the other unshielded. The shielded system was enclosed by a lucite shield 0.794cm thick, and by a lead shield 0.0111cm thick. This combination produced a total shielding thickness for the Toshiba Glass units of 112 mg/cm^2. Currently the Toshiba Glass dosimetry system finds extensive use at the Naval Radiation Defense Laboratory in San Francisco. This laboratory supplied and evaluated four of the dosimeters for the Air Force Weapons Laboratory (AFWL). Subtraction of the ground-control data was performed at the AFWL. The self-shielding of each Toshiba Glass dosimeter within the pack cannot be neglected, as each "unshielded" unit was surrounded on three sides by emulsion packs, and on a fourth by the pocket ionization chamber. The low readings registered on the Toshiba Glass are in all likelihood results of this shielding.

Several lithium fluoride dosimeters were flown, each dosimeter including a small teflon cylinder with a minimum thickness 0.22 gm/cm^2 and filled with powdered lithium fluoride. Such a dosimeter is capable of measuring dosages down to 10 millirads with an error of ±40%; its accuracy increases with the dose. About 6% of the powder contains the lithium isotope Li_6 and will respond to ionizing radiation and to neutrons. Since the other isotope of lithium in this compound, Li_7, has practically no neutron cross-section, the difference between the readings obtained on these two isotopes can be used to determine the neutron-radiation component within the spacecraft cabin. The feasibility of this approach was tested in the fission spectrum of a pulsed neutron reactor located at Albuquerque, New Mexico, and was found to be true for this experiment.

Comparison of the Gemini IV data from each isotope indicates that, within the limits of the experimental error, no neutron dose occurred. This result is reasonable in that the only neutron expected would come from secondary radiation produced by interaction of the high energy protons with the spacecraft and its occupants. Analysis of the activation foils discussed in the next paragraph further substantiates the lithium-fluoride results.

A complete set of activation foils was included also in the passive dosimetry packages and for the purpose of determining the presence, or the absence, of neutrons. These foils were chosen for detection of neutrons over a wide range of energies, including thermal energies; they were made of zirconium, sulfur, tantalum, gold, cobalt, and

aluminum, respectively. None of these foils indicated the presence of neutrons during the Gemini IV mission.

A film emulsion pack was supplied and is being evaluated by the Naval School of Aviation Medicine in Pensecola, Florida. Although this work is not yet complete, the particle tracks in the emulsion are over 95 percent protons with only residual electron, alpha, and heavy particle tracks. Less than 2 millirads of dose was caused by particles other than protons.

An exploded view of the passive dosimetry packages flown is shown in figure 13-27. A summary of the passive dosimetry results is presented in table 13-IV.

Temperature Dependence

Since many of the dosimeters flown were to some extent temperature dependent in their response and in dose fading, a temperature profile of the hatch area was obtained from data gathered in the Type-I active ionization chamber. Temperatures at the other four locations in which passive dosimeter packs were located are not expected to differ significantly. The extremes in temperatures were never more than two degrees on either side of the mean, and were usually much less. At present, temperature profiles are available only for those revolutions listed.

Gemini IV Temperature Profiles on Left Hatch

Revolution	Mean Temperature Degrees (^{O}C)
6	22.6
7	23.8
8	23.8
21	20.9
22	20.9
36	20.4
37	20.9
38	20.4
45	20.9
50	26.2
51	25.6
52	25.0

CONCLUSION

Both passive and active dosimetry data show without doubt that no radiation hazard is associated with manned space operations within the Gemini spacecraft at the altitudes of concern. This conclusion is borne out also by theoretical calculations, and has been verified by the measurements carried out on the Gemini IV mission. However, due to the rather high interior dose rates received during several of the anomaly region passes, it appears that limited hazard to biological systems might be realized at considerably higher altitudes during long or extended operations with shielding similar to that of the Gemini spacecraft.

The agreement between the active and passive dosimeters proved to be even better than had at first been anticipated. The differences between the integrated dose readings of the tissue-equivalent ionization chamber and the passive dosimeter in the same area of the left hatch ranged from 30% for the thermoluminescent devices, to but 12% for the discharge ionization chamber. The differences in the dose readings that do occur between the passive and the active instruments results from the tissue dose responding to protons of the thermoluminescent devices. The tissue-equivalent ionization chambers provide, for example, a response to the spectrum of corpuscular radiation of the type encountered on the Gemini mission; that is, to less than 3 percent deviation from the standard-tissue response to the same radiation. The calcium, however, responds to radiation of the type encountered at values from 18 to 32 percent below those of the tissue response. Intricate differences in the shielding interposed between the various passive devices was also somewhat greater than the shielding surrounding the ionizing cavities of the two active dosimeters. A variation in the shielding in both the active and passive dosimeters will be accomplished on Gemini VI mission. This variation will allow suitable correction factors for the passive devices so that they can provide a more reliable assessment of the radiation dose on future space missions.

Another extremely valuable achievement in this effort has been the development of flight-qualified space-dosimetry instrumentation packages the feasibility of operation of which has signaled their adaptation to a variety of other types of satellite, where they can provide adequate and instantaneous warning in the event of an onset of radiation hazards due to unexpected or unpredicted radiation environments.

TABLE 13-I - DOSE RATES OF COSMIC RADIATION FOR SPECIFIC REVOLUTIONS

OF GEMINI IV OUTSIDE OF THE SOUTH AMERICAN ANOMALY REGION

Revolution number	Average dose rate, millirad/hour	Maximum observed dose rate	Minimum observed dose rate
1	.25	.65	.1
2	.25	.64	.1
3	.20	.30	.1
14	.15	.30	.1
15	.15	.30	.1
16	.18	.30	.1
17	.15	.30	.1
18	.22	.50	.1
29	.12	.45	.1
30	.18	.40	.1
31	.12	.50	.1
32	.12	.30	.1
44	.15	.30	.1
45	.12	.40	.1
46	.12	.30	.1
48	.15	.30	.1
59	.10	.15	.1
60	.10	.10	.1
61	.10	.10	.1

TABLE 13-II – CABIN RADIATION DOSAGES DURING REVOLUTION 8

(All dose rate levels in millirad/hour)

Location	Portable Dose Rate	Fixed Base Line Dose Rate
Chest	27	58
Groin	30	100
Armpit	36	105
Window	50	100
Panel	30	90
Floor	15	45

TABLE 13-III - CABIN RADIATION DOSAGES DURING REVOLUTION 52

(All dose rate levels in millirad/hour)

Location	Portable Dose Rate	Fixed Base Line Dose Rate
Chest	15	29
Groin	9	27
Armpit	6	14
Window	9	12
Panel	6	9
Floor	2.2	4.5

TABLE 13-IV.- PRELIMINARY SUMMARY OF THE PASSIVE-DOSIMETRY

RESULTS[1] ABOARD GEMINI IV SPACECRAFT

	1	2	3	4	5
LiF	50 ±10(Li^6)	52.5±19.5(Li^7)	44 ±19(Li^6) / 43 ±12(Li^7)	50 ±14(Li^7)	53 ±18(Li^6) / 59 ±14(Li^7)
CaF_2 unshielded	54.7±7.0	49.4±6.1	55.3±5.4	57.9±6.5	49.4±4.7
CaF_2 unshielded		47.1±4.1		55.7±5.1	
CaF_2 shielded	53.6±5.7	48.9±3.8	49.0±3.8	55.9±5.9	48.5±6.1
Pocket ionization Chamber	73 ±5.1	45 ± 2.3	46 ±3.2	54 ±3.8	47 ±3.3
Toshiba glass[2] unshielded	52 ± 23	27 ± 15	42 ± 20		37 ± 18
shielded	37 ± 18	17 ± 12	37 ± 18		12 ± 10
Emulsion[3]	68				35

[1] With the exception of the emulsion, all readings in this table are in milliroentgens equivalent exposure.

[2] The Toshiba glass was calibrated using Co^{60}; all other calibrations used Cs^{137}.

[3] The emulsion readings are in millirads and are based on preliminary grain counting. The error is probably less than 5 percent.
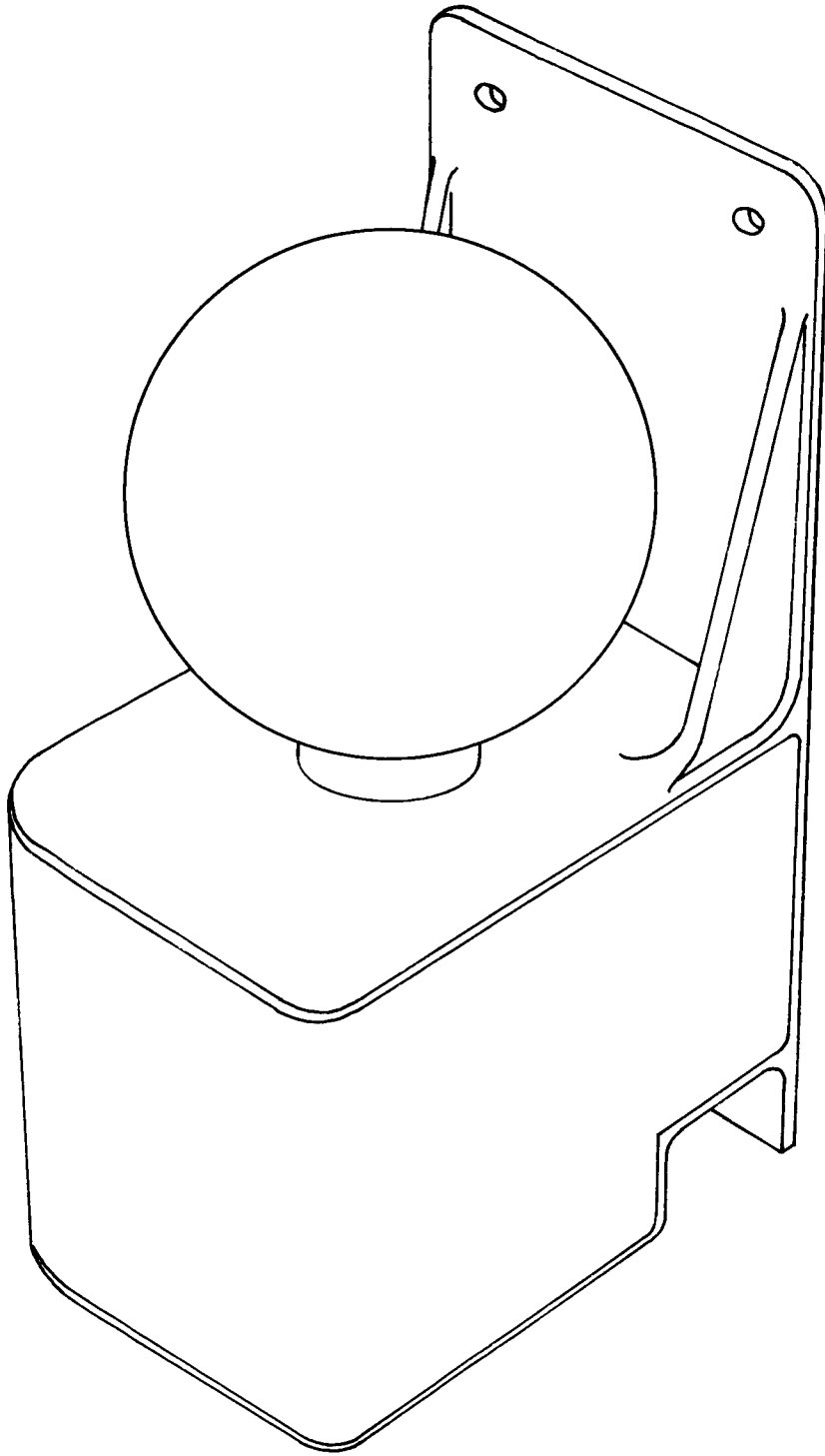
Figure 13-1.- Type I active ionization chamber.
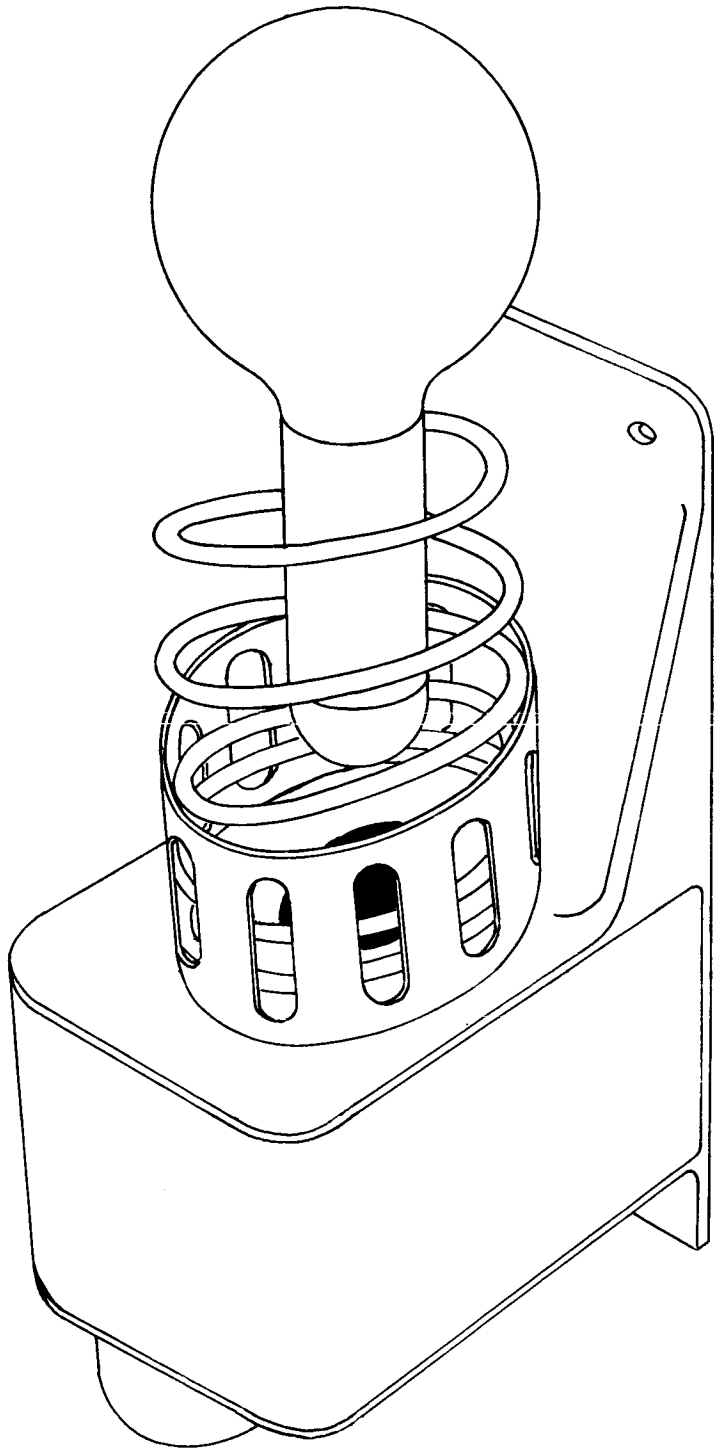
Figure 13-2. - Type V portable ionization chamber.
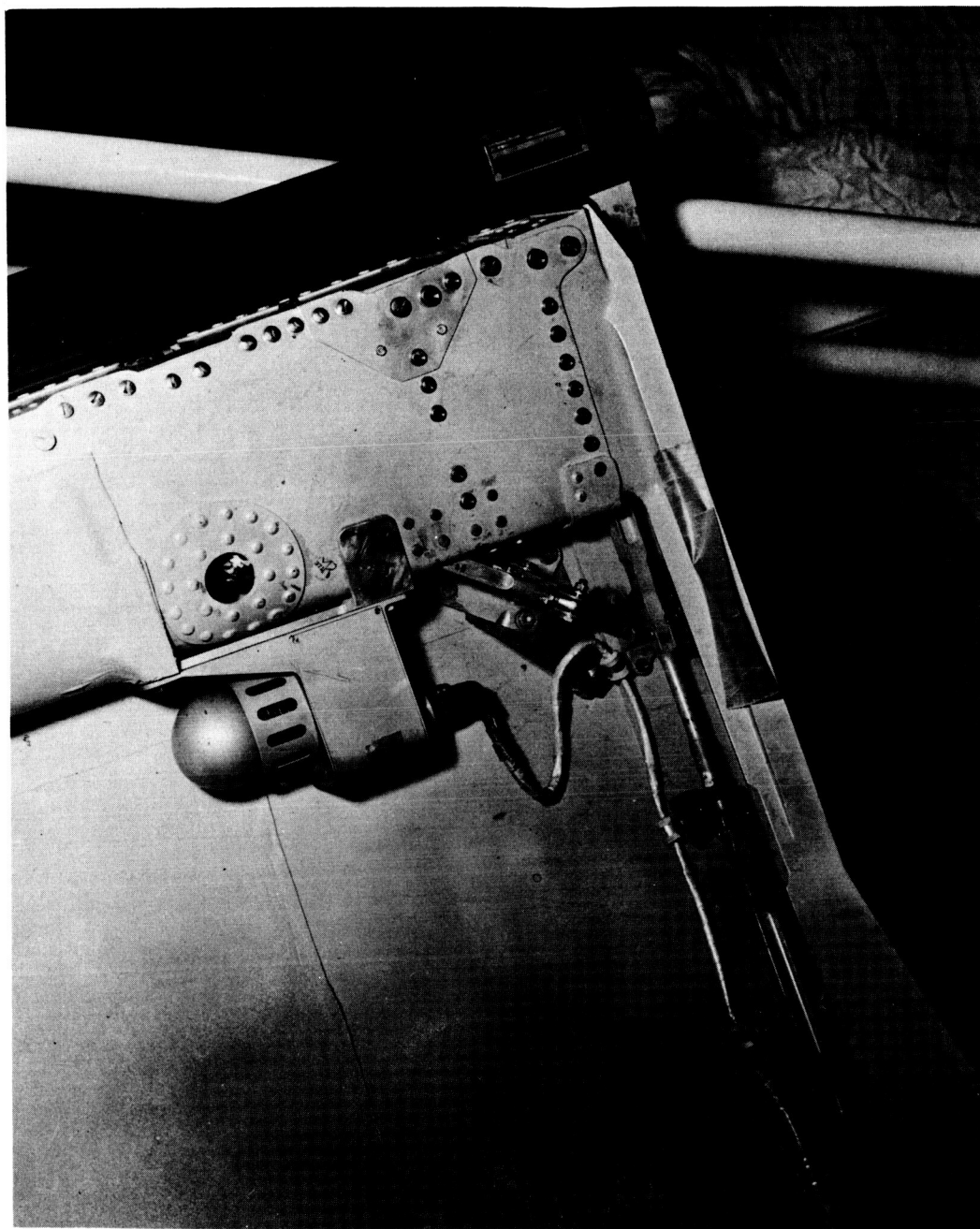
Figure 13-3. - Portable ionization chamber in position.

Figure 13-4.- Portable ionization chamber against chest and glove-covered.

Figure 13-5.- Portable ionization chamber between legs, groin area.

Figure 13-6.- Portable ionization chamber under left armpit.

Figure 13-7.- Portable ionization chamber before cabin window.

Figure 13-8.- Portable ionization chamber centered before
instrument panel.

Figure 13-9.- Portable ionization chamber on floor between feet.
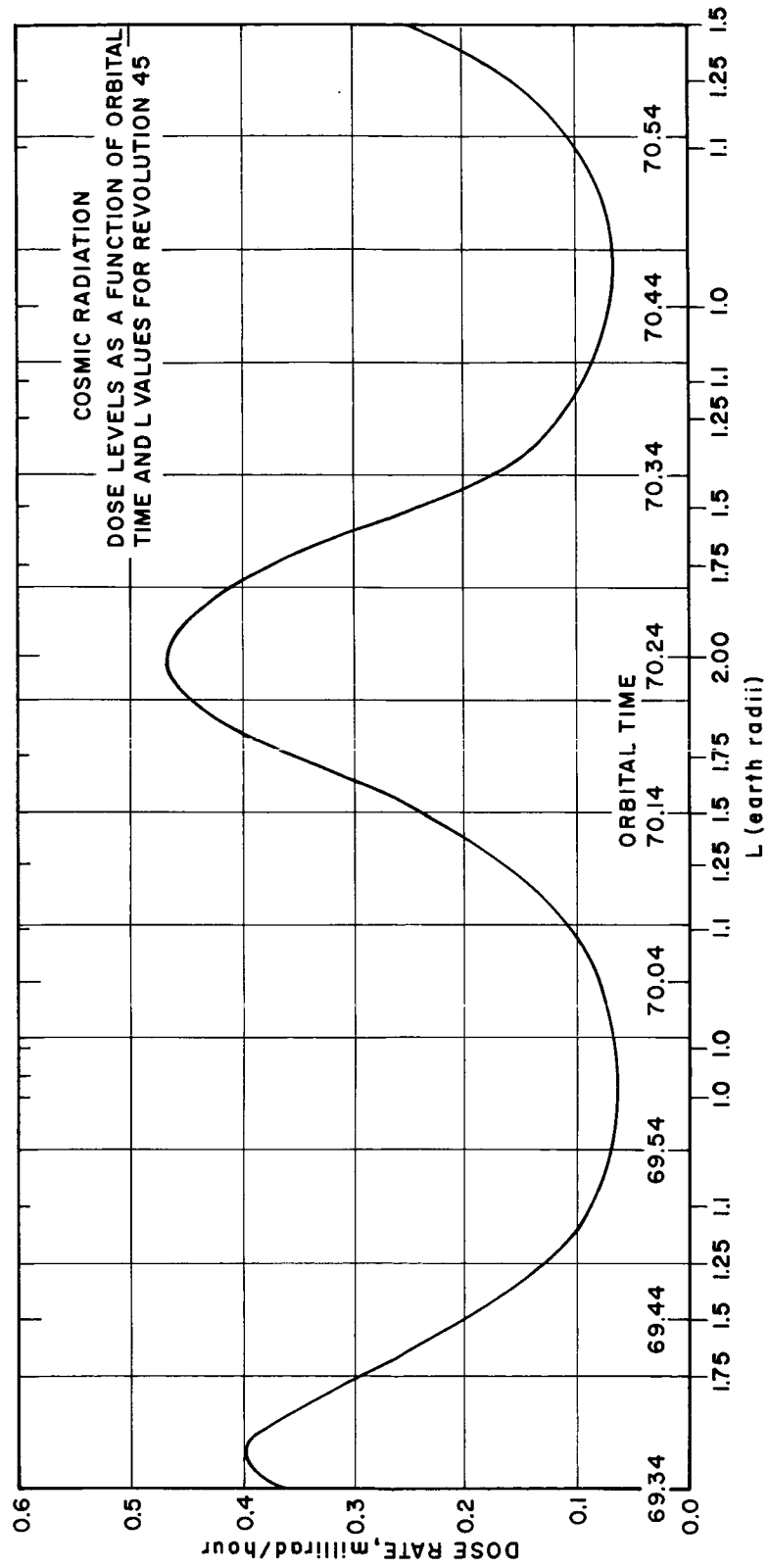
Figure 13-10.- Cosmic radiation dose levels as a function of orbital time and L values for revolution 45.
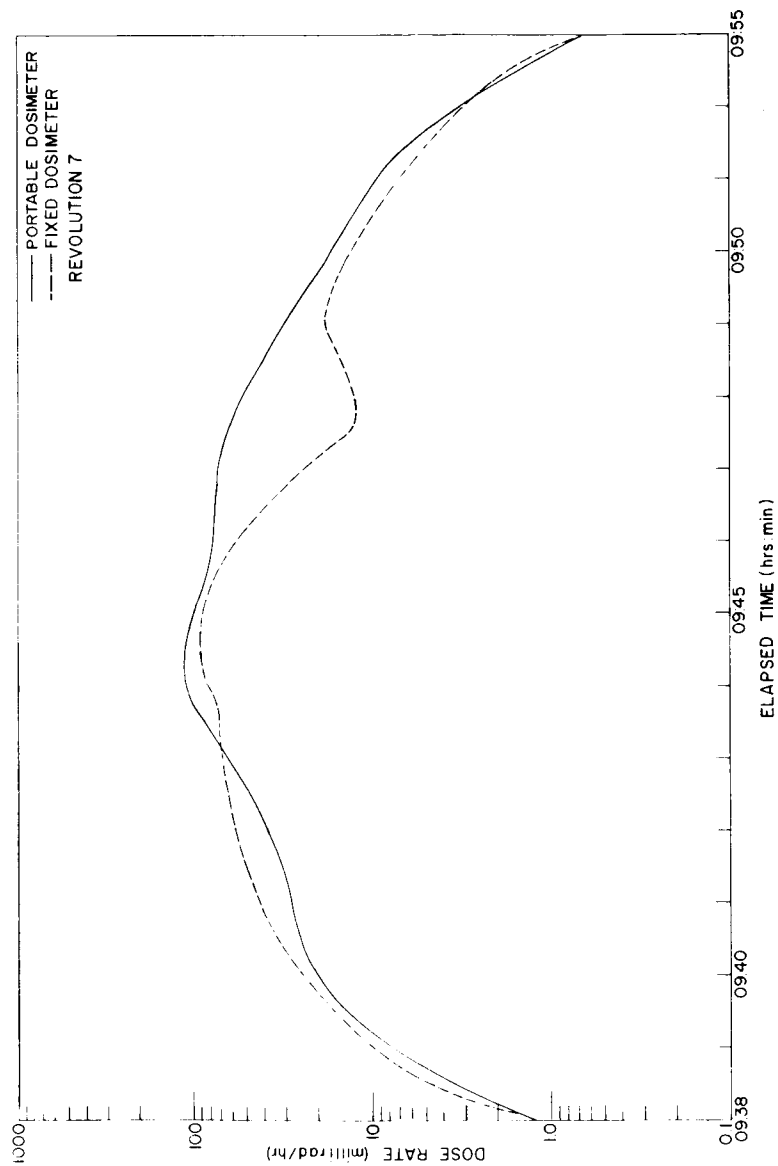
Figure 13-11. - Instantaneous dose rate, revolution 7.
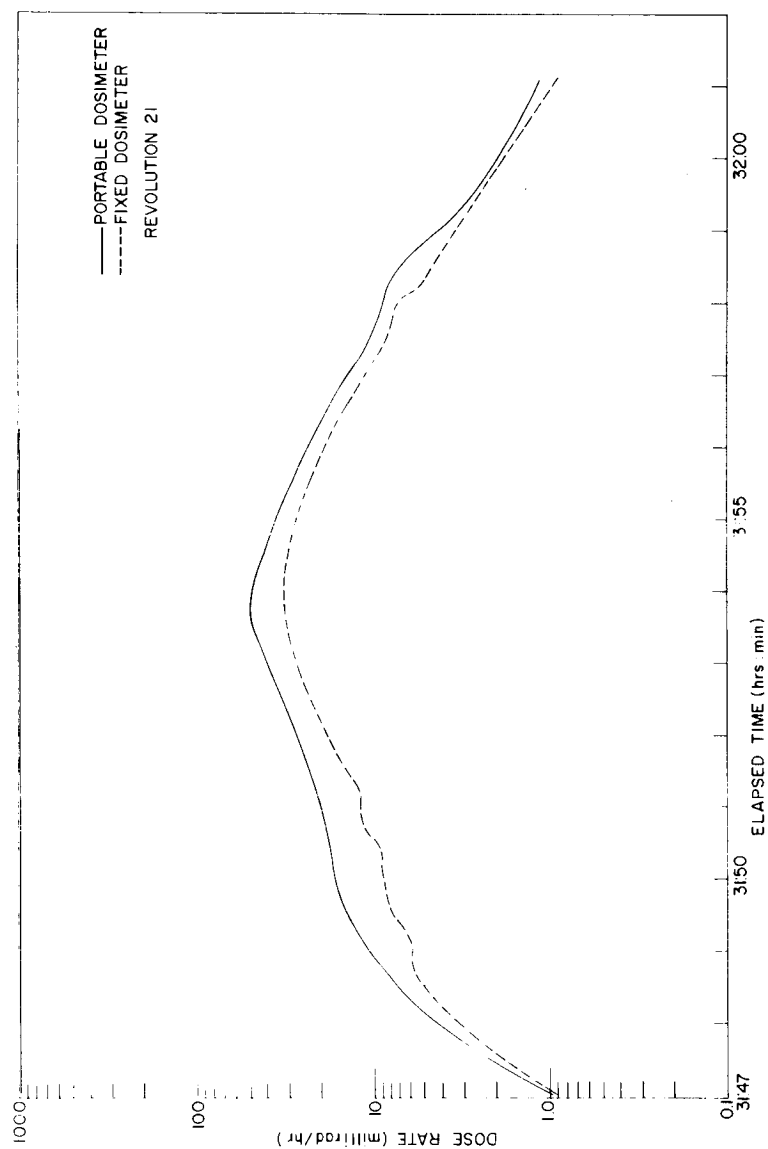
Figure 13-12.- Instantaneous dose rate, revolution 21.
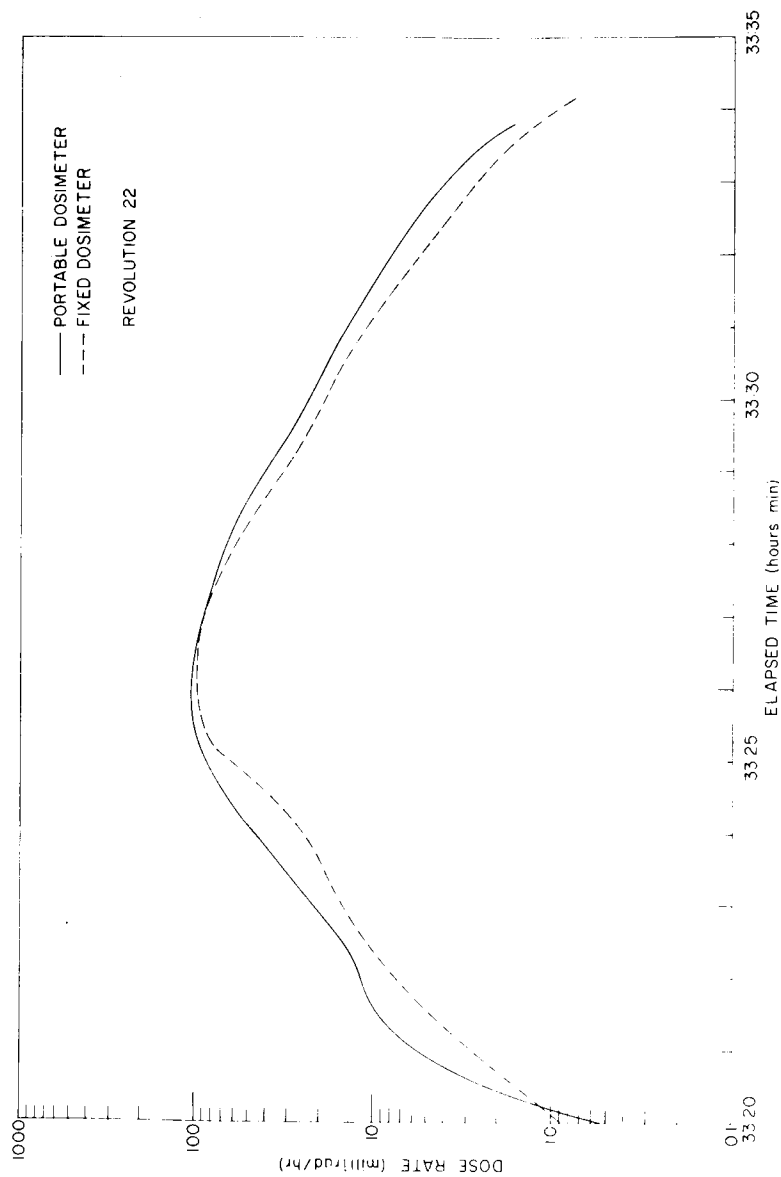
Figure 13-13.- Instantaneous dose rate, revolution 22.
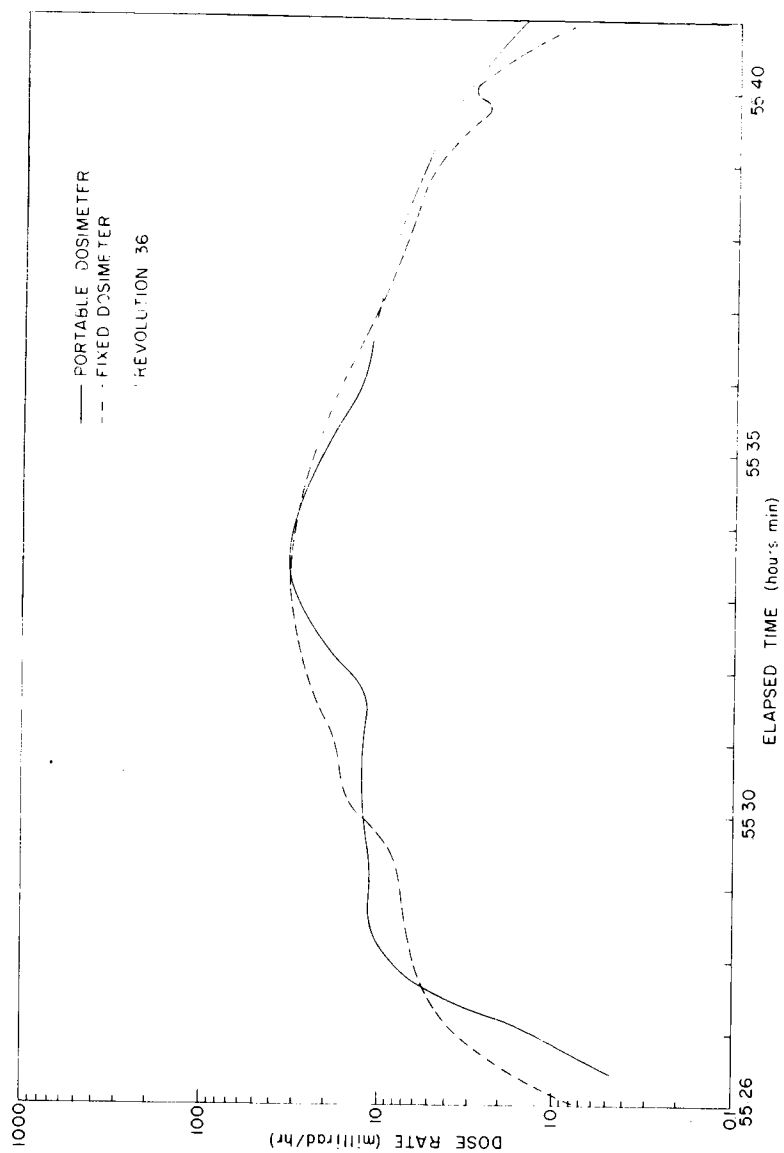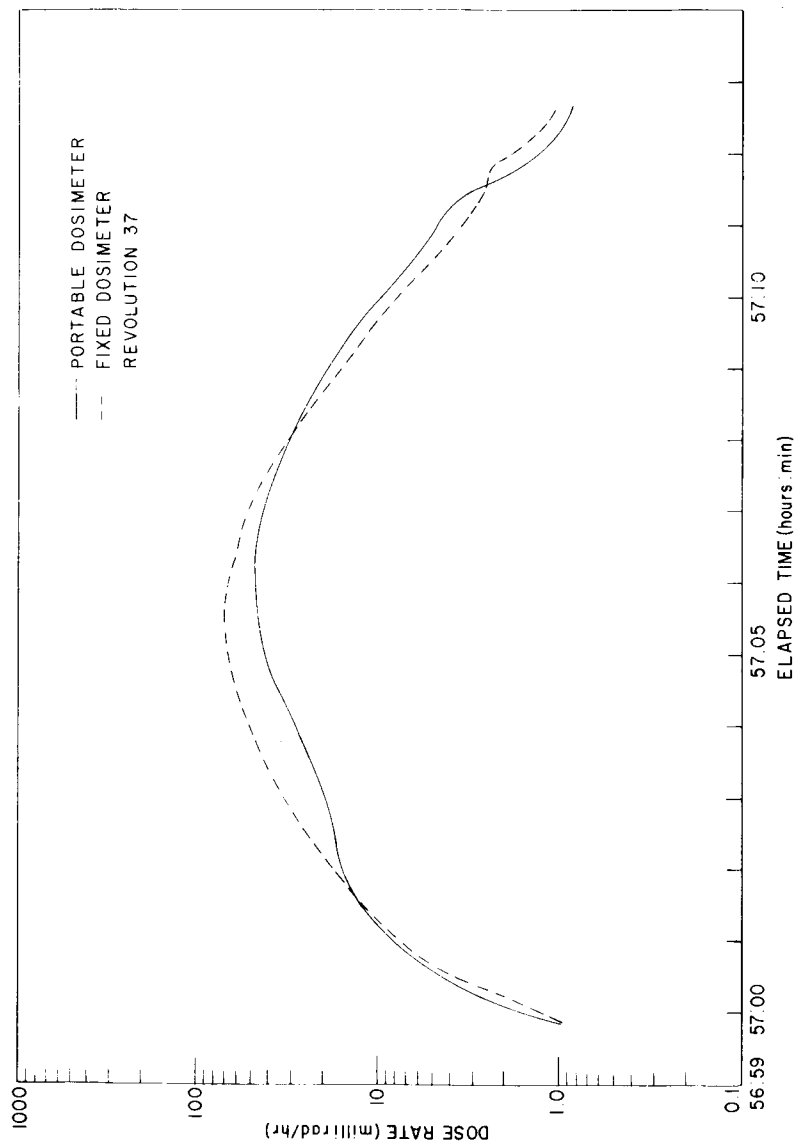
Figure 13-14.- Instantaneous dose rate, revolution 36.

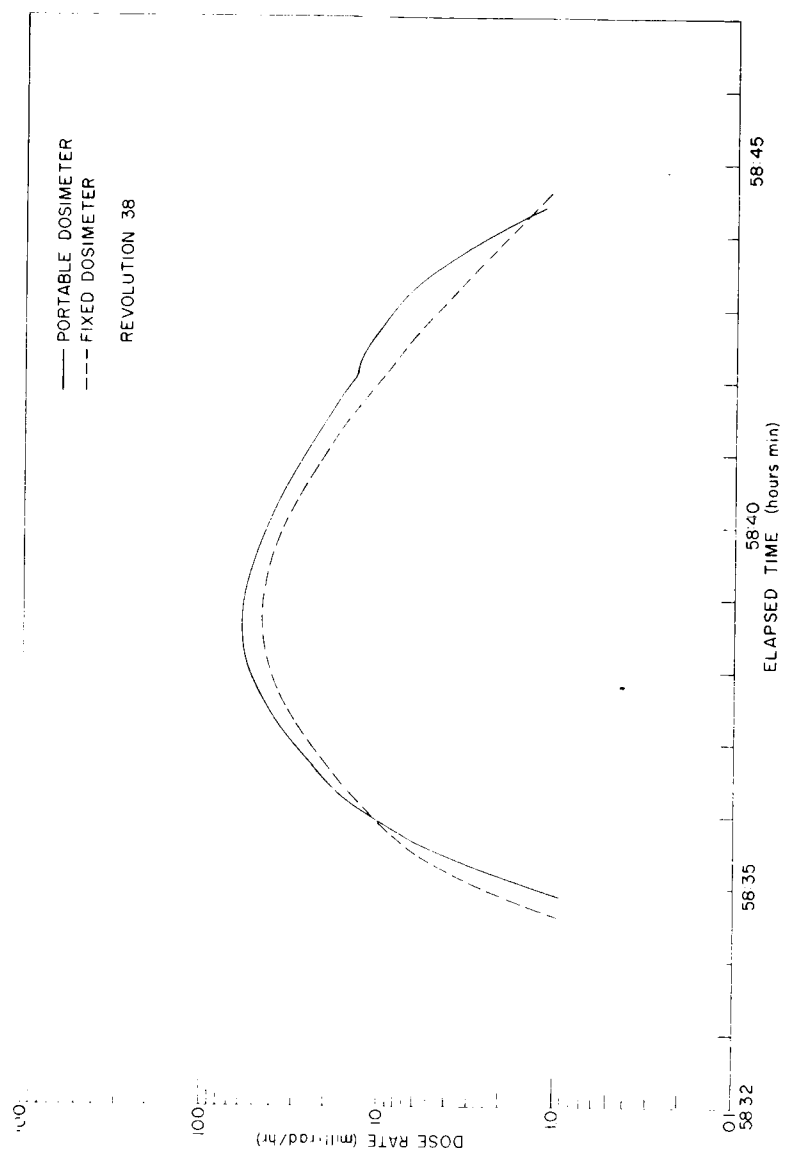Figure 13-15.— Instantaneous dose rate, revolution 37.

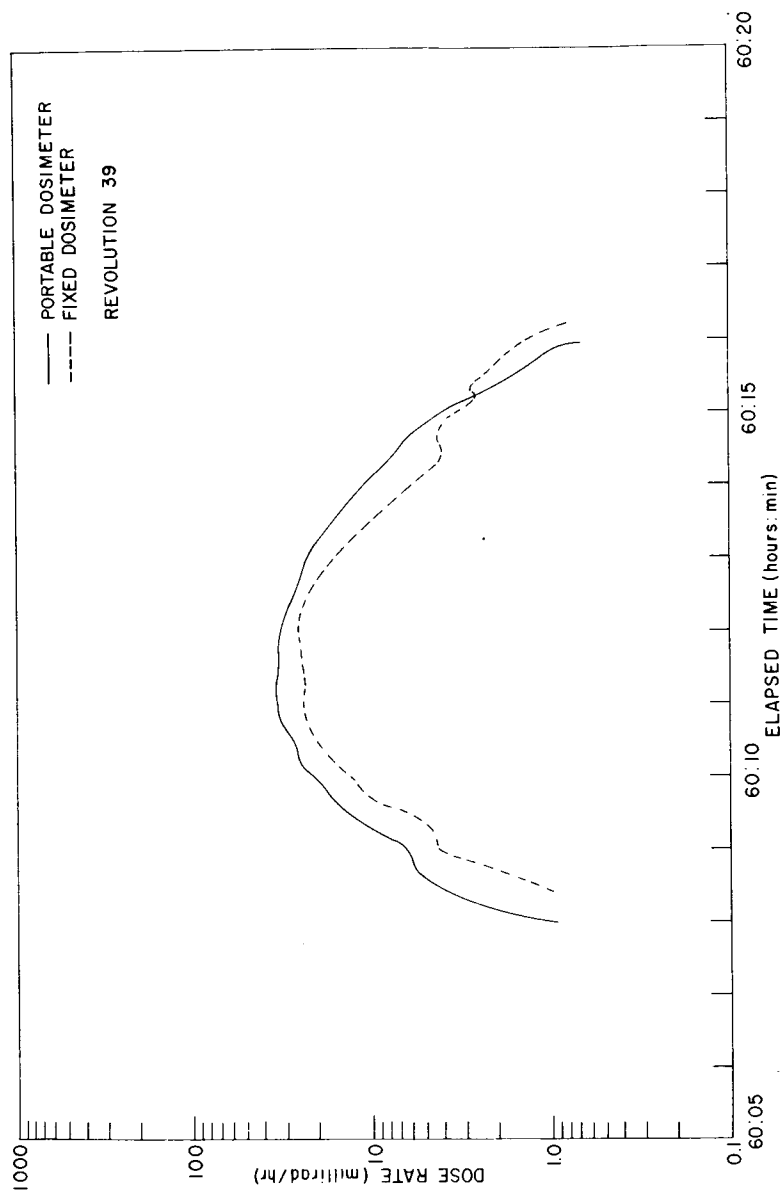Figure 13-16. - Instantaneous dose rate, revolution 38.
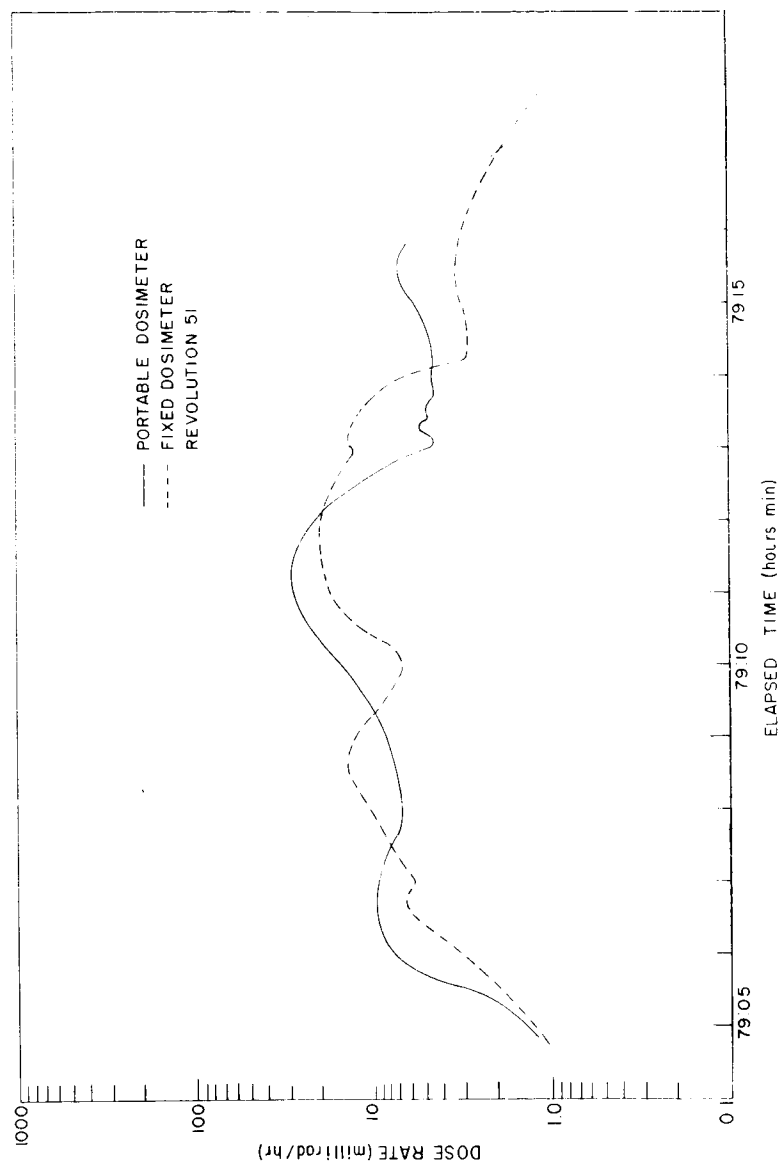
Figure 13-17.- Instantaneous dose rate, revolution 39.

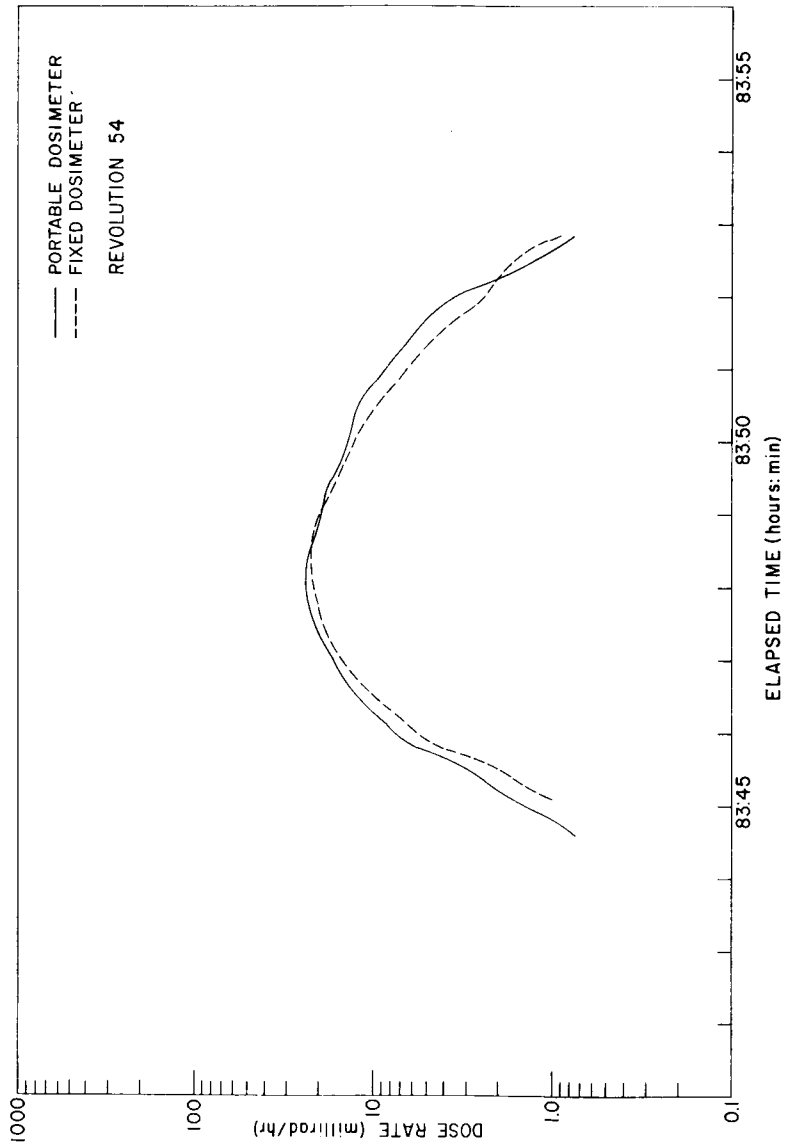Figure 13-18.- Instantaneous dose rate, revolution 51.

Figure 13-19.- Instantaneous dose rate, revolution 54.
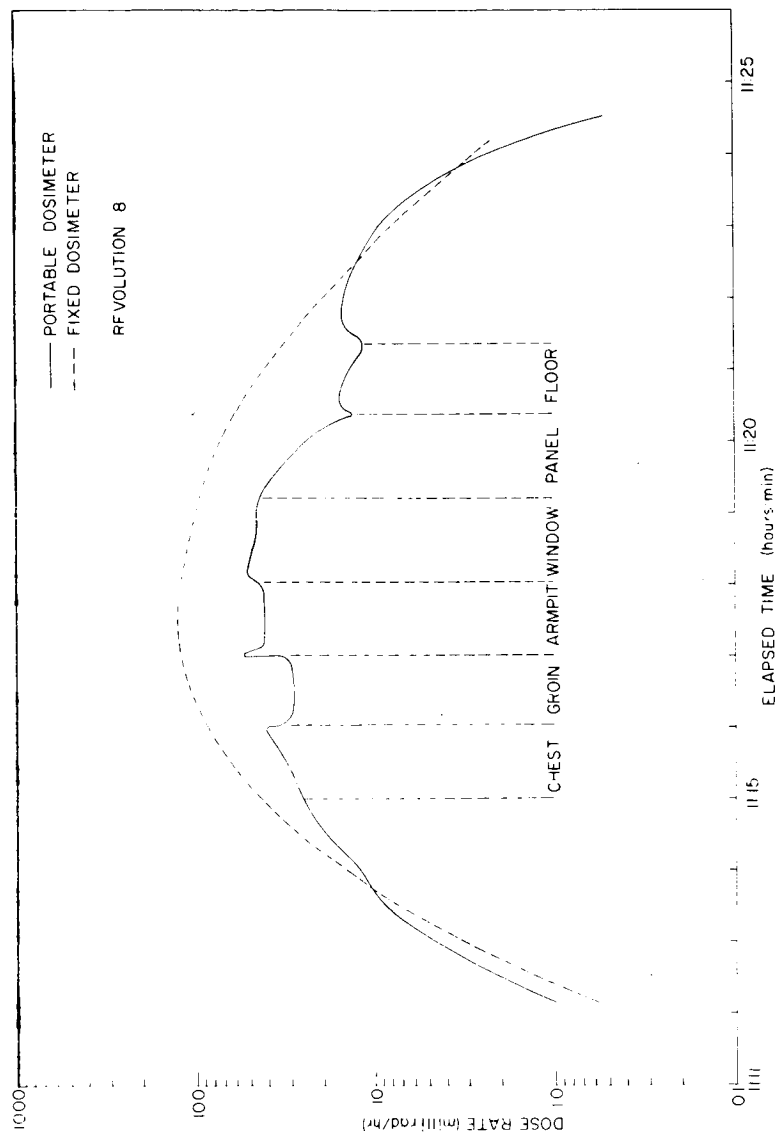
209

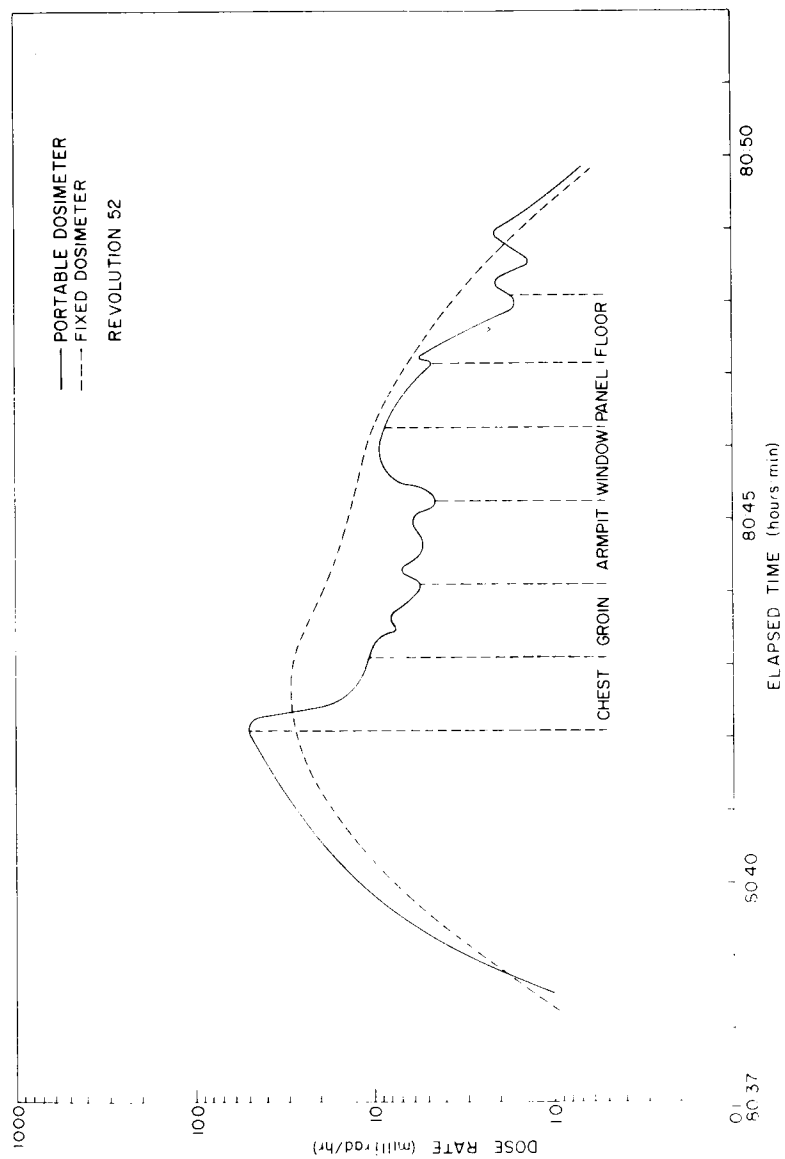Figure 13-20.- Radiation survey, revolution 8.

Figure 13-21.- Radiation survey, revolution 52.
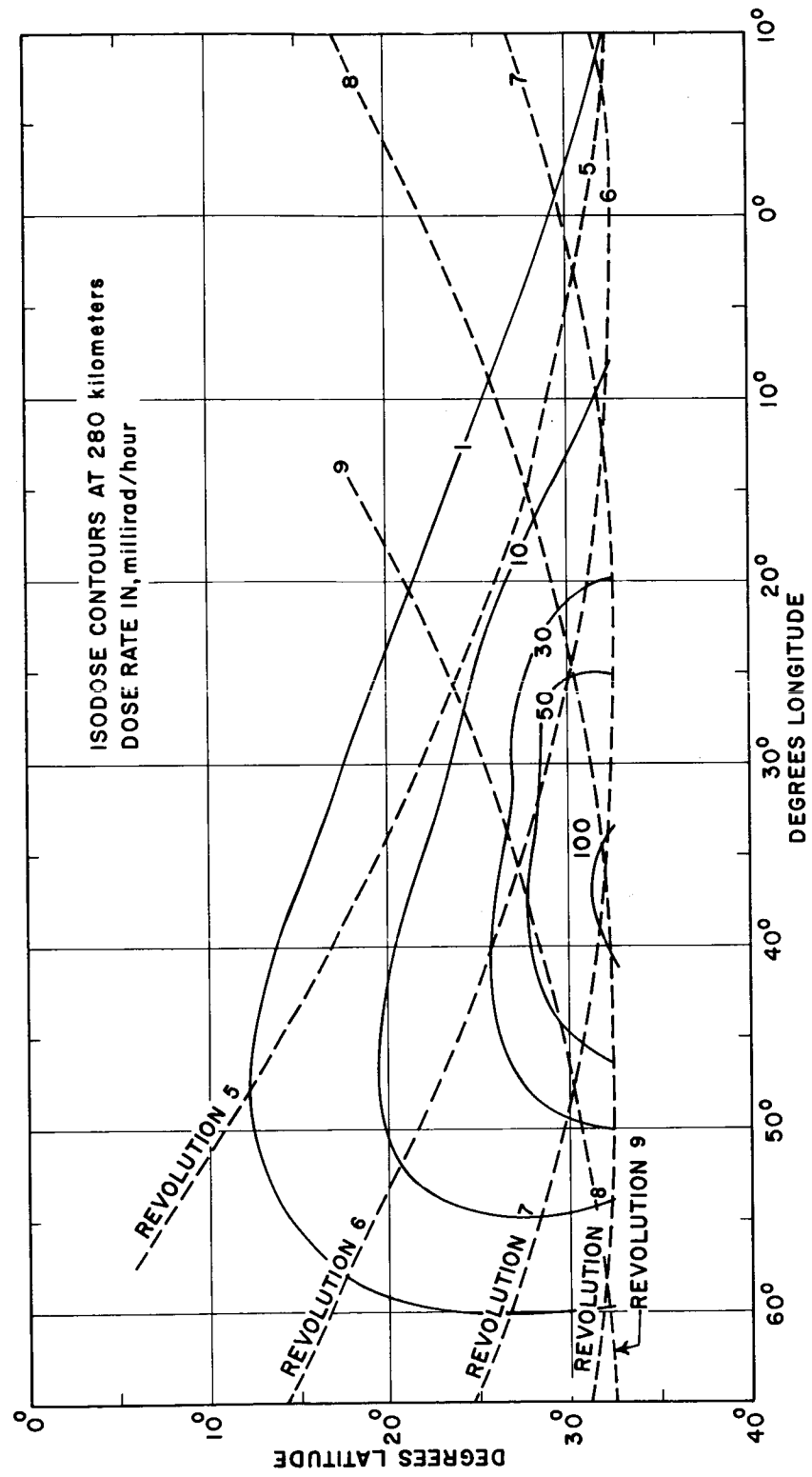
Figure 13-22.- Isodose contours at 280 kilometers.
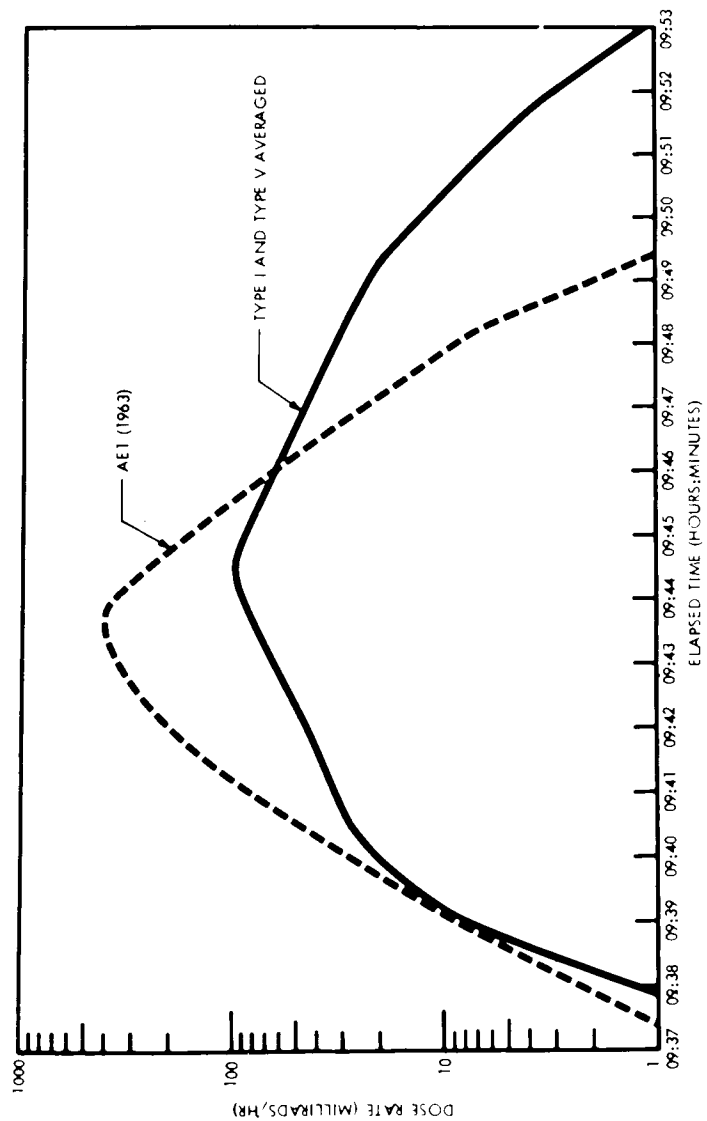
Figure 13-23. - Comparison of dose rate profiles with electron spectrum.
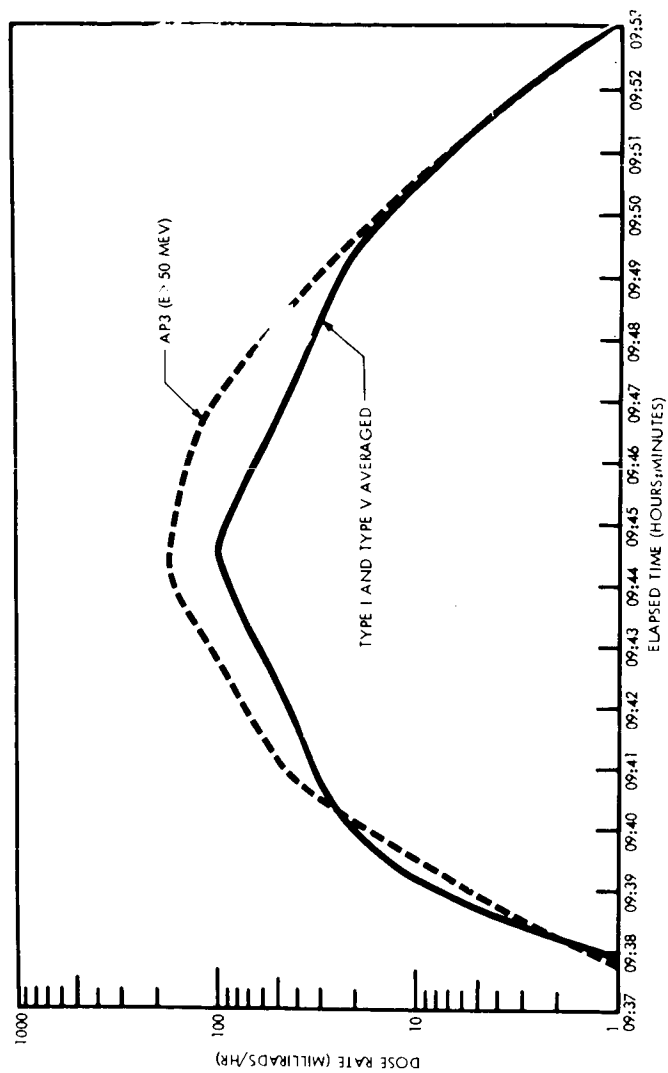
Figure 13-24. - Comparison of dose rate profiles with proton spectrum.

TYPE I ACTIVE DOSIMETER

NEAR ACTIVE DOSIMETER

ACTIVE DOSIMETER

TYPE I

TYPE V

NEAR ACTIVE DOSIMETER

RIGHT HAND CIRCUIT
BREAKER SWITCH
PANEL

IMMEDIATELY
LEFT OF SEAT

NEAR ABORT
HANDLE

ON DEBRIS
GUARD

PDX – PASSIVE DOSIMETER UNIT

SIDE VIEW

FRONT VIEW
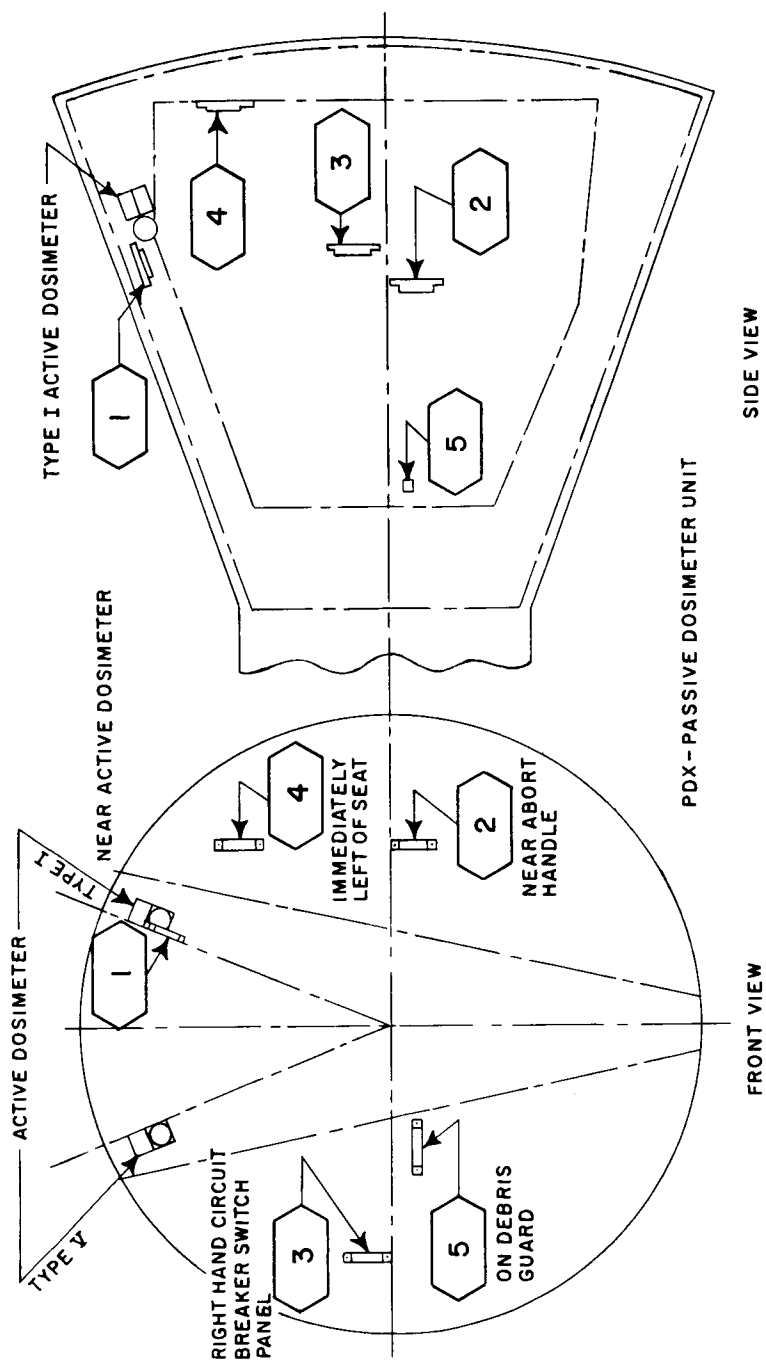
Figure 13-25.- Passive dosimeter locations in spacecraft.
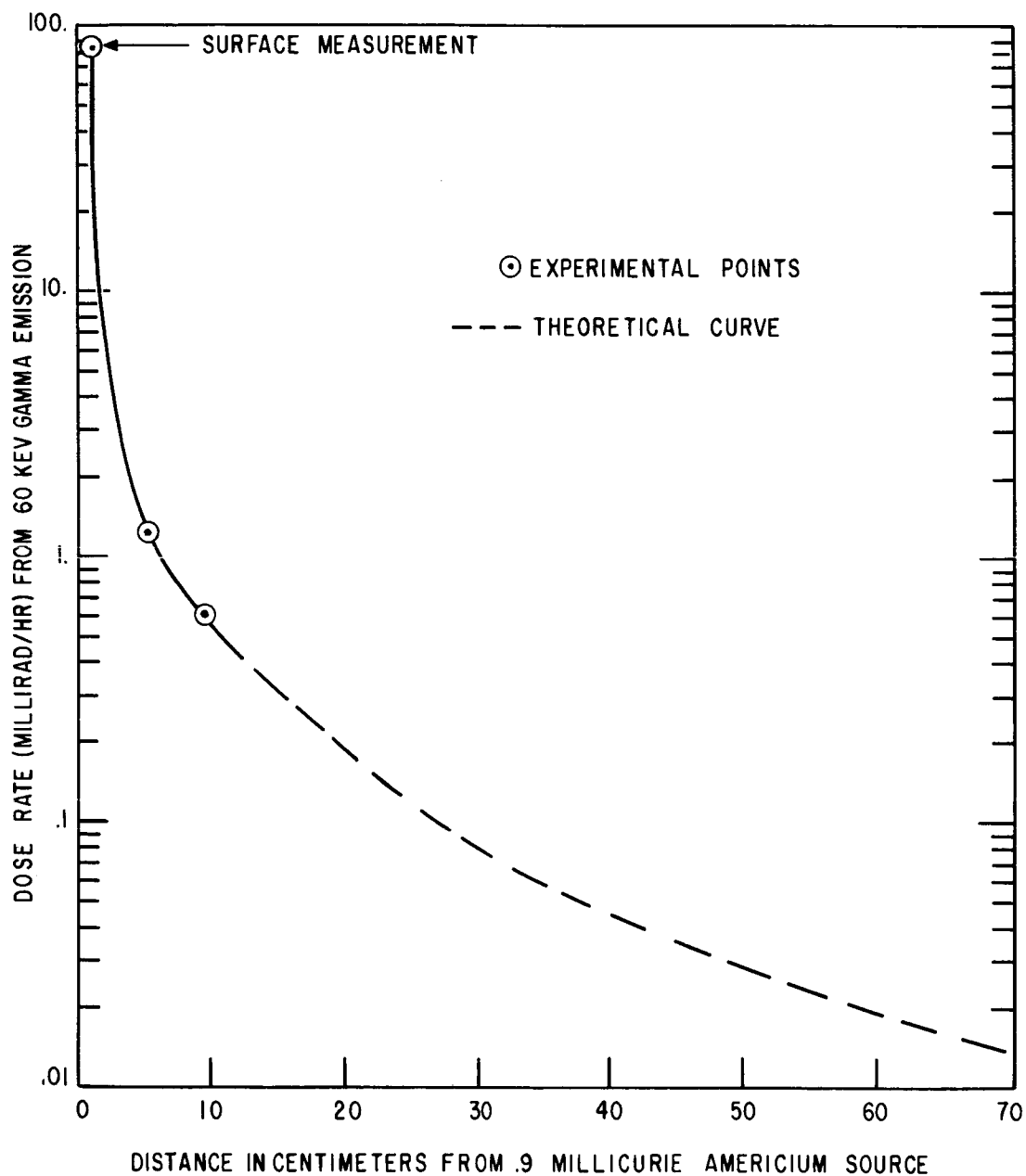
Figure 13-26.- Distance in centimeters from 0.9 millicurie Americium source.

ALUMINUM HOUSING

GLASS NEEDLES IN
TEFLON CAPSULE

FILM EMULSION PACKS

POCKET IONIZATION
CHAMBER

UNSHIELDED CaF$_2$
DOSIMETER

CADMIUM COVERED
GOLD

ACTIVATION FOILS

SULPHUR

ZIRCONIUM

TANTALUM

SHIELDED CaF$_2$
DOSIMETER

GOLD

LiF CAPSULES

COBALT

ALUMINUM

SHIELDED TOSHIBA
GLASS

UNSHIELDED TOSHIBA
GLASS

Figure 13-27.- Exploded view of passive dosimeter.

14. EXPERIMENT S-4, ZERO g AND RADIATION ON BLOOD DURING GEMINI III

By Michael A Bender, P. Carolyn Gooch, and Sohei Kondo*
Oak Ridge National Laboratory
Oak Ridge, Tennessee

SUMMARY

The S-4 experiment, "Synergistic Effect of Zero-g and Radiation on White Blood Cells", was performed during the Gemini III manned space flight under interagency agreement between the National Aeronautics and Space Administration and the U. S.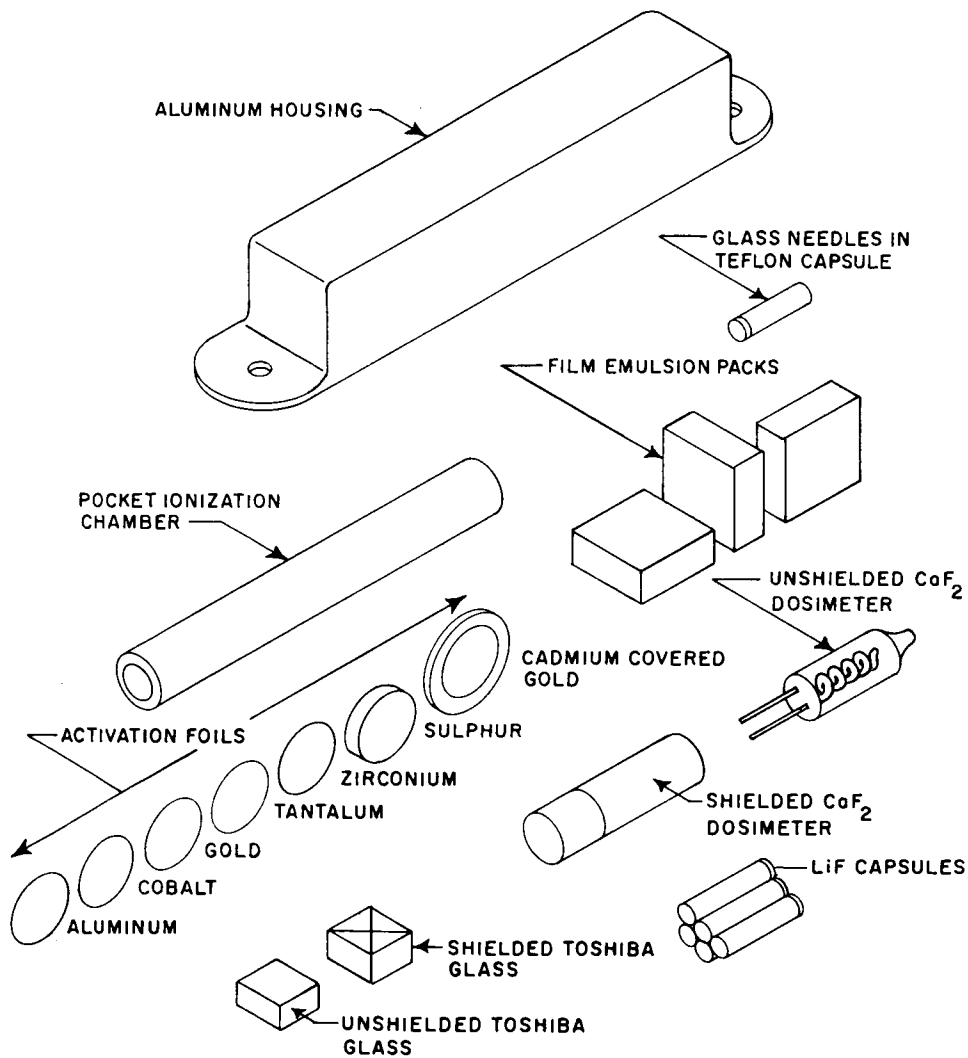 Atomic Energy Commission. Design, fabrication, and testing of the experimental hardware was done by the Oak Ridge Y-12 Plant, while isotope preparation and biological work was done at the Oak Ridge National Laboratory.

The experiment consisted of the simultaneous irradiation of a series of samples of whole, human blood with ^{32}P β-rays during the orbital phase of the mission. Irradiation was accomplished by identical experimental devices, one located on the righthand hatch of the spacecraft; the other, on the ground at the launch site. Upon completion of the mission, a cytogenetic analysis was made of each blood sample, and the frequencies of chromosome aberrations were determined. The yields of both single- and multiple-break aberrations were calculated both for the flight and for the ground-control portions of the experiment. Comparison of the results showed that while there was no significant difference between the yields of multiple-break aberrations, the frequency of single-break aberrations was significantly higher in the flight samples. Several lines of evidence rule out the possibility that this difference arose from differences in absorbed dose, temperature, oxygen tension, or other parameters known to influence chromosome aberration yields. That the space flight by itself induced aberrations is ruled out by the experiment control-blood samples and also by preflight and postflight blood samples obtained from the flight crew. A synergism between radiation and some space flight parameter thus appears to exist for human-chromosome aberration production. It appears likely that this effect is on the normal

*Present address: Department of Fundamental Radiology, Faculty of Medicine, Kyoto University, Kyoto, Japan.

restitution of chromosome breaks, rather than on chromosome breakage itself.

The small positive effect demonstrated by this S-4 experiment is of definite scientific interest. The experiment however failed to confirm the existence of any large effect, such as had previously been suggested by other authors and which might constitute a special obstacle to prolonged manned space flights.

INTRODUCTION

Biological effects, of types usually associated with radiation damage, have been observed following both ballistic and orbital space flights (see, for example, refs. 1 and 2). These effects include mutation, production of chromosome aberrations, and cell killing. In some cases these effects were of magnitudes many times greater than would have been predicted from the radiation exposure received during flight. Such phenomena, if real, would be of obvious concern to manned space flight programs, and also of general interest to radiobiologists. An unpredicted radiobiological effect could be due to either, or to both, of two things. Since one component of the radiation encountered above the earth atmosphere (the heavy primaries) is not available for test use have in terrestrial laboratories, the possibility that these particles have unexpected biological effects must be admitted. It is possible also that other parameters associated with space flight, such as prolonged "weightlessness", do interact synergistically with radiation, to produce unexpectedly large effects. The S-4 experiment was prepared in order to test just such possibilities, and to settle the question of whether there are, in fact, large radiobiological effects following space flights. This experiment was executed with success during the Gemini III manned space flight of March 23, 1965.

EXPERIMENTAL DESIGN

A practical plan to test for synergism between radiation and space flight parameters such as "weightlessness" is to irradiate a thoroughly studied biological material with a known quantity and quality of radiation during the "zero-g" phase of an orbital space flight, and to compare the types and rates of effects thus found, with those observed in suitable "in-flight" and "ground" controls (see ref. 3). An increased effect in the experimental material, including the in-flight control, would be evidence of an effect of some space-flight parameter. On the other hand, any increased effect in the experimental material, that did not include

the in-flight control, would be evidence of a synergism between the radiation administered and some space flight parameter. Substitution of a whole series of doses and samples in this simple experimental plan allows determination of dose-effect curves, and the study of any effect observed in terms of the kinetics of the response studied, and, possibly, with elucidation of its mechanism. That was the plan that was adopted for the S-4 experiment.

The production of chromosomal aberrations is one of the best known of the biological effects of radiation (see ref. 4 for a recent review); hence, it was selected as a suitable response for the study. Human leukocytes were chosen as the experimental material because they offer several technical advantages: (1) the fact that the cells used are all in a uniformly sensitive stage in the cell cycle (G_1) when the whole blood is irradiated, either in vivo or in vitro; and also (2) because our group has had extensive experience with the system (refs. 5 to 10). The small volume and mass which could be alloted to the experimental device aboard the spacecraft precluded the use of X- or γ-rays to irradiate the blood samples, primarily because of the shielding which would have been necessary to protect the flight crew. β-rays, against which shielding is easy, were chosen instead. Radioisotope phosphorous 32 was selected as the source (1) because it emits only a single β-particle, (2) because the particle energy (average e = 0.7 MeV) is suitable, and (3) because ^{32}P had already been used extensively in radiobiology. The use of a liquid-phase biological test material, together with isotopic radiation sources, allowed a "plane parallel" irradiation geometry to be adopted. This provided a compact physical arrangement that would give reasonably homogeneous radiation exposures over the whole sample volume.

Because induction of chromosome aberrations is a non-linear function of dose, a graded series of four different radiation exposures, plus an unirradiated control, was used. In order to ensure against loss of one or more samples, two complete sets of blood samples were used, with blood from a different donor for each set. The experimental material thus consisted of ten 3-ml whole-blood samples, a pair irradiated with each of the radiation doses, and a pair unirradiated as the in-flight control. The simultaneous ground experiment (ground control) consisted of a complete duplicate set of samples drawn from the same donors and at the same time as was the in-flight material. As additional in-flight control, blood samples were obtained also from the flight crew, both before and after the mission.

EXPERIMENTAL DEVICE

The device developed to carry out the experiment is shown in figure 14-1. It includes a sealed aluminum box about 9 by 9 by 3.2 cm. From one end an operating handle protrudes. The major components of the device are illustrated in figure 14-2. The exploded, cut-away drawing (fig. 14-3) shows the arrangement of parts within the assembled device with the blood-sample holders and operating handle shown in the "nonirradiate" position. Each of the five epoxy-resin and fiberglass holders contains two sterile, heparinized, 3-ml blood samples in the form of discs 3 mm thick. The four blood-sample holders which are to be irradiated are inserted in the aluminum housing in tracks running between the paired aluminum and platium ^{32}P-source plate holders. When the operating handle is pushed in these four blood sample holders are moved into position between the pairs of ^{32}P-source plates, thus starting irradiation of the blood samples through the thin blood-chamber "window". When the operating handle is pulled out, the blood-sample holders are withdrawn, thus stopping the irradiation. The unirradiated control-blood sample holder is located behind, and shielded from, the ^{32}P-source plate array. The space above the control holder is occupied by an instrument-package assembly. The ^{32}P-source plate pairs are arranged in a graded series of total activities in a ratio of 1:2:3:4, so as to yield the required series of irradiation doses during the simultaneous exposure of the blood samples. The cross-section drawing (fig. 14-4) shows more clearly the geometrical relationships between the ^{32}P-sources and the blood samples.

A number of measuring devices were included within the experimental device in order to help confirm correspondences between the in-flight and the ground portions of the experiment. Two silver-metaphosphate fluoroglass-dosimeter rods were located within the stems of the blood-sample chamber-sealing screws (figs. 14-3 and 14-4), where they would record the dose received by each blood sample. The instrument package was designed to provide records of the temperature within each device during the experiment, and particularly records of excessively high or low temperatures, with a record of the time of irradiation. These records were written by means of spots of colored light moving slowly across strips of color film. The time is then read across the strips resulting on the developed film while the color at any given point indicates the temperature at that time. The times at which an irradiation is begun and ended are recorded by still another colored spot. The instrument package contains also a pair of large-volume silver-metaphosphate fluoroglass-dosimeter blocks. These measure the ambient radiation within the experimental device. A more complete description

of the design of this experimental device and of its qualifications for
flight use can be found in reference 11.

EXECUTION OF THE EXPERIMENT

The short time over which the blood samples would remain viable,
the relatively short half-life of radioisotope ^{32}P, and the tissue-
culture procedure required, in order to produce chromosome preparations
for analysis, made the actual carrying-out of the experiment a fairly
complex operation. The blood samples had to be obtained as late as
possible. The experimental devices then had to be assembled and tested.
The flight device had to be inserted into the spacecraft just shortly
before launch. Then, immediately upon recovery of the spacecraft, the
experimental device used in flight had to be recovered from the space-
craft, and opened. Tissue cultures had then to be made from each blood
sample, as well as from postflight blood samples from the flight crew.
To carry out this program, special facilities had to be provided at
the launch site, as well as on board the prime recovery vessel (and
on the vessels in the first- and secon orbit recovery areas as well).

Preflight

Two days before launch sterile peripheral blood samples were
obtained from the flight crew (as well as from the backup crew). Short-
term leukocyte cultures (ref. 12) were prepared and incubated at 37° C.
At approximately nine hours before launch, sterile peripheral blood
samples were obtained from two pretested donors. Two complete experi-
mental devices were then assembled and tested. Approximately 210 minutes
before launch, the flight device was mounted in an insulated bracket
located inside the righthand hatch of the spacecraft. The ground-control
experimental device was placed in a controlled-temperature cabinet, in
which the temperature was periodically adjusted so it constantly corre-
sponded to the temperature being read out from the spacecraft cabin.

Flight

After the launch phase of the flight had ended, the in-flight
experimental device became and remained essentially weightless, until
irradiation was started. The irradiation was initiated by the pilot
50 minutes and 18 seconds after liftoff. Twenty minutes later (70 min-
utes and 18 seconds after liftoff), the pilot terminated the irradiation.
The corresponding activation and deactivation of the ground experimental

device occurred at 52 minutes and at 72 minutes after liftoff, respectively. Except for minor accelerations produced by the "Texas burn" at 1:32:59 g.e.t., the "lateral burn" at 2:16:59 g.e.t, and the "preretroburn" at 4:21:23 g.e.t, the in-flight experimental device remained essentially weightless for approximately three and one-half hours following irradiation.

Postflight

Peripheral blood samples were obtained from the flight crew approximately 6-1/2 hours after launch. All blood samples had been put into culture by 10 hours after launch; those from the ground-control experimental device, at the launch site; and those from the in-flight samples, on the prime recovery vessel.

The crew pre-flight cultures were fixed the day after launch, approximately 72 hours after they had been made. The experimental cultures, plus the crew postflight cultures, were all fixed at approximately 77 hours after launch.

RESULTS

Postflight analysis of the fluoroglass dosimeters and of other instruments showed that the doses, the times of actuation, and the temperatures of the in-flight and ground-control experiments all agreed well. The instrument package-film records agreed well with the actuation- and temperature-information provided by other sources. Indications were that the flight experimental device reached a temperature of 30°C during assembly (i.e., during the Heliarc welding of the top). The temperature did not exceed 38°C nor drop below 14°C at any time during the preflight, flight, or recovery periods. The ground-control experimental device never became as warm; it remained between 29°C and 2°C during these same periods. Postflight determinations of circuit-element function of battery voltages, and of coulometer gap positions indicate that both instrument packages had functioned perfectly. No indicator of excessively high or low temperature had been activated. On both the in-flight and the ground-control instrument-package film records, the activation markers appear in proper position, and in that position only, thus agreeing well with the communciations records. That the exposures were of the required duration is confirmed by the fluoroglass dosimeters incorporated into the blood-sample chamber screws.

The 44 dosimeters were read on a fluorometer calibrated against fluoroglass standards which had been given known ^{60}Co γ-ray exposures at the National Bureau of Standards. The readings for each pair of dosimeters agreed well. Doses were also estimated for both preflight and postflight by means of both fluoroglass and Fricke-solution dosimetry. The results are presented in table 14-1. Reading values were averaged for the dosimeters from each blood sample. Both the readings and the dose estimates agreed well with both the theoretical expectations and with the results of previous control experiments. A large part of the approximately two-rad dose to the control-blood samples was due to Bremsstrahlung with a peak energy of about 65 keV. The large volume fluoroglass-dosimeter blocks located in the ground-control instrument package also registered this level of exposure. Those from the in-flight instrument package registered somewhat higher exposures.

All of the blood sample cultures were successful and yielded satisfactory chromosome preparations. Very little haemolysis was noted after the blood samples had been centrifuged, and no other evidence of gross cell damage was seen. For the entire experiment, a total of 4,600 cells were analyzed. The results are shown in table 14-II.

The flight-crew chromosome aberration analyses show no increase in aberration frequency due to the space flight. The two dicentric chromosomes seen in the samples from one crew member appear to be identical, and were without acentric fragments. They therefore cannot be attributed to the space flight. The deletion frequencies seen are typical of normal individuals.

The aberration frequencies seen in the control-blood samples are what is expected in cells exposed to such a low radiation dose (from β-ray leakage and Bremsstrahlung within the experimental devices). They agree well with what was seen in previous control experiments. The irradiated samples yielded the expected types of aberrations. Figures 14-5 and 14-6 illustrate the two major classes of aberration induced. The cell shown in figure 14-7 is normal, showing 46 chromosomes and no breaks, fragments, or rearrangements. The cell shown in figure 14-5 contains one chromosome deletion, with resulting acentric fragments. Because only one break is required, the yield of this type of aberration is a linear function of dose, and follows the expression

$$Y = a + bD$$

where Y is the yield, D is the dose, a is the spontaneous frequency, and b is the coefficient of aberration production. The cell illustrated

in figure 14-6 contains a dicentric chromosome and the resulting acentric fragments. This class of aberration, including rings as well as dicentric chromosomes, requires two independent chromosome breaks; consequently the yield is a function of the square of the dose and approximates the expression,

$$\underline{Y} = \underline{c}D^2$$

where c is the coefficient of dicentric production. The data of table 14-II were fitted to these expressions by iterative least-squares regression analyses. The resulting coefficients of aberration production are shown in table 14-III, together with those for a typical control experiment made prior to the flight ("Run 5").

The yields for ring and dicentric chromosomes in the in-flight and ground-control experiments and for deletions in the ground-control experiment agree well with the results of the previous control experiments. The ring and dicentric yields for the in-flight and ground-control experiments do not differ significantly from each other. The yield of deletions in the in-flight experiment, however, is roughly twice that seen in both the ground-control experiment and the previous control experiments. The difference is significant and, as can be seen from table 14-II, completely consistent.

DISCUSSION

The lack of aberrations in the blood samples obtained from the flight crew after the flight makes the possibility unlikely that the radiation encountered during such a space flight produces any unprecedented effect, at least for genetic systems, such as for the one used in this experiment. This conclusion is strengthened by the low aberration levels seen in the flight contol-blood samples. All physical evidence contradicts the possibility that the flight and the ground-control samples received significantly different radiation doses. In addition, the aberration data show the doses to be substantially the same. If the high-deletion yields from the flight samples were due to their having received a higher does than the ground-control samples received, then the ring and dicentric chromosome yields would also have been increased in the flight samples. The possibility that something associated with the spaceflight produced chromosome breaks quite independently of the radiation can, of course, be dismissed on several grounds.

It appears, then, that some space flight parameter does in fact interact synergistically with radiation. Since only single-break aberrations (deletions) show this effect, it seems likely that the effect is on the chromosome-rejoining system, rather than on breakage itself. If it were on breakage, the effect would be the same as increasing the dosage, which would then affect all aberration classes. Stated differently, this interaction would seem to be on the cell's ability to repair damage caused by radiation, rather than on the amount of the damage incurred. Although this effect is not large from the point of view of radiation cytogenetics, it is certainly of great interest.

Further experiments will be necessary, however, in order to confirm the synergistic effect and to determine just which space flight parameter, or parameters, are involved, as well as the mechanism of the action.

ACKNOWLEDGMENTS

REFERENCES

1. Sisakyan, N.M., ed.: Problemy Kosmicheskoy Biologii. Vol. 1, U.S.S.R. Academy of Sciences Publishing House, Moscow, 1962 (NASA TT F-174).

2. Sisakyan, N.M.; and Yazdovskiy, V. I., eds: Problemy Kosmicheskoy Biologii. U.S.S.R. Academy of Sciences Publishing House, Moscow, 1962 (JPRS: 18,395; OTS: 63-21437).

3. Environmental Biology Committee Panel on Radiation Biology, Space Science Board: Position Paper on Theoretical Aspects of Radiobiology as Applied to the Space Program. NAS-NRC, Washington, 1963.

4. Evans, H. J.: Chromosome Abberations Induced by Ionizing Radiations. International Reviews of Cytology 13; 1962. pp. 221-321.

5. Bender, M. A and Gooch, P. C.: Types and Rates of X-ray-Induced Chromosome Aberrations in Human Blood Irradiated in Vitro. Proc. National Academy of Sciences (Wash.) vol. 48, 1962, pp. 522-532.

6. Bender, M. A and Gooch, P. C.: Persistent Chromosome Aberrations in Irradiated Humans. Radiation Research, vol. 16, 1962, pp. 44-53, and Radiation Research, vol. 18, 1963, pp. 389-396.

7. Bender, M. A; Gooch, P. C.; and Prescott, D. M.: Aberrations Induced in Human Leukocyte Chromosomes by ^{3}H-labeled Nucleosides. Cytogenetics, vol. 1, 1962, pp. 65-74.

8. Bender, M. A and Gooch, P. C.: Chromatid Type Aberrations Induced by X-rays in Human Leukocyte Cultures. Cytogenetics, vol 2, 1963, pp. 107-116.

9. Gooch, P. C.; Bender, M. A.; and Randolph, M. L.: Chromosome Abberations Induced in Human Somatic Cells by Neutrons. IAEA Symposium on the Biological Effects of Neutron Irradiations, Brookhaven National Laboratory, Oct. 7-11, 1963.

10. Bender, M. A: Chromosome Aberrations in Irradiated Human Subjects. Annals of the New York Academy of Sciences, vol. 114, 1964, pp. 249-251.

11. Oak Ridge National Laboratory: Synergistic Effect of Zero-G and of Radiation on White Blood Cells. An experiment for the Gemini III manned space flight. Annual report, period ending June 30, 1964. ORNL - TM - 940, 1964.

12. Moorhead, P. S.; Nowell, P. C.; Mellman, W. J.; Battips, D. M.; and Hungerford, D. A.: Chromosome Preparations of Leukocytes Cultured from Human Peripheral Blood. Experimental Cell Research, vol. 20, 1960, pp. 613-616.

TABLE 14-7. - DOSE ESTIMATES FROM FLUOROGLASS DOSIMETERS INCORPORATED

IN EXPERIMENT S-4 BLOOD-SAMPLE CHAMBERS

Device	Theoretical dose (rad)	Average reading (μA)*	Net β-ray dose (μA)	Estimate of β-ray dose (rad)	Estimated total dose (rad)
Ground Control	2	4.5	-	-	2
	45	18.1	13.6	50	52
	91	27.7	23.2	86	88
	136	41.9	37.4	138	140
	181	51.0	46.5	172	174
Flight device	2	4.2	-	-	2
	45	18.0	13.8	51	53
	91	29.5	25.3	94	96
	136	38.3	34.1	126	128
	181	46.8	42.5	157	159

*As the instrument was set up, one μA equals two Co^{60} γ-ray rad.

TABLE 14-II.- RESULTS OF EXPERIMENT S-4 CHROMOSOME ABERRATION ANALYSES

Subject	Sample	Cells scored	Estimated dose (rad)	Chromatid deletions	Chromosome deletions	Ring and dicentric chromo- somes
			Crew			
A	Pre-fl	100	-	3	0	0
	Post-fl	200	-	2	0	0
B	Pre-fl	100	-	0	1	1*
	Post-fl	200	-	0	1	1*
			Experiment			
	Gr	400	2	3	3	1
	Fl	400	2	1	3	0
	Gr	400	52	1	6	5
	Fl	400	53	3	14	1
	Gr	400	88	5	13	13
	Fl	400	96	6	28	16
	Gr	400	140	6	32	43
	Fl	400	128	6	48	34
	Gr	400	174	6	45	36
	Fl	400	159	2	88	48

*These two dicentric chromosomes appear identical; both lacked acentric fragments.

TABLE 14-III.- COEFFICIENTS OF ABERRATION PRODUCTION FOR S-4 EXPERIMENT

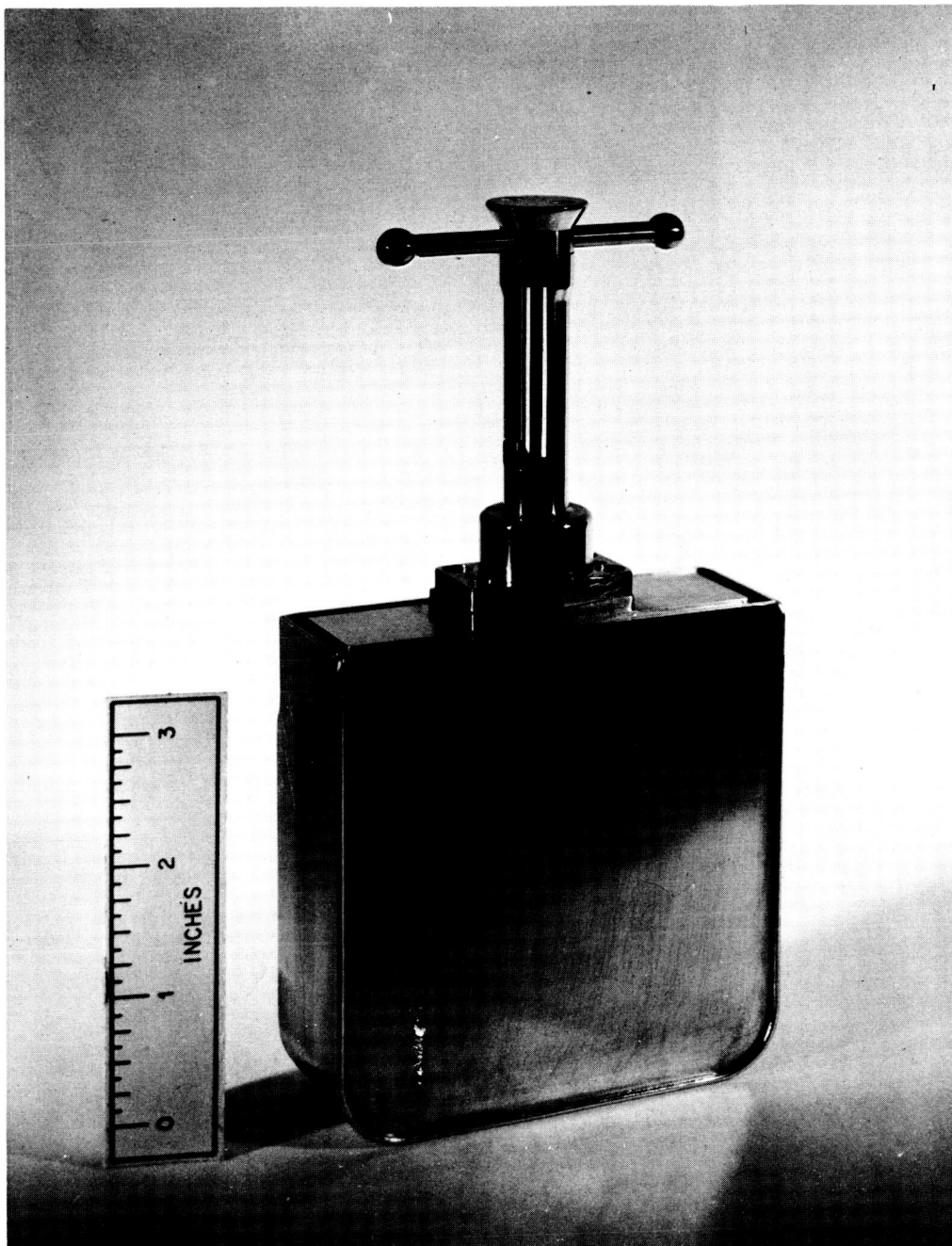|	Deletions $\left(\times 10^4\right)$ per cell per rad	Rings and dicentrics $\left(\times 10^6\right)$ per cell per rad^2
Ground control	4.79 ± 0.72	3.23 ± 0.59
In-flight	9.11 ± 1.02	3.48 ± 0.53
Run 5	5.36 ± 0.86	2.66 ± 0.60

Figure 14-1.- Ths S-4 experimental device before final sealing.   The
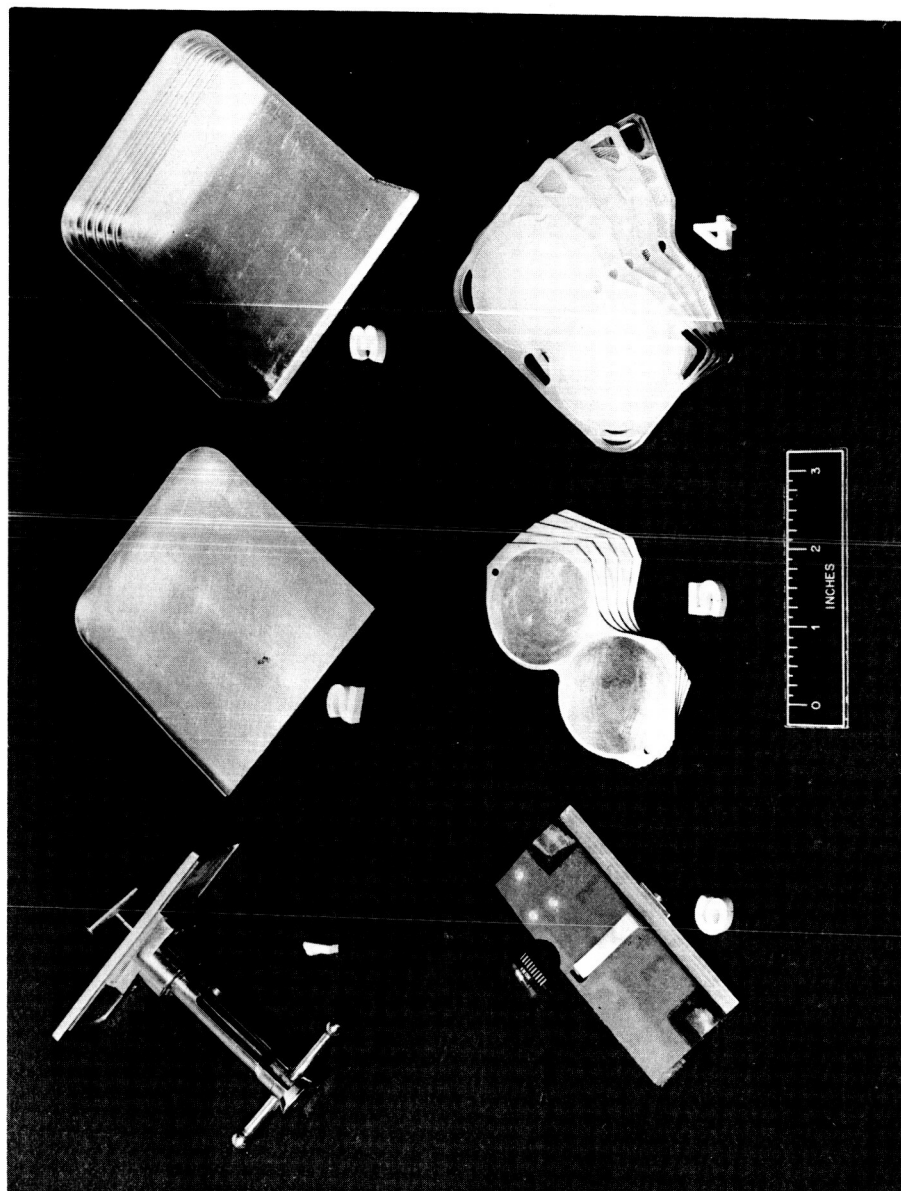operating handle is in the "non-irradiate" position.

Figure 14-2.- Major components of the S-4 experimental device showing: 1, operating handle and top assembly; 2 and 3, aluminum housing before welding; 4, set of five fiberglass-reinforced blood sample holders; 5, set of five aluminum and platinum ^{32}P β ray source plates; 6, instrument package with shorting plug.
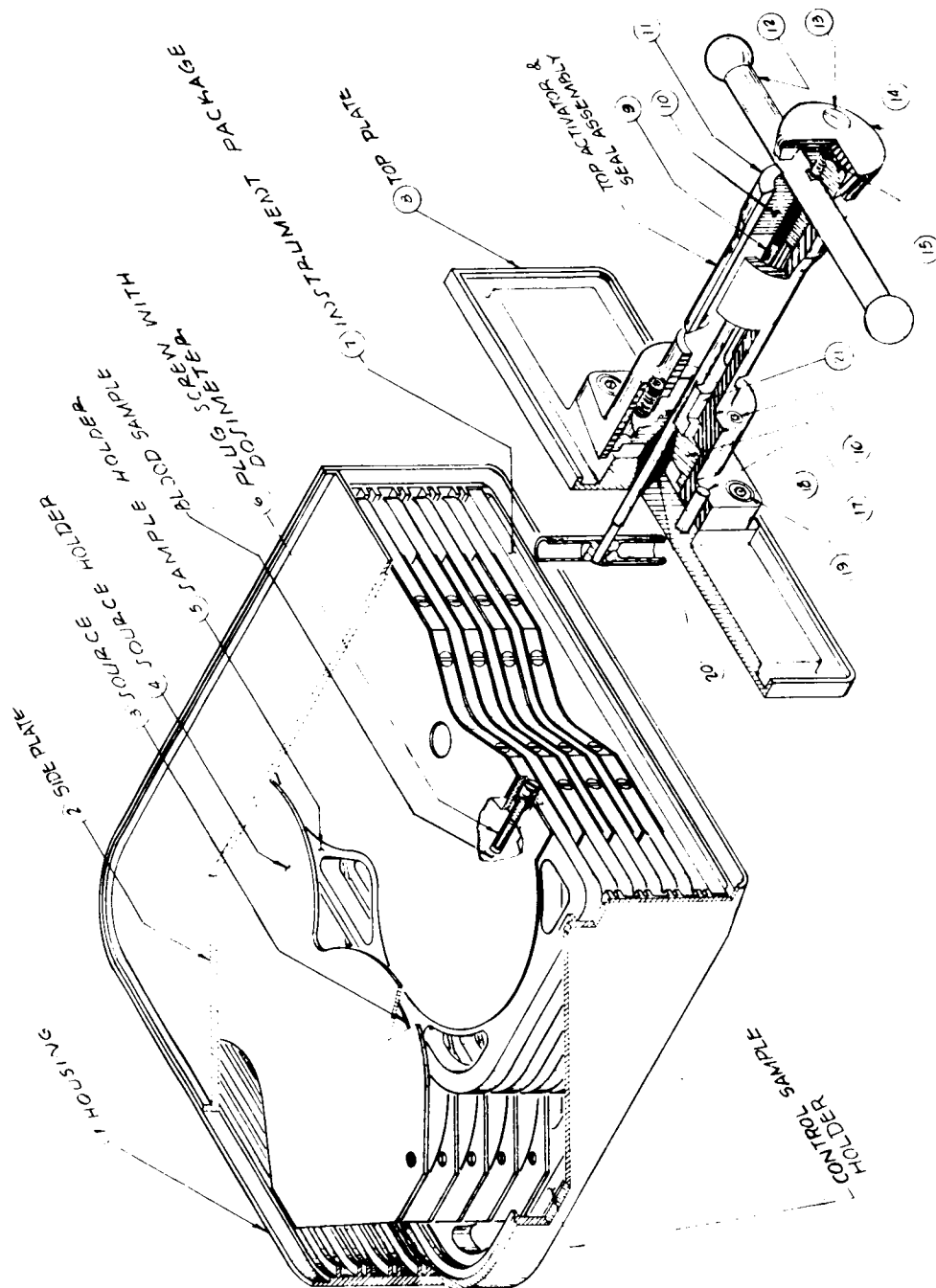
Figure 14-3. — Cross-section drawing of the experimental device showing the geometrical relationships between the blood samples and the $^{32}P\beta$ ray source plates. The blood sample holders are shown in the "non-irradiate" position. During irradiation the blood sample holders are moved into the vacant spaces between the paired source plates.
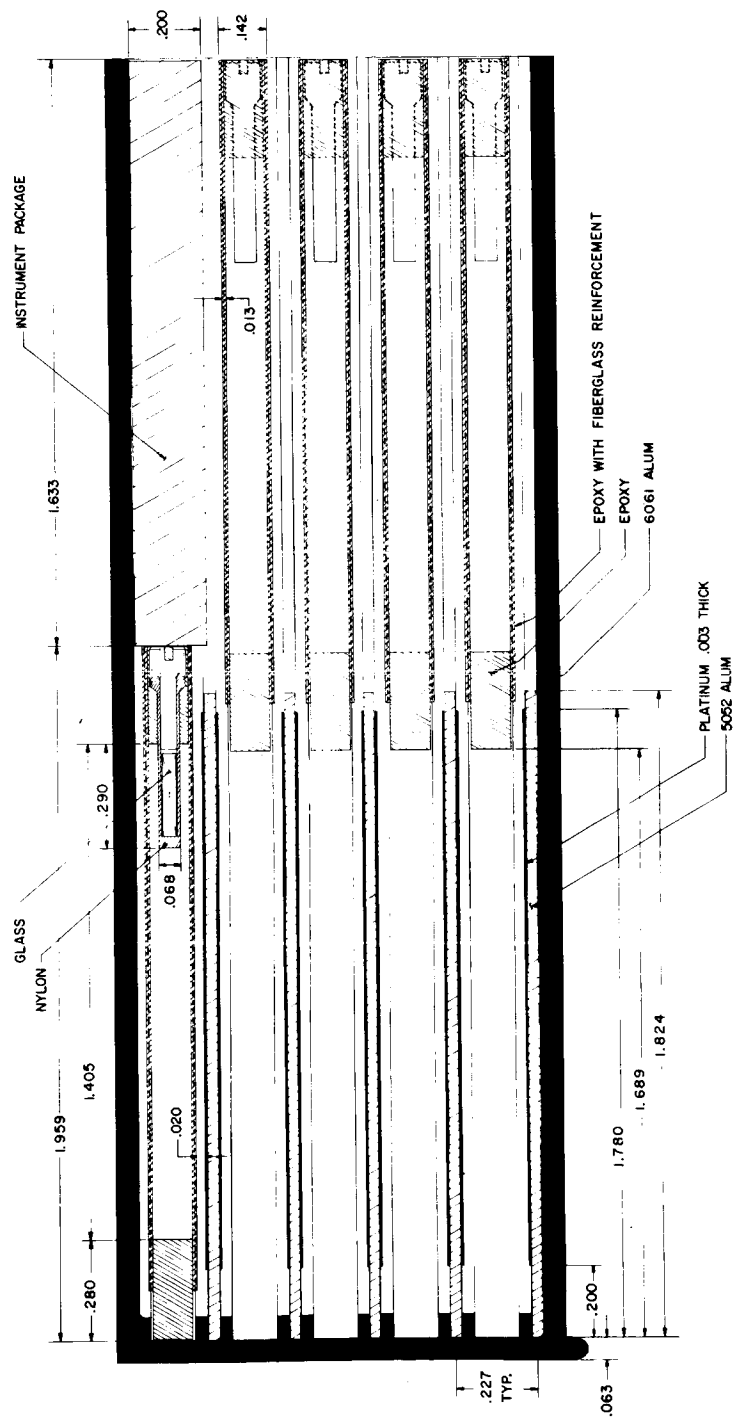
Figure 14-4.- Exploded, cut-away drawing of the experimental device showing the relationships between the component parts. The blood sample holders and the operating handle are shown in the "non-irradiate" position.

Figure 14-5.- Irradiated cell showing a single-break
chromosome deletion (arrow).

Figure 14-6.- Irradiated cell showing a typical two-break aberration, a dicentric chromosome with fragment (arrows).

Figure 14-7.- Chromosome preparation of a normal unirradiated cell
without chromosome breaks, fragments, or rearrangements.